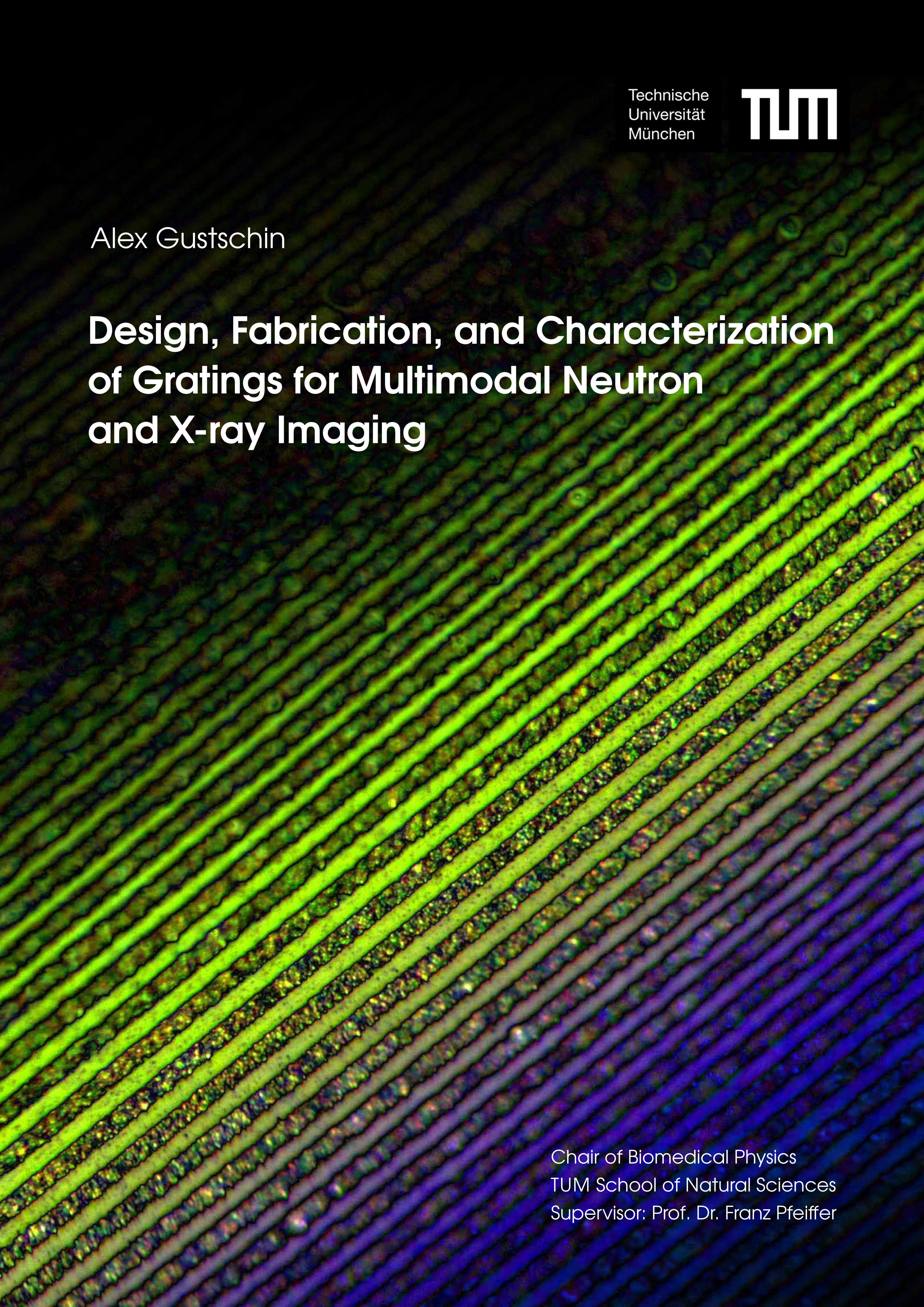

Technische
Universität
München

Alex Gustschin

Design, Fabrication, and Characterization of Gratings for Multimodal Neutron and X-ray Imaging

Chair of Biomedical Physics
TUM School of Natural Sciences
Supervisor: Prof. Dr. Franz Pfeiffer

TECHNISCHE UNIVERSITÄT MÜNCHEN
TUM School of Natural Sciences

Design, Fabrication, and Characterization of Gratings for Multimodal Neutron and X-ray Imaging

Alex Gustschin

Vollständiger Abdruck der von der TUM School of Natural Sciences der Technischen Universität München zur Erlangung eines

Doktors der Naturwissenschaften (Dr. rer. nat.)

genehmigten Dissertation.

Vorsitz: Prof. Dr. Karen Alim

Prüfer*innen der Dissertation:

1. Prof. Dr. Franz Pfeiffer
2. Prof. Dr. Christian Pfleiderer

Die Dissertation wurde am 28.06.2023 bei der Technischen Universität München eingereicht und durch die TUM School of Natural Sciences am 12.12.2023 angenommen.

Abstract

Differential phase-contrast and dark-field imaging with X-rays and neutrons are enabled by an interferometric arrangement of absorption and phase gratings which allow exploiting the wave properties of the radiation for multimodal contrast formation. A widespread optical configuration known as the Talbot-Lau interferometer allows using conventional low-coherence radiation sources and common low-resolution pixel detectors for these novel image modalities. Numerous studies have evaluated their potential for diagnostical applications and non-destructive testing, yielding particularly promising results for lung imaging. However, some technical challenges related to the fabrication of the necessary gratings remain a bottleneck for the cost-effective and reliable introduction of this method for clinical application.

The present work first reviews current fabrication and characterization methods for X-ray and neutron diffraction gratings, discussing their possibilities and limitations. Subsequently, a novel approach to producing absorption gratings by deposition of micro-sized particles into high aspect ratio grating structures etched into silicon is developed. For X-ray absorption gratings, tungsten is used as an absorber material and is deposited from a particle dispersion by a centrifugation method to improve the particle penetration in the deep trenches. For neutron absorption gratings, ball-milled gadolinium powder is deposited from a dispersion without centrifugation. After manual surface cleaning, several methods are applied to characterize the fabricated gratings. Tests with X-ray and neutron Talbot-Lau interferometers showed good visibility and imaging performance.

As an application example, combined multimodal hard X-ray and thermal neutron tomography were conducted on a geological sample. The complementary character of both methods was discussed and the potential advantages of using neutrons for strongly absorbing objects were investigated.

In the last part, a single grating multimodal X-ray imaging method based on diffractive 2D phase modulators, the so-called Talbot Array Illuminators, was developed. Compared to conventional 2D phase gratings or diffusers used in Speckle-based Imaging, the novel modulators create a diffraction pattern with a higher compression ratio allowing for higher visibilities at relatively low periods. This enables very efficient sampling schemes and high phase sensitivity and resolution with a low number of exposures. With a demonstrated resolution of 3µm in phase tomography and a contrast-to-noise ratio of >50 between the embedding material and the soft tissue of the sample, the method provides a convenient pathway to quantitative, high-resolution 3D virtual histology.

Zusammenfassung

Differentielle Phasenkontrast- und Dunkelfeld-Bildgebung mit Röntgen- und Neutronenstrahlen werden durch eine interferometrische Anordnung von Absorptions- und Phasengittern ermöglicht, wobei Welleneigenschaften der Strahlung für eine multimodale Kontrastbildung ausgenutzt werden. Eine weit verbreitetes, optisches System, das als Talbot-Lau-Interferometer bekannt ist, ermöglicht die Verwendung von Strahlungsquellen mit geringer Kohärenz und herkömmlicher Pixeldetektoren mit geringer Auflösung für diese neuartigen Bildmodalitäten. In zahlreichen Studien wurde ihr Potenzial für diagnostische Anwendungen und zerstörungsfreie Prüfungen untersucht, wobei besonders vielversprechende Ergebnisse für die Lungenbildgebung erzielt wurden. Einige technische Herausforderungen im Zusammenhang mit der Herstellung der erforderlichen Gitter stellen jedoch nach wie vor einen Engpass für die kosteneffiziente und zuverlässige Einführung der Methode für die klinischen Anwendung dar.

Die vorliegende Arbeit gibt zunächst einen Überblick über die derzeitigen Herstellungs- und Charakterisierungsmethoden für Röntgen- und Neutronenbeugungsgitter und diskutiert deren Möglichkeiten und Grenzen. Anschließend wird ein neuartiger Ansatz zur Herstellung von Absorptionsgittern durch Einbettung mikroskopisch kleiner Partikel in Gitterstrukturen mit hohem Aspektverhältnis, die in Silizium geätzt werden, entwickelt. Für Röntgenabsorptionsgitter wird Wolfram als Absorbermaterial verwendet, das aus einer Partikeldispersion durch ein Zentrifugationsverfahren eingelagert wird, um das Eindringen der Partikel in die tiefen Gräben zu verbessern. Für Neutronenabsorptionsgitter wird kugelgemahlenes Gadoliniumpulver aus einer Dispersion ohne Zentrifugation abgeschieden. Nach der manuellen Oberflächenreinigung werden verschiedene Methoden zur Charakterisierung der hergestellten Gitter angewandt. Tests mit Röntgen- und Neutronen-basierten Talbot-Lau-Interferometern zeigen eine hohe Visibilität und gute Eigenschaften in der Bildgebung.

Als Anwendungsbeispiel wurde eine kombinierte multimodale Tomographie mit harter Röntgenstrahlung und thermischen Neutronen an einer geologischen Probe durchgeführt. Der komplementäre Charakter beider Methoden wurde diskutiert und die potentiellen Vorteile des Einsatzes von Neutronen bei stark absorbierenden Objekten wurden erörtert.

Im letzten Teil wurde eine multimodale Röntgenbildgebungsmethode mit einem einzigen Gitter implementiert, die auf diffraktiven 2D-Phasenmodulatoren, sogenannten Talbot-Array-Illuminatoren, basiert. Im Vergleich zu konventionellen 2D-Phasengittern oder Diffusoren, die in der Speckle-basierten Bildgebung verwendet werden, erzeugen die neuartigen Modulatoren ein Beugungsmuster mit einem höheren Kompressionsverhältnis, was höhere Kontraste bei relativ niedrigen Perioden erzeugt. Dies ermöglicht sehr effiziente Abtastschemata und eine hohe Phasenempfindlichkeit und Auflösung bei einer geringen Anzahl von Phasenschritten. Mit einer erreichen Auflösung von 3 µm in der Phasentomographie und einem Kontrast-Rausch-Verhältnis von >50 zwischen dem Einbettungsmaterial und dem weichen Gewebe der Probe bietet die Methode eine praktische Realisierung von quantitativer, hochauflösender virtuellen 3D-Histologie.

Contents

1 Introduction

"We have to remember that what we observe is not nature in itself but nature exposed to our method of questioning."

— Werner Heisenberg

1.1 Historical Background

Our understanding of the micro- and macrocosm has been consistently shaped by the imaging methods that have allowed us to observe nature, be it down on the atomic level or all the way out to the distant galaxies. Antiquity and the Middle Ages – in particular the Greek and the Islamic world – are peppered with impressive insights from astronomical observations and findings in the field of geometrical optics. However, the development of high-quality optical instruments only began to take place in early 17th-century Europe. This was the time of the scientific revolution and a new era of discoveries. Early telescopes made possible the precise observation of celestial bodies, challenging centuries-old assumptions concerning our universe. At the same time, the first optical microscopes lead to ground-breaking progress in the study of living organisms. The early pioneer of lens fabrication and optical microscopy, Antoni van Leeuwenhoek, was the first to discover microorganisms, estimating there to be several thousand in a single drop of water. His work described the arteries and veins branching out into fine capillaries with diameters close to the size of a red blood cell, and he observed the latter moving through these minuscule vessels. Among his most important achievements was the description of the entire life and reproductive cycle of various species of animals, providing strong evidence against the – at that time – widespread theory of spontaneous generation. While the early optical systems were built based on the principles of geometrical optics further development needed a more fundamental understanding of diffraction, leading to the wave theory of light. Although these diffraction effects had been observed before, it was Thomas Young with his famous double-slit interferometer who headed the systematic study of this property and provided a sound explanation with his concept of wave interference in 1803. Later, Joseph von Fraunhofer, who fabricated various optical instruments and studied the spectral effects of light, described diffraction phenomena from a single slit. He also fabricated diffraction gratings for the measurement of the refractive properties of glasses. It was with one of these gratings that William Talbot discovered the eponymous Talbot effect in 1836 – though he was not able to provide the theoretical explanation for the alternating appearance of grating lines which varied in color with increasing propagation distance. Ultimately, John Strutt – better known as Lord Rayleigh – explained this effect as a consequence of Fresnel diffraction. Later in 1873, Ernst Abbe identified the diffraction of light in optical systems as the limiting factor for resolution. He argued that close features in an image can only be resolved when at least the first-order diffraction maximum is collected by the lens. From that, he deduced that the resolution is fundamentally limited by the wavelength and the numerical aperture of the objective lens. An optically dense medium between the objective and the sample (*Immersion Microscopy*) can be used to further increase the resolution, achieving a limit at about 200 nm with visible light.

At the beginning of the 20th century, demand for resolving power beyond this limit grew as objects in the nanometre range became of interest. For instance, Michael Faraday made colloidal solutions with gold particles and assumed that their color depended on the size of these particles. However, he had no way to measure their sizes because they were in the lower nanometre range. One approach to detect such particles turned out to be the contrast-enhancing method of dark-field microscopy. Through a sophisticated arrangement of the optics, the illumination of the specimen in this modality is performed outside of the beam path, resulting in a dark background. Only the light scattered by thin microstructures enters the objective and contributes to the image formation. However, this method only creates a visible signal (Tyndall cone) without providing any information on the size or shape of a particle. Henry Siedentopf and Richard Zsigmondy developed a sophisticated system with thin light sheet illumination from the side which allowed them to visualize and count individual particles in a defined volume. With their so-called *Ultramicroscope*, they were able to determine particle sizes of 4 nm in gold ruby glass from the known gold concentration and particle count [Mappes, 2012]. Zsigmondy won the Nobel Prize in Chemistry in 1925 for his study of colloids, which was in large part made possible by the Ultramicroscope. In 1908, Jean Baptiste Perrin used the Ultramicroscope to study Brownian motion on nanoparticles and confirmed Einstein's predictions, settling a century-long debate on the atomic theory. For his work, Perrin received the Nobel Prize in Physics in 1926. In 1909 Robert Millikan and Harvey Fletcher used the same imaging mechanism to observe the motion of nano-sized oil droplets in an electric field to determine the elementary electric charge. This discovery earned Millikan the Nobel Prize in Physics in 1923. As these examples show, the observation of particles beyond the range of classical diffraction-limited optical microscopes provided incredibly valuable insights.

Besides scattering and absorption, image contrast can also result from refraction within a specimen. Spatial modulation of the refractive index in a transparent sample changes the beam path and alters the intensity modulation. This is the same effect one can observe in the hot air flow above a candle flame or a fire, which creates a density fluctuation in the air and distorts the image seen in the background. Robert Hooke and later August Toepler developed different optical setups to visualize and capture these modulations. This method is often called *Schlieren photography* and is still used to study phenomena such as supersonic wave propagation or thermal convection in air. In 1932 Frits Zernike developed an optical system to apply this contrast mechanism to optical microscopy for transparent biological samples which do not provide enough contrast by light absorption. The phase-contrast microscope uses a condenser annulus before the specimen and a phase shift ring with a grey filter to bring the background illumination and the light refracted by the specimen into constructive interference, thereby creating a strongly visible intensity modulation. This method was particularly successful in life cell imaging and led to several similar developments including differential interference contrast and Hoffman modulation microscopy. Frits Zernike was awarded the Nobel Prize in Physics in 1953 for the introduction of this versatile imaging method.

To push the limits of the resolvable even further, the wavelength can be reduced according to the diffraction limit. However, radiation beyond the ultraviolet range is strongly absorbed by most materials, which makes transmissive optics hardly applicable. It has also proven difficult to produce radiation in the sub-100 nm range without large and expensive synchrotron facilities or plasma sources. For this reason, the idea of using electrons instead of photons was pursued. As known from quantum physics, electrons have a de-Broglie wavelength, and it lies in the sub-nm range for strongly accelerated electrons. Several years after the development of electromagnetic lenses, in 1933, Ernst Ruska demonstrated a *Transmission Electron Microscope* (TEM) with a superior resolution to optical microscopes. Several years later Manfred von Ardenne introduced *Scanning Electron Microscopy* (SEM), which further increased the resolution and application range. As the contrast formation mechanism has some fundamental differences compared to optical microscopy a suitable sample preparation is necessary. In TEM mode, the specimens have to be extremely thin while in SEM, they should ideally be covered with a thin conducting layer to avoid image artifacts. Electron microscopy opened the door to nanoscience and, alongside related semiconductor fabrication techniques, has paved the way for the development of advanced electronics.

The resolution of electron microscopy is surpassed by two scanning probe microscopy methods developed in the later 1980s by Gerd Binnig and Heinrich Roher at IBM: *Scanning Tunneling Microscopy* (STM) and *Atomic Force Microscopy* (AFM). These methods use a tiny, sharp probe that is scanned above the sample surface. In AFM the probe is oscillated above the surface and the atomic forces between the cantilever and the sample result in measurable frequency deviations which are used as a feedback signal to map the surface in the raster scan. In STM the quantum tunnel effect is exploited to induce a current between the probe and the sample surface, which is used as the feedback signal. These methods achieve atomic resolution, i.e. one can image atomic lattices and even individual electron orbitals of molecules. Further, it allows the manipulation of individual atoms or molecules by picking them up and placing them in a desired environment. Today, scanning probe microscopy techniques are combined with a variety of other methods such as spectroscopy to gain additional information about the imaged specimen. In 1986 Ernst Ruska, Gerd Binnig, and Heinrich Roher were awarded the Nobel Prize in Physics for the development of their new microscopy techniques.

Despite an excellent resolution down to 1 nm and below, electron and scanning probe microscopy have a decisive disadvantage with biological samples. Since the specimens are scanned under a vacuum they have to be dried or cryogenically frozen to avoid damage to the sample and the emergence of vapor during evacuation. Although there are SEM, STM, and AFM systems that are optimized for certain biological boundary conditions, the observation of biological processes in liquids, as is feasible with optical microscopy, is impossible. For this reason, a series of alternative optical microscopy methods with improved resolution have been developed, often referred to as *super-resolution microscopy.* They use chemical compounds named fluorophores that reemit light upon excitation. These compounds are chemically attached to bioactive molecules and can be used to optically stain certain structures and trace dynamic processes. Upon excitation of a small volume in the sample with a scanned focus the fluorophores light up and can be detected and located by the exact knowledge of the focus position. In *Stimulated Emission Depletion Microscopy* (STED) the focus can be made even narrower by selective deactivation of the fluorophores around the main excited focal spot. With that, a resolution in the lower two-digit nm range is achieved. Similar super-resolution methods even allow tracing single molecules in cells. Recent progress even allows tracking protein movement with a spatiotemporal precision of 1.7 nm per millisecond [Wolff, 2023]. One must, however, keep in mind that the structures are not directly resolved. Instead, they generate signals that allow their localization and spatial correlation to other structures, which can be, for example, stained with another color. Nevertheless, this conjunction of biological functionality and imaging has proven to be extremely versatile and offers inexhaustible potential in life sciences.

For their development of optical super-resolution imaging, Eric Betzig, Stefan Hell, and William Moerner were awarded the Nobel Prize in Chemistry in 2014.

Parallel to the development of these modern microscopy techniques, a new imaging modality came to be with the discovery of X-rays by Wilhelm Conrad Röntgen in 1895. One fascinating aspect of this type of radiation is that it penetrates many materials, including the human body, making possible the non-destructive imaging of internal structures within optically opaque objects. Röntgen quickly recognized the potential for medical applications as he found that bones absorb X-rays stronger than soft tissue. General excitement soon followed as images of body parts with clearly distinguishable bones enabled quick and reliable diagnoses of fractures and the identification of foreign bodies after injury. Just within a year after Röntgen's publication, over one thousand papers related to the subject were published [Behling, 2023]. Rarely has a discovery in physics created such resonance and experienced such a rapid transfer to medical applications. As radiography equipment improved, more and more diseases, such as tuberculosis during World War I, became diagnosable with X-rays. Röntgen was awarded the first Nobel Prize in Physics in 1901 "in recognition of the extraordinary services he has rendered by the discovery of the remarkable rays subsequently named after him".

A single projectional X-ray radiograph does not provide any information about the depth of certain features – information that is very beneficial for many diagnostical tasks. Therefore, quite some effort was made to develop systems that would display the features from a given plane inside a given object. From the 1930s on, this was achieved by the synchronized movement of the source and the detector in opposite directions, keeping the features in the target plane in focus while out-of-plane structures were blurred. In the 1960s, both Allan Cormack and Godfrey Hounsfield independently experimented with a new, more dose-efficient, and powerful approach called *computed tomography* (CT). In their schemes, the imaged object was recorded from different angles, and a 3D image was mathematically reconstructed from the measured transmission values. This method quickly established itself in clinical radiology and its pioneers Cormack and Hounsfield were awarded the Nobel Prize in Physiology or Medicine in 1979. It is also worth mentioning that the principles of tomographic reconstruction were applied with great success to many other domains of imaging. *Magnetic Resonance Imaging*, *Positron Emission Tomography*, and *Optical Coherence Tomography* are a few prominent examples. A more detailed description and mathematical treatment of CT are covered in Chapter 2.4.

Despite its success in medicine, X-ray imaging had to overcome serious technical challenges before becoming an established microscopy technique. Highly coherent X-ray sources, optics, and high-resolution detectors had to be developed and made accessible to the wider research community. The simplest approach to achieving a high-resolution system is to use an X-ray source with a small spot size and a high-resolution detector. With additional geometric magnification, it is possible to achieve decent resolutions in the single digit µm range. Two-dimensional flat panel X-ray detectors enabled versatile cone beam CT systems which remain reliable workhorses in various industrial applications such as non-destructive testing. The demand for sub-µm resolution, mainly for the study of biomedical samples, facilitated the development of X-ray optics. While there were some early developments from the 1940s with grazing-incidence reflective mirrors, the breakthrough was achieved with the emergence of highly coherent synchrotron sources and Fresnel zone plates that acted as lenses. Making available high fluxes of radiation and monochromatic filtration, these facilities saw the birth of a plethora of new multimodal imaging techniques (e.g. elemental mapping by X-ray fluorescence analysis) that could be combined with X-ray imaging and CT. Finally, the steep rise in available computing power enabled algorithms that could iteratively retrieve the spatial distribution of the refractive index from the propagated and magnified diffraction patterns acquired in a raster scanning process (*Ptychography*). This approach overcomes the fabrication-related deficiencies of the optics and is theoretically only limited by the wavelength [Pfeiffer, 2017]. Ptychography can be seen as the pinnacle of 3D X-ray microscopy, with an isotropic resolution reaching 16 nm [Holler, 2014]. However, this precision comes at the cost of high experimental and algorithmic complexity. The field of view is not directly limited since it is a scanning approach, but the samples are typically <50 µm in diameter due to other practical reasons.

Another imaging technique that is also able to penetrate opaque and dense matter is *Neutron Radiography*. After the discovery of the neutron in 1932, the idea to use neutrons for imaging was pursued by Hartmut Kallmann and his assistant Ernst Kuhn in Berlin. Kallmann lost his employment at the Kaiser Wilhelm Institute in Berlin due to his Jewish descent and the upcoming antisemitic laws. He nevertheless continued his research, without any formal employment, in an improvised laboratory in a former horse stable that was provided to him by the I.G. Farben company. After developing the equipment and successfully acquiring the first radiographs in 1938, his work was blocked from release due to racial discrimination and could only be published after the end of World War II in 1948. Despite intensive research in nuclear physics in the 1950s, neutron imaging developed slowly since it was dependent on expensive and sophisticated neutron sources. In the 1960s, several works were published elaborating on the methods, capabilities, and applications of neutron radiography. A short introduction is also given in Chapter 2.2 of this work.

As with the other imaging methods, digital image sensors brought decisive progress to method development and enabled the acquisition of dynamic processes and quantitative image processing algorithms. However, high-resolution neutron imaging is still complicated by several factors. To obtain a sharp image, the source size (usually shaped by a pinhole) has to be sufficiently small and the sample must be placed close to the detector to avoid geometrical blur. Consequently, geometric magnification is only made possible by choosing a smaller pinhole with even less flux. Additionally, the absorption of a neutron in the scintillator material by a nuclear reaction creates multiple light spots, that can be displaced by several µm from the original impact point. With all that, a resolution of 5 µm or below is only achievable with a very thin scintillator screen and extended exposure times. Common applications for neutron radiography are non-destructive analysis of samples involving heavy metals or organic materials, where X-ray imaging does not provide sufficient penetration or contrast. Some examples are batteries, fuel cells, geological samples, archaeological artifacts, building materials, or water uptake in plants.

1.2 Motivation

The historical overview shows that imaging techniques are highly optimized for specific applications, deciding which type of radiation is used, which contrast mechanisms are employed, and which resolution and field of view are provided. In order to further improve the imaging performance and expand the field of application, the established principles of different methods are often combined. For example, the strong penetrating power of X-rays can be extended with the phase contrast mechanism known from optical microscopy to study large opaque samples and gain more sensitivity for soft tissue. The use of wave properties of X-rays for imaging is a relatively recent development. With the advent of strongly coherent X-ray sources and high-resolution detectors, propagation-based phase imaging has become widely used at synchrotron facilities. This method does not require optics and only relies on intensity modulations created by phase-shifting features in the sample which appear after some propagation in space. A decisive disadvantage of this method is its lower phase sensitivity and that certain assumptions about the composition of the sample have to be made for the reconstruction. Therefore, other methods were developed using optics to modulate the wavefront and translate the sample's phase-shifting features into deflected intensity spots. This approach acquires quantitative data on the electron density and allows a robust reconstruction of a larger variety of specimens. This thesis addresses a further recent development using 2D phase arrays fabricated on thin silicon wafers, enabling quantitative phase CT with a resolution of 3 µm at a synchrotron source [Gustschin, 2021].

The most decisive advantage of using modulators as opposed to propagation-based methods is the possibility to use conventional X-ray sources and large-pixel detectors with some additional experimental adaptations. The most widely spread optical system, the so-called *Talbot-Lau Interferometer* [Pfeiffer, 2006b], has been used to study different biological organs and their respective pathologies with a focus on soft tissue contrast. For example, the phase sensitivity of such a system is high enough to distinguish different kinds of soft tissue content, such as lipid, protein, and water [Willner, 2016]. High-sensitivity measurements mapping the electron density distribution have also enabled the visualization of interior structures of the human cerebellum in centimeter-sized samples [Birnbacher, 2016]. Also, better identification of breast cancer tissue compared to the conventional attenuation signal was addressed and correlated with histology [Hellerhoff, 2019]. Some further developments allow phase imaging of an entire fixated murine sample with excellent organ differentiation and a sub-50 µm resolution [Viermetz, 2018]. The study of such specimens with low soft tissue contrast employing grating-based phase contrast imaging is a valuable contribution to the emerging field of virtual histology. In contrast to conventional histology, where a fixated sample is dissected in thin slices and studied by microscopy, this non-destructive technique delivers 3D data exploiting the principles of CT. This makes sample preparation easier and faster and eliminates the need to register individual layers to obtain 3D data. Although the resolution of conventional histology is not achieved and the variety of suitable stains is still limited, virtual histology is a growing field of research and will open new applications in the future.

In addition to the phase contrast modality, the data acquired in an X-ray grating interferometer carries a scattering signal which manifests in a disproportional amplitude reduction of the measured intensity modulation [Pfeiffer, 2008]. Because of its similarity to the analog in optical microscopy, it is also often called *X-ray Dark-field Imaging* or radiography. The scattering signal is formed when the radiation passes through microstructured tissue with many interfaces, like the lung. Consequently, this signal is also sensitive to certain changes in the microstructure which can be caused by different pathologies. Similar to dark-field microscopy, this method obtains information about the transmitted microstructure without being able to directly resolve it.

The first in-vivo multi-contrast radiographs of a mouse were reported in [Bech, 2013], where a strong dark-field signal of the lung was observed. Studies with several mouse models and respective pathologies were then conducted with a focus on the lung. Among others, a potential in-vivo diagnosis of lung cancer [Scherer, 2017] and pulmonary fibrosis [Hellbach, 2017] was reported using the dark-field signal. Soon, the extension of the field of view and an increase of the X-ray energy were tackled to image larger and thicker objects. This was first achieved using a slit scanning system and demonstrated with the acquisition of in-vivo chest radiographs of a pig [Gromann, 2017] and deceased human bodies [Willer, 2018; Andrejewski, 2021]. These studies showed great potential to map the microstructure of the lung with the dark-field signal at clinically acceptable dose levels, despite being embedded in the strongly absorbing thorax. For that, an accurate dark-field signal retrieval enabled by calibration measurements with phantom materials is necessary to correct spectral effects. Recently, in-vivo human thorax radiography at dose levels of 36 µSv and 7 s scan time was demonstrated for the first time [Willer, 2021]. The study elaborated on the diagnosis of pulmonary emphysema in patients with chronic obstructive pulmonary disease (COPD) using dark-field chest radiography as a low-dose alternative to CT. COPD is the third leading cause of death globally (2019) according to the World Health Organization [WHO, 2020]. So far, it cannot be cured and its progression can only be slowed down through medication. Therefore, a screening method among risk patients would be very beneficial for early detection and treatment. In a recent study, COVID-19 pneumonia was assessed with dark-field chest radiography [Frank, 2022]. It was found that the dark-field signal is significantly reduced in COVID-19 pneumonia patients compared to a healthy control group. Furthermore, the additional dark-field radiograph facilitated a more reliable diagnosis in a reader study. It is to be expected that the dark-field signal will prove useful for the diagnosis of other lung-related pathologies, particularly affecting its microstructure. Due to its low dose compared to CT, X-ray dark-field radiography might enable longitudinal patient studies exploring novel therapeutic approaches and drug development. Beyond projectional dark-field radiography, an implementation of CT on the human scale with this modality is in development. Recently, a compact Talbot-Lau system on a clinical scanner was demonstrated in [Viermetz, 2022].

Apart from biomedical applications, grating-based multimodal imaging has also been explored in several other fields like material science, security screening, non-destructive testing of complex parts, and the study of objects from cultural heritage or archaeological artifacts. Much like in biomedical applications, porosity in metals (e.g. welds) that is smaller than the pixel size of the imaging system can be revealed [Revol, 2011]. Dark-field radiography can be used to determine the fiber orientation of carbon fiber-reinforced polymer parts [Prade, 2017] and detect microcracks [Senck, 2018]. Defects in additively manufactured polymer parts can be investigated by X-ray interferometry [Kio, 2018]. Water transport in cement can also be visualized by time-resolved dark-field imaging [Prade, 2016]. Archaeological artifacts can be studied non-destructively using grating-based imaging [Ludwig, 2018]. And, if neutrons are used instead of X-rays, even more special samples or their physical properties become accessible. One example is the study of stress-induced magnetic degradation in electrical steel with neutron interferometry [Neuwirth, 2020]. In this thesis, a geological sample will be investigated by both X-ray and Neutrons grating interferometry to evaluate the complementarity of both multimodal methods.

Although many applications of grating-based imaging have been demonstrated, the technology has not yet matured enough to allow routine and efficient scanning with commercially available devices. The biggest obstacle is the field of view, which is limited by the active surface of the gratings. They must be manufactured to a high quality and precisely adjusted to the beam path. Due to the high aspect ratio of the absorbing lamellae and the cone-shaped beam of conventional X-ray tubes, the gratings must be bent to spherical or cylindrical surfaces. Gratings of several cm side length can be shaped to the desired form by mechanically clamping them into individually machined frames. For source gratings placed close to the X-ray tube, flexible substrates such as graphite or polyimide are used, as small bending radii are required. Given their relatively small size, they still fit on a single 100 mm wafer and do not pose severe challenges in system design. However, the situation is different with the analyzer grating, which is mounted close to the detector and must have a side length of several tens of centimeters. To cover the large area, these gratings must be stitched together from several tiles and glued to a substrate that is subsequently bent [Schröter, 2017]. Already on an area of 20×20 cm^2, bending the carrier substrate has not been able to transfer the curvature evenly across individual tiles. The defects resulted in shadowing effects on several tiles, which is unfavorable for dose-efficient imaging systems. A second concern is the expensive and error-prone fabrication process involving deep X-ray lithography and gold electroplating, as will be elaborated in Chapter 3. To bypass these issues, the field of view has been extended by slit-scanning systems where the image is formed from several exposures during a movement of the optical system. However, this approach comes with its own downsides like bulky mechanical setups, long exposure times, vibrations, and movement artifacts complicating image reconstruction. Hence, finding a reliable and cost-effective fabrication method for large-area absorption gratings is a major concern in the development of full-field systems. A potential alternative fabrication approach based on silicon processing is explored in Chapter 4 of this thesis. Unlike conventional techniques using gold as the attenuating material, tungsten is deposited in the deep trenches as an absorber. For neutron applications, a similar process can be elaborated with gadolinium particles. The goal of this thesis is to contribute to grating development and facilitate a further spread of these multimodal imaging methods to eventually make them diagnostically available.

2 Fundamental Principles of Grating-based X-ray and Neutron Imaging

This chapter covers the most important concepts of X-ray and neutron imaging needed to understand the experimental achievements of this work. At first, an introduction to X-ray radiation and its generation with laboratory-based X-ray sources and in synchrotron facilities is given. Later, it is discussed how this radiation interacts with matter to understand how contrast is formed in radiography. Then, different types of detectors and their areas of application are briefly mentioned.

The second part of this chapter provides an overview of the respective technologies in neutron imaging. Excessive detail will be avoided, as neutron work is only relevant for a minor part of this thesis. Though most concepts from X-ray radiation are, in fact, also applicable to neutron imaging.

In the third part, grating-based imaging will be introduced and briefly classified among other phase-sensitive methods. For a more detailed understanding, Fresnel diffraction and the Talbot effect will be elaborated. After that, the Talbot-Lau interferometer will be introduced as the most suitable method for phase-sensitive imaging with low-coherence sources. The mechanism of contrast formation will be explained and experimental aspects of signal extraction will be discussed.

In the last part, the principles of computed tomography will be introduced. This will also include a brief historical note and the mathematical treatment of image reconstruction addressing the Radon transform, the Fourier slice theorem, and the filtered back projection.

2.1 X-ray Imaging

2.1.1 Introduction

Electromagnetic waves propagate with the speed of light c_0 in vacuum and are characterized by their wavelength λ or frequency f with the relation $c_0 = \lambda f$. The energy of a photon can be calculated by:

$$E = \frac{hc}{\lambda}, \tag{2.1}$$

where h is Planck's constant. X-rays are electromagnetic waves in the energy range from a few to several hundred keV and have wavelengths in the range of $1\,\text{Å}$ – the length scale of interatomic distances. Due to their high energy, they can penetrate solid objects and generate contrast between structures of different absorption power. Their energy is also high enough to ionize matter which makes them harmful to biological tissue upon high exposure doses. Similar to visible light they can have different interactions with matter like absorption, refraction, and scattering. However, the latter both are very weak and hard to measure, let alone use for imaging. To be sensitive to those wave-related interactions one has to use special sources, detectors, or sophisticated arrangements of optics. This will be the main topic of this chapter.

2.1.2 Discovery and Generation of X-rays

The discovery of X-rays by Wilhelm Conrad Röntgen in 1895 was made with a partially evacuated glass vessel with two electrodes (often called Crookes tube) [Röntgen, 1895]. Such tubes were used at that time to study so-called cathode rays, which later turned out to be electrons. When a high voltage is applied between the two electrodes, some of the residual gas is ionized and electrons are accelerated toward the anode by the electric field. This phenomenon is only perceivable when the electrons travel in a sufficiently evacuated vessel with a relatively low number of collisions with gas atoms and some fluorescent material applied on the inner side of the tube. Experimenting with such tubes, Röntgen identified an additional type of radiation that created some fluorescence outside the tube despite it being completely covered with cardboard. He determined its origin as being emitted by the anode and studied its penetrative properties. Later, he performed the first radiographs and quickly recognized its potential for medical imaging.

The most common way to generate X-ray radiation today is very similar to the experimental arrangement Röntgen used and is based on physical interactions that occur when

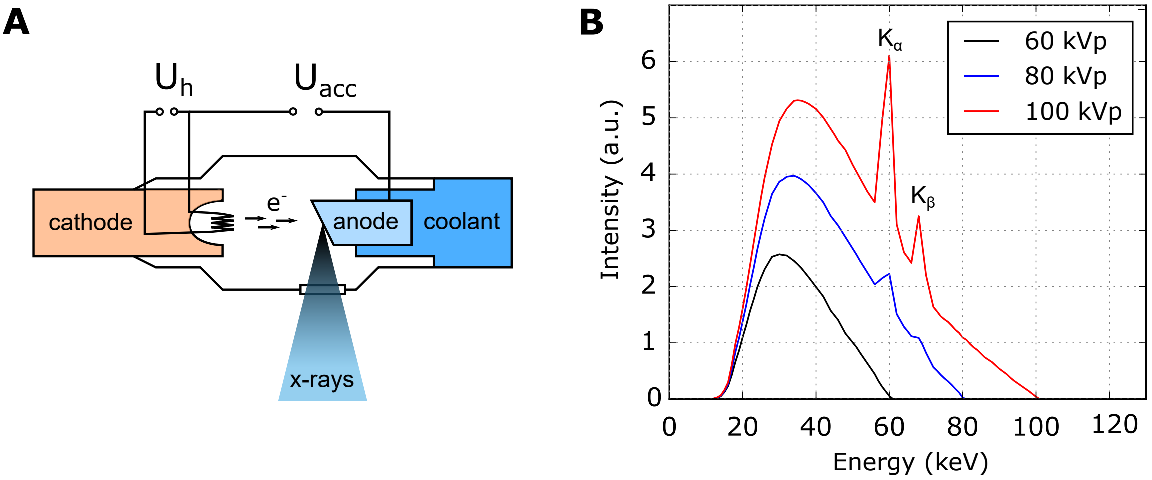

Figure 2.1: (A) Schematic of a stationary X-ray tube. The filament in the cathode emits electrons when a heating voltage U_h is applied. The electrons are accelerated by the potential U_{acc} and generate X-rays upon collision with the anode. (B) Tungsten anode spectra at different acceleration voltages as produced by common medical X-ray tubes with 3 mm aluminum filtration. The fluorescent K-lines are well visible overlaying the continuous Bremsstrahlung at energies of about 59 keV and 67 keV.

highly accelerated electrons are directed onto a target material. Figure 2.1 A shows a simplified schematic of an X-ray tube. The cathode consists of a filament similar to a light bulb which provides a high number of electrons via thermal emission when a heating voltage (U_h) is applied. An acceleration voltage in the range of several tens of kV is also applied between the cathode and anode to accelerate the electrons. To get a very small focal point of the impinging electrons on the anod, modern tubes have various electron-focusing devices that can be electronically tuned. The production of X-rays is based on two physical interactions that occur when highly accelerated electrons are directed onto a target material. Being decelerated and scattered by the strong electric fields of the nuclei, the electrons generate X-rays with a continuous spectrum (*Bremsstrahlung*). The second effect is the emission of characteristic X-ray radiation which is generated by fluorescence. This occurs when the accelerated electrons knock out bound electrons in the target material and the vacancies are occupied by electrons transitioning from upper states. Typically those are transitions into the K- or the L-shell of the anode material. These transitions have distinct energies characteristic for every element and therefore generate distinct peaks in the spectrum as seen in Figure 2.1 B. X-rays are irradiated isotopically at the focal spot and a small fraction of them leaves the tube through the window made from an X-ray transparent material such as beryllium. Since only a small fraction of the electron energy is converted into X-rays, the rest is deposited as thermal energy in the anode which has to be cooled. The dissipation of thermal energy at the anode has turned out to be the bottleneck in tube development and has triggered many innovations in X-ray tube engineering. To withstand high temperatures, anodes are often made of tungsten-based alloys with high melting points. Further, rotating anodes were introduced to distribute the heat on a larger area and enable a better dissipation thereof. Most of the tube development was driven by the need for high X-ray fluxes for medical CT scanners, which acquire several thousands of image frames per second. Other tubes are optimized for very small focal spots typically used for high-resolution imaging or non-destructive testing. Such tubes typically have sophisticated electron optics and can also have a transmission target consisting of a thin diamond substrate covered with a few µm of tungsten. Such microfocal tubes can be used to exploit phase-related effects for imaging and provide enough coherence for multimodal techniques which will be discussed later. However, their flux is too low for diagnostic imaging. A relatively new approach is liquid metal jet sources, where the target consists of a thin stream of a liquid metal such as galium. It can reach higher power densities since it is not limited by the melting point of the material.

An alternative but less common way to generate X-rays similar to Bremsstrahlung is the acceleration of fast electrons perpendicular to their velocity vector by magnetic fields. This can be achieved by the Lorentz force $\vec{F} = -e\vec{v} \times \vec{B}$ when the electrons are guided through a constant magnetic field $\vec{B}$. As the force always acts perpendicularly to the direction of movement and the $\vec{B}$ field, the electron trajectory becomes circular. Its orbit can be calculated by equating the Lorentz force with the centripetal force mv^2/r. For relativistic particles, the momentum is $\vec{p} = \gamma m\vec{v}$ with $\gamma = E_e/mc^2$. As the speed of the electrons $\vec{v}$ in that kind of particle accelerator is close to the speed of light c, one can approximate [Als-Nielsen, 2011]:

$$\gamma mc = reB. \tag{2.2}$$

The deflection of electrons according to this principle is typically performed in so-called bending magnets that are used to guide the electrons in a closed loop. Upon ‘bending’, the charged electron experiences radial acceleration and is therefore radiating tangentially to its circular orbit. This special kind of Bremsstrahung is called *Synchrotron radiation* and its generation slows down the electrons due to the conservation of energy. Hence, such storage rings have special cavities where the electrons are accelerated again to have a constant velocity. Due to relativistic effects, the synchrotron radiation is emitted in tangential cones (see Figure 2.2 A) with an opening angle of $\gamma^{-1} = mc^2/E_e$ – typically close to 0.1 mrad [Als-Nielsen, 2011]. Despite a very broad spectrum ranging from infrared

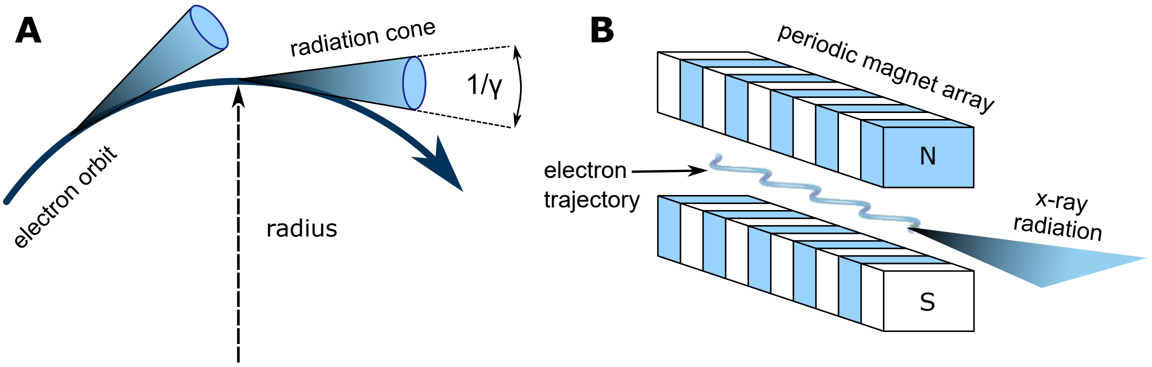

Figure 2.2: (A) Fast electrons in a magnetic field are accelerated perpendicularly to their direction of movement, resulting in a circular trajectory. In this process, synchrotron radiation is emitted tangentially in cones with opening $1/\gamma$. (B) Wigglers and undulators consist of periodic magnet arrays with reversed polarity which force electrons on sinusoidal trajectories. This leads to the emission of synchrotron radiation in the plane of the electron trajectory.

to the hard X-ray regime, such bending magnet radiation is very intense and can be exploited for many different methods in synchrotron research.

To produce X-ray radiation of higher brilliance, one can use alternating magnetic fields which force traversing electrons to oscillate in the horizontal plane as illustrated in Figure 2.2 B. Such an insertion device is called a *Wiggler* and is composed of an array of magnets with alternating polarity. It is placed in straight sections between circular segments of a storage ring. Such a device guides the electrons through a series of circular arcs with alternating directions where the radiation from multiple cones is emitted in one single direction. The produced spectrum is similar to that of a bending magnet, but the intensity after passing N periods of the array is increased by a factor of $2N$. The magnet arrays have a typical length of 1 m and are capable of producing high-power radiation in the range of 1 kW.

Further, it is possible to design the device such that the periodically emitted radiation cones of every oscillation are in phase with each other resulting in a quasi-monochromatic spectrum. Such devices are called *Undulators* and they have to be tuned for a distinct amplitude of the oscillation. An undulator is characterized by the period of the magnetic arrays λ_u, the number of periods N, and a dimensionless parameter K, which is related to the amplitude of the undulated electrons. It is proportional to the B field and connected to other parameters via [Als-Nielsen, 2011]:

$$K = \frac{eB_0}{2\pi mc}\lambda_u \tag{2.3}$$

The spectrum of radiation produced by this device consists of a fundamental wavelength λ_1 and multiples thereof (called *harmonics*) and can be calculated by relativistic consideration, as the electrons see the periodic magnetic array Lorentz-contracted. On the undulator axis, the fundamental wavelength is [Als-Nielsen, 2011]:

$$\lambda_1 = \frac{\lambda_u}{2\gamma^2}\left(1 + \frac{K^2}{2}\right). \tag{2.4}$$

With $\lambda_u \approx 1\,\mathrm{cm}$ and $\gamma \approx 10^{-4}$, the fundamental wavelength is in the Angstrom range ($10^{-10}\,\mathrm{m}$) – the X-ray regime. The fundamental wavelength can be tuned by adjusting the K parameter. This is done by mechanically varying the gap between the poles of the magnet array which changes the magnetic field B_0. Compared to a Wiggler, the horizontal divergence of an undulator beam is also much smaller, namely $1/\sqrt{N}\gamma$ instead of $1/\gamma$. The higher harmonics are usually filtered out by crystal monochromators operating according to Bragg's law.

There are several alternative, more exotic ways to generate X-ray radiation such as over the triboelectric effect or the inverse Compton effect, which allows building more compact devices with beneficial beam properties. There are also sources of even higher brilliance than conventional undulators – free-electron lasers which push the boundaries further than third-generation synchrotron facilities. Since this work only uses X-ray tubes and synchrotron radiation, those other approaches are not further discussed.

2.1.3 X-ray Beam Parameters

The beam parameters are characterized by several quantities that are essential for imaging. First, the flux measured in photons/second and sometimes normalized to a certain area determines what exposure time has to be chosen to reach the required image quality. The spectral composition of the radiation is also of significance. For X-ray tubes, there are mainly two parameters that are used to alter the spectrum. The acceleration voltage defines the maximum wavelength, as also seen in Figure 2.1 B and filtration (e.g. a few mm of aluminium) is used to reduce the fraction of lower energies. For medical applications, this is done since the softer part is almost completely absorbed by the imaged body part and therefore does not contribute to the contrast. However, filtration is also connected to a significant flux loss and enables very limited possibilities to reduce the spectral bandwidth. A narrow spectrum is of importance for quantitative measurements and often allows one to optimize measurements and facilitate data analysis. For methods that rely on wave-related properties of the radiation like phase-contrast imaging, the concept of coherence length should be briefly addressed. For wave-related effects like interference or diffraction to be measurable, the radiation source has to fulfill certain criteria. When two plane waves with wavelength λ and $\lambda - \Delta\lambda$ travel in the same direction they will be out of phase after a certain distance called *longitudinal coherence length* L_L [Als-Nielsen, 2011]:

$$L_L = \frac{\lambda^2}{2\delta\lambda} \tag{2.5}$$

Consequently, effects based on the wave properties like interference or diffraction will deteriorate at this propagation distance. The same degradation can occur when two waves with the same wavelength are traveling in a slightly different direction, say having an angle $\Delta\theta$ between them. This can be the case if they are emitted from two different points in the source with a distance D apart. If the plane of observation is at a distance R from the source, the relation $\Delta\theta = D/R$ applies. The distance where both waves would be out of phase is the *transversal coherence length* L_T. From basic geometrical consideration, it is derived to be [Als-Nielsen, 2011]:

$$L_T = \frac{\lambda}{2\theta} = \frac{\lambda}{2}\frac{R}{D} \tag{2.6}$$

Therefore, the source spot should be small and the distance to the detector should be high for sufficient coherence to exploit wave-related beam properties. The dimensions of the source are also important for a high image resolution in absorption-based imaging, as the source introduces a geometrical blur in the detection plane.

Brilliance

The combination of these desired beam parameters is summarized in the brilliance, which is often used as a quality measure for a beamline or an experimental setup [Als-Nielsen, 2011]:

$$\text{Brilliance} = \frac{\text{photons}/s}{(\text{mrad}^2)(\text{mm}^2)(0.1\%\text{BW})}. \tag{2.7}$$

It consists of the flux (photons/second) normalized to the angular divergence set by the horizontal and vertical apertures (in mrad), the source area (in mm^2), and the relative bandwidth of the monochromator crystal relative to 0.1%. Third-generation undulators can have up to 10 orders of magnitude higher brilliance than modern rotating anode X-ray tubes at the K_α-line. Undulator brilliance in the range of 10^{20} - 10^{23} is also more than 5 orders of magnitude higher than bending magnet radiation. Hence, X-ray beamlines at such large-scale facilities allow unique investigations that are hardly possible with laboratory-based X-ray tubes. Particularly for imaging, they allow performing quantitative experiments benefiting from the high flux, monochromaticity, and coherence of the radiation. These beam properties can be exploited to generate novel contrast mechanisms which are based on the refractive and dispersive properties of waves. In Chapter 6 of this work, such undulator radiation with a newly developed refractive optic was used for high-resolution phase imaging and tomography.

2.1.4 X-ray Interaction with Matter

A deeper insight into the interaction of X-rays with matter is essential for understanding contrast formation in radiography and computed tomography. For the mathematical treatment, both a particle and a wave formalism are useful. The scattering of X-rays is often described in the particle picture and many calculations regarding refraction and wave propagation are easier performed with the wave approach using the refractive index well known from visible light. The attenuation of X-rays mainly used for X-ray imaging today is caused by absorption and to a smaller degree by scattering. The following three kinds of X-ray interactions with the atomic shell consisting of electrons will be addressed [Als-Nielsen, 2011]:

1. Photoelectric absorption
2. Thomson / elastic scattering
3. Compton / inelastic scattering

Note here, that the pair production effect is omitted since it occurs only above 1022 keV and is irrelevant for conventional radiographic applications. The probability of interaction depending on the energy of the impinging photon, atomic and macroscopic properties can be described by so-called interaction cross sections abbreviated with σ. All interactions are described by the total interaction cross section σ_{tot} consisting of the individual parts:

$$\sigma_{tot} = \sigma_{ph} + \sigma_T + \sigma_C, \tag{2.8}$$

where $\sigma_{ph}, \sigma_T, \sigma_C$ are the photo-absorption, Thompson-, and Compton scattering cross sections. These interactions are also often given in the form of the *mass attenuation coefficient* $\mu/\rho = \sigma_{tot}/uA$, where A is the relative atomic mass of the element and u is the atomic mass unit. In the following subsections, the different kinds of interactions will be reviewed in detail. Their dependencies on the X-ray energy and the material properties will be elaborated and their influence on image formation will be discussed.

Photoelectric Absorption

The light quantum hypothesis introduced by Planck in his calculations and interpreted by Einstein as a physical reality in 1905 explained the so-called photoelectric effect. It describes the emission of electrons from atoms initiated by irradiation with light which could not be explained with classical theory. Weakly bound electrons on the outer shells (e.g. valence electrons) can be excited by visible light when their quanta have enough energy to initiate such a transition. X-rays can even ionize atoms by transferring so much energy to the inner shell electrons, that they can be ejected from the atom. This happens when photon energy E_γ is higher than the binding energy E_B of the electron. The photon is completely absorbed and the energy difference $\Delta E = E_\gamma - E_B$ is transferred to the free electron as kinetic energy. The probability of this process is strongly correlated with the atomic number Z of the elements involved and with the photon energy E_γ. Figure 2.3 B and C show μ/ρ (which is proportional to σ_{tot}) for a rather weakly absorbing (water) and a strongly absorbing (gold) material. The plots also show individual contributions from the three interactions mentioned previously. For water, photoelectric absorption is the dominant contributor to the total interaction up to 20 keV. It decreases with $\approx 1/E^3$ (note the linear decrease on the log-log scales). For a material with a high Z like gold, the absorption interaction is much stronger, as σ_{ph} scales with $Z^4 - Z^5$ [Als-Nielsen, 2011]. Additionally, there are strong discontinuities observable (Figure 2.3 C) between parts of linear decrease. Those so-called *absorption edges* occur at ionization energies of the inner shell electrons. As soon as the photon has enough energy to ionize e.g. the K-shell electron from the Au atom at 80.7 keV, the probability for this absorption interaction increases strongly. Therefore, relation $\sigma_{ph} \propto 1/E^3$ loses its validity in the vicinity of these absorption edges. The energies at which these edges occur are characteristic for each element since they relate to the binding energies of the electrons. This plays an important role in the choice of chemical compositions for X-ray contrast agents, scintillator materials for detectors, or absorption materials for X-ray optics.

Thomson Scattering

Thomson scattering is a process between an incident photon and an electron described in the framework of classical electrodynamics. The electron absorbs the photon, is ac-

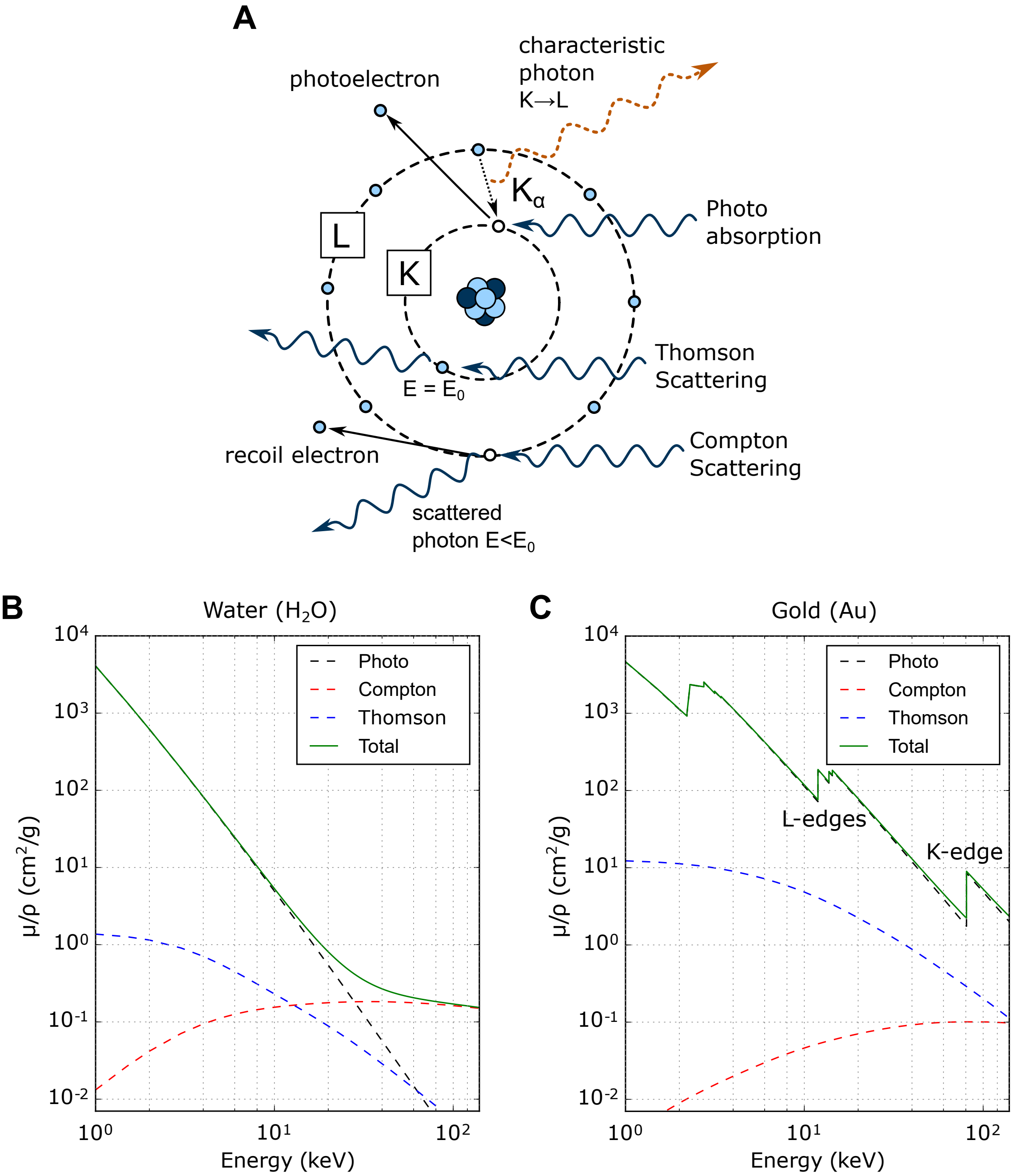

Figure 2.3: (A) schematic illustration of the three different interaction processes: photo absorption, Thomson, and Compton scattering. (B) Mass attenuation coefficient μ/ρ for water and its contributions from the three types of interaction. (B) μ/ρ of strongly absorbing gold (Au) with $Z = 79$ showing that the photo absorption dominates the attenuation behavior. The sharp increases of μ/ρ at distinct energies occur when the energy is high enough for ionization of the electrons in the L- or the K-shell, denoted as the L- and K-edges.

celerated by its electric field and its oscillation emits a secondary wave with the same frequency in a slightly different direction. As the electron remains in its original state without any energy transfer it is also called elastic or coherent scattering. Its interaction cross section is derived from the Rayleigh cross section for the case that the impinging photon has much higher energy than the binding energy of the electron. For a quasi-free electron, the Thomson cross section is [Als-Nielsen, 2011]:

$$\sigma_T = \frac{8\pi}{3}{r_0}^2, \tag{2.9}$$

where r_0 is the classical electron radius:

$$r_0 = \frac{1}{4\pi\epsilon_0^2}\frac{e^2}{m_e c^2} \approx 2.82 \cdot 10^{-15} m \tag{2.10}$$

Interestingly, the Thomson cross section is a constant value and is not energy-dependent. Although it is a weak interaction and therefore does not contribute to the image formation process of conventional absorption-based radiography, it provides useful information about the matter it interacted with. When the calculations are extended from simple electrons to three-dimensional electron density distributions, that are found in molecules, crystals, and even in micro-sized samples with porous or ordered morphologies one can calculate the resulting scattering patterns. Conversely, by measuring the diffraction or scattering patterns, one can also draw conclusions about the morphology of the specimen. Based on that, multiple methods of structural analysis like *Small-Angle X-ray Scattering* (SAXS) or *Small Angle Neutron Scattering (SANS)* have been developed.

The more interesting aspect for this work is that this interaction creates a phase shift of the beam as it passes through matter, which can be exploited for imaging. This will be addressed in more detail when the refractive index n will be introduced. Further, when the radiation transmits porous media with many interfaces, this scattering process leads to a weak dispersion of the beam on the micron scale. In this work, systems that are capable to sense such beam modulations and use them for imaging will be discussed. It is particularly advantageous that this radiation, which carries information about the transmitted structure, is not absorbed in the process (as is partly the case in conventional radiography) and therefore does not deposit dose to the imaged object.

Compton Scattering

A scattering process of a photon and an electron can also be inelastic, i.e. some energy is transferred to the electron and the directions of both particles are significantly changed. Consequently, the wavelength of the photon is increased following the conservation of energy. Unlike Thomson scattering, this process can only be explained quantum-mechanically assuming a momentum $p = h/\lambda$ and an Energy $E = hf$ of the photon. Using relativistic energy and momentum conservation of electron and photon, the change of wavelength $\Delta\lambda$ connected to a scattering angle ϕ can be derived [Als-Nielsen, 2011]:

$$\Delta\lambda = \lambda' - \lambda = \frac{h}{m_e c}(1 - \cos\phi) \tag{2.11}$$

Here, the proportional factor $h/(m_e c)$ is often called the Compton scattering wavelength λ_C. Its interaction cross section is derived from the *Klein-Nishina* scattering cross section and is only weakly dependent on energy. Unlike in Thomson scattering, the photons are scattered in all directions, albeit not isotopically. The contribution from Compton scatter to the beam attenuation is proportional to the electron density. Unlike photo absorption, it does not depend on the atomic number Z and is therefore not contributing to a contrast formation. As shown in Figure 2.3 B it becomes the dominant interaction for soft matter above 30 keV energy. It deteriorates the contrast in radiography, since a fraction of scattered photons is detected which does not carry any spatial information. Hence, it is particularly detrimental for soft tissue differentiation which is of interest in medical Computed Tomography. To suppress this, anti-scatter grids consisting of thin absorbing lamellas are often used in such medical imaging systems.

Complex Refractive Index

For many calculations, the treatment of X-rays as waves with the refractive index n as known from visible light is more practical than in the particle picture. Especially when simulating diffractive optics and calculating the propagation of wave fronts, this approach is extremely helpful. For X-ray radiation, the complex refractive index for a medium is written as:

$$n = 1 - \delta + i\beta, \tag{2.12}$$

where δ is a very small number compared to 1 and is called the refractive index increment. The real part $1–\delta$ is the origin of the refractive properties caused by a phase shift of the radiation transmitting the medium. The imaginary part β represents the inelastic interactions that lead to an attenuation of the beam. The influence of both factors should be illustrated by applying the refractive index to a plane wave propagating in the z-direction:

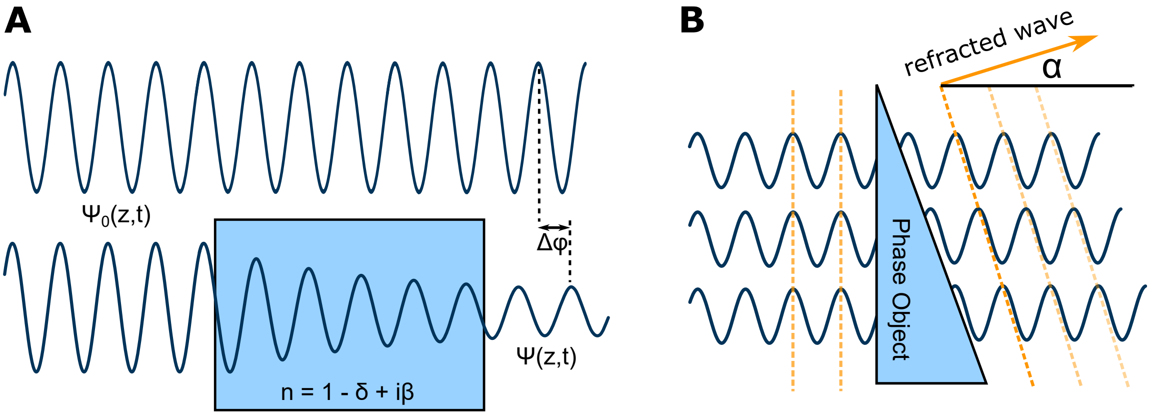

Figure 2.4: (A) Illustration of a wave transmitting an object with refractive index n. An amplitude reduction corresponds to the attenuation introduced by the complex part of n. The real part leads to a phase shift introducing a phase difference $\Delta\varphi$ compared to the reference wave. (B) A wedge-shaped phase object transmitted by a plane wave creates a multitude of phase-shifted waves which result in a refracted wave deflected by an angle α.

$$\Psi(z,t) = \Psi_0 \cdot e^{-i(\omega t - k_0 \cdot z)}, \tag{2.13}$$

with the amplitude Ψ_0, propagation distance z, angular frequency ω, and the wave number $k_0 = 2\pi/\lambda_0$. When the wave enters a medium with refractive index n, the wave number changes from k_0 to $k = nk_0$ which enables representing the wave as a product of the following factors:

$$\Psi(z,t) = \Psi_0 \cdot e^{-i(\omega t - k_0 \cdot z)} \cdot e^{-i\delta k_0 \cdot z} \cdot e^{-\beta k_0 \cdot z}. \tag{2.14}$$

The first term represents the initial wave that would be expected in vacuum (see Figure 2.4 A). The second term represents a phase shift introduced by the transmitted medium. At the same time, the amplitude of the wave reduces which is caused by the last factor in the form of exponential decay. Figure 2.4 A illustrates this behavior where a decrease of the amplitude and a phase difference $\Delta\varphi$ are visible compared to a reference wave in vacuum.

The measured intensity by the detector is the product of the wave $\Psi(z,t)$ with its complex conjugate $\Psi^*(z,t)$, which yields:

$$I(z) = \Psi(z,t) \cdot \Psi^*(z,t) = \Psi_0^2 \cdot e^{-2\beta k_0 \cdot z} \tag{2.15}$$

When comparing the attenuated intensity $I(z)$ with the initial intensity $I_0 = \Psi_0^2$ and inserting the absorption coefficient $\mu = 2\beta k_0$. Equation 2.15 turns directly into the *Lambert-Beer* law:

$$I(z) = I_0 \cdot e^{-\mu \cdot z} \tag{2.16}$$

The phase shift introduced by the second term of Equation 2.14 is given by:

$$\Delta\Phi = \delta k z, \text{ with } \delta = \frac{2\pi \rho_e r_e}{k^2} \tag{2.17}$$

The refractive index increment δ is directly proportional to the electron density ρ_e, is energy dependent through k and its typical values are in the range of 10^{-6} to 10^{-8}. Consequently, refraction with X-rays is very weak compared to visible light and could not be detected by Röntgen when he tried to prove the wave character of the newly discovered radiation.

Figure 2.4 B illustrates how a transmitted wedge-shaped object creates a multitude of phase-shifted waves, that appear as a new wavefront under the angle α which is the refracted wave. The deflection angle α is given by:

$$\alpha = \frac{1}{k}\frac{\partial \Phi(x)}{\partial x}, \tag{2.18}$$

where $\partial\Phi(x)/\partial x$ is the differential phase in the x-direction. By measuring the displacement of a certain intensity modulation compared to a modulation without the object in the beam, the differential phase can be retrieved and integrated to obtain a phase image. There are two major challenges for systems to be sensitive to that kind of signal. First, such an intensity modulation has to be created. Conventional X-ray sources have large focal spots with insufficient coherence to create modulations on the micron scale using e.g. absorption masks or gratings. Hence, either micro-focal sources or sophisticated arrangements of optics have to be used. The second challenge is to measure the deflection of the created modulation. Current flat panel detectors used for medical imaging have about one order of magnitude lower resolution that would be required to detect such changes. Hence, either special high-resolution detectors or absorption optics have to be used to be sensitive to such tiny spatial modulations. This will be revisited in further detail in the discussion of phase-sensitive methods in the next chapter.

2.1.5 X-ray Detectors

The original mechanism to make X-ray radiation visible was a fluorescence screen consisting of a material emitting visible light when irradiated with X-rays. It was also soon discovered that photographic films containing silver salts are also sensitive to X-rays. Unlike fluorescent screens, they could be used to create a permanent image which is of greater benefit for diagnostical applications. Hence, this principle was adapted to create X-ray films. The exposure to X-rays leads to chemical modifications of the silver salt emulsion which introduces a blackening proportional to the received dose. Since such a thin film typically absorbs only a small fraction of the X-rays, an intensifier screen that converts X-rays into visible light was often used in combination with X-ray films. With decent image quality and a low cost, X-ray films have been used for many decades. However, with the growing requirement for advanced applications where the images had to be digitally processed, such analog detection methods turned out to be very impractical.

With the development of digital pixel sensors for visible light, photosensitive film could be replaced. In such *flat panel detectors*, X-rays are absorbed in a scintillator layer which emits visible light that is detected by a 2D photodiode array. The latter creates charges in every pixel that are proportional to the amount of light. An array of thin film transistors enables to read out the charges which are then amplified and converted to digital values by an analog-to-digital converter. Since the X-rays are first converted to visible light and then to an electrical signal, this approach is often called an indirect conversion. Further, this approach is not sensitive to the number and energy of individually detected photons but only measures the amount of light that is generated in every pixel. Therefore, such imagers are also called energy-integrating detectors. They have pixel sizes down to 75 µm, however, their resolution is usually limited by the scintillator thickness and its light-guiding properties. With increasing scintillator thickness, more X-ray radiation can be absorbed and, consequently, more light can be generated. However, thicker scintillators enable more scattering of light which blurs the image. For medical applications, scintillators are usually tuned for better dose efficiency and can be therefore up to 600 µm thick. Thallium-doped cesium iodide (CsI), one of the most widely used scintillators, has a high light conversion efficiency and can be grown in columnar crystals of several tens of µm diameter. These columns suppress isotropic scattering of the generated light and guide a high fraction of it down to the photodiode matrix.

A similar concept is also realized in high-resolution X-ray detectors with an optical coupling to a digital image sensor like a Charge-Coupled Device (CCD) or a Complementary Metal–Oxide–Semiconductor (CMOS) sensor. In such systems, a very thin crystal scintillator (20-100 µm) is focused with microscope optics with $2-20\times$ magnification reaching effective pixel sizes of < 1 µm. Here, the efficiency is not only reduced by the thin scintillators, but also by the limited light collection efficiency of the objective, i.e. its numerical aperture. Hence such detector systems are often used at X-ray imaging beamlines where the poor efficiency can be compensated by the high flux. With such cameras, phase-induced effects are directly resolved and enable so-called propagation-based phase-contrast imaging.

An alternative, currently upcoming advanced X-ray technology is the so-called *photon-counting* or *direct conversion detection*. In contrast to the previously described methods, the absorbed X-ray photon ionizes the semiconductor material (such as a-Se, GaAs, CdTe) and creates electron-hole pairs which are pulled apart by an applied voltage between two electrodes at the opposite surfaces of the conversion material. This creates a stronger charge compared to indirect conversion devices. In addition, such detectors have extremely fast readout electronics that enable the detection of individual photons. Consequently, they can acquire images without dark current and readout noise and achieve a much higher frame rate and dynamic range. For many applications low energy photons create a higher contrast, however, they are weighted less in energy-integrating detectors. In photon-counting mode, they contribute equally and are thus beneficial for contrast formation. Further, since the detected charge is also directly proportional to the photon energy and every photon is temporarily resolved, it becomes possible to acquire some information about its energy. Such detectors with some additional sophisticated readout circuitry can do energy discrimination and distribute the counts into several bins that correspond to different ranges of energy. This information can then be used for further contrast enhancement or even material differentiation. Current innovation based on this kind of detector is on the doorstep to be introduced into medical computed tomography (CT) and is often referred to as photon-counting CT or spectral CT. Despite many advantages, these kinds of detectors are still expensive and limited in sensor size. Hence, their introduction into radiography systems with a large field of view is questionable in the near future.

2.2 Neutron Imaging

2.2.1 Introduction

The discovery of the neutron in the early 1930s was only possible after significant progress in atomic physics and the newly emerging exploration of radioactivity. It was found that irradiation of beryllium with α-particles (e.g. emitted by polonium) produced some kind of strongly penetrating radiation. It was not affected by electric fields, unlike α- or β-particles which was an important indication that it does not carry any charge. Further, when the unknown radiation interacted with hydrogen-rich material such as paraffin wax, it produced high-energy protons. James Chadwick showed in 1932 that the known findings could not be explained by γ-rays as was speculated before. Instead, he proposed a new elementary particle with a similar mass to the proton and a zero charge which explained the experimental observations [Chadwick, 1932].

Neutrons are an essential component of the nuclei of all elements (except one isotope of hydrogen) and are stably bound with protons by nuclear forces. Hence, their isolation for experiments requires some kind of nuclear reaction. Similar to photons unbound neutrons have a dual nature and can be understood both as particles and waves. Consequently, they can also be used for multimodal imaging based on their refractive and dispersive behavior. Free neutrons can be characterized by their kinetic energy E, velocity v, De Broglie wavelength $\lambda = h/mv$, or temperature T, which are given by the relation [Squires, 2012]:

$$E = \frac{1}{2}mv^2 = \frac{h^2}{2m\lambda^2} = k_B T, \tag{2.19}$$

where m is the neutron mass and k_B the Boltzmann constant.

Table 2.1 gives different kinds of neutrons with typical labels and parameter ranges. In neutron imaging, mostly thermal and cold neutrons are used due to their suitable interaction cross sections for many different elements. In the following neutron sources, detectors and their interaction with matter will be briefly discussed.

2.2.2 Neutron Sources

Although there is a variety of neutron sources, only two kinds of them are mainly used for imaging since they provide enough neutron flux. The first kind is nuclear research reactors, which use fission processes to produce neutrons. The most common fission material is

Classification	Energy range [meV]	Wavelength [Å]	Velocity [m/s]
Ultra- / very cold	< 0.12	> 26.1	< 152
Cold	0.12 - 12	26.1 - 2.6	152 - 1515
Thermal	12 - 100	2.6 - 0.9	1515 - 4374
Epithermal	100 - 1000	0.9 - 0.28	4374 - 13800

Table 2.1: Classification of neutrons with respective ranges of energy, wavelength and velocity. Values obtained from [PSI, 2022].

uranium ^{235}U and its various nuclear fission reactions can be represented as [Arai, 2009]:

$$^{235}\mathrm{U} + \mathrm{n} \longrightarrow \mathrm{X} + \mathrm{Y} + 2.5\,\mathrm{n}, \tag{2.20}$$

where X and Y can be different elements or other fission fragments with a smaller atomic weight in sum. With an average energy release of $\approx 200\,\mathrm{MeV}$ per fission, only $2\,\mathrm{MeV}$ is released per neutron. Consequently, the reactor has to be constantly cooled for a stable operation. As the reaction shows, about one neutron is required to keep the chain reaction running, which produces 2.5 neutrons on average. Hence, such a nuclear reactor must be carefully designed to control the reaction rates and avoid an exponential increase of the neutrons in the fuel. This is done by neutron absorbers, that can be introduced with the cooling water or with control rods. From the 1.5 effectively remaining neutrons in the reaction about one is available for external use and the rest is lost. One further aspect is that the released fast neutrons have a rather small interaction cross section for inducing fission at their high energy. Hence, they have to be ”slowed down” by inelastic scattering within the reactor by a so-called moderator (e.g. water) which also serves as the coolant. Heavy water (D_2O) is often used as a moderator since it has a high scattering cross section and a lower absorption cross section for neutrons compared to H_2O. The moderator tank can have a neutron reflector layer to keep fast neutrons inside the moderator volume and enhance the neutron flux. The beam tubes serving as exit points for the experiments are directed tangentially to the central volume of maximum flux and do not point directly at the fuel element to avoid fast neutrons and γ-rays in the beam path. By placing special moderators in the reactor core, one can further shift the neutron energy spectrum towards higher or lower energies for certain exit tubes that are directed on the respective arrangement.

The second kind of neutron sources are accelerator-based spallation sources. First, protons are brought to several hundreds MeV in a particle accelerator and directed to a target made of heavy metal. The collisions trigger nuclear spallation reactions yielding neutrons, pions, and spalled nuclei that undergo inter-nuclear cascades. During that process, a high number of neutrons with energies below 2 MeV are evaporated. In this way, one proton of e.g. 1 GeV energy can produce 25 neutrons on average from a lead target, and only about half of its energy is deposited as heat in the target [Arai, 2009]. Compared to a fission reactor, that is about one order of magnitude less heat that has to be dissipated at comparable neutron flux. Further, spallation sources do not require radioactive or even isotopically enriched fuel and produce much less radioactive waste. One further advantage is that such sources can be operated in pulsed mode enabling energy discrimination for various experimental methods via time-of-flight measurements. These and several other advantages make spallation sources more attractive than nuclear reactors for future neutron research. However, the average neutron flux of spallation sources is still significantly below that of nuclear reactors.

2.2.3 Neutron Interaction with Matter

Since the neutron does not carry any charge, it does not interact with the electron shell and the Coulomb field of the nucleus like e.g. impinging electrons. Instead, it interacts with the atomic nucleus via the strong nuclear force. An exception is unpaired electrons that neutrons can interact with via the magnetic dipole forces since the neutron has a magnetic dipole moment. There are many different types of interactions (including fission and fusion reactions) that occur over a broad neutron energy range. Those relevant for imaging with thermal and cold neutrons will be briefly discussed here. Similar to X-ray interaction, the attenuation of a neutron beam transmitting matter is caused by scattering and absorption processes. While there are many similarities in physical formalism like the complex refractive index and the Beer-Lambert law, the interaction cross sections differ fundamentally. Figure 2.5 shows the X-ray and neutron mass attenuation coefficient by element. While there is no correlation with atomic number recognizable for neutrons, there is a slow and continuous increase with X-ray radiation. Neutrons interact stronger with hydrogen and oxygen which results in higher absorption by organic materials and enables a much better contrast in imaging compared to X-rays. For some heavy metals like W or Pb, the neutron mass attenuation coefficient is more than one order of magnitude smaller compared to X-rays. This enables the generation of contrast with many metallic samples that are hardly accessible with X-ray radiography. In fact, this opens many possibilities for investigating organic components in environments that are hard to penetrate with

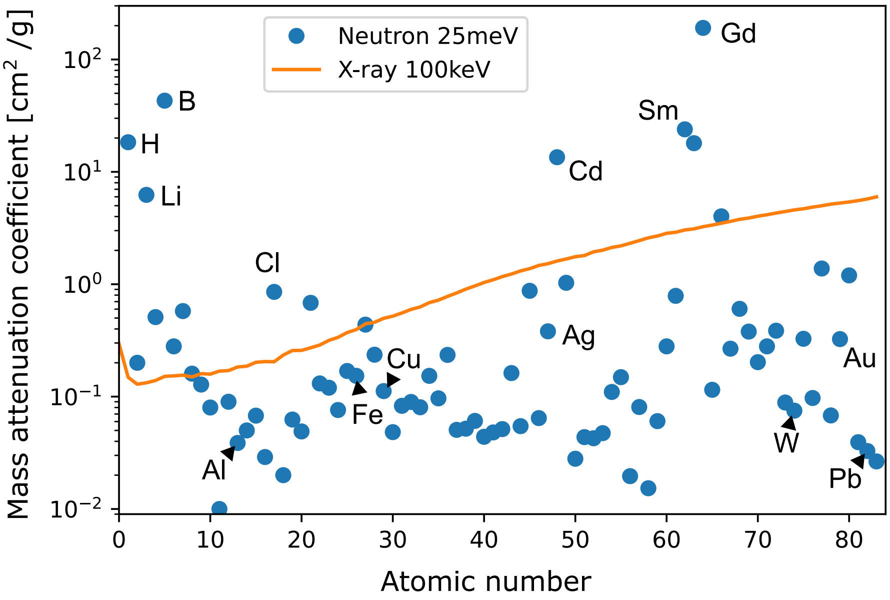

Figure 2.5: Mass attenuation coefficient by atomic number for X-ray and neutron radiation. While there is a continuous increase with X-rays the neutron attenuation varies strongly with the element. In particular, the penetration depth with heavy elements like W or Pb is significantly higher with neutrons while organic materials absorb stronger due to their hydrogen content. Gadolinium (Gd) is an excellent neutron absorber and is therefore used in scintillator materials and absorption gratings. Data obtained from [Sears, 1992] and xraylib [Schoonjans, 2011].

X-rays.

Neutron scattering processes can be elastic (conservation of kinetic energy) and inelastic, where a part of the neutron energy is transferred into nuclear excitations. The elastic processes consist of a coherent (carrying information about structures) and an incoherent part, which are quantified by respective interaction cross sections [Squires, 2012]. As with X-ray radiation, isotropic scattering processes degrade the resolution in imaging. However, for small-angle scattering, one can design the imaging system in a way that it becomes sensitive to minuscule dispersive effects. This enables the acquisition of images of scattering features additional to absorbing structures like in conventional neutron radiography. One further unique effect is the scattering of neutrons by magnetic domains or structures in materials induced by external magnetic fields. Those can be also visualized in the dark-field modality using a neutron interferometer.

2.2.4 Neutron Detectors

Similar to X-ray detectors, current neutron detectors rely on an interaction with a conversion material which produces secondary particles that can be detected. Thermal and cold neutrons do not ionize matter but require a nuclear neutron capture reaction for their detection. Hence, the used material, the so-called neutron converter, should have a strong neutron absorption cross section to be efficient. Typical converters are ^{3}He, ^{6}Li, ^{10}B, and ^{157}Gd [Crow, 2009]. Upon neutron capture, those materials release large amounts of energy in γ-radiation, X-rays, and charged particles such as protons, α-particles, and electrons. One such exemplary common conversion process is:

$$^{6}\mathrm{Li} + \mathrm{n} \longrightarrow {}^{3}\mathrm{H}^{+} + \alpha + 4.78\,\mathrm{MeV}. \tag{2.21}$$

The different high-energy reaction products ionize the surrounding material and have ranges of up to several tens of µm depending on the density of the conversion layer. To obtain the spatial position of the neutron capture reaction, the detector has to register at least one of the products as close to the point of incidence as possible. At the same time, the high-energy by-products such as γ-rays should not create detrimental signals far away from the point of incidence. Depending on the application and resolution requirements, different kinds of detectors have been implemented. For imaging, scintillating materials mixed with neutron converters have been established. They generate photons from ionization by the charged particles. A common binary scintillator is ^{6}LiF:ZnS which consists of a mixture of ^{6}LiF and ZnS particles of a few µm sizes glued together by an organic binder and deposited as a film of several hundred µm. This system was reported to provide about 160000 photons/neutron [Crow, 2009]. Since the single components of the mixture have differences in their refractive index, the created light scatters in the scintillating layer and leads to a resolution decrease with increasing layer thickness. Hence, a trade-off between absorption efficiency and resolution has to be made. For high-resolution imaging, thin powder scintillators such as Gd_2O_2S with the highest absorption efficiency are used. Here, about 10 µm is enough to absorb a high fraction of a cold neutron beam. However, the light yield is significantly smaller compared to ^{6}LiF:ZnS.

The detector usually consists of a CMOS or CCD camera with optics that can be focused on the scintillator screen. To protect the image sensor from the direct neutron beam partially transmitting the scintillator, a 45° mirror is often implemented. It allows placing the camera perpendicular to the beam and shielding it from scattered and secondary radiation. However, such a design also reduces the light collection efficiency. Further design aspects and also alternative detection mechanisms such as semiconductor sensors with neutron counting capabilities are described in [Crow, 2009].

2.3 Theory of Grating-based Multimodal Imaging

2.3.1 Classification among Phase-sensitive Methods

Phase-sensitive methods will be defined here as imaging approaches where the contrast is generated by the refractive or dispersive interaction with the sample exploiting wave properties of X-rays. A more extensive overview of the different techniques can be found in a recent review [Tao, 2021]. Since the phase of the wave cannot be measured directly (phase problem), it has to be translated into intensity modulation. Such imaging systems are designed in a way that refractive interactions with the sample would spatially shift or alter the intensity modulation. Some of the methods do not need optics such as propagation-based phase-contrast imaging. This method uses relatively coherent beams and high-resolution detectors which can resolve phase-related effects directly. Due to its simplicity, it is widely used at synchrotron facilities with computed tomography for soft tissue samples. However, the reconstruction requires several simplifying assumptions about the sample which complicates obtaining quantitative values. There are also lensless propagation-based techniques like coherent diffraction imaging which operate in the far-field and use phase retrieval algorithms to obtain quantitative images. Ptychography combines those with scanning techniques and iterative reconstruction algorithms reaching resolutions down to several tens of nm [Pfeiffer, 2017].

Different methods use optical elements to create an interference pattern that is sensitive to refractive objects placed in the beam. Single crystal interferometers were one of the early instruments that were implemented and used for this purpose. By cutting two grooves into a silicon ingot, there are three precisely aligned crystal slices acting as a beam splitter, mirror, and analyzer. Another similar technique called *Diffraction-enhanced Imaging* (DEI) or *Analyzer-based Imaging* (ABI) uses two crystals to monochromatize and analyze the X-ray beam after transmitting the sample. Similar to visible light phase-contrast microscopy, some systems have been developed for the X-ray regime, such as Zernike or differential interference contrast analogs using Fresnel Zone plates as X-ray lenses [Tao, 2021]. Further, there are absorptive optics employed as wavefront markers. Hartmann masks and coded apertures create beamlets that are directly resolved by the detector. After passing through the sample, the beamlets are deflected and their displacement relative to the reference position is retrieved yielding the differential phase image. A similar method called *Speckle-based Imaging* (SBI) uses non-periodic, random phase modulators (sometimes called diffusers) which create a speckle pattern as a wavefront marker [Zdora, 2018]. Such modulators are among others sandpaper with fine grains or steel wool for higher energies. Despite the wide availability of such diffusers, this method has some disadvantages which will be discussed in Chapter 6. A more efficient way is to use phase arrays that create a strong intensity modulation without absorbing a high fraction of the beam. Several such refractive arrays have been demonstrated ([Kagias, 2019; Reich, 2018; Dos Santos Rolo, 2018]) with periods in the range of several tens of µm. In Chapter 6 of this work, a novel two-dimensional Talbot Array Illuminator is introduced for high-resolution computed phase tomography and compared to current similar modulators.

The techniques mentioned so far rely on highly coherent radiation, high-resolution detectors, and have very small fields of view (FOV) making them unfeasible for diagnostical imaging. To address this issue, grating interferometry has shown the most potential and has experienced a steady development toward clinical application in the past decade. The main idea is to create periodic modulations with a phase grating and sample them with a respective absorption grating enabling detectors with large pixel sizes to record the modulation signal. An additional source grating enables the use of sources with large focal spots which is decisive for medical applications. This so-called Talbot-Lau interferometer will be introduced and discussed in the following. To date, it provides a FOV and scanning speed with common medical X-ray devices that is not achieved by the other techniques.

A somewhat similar, but less efficient and sensitive approach is so-called *Edge-Illumination Imaging* [Olivo, 2007]. Similar to Hartmann masks and coded apertures, it creates beamlets that are deflected by the sample. To make the deflection detectable with large pixels, an additional absorption mask is placed in front of the pixel matrix. The system is aligned in a way that the beamlets are illuminating the edges of the mask and any deflection of those leads to an increase or decrease in intensity. The method is also suitable for larger samples and high X-ray energies, however, it requires significantly smaller focal source spots. Furthermore, it requires a precise alignment of the mask to the detector pixel matrix and is therefore not compatible with some scanning approaches (movement of interferometer) used for the FOV extension with Talbot-Lau systems.

2.3.2 Fresnel Diffraction and Talbot Effect

An intensity modulation can be created by diffraction, a phenomenon resulting from wave propagation and interference after passing through slits or periodic apertures such as gratings. One such diffraction effect was discovered by H.F. Talbot in 1836 when he studied the propagation of sunlight passing through a small aperture and an absorption grating with a lens. Moving the lens along the propagation direction, he observed linear structures of different alternating colors (self-images of the absorbing grating) appearing at certain periodic distances [Talbot, 1836]. This phenomenon is called the Talbot effect and was theoretically explained by Lord Rayleigh in 1881.

With X-ray radiation (wavelength in the low Å range) and apertures in the µm range, the respective diffractive effects appear already at propagation distances of several tens of cm. This regime (combination of wavelength, apertures size, and propagation distance) is often called the near-field and is mathematically described by Fresnel diffraction. The propagated planar wave $E(x, y, z)$ can be calculated from the initial wave $E(x', y', 0)$ after propagation to z by [Goodman, 1996, p. 67]:

$$E(x,y,z) = \frac{e^{ikz}}{i\lambda z} \iint\limits_{-\infty}^{+\infty} E(x',y',0)\, e^{\frac{ik}{2z}[(x-x')^2+(y-y')^2]}\, dx'dy' \tag{2.22}$$

Analytical calculations can obtain certain propagation distances where the self-image condition $(E(x, y, z) = E(x', y', 0))$ is fulfilled. This happens at multiples of the Talbot-distance $d_T = 2p^2/\lambda$, where p is the period of the grating [Suleski, 1997]. Additionally, binary intensity modulations appear laterally shifted by $p/2$ at $z = 1/2d_T, 3/2d_T, ...$ An adaptation of Formula 2.22 employing Fourier transforms allows a fast numerical calculation of the propagated wave field after passing through any arbitrary absorption or phase modulator. Figure 2.6 A shows the evolving intensity modulation after an absorption grating with propagation in the z-direction, which is often denoted as *Talbot carpet*. A similar effect also appears with binary phase gratings creating even more self-images at certain fractional Talbot distances which are given by [Donath, 2009]:

$$d_n = \frac{1}{\eta^2}\frac{(2n-1)p^2}{2\lambda}, n = 1, 2, ..., \tag{2.23}$$

with $\eta = 1$ for $\pi/2$-shifting and $\eta = 2$ for π-shifting phase gratings. In between those self-images in the phase domain, binary intensity modulations appear that can be used like those from absorption gratings. Figures 2.6 B and C show the Talbot carpets of binary $\pi/2$-shifting and π-shifting gratings where binary modulations appear at fractions of d_T. Suleski reported a list of even more phase grating designs with different duty cycles and phase shifts that create binary intensity modulations at fractions of d_T [Suleski, 1997]. One such combination will be used to create a phase array with a higher compression ratio in Chapter 6.

With polychromatic sources, the intensity modulation is blurred as it is a superposition of Talbot carpets with different energies. This has to be considered in system design and adapted to the spectrum, especially if gratings are used that induce a lateral shift

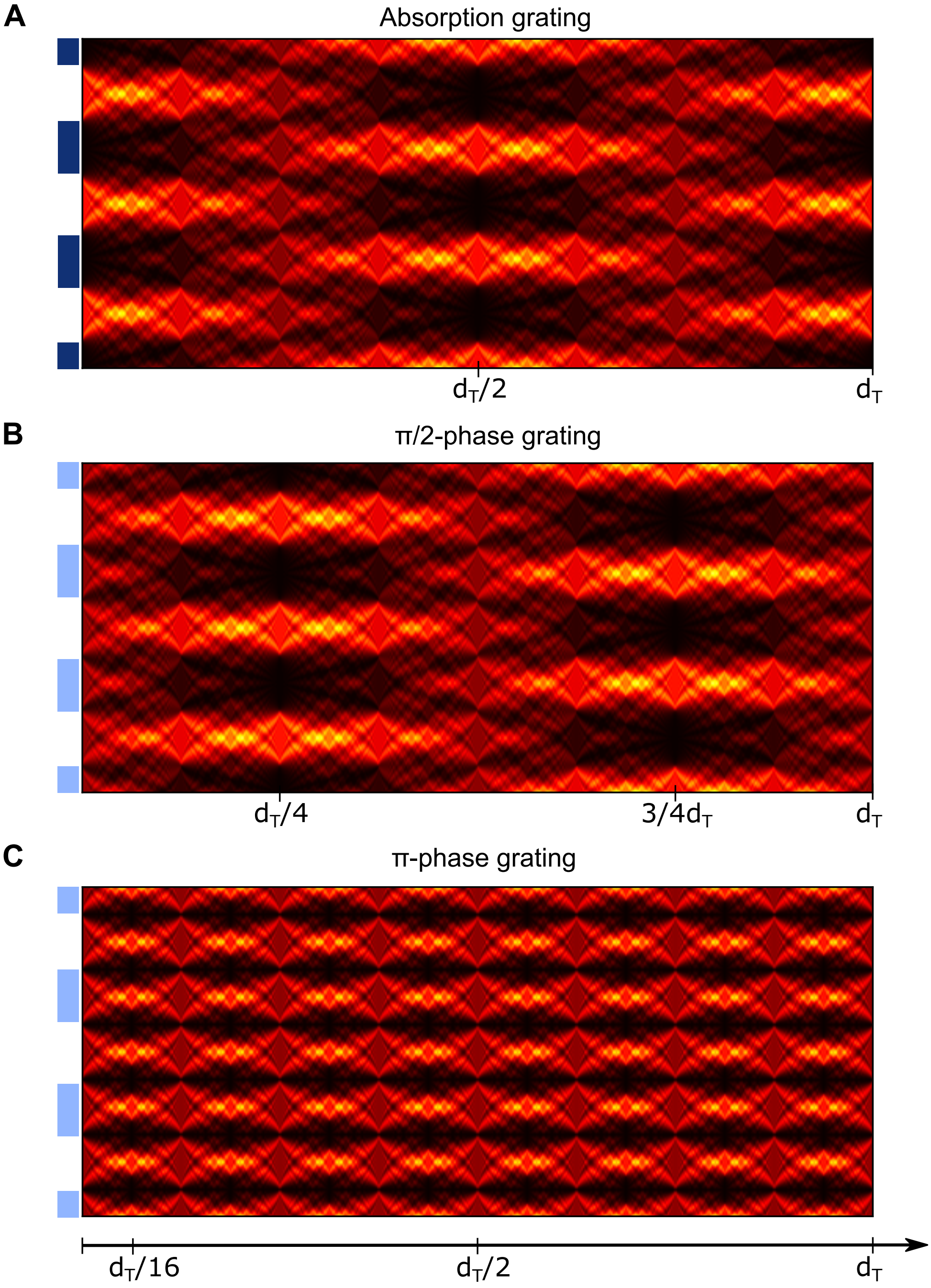

Figure 2.6: (A) Talbot carpet of an absorption grating showing a self-image in the intensity domain at d_T and a shifted binary intensity modulation at $1/2d_T$. (B) Talbot carpet of a $\pi/2$-phase grating showing binary modulations at $1/4d_T$ and $3/4d_T$. (C) Talbot carpet of a π-phase grating showing binary modulations with half period $(p/2)$ at odd multiples of $1/16d_T$.

at higher Talbot orders such as seen with absorption and $\pi/2$-phase grating (Figure 2.6 A and B). Since phase gratings transmit a high fraction of the radiation and are also easier to fabricate, they are preferred over absorption gratings to create the modulation used for phase imaging. For that reason, this grating is often called *modulation grating* and is denoted as G_1. Typically, it creates modulations on the scale of a few µm on propagation distances of a few tens of cm. To be sensitive to the change of this modulation by the sample with conventional detectors an additional absorption grating forming an interferometer system is needed.

2.3.3 Talbot-Lau Interferometer

To use the Talbot effect for multimodal X-ray imaging with current medical hardware, two main challenges occur. First, the radiation has to have a degree of spatial coherence enabling it to form a clear diffraction pattern after propagation in space. Second, the modulation has to be recorded by a detector with a larger pixel size ($>100\,\mu\text{m}$) than the period of the modulation (typically $\approx 10\,\mu\text{m}$). To address the latter problem, an absorption grating with a period close to the modulation period is placed before the detector. As a result, every pixel records a periodic sample of intensity that transmits the transparent fraction of the grating. As illustrated in Figure 2.7 A the stepping of the grating and taking separate images in several positions over the range of one period allows sampling of the fringe modulation. Thus, this absorption grating is often called the *analyzer grating* and is denoted as G_2. The stepping procedure is performed with and without the sample, acquiring several intensity points that can be modeled by sinusoidal functions as illustrated in Figure 2.7 B. The images are calculated from the determined fitting parameters and will be addressed later. Such a system consisting of two gratings is called a *Talbot interferometer* and was first demonstrated for X-rays by Momose et al. with a coherent undulator synchrotron source [Momose, 2003]. Similar systems have also been used with micro-focal laboratory X-ray tubes that provide enough coherence to induce the Talbot effect. However, those kinds of sources are several orders of magnitude away from the high flux that is needed for in-vivo diagnostic imaging.

A solution to this problem is an effect described by Ernst Lau, where he found that two absorption gratings create diffraction patterns at different distances under incoherent illumination [Lau, 1948]. The first grating creates an array of periodic light sources which are individually sufficiently coherent to create a diffraction pattern by the second grating. At certain distances, the patterns created by individual periodic slits of the first grating overlap, and an image of the first grating is created in a certain color when visible light is used. Employing this principle, one can use extended radiation sources that are not sufficiently coherent to produce diffractive patterns for diffraction experiments with a much higher intensity than sources with small spatial dimensions or apertures. To combine it with the Talbot interferometer, the periods must be chosen such that the generated periodic pattern emerges at the G_2 position and their periods match for good contrast. For that, the *source grating* G_0 has to fulfill the geometric relation:

$$p_0 = p_2 \frac{l}{d}, \tag{2.24}$$

where p_0 and p_2 are the periods of the G_0 and G_2, l the G_0-G_1 distance, and d the G_1-G_2 distance. This arrangement was proposed and employed to study matter waves by J.F. Clauser and M.W. Reinsch, who also suggested such a three-grating interferometer for X-ray phase-contrast imaging [Clauser, 1992; Clauser, 1997]. It was experimentally realized for X-ray and neutron phase imaging by Pfeiffer et al. [Pfeiffer, 2006b; Pfeiffer, 2006a].

A detailed discussion of possible geometries for Talbot-Lau interferometers considering aspects of grating fabrication will be provided after discussing the contrast formation and image retrieval.

2.3.4 Contrast Mechanisms and Signal Extraction

Quantitative mathematical modeling of the Talbot-Lau interferometer operates with grating transmission functions which provide the spatial intensity distribution created by the grating for a certain wavelength. The intensity modulation acquired in the stepping process can be mathematically described as a convolution of the transmission functions of G_1 and G_2 [Chabior, 2012]. In the case of binary rectangular transmission functions, this gives a triangular function. A third convolution is done to consider the G_0 grating which results in piecewise-defined second-degree polynomial functions which can be well approximated with a sinusoidal function when the duty cycles of the gratings are close to 0.5 [Pinzek, 2021b]. Hence, the pixel intensity acquired over several steps might be fitted with:

$$I(x) = a_0 + a_1 \sin\left(2\pi \frac{x}{p_2} - \psi\right), \tag{2.25}$$

where p_2 is the period of the stepped grating and x is the grating position within the stepping range $[0, p_2]$. The fitted parameters are the mean a_0, the amplitude a_1, and a phase-related offset ψ. Three stepping positions are required as a minimum for a reasonable fit, however, significantly more points are usually recorded for better signal quality.

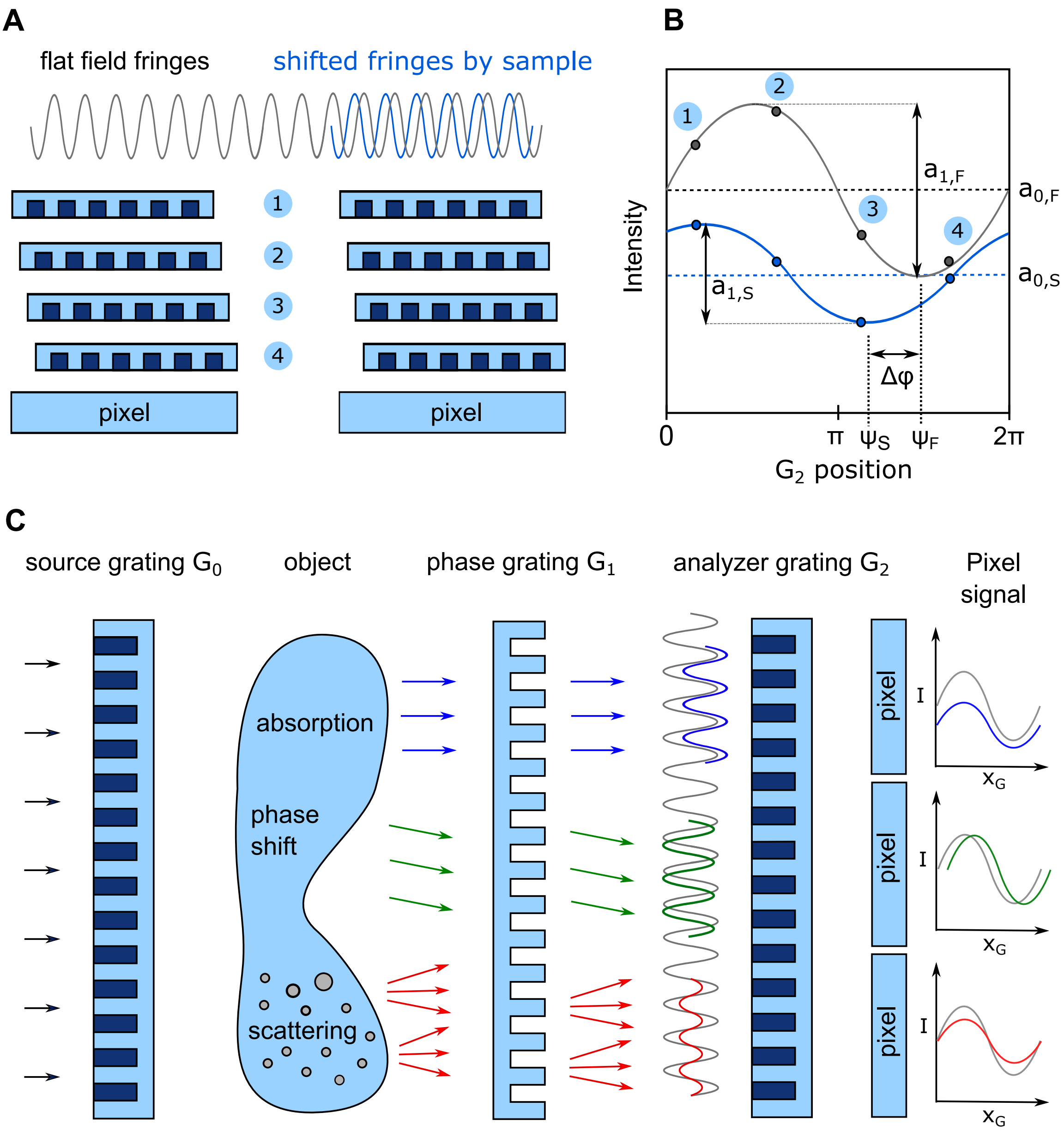

Figure 2.7: (A) Illustration of the stepping procedure with 4 grating positions to sample a high-frequency fringe pattern with an absorption grating. (B) Measured intensity values for sample and flat field scan for the 4 steps and their sinusoidal fits with respective parameters. (C) Illustration of the Talbot-Lau interferometer with the signal formation process. Absorption reduces the overall intensity signal. The refractive interaction shifts the phase of the pattern relative to the reference signal and scattering introduces a disproportional reduction of the amplitude.

Due to positioning deficiencies of the gratings, the acquired steps are often not precisely equidistant or the stepping range is not perfectly matched with the period. Hence, the most advanced processing pipelines also iteratively estimate the grating positions based on the entire interferogram using expectation maximization algorithms. Figure 2.7 B shows an exemplary fit of a scan with and without the sample with respective fit parameters. As seen in Figure 2.7 C, the attenuation by the sample causes an overall signal decrease and the quotient of the mean values $a_{0,S}/a_{0,F}$ corresponds to the conventional absorption image acquired in radiography. A phase-shifting object introduces a refractive deflection of the fringes which is retrieved by the difference of the phase offsets $\Delta\varphi = \psi_F - \psi_S$, which can have values in the range $[0, 2\pi]$. Shifts larger than this range are measured $\bmod 2\pi$ which is inherent in the periodic sampling principle and is often referred to as *phase wrapping*. Since the image retrieved by this procedure shows the local change of the phase $\Delta\varphi$, it is often called *differential phase-contrast* (DPC). The phase shift Φ in every pixel is calculated by integrating the differential signal and can be used for tomographic reconstruction to obtain a three-dimensional representation of δ employing Equation 2.17. It reveals soft-tissue structures with much higher contrast than the respective absorption channel.

The third modality is related to small-angle X-ray scattering occurring in porous, interface-rich structures and leads to an amplitude decrease of the fringe pattern as seen in Figure 2.7 C. An important metric quantifying the amplitude in relation to the mean is the visibility defined by:

$$V = \frac{a_1}{a_0} = \frac{I_{max} - I_{min}}{I_{max} + I_{min}}, \tag{2.26}$$

where I_{max} and I_{min} are the maximum and minimum of the fitted modulation in every pixel. The flat field visibility V_F (no sample in the beam) is also quantifying the interferometer performance and depends on many system parameters such as the grating transmission, the duty cycle, the alignment precision, the geometrical design, and the used X-ray spectrum and spatial source size. The reduced visibility with the sample in the beam is denoted as V_S and its normalized signal:

$$D = \frac{V_S}{V_F} \tag{2.27}$$

is called the *Dark-field Image* (DFI) or scattering contrast image [Pfeiffer, 2008]. Sometimes the dark-field image is also displayed in the logarithmized form $-ln(D)$ with a dark background corresponding to 0. For weakly absorbing but strongly scattering samples, an exponential decrease of D with transmitted thickness t can be observed. Hence, similar to the Lambert-Beer law, a so-called *linear diffusion coefficient* ϵ can be introduced fulfilling [Bech, 2010; Malecki, 2012]:

$$D = \exp\left(-\int_0^t \epsilon(z)dz\right) \tag{2.28}$$

Accordingly, the signal can also be used for quantitative CT reconstruction similar to the attenuation signal [Bech, 2010]. However, it becomes significantly more complicated for objects consisting of strongly absorbing and scattering materials. The absorption causes a disproportional decrease of visibility due to spectral effects leading to absorbing structures appearing in the dark-field image [Yashiro, 2015]. One such example will be further discussed in Chapter 5 where X-ray and neutron dark-field CT will be compared. To solve this problem for thorax imaging where the dark-field signal of the lung is of interest, calibration measurements with various slices of absorbing and scattering phantom materials are performed. From both the attenuation and the scattering signals of different material combinations, the fraction of the absorption-induced artificial dark-field signal is estimated and subtracted from the image.

2.3.5 Aspects of Interferometer Design

Up to now the Talbot effect and its emerging intensity modulations at fractional Talbot distances have been discussed for a parallel X-ray beam. For divergent beams provided by X-ray tubes, some geometrical relations have to be adapted. In cone beam geometry, the distances and parameters of the gratings have to be magnified by a factor M given by the intercept theorem [Donath, 2009]:

$$M = \frac{l+d}{l}. \tag{2.29}$$

Here, M is the magnification of G_1 onto the G_2 grating with the point sources created by the G_0 as the origin. It should not be confused with the magnification of the imaged object which depends on the source, detector, and sample placement. The Talbot distance D_n rescales according to the Fresnel scaling theorem to:

$$d_n = MD_n, \tag{2.30}$$

when D_n is the fractional Talbot distance in parallel geometry. The period of G_2 has to be also adapted to the magnification by:

$$p_2 = Mp_1, \tag{2.31}$$

Combining Equations 2.29 and 2.30 and setting $d_n = d$, one obtains a relation similar to the classic lens equation [Donath, 2009]:

$$\frac{1}{D_n} = \frac{1}{l} + \frac{1}{d_n}. \tag{2.32}$$

Defining a total interferometer length $s = l + d_n$ and substituting d_n in Equation 2.32, a quadratic formula emerges:

$$l^2 - sl + SD_n = 0, \tag{2.33}$$

which is solved by:

$$l_{1,2} = \frac{s}{2} \pm \sqrt{\frac{s}{4}(s - 4D_n)}. \tag{2.34}$$

For $s < 4D_n$, there is no solution due to the negative discriminant. For $s = 4D_n$, the inter-grating distances become equal with $l = d_n = s/2 = 2D_n$ and a magnification factor of $M = 2$. Such a setup is illustrated in Figure 2.8 B and is called *symmetric*. For a positive discriminant with $s > 4D_n$, there are two solutions. For l_1 with $l > d$, the phase grating G_1 is closer to G_2 and the period p_0 of G_0 is larger than p_2 of the G_2 as shown in Figure 2.8 A. Since such setups were more common at early stages, this configuration is often called *conventional geometry*. The opposite case of l_2 with $l < d$ and $p0 < p2$ is shown in Figure 2.8 C and is called *inverse geometry* [Donath, 2009]. The three possible geometries offer scope for design, but also define the requirements for grating fabrication. Common limits for diagnostic systems are the total system length which is about 2 m for radiography and typically 1 m for medical CT to fit on a rotating gantry. Further, the design is driven by the requirement of space for the imaged object. In this regard, asymmetric geometries offer advantages since there is more space between either G_0 and G_1 or G_1 and G_2. In both cases, the sample should be placed as close as possible to G_1 for maximal sensitivity as shown by [Donath, 2009].

As also evident from Figure 2.8, the different geometries require different grating areas to cover a certain FOV. In particular, the inverse geometry is beneficial since it needs a much smaller G_1 compared to the conventional geometry. Further, the G_2 having the largest grating area has a much greater period than in conventional geometry and can therefore be fabricated easier. With larger periods, the absorptive part of the grating

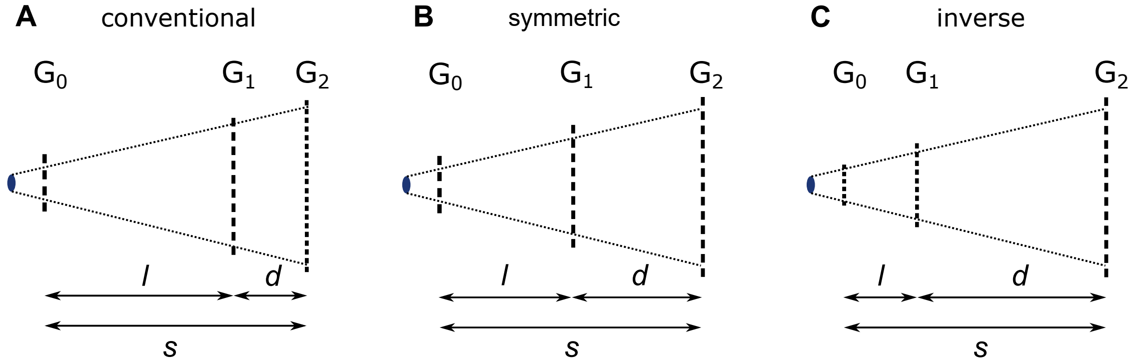

Figure 2.8: Sketches of different grating interferometer geometries fulfilling Equation 2.33. (A) Conventional geometry with $l > d$ and $p_0 > p_2$, (B) symmetric design with $l = d$ and $p_0 = p_2$, and (C) inverse geometry with $l < d$ and $p_0 < p_2$.

can be made significantly deeper. As will be shown in Chapter 4, this allows using cheaper absorber materials like e.g. tungsten and simpler deposition techniques compared to current methods. However, the inverse geometry also brings a serious challenge to producing a source grating G_0 with a small period and a high aspect ratio. In addition, it must be bent to a cylindrical plane with the source-to-G_0 distance as the radius to avoid shadowing, as will be elaborated in the next chapter. Still, it proves to be reasonable to put the most stringent fabrication requirements on the grating with the smallest area.

An implementation of a Talbot-Lau interferometer in a CT gantry with an interferometer length of about 1 m with 60 cm in the center being reserved for the patient poses further challenges. At tube voltages of 70-80 kV (mean energies around 40-50 kV), the fractional Talbot distances with reasonably producible G_1 periods are too long. A possible solution is to use triangular phase gratings with phase shifts beyond π, which can produce modulations at shorter propagation distances [Yaroshenko, 2014]. Despite these challenges, an inverse geometry Talbot-Lau system in a CT gantry of a clinical scanner has been recently demonstrated in [Viermetz, 2022]. Chapter 4 of this work elaborates on a novel fabrication process for a G_2 grating for such a system using tungsten as the absorber material.

2.4 Principles of Computed Tomography

2.4.1 Introduction

So far, mainly the generation of projectional X-ray images with different contrast mechanisms have been discussed. The obvious disadvantage of such images is that no information about the depth of the depicted features inside the object can be obtained from them. To address this problem, a method called *tomography* (Greek: tomos, slice, section) was developed in the 1920s and 1930s. During the acquisition, the X-ray source and the detecting film were moved in opposite directions with precisely chosen velocities such that there was a plane in the imaged object whose features were always projected onto the same points of the detector. Structures that were far from the plane were smeared out and created a diffuse background that did not interfere too much with the imaged plane. While this approach was realized in many different geometries and could address some diagnostic tasks, it was inefficient for obtaining fully three-dimensional (3D) data.

A significant advance came with the idea of reconstructing the three-dimensional distribution of the linear attenuation coefficient from many projections recorded at different angles. While the underlying mathematical problem was already solved by Johann Radon in [Radon, 1917], several pioneers came up with the reconstruction regarding the X-ray application independently without being aware of Radon's work. Semyon Tetelbaum and Boris Korenblum [Tetelbaum, 1957; Korenblum, 1958] first suggested a setup with a rotating sample and a collimated fan beam recording transmission data on film. They also proposed a reconstruction algorithm with an analog computing device that should read the data from the film and display the tomogram on a TV screen. It remains unknown if there was an experimental realization with final results. A few years later Allan Cormack published a paper [Cormack, 1963] solving the same problem with some proof of concept experiments with a gamma source. However, he did not pursue further development toward applications due to the lack of interest in his publication. In the late 1960s, Godfrey Hounsfield started to work on the same problem and developed a scanner with a collimated pencil beam and a point detector that recorded the transmission of a slice by linear movement of the source and detector. The measurement consisted of a sequence of linear scans and incremental sample rotations which was later referred to as rotate-translate scanning. Hounsfield implemented his design on a rotating gantry enabling a static object scan and demonstrated its first clinical in-vivo application in October 1971 visualizing a brain tumor [Hounsfield, 1973]. After this breakthrough, the method developed very quickly in scanning time and image quality and was soon commercially available. In 1979

Cormack and Hounsfield were awarded the Nobel Prize in Physiology or Medicine for their development of CT.

In the past decades, CT scanning has become a powerful instrument for countless applications and its principles have been translated to other types of radiation. Both hardware implementation and reconstruction algorithms remain versatile fields of research with many innovations. In this work, CT is employed for several tasks starting from characterizing samples for grating fabrication to comparing multimodal techniques with X-rays and neutrons for various applications in material science and medicine. In the following, the principles of CT reconstruction will be discussed using the simplified case of a parallel beam. The condensed discussion is based on [Kak, 2001], where a comprehensive treatment of CT-related theory is available.

2.4.2 Radon Transform and Fourier Slice Theorem

Let the quantity characterizing the sample (e.g. the linear attenuation coefficient) in one layer be given by a two-dimensional function $f(x, y)$ as shown in Figure 2.9 A. To calculate the projection information obtained under an angle θ, a rotated coordinate system (s, t) should be introduced:

$$\begin{pmatrix} s \\ t \end{pmatrix} = \begin{pmatrix} \cos\theta & \sin\theta \\ -\sin\theta & \cos\theta \end{pmatrix} \begin{pmatrix} x \\ y \end{pmatrix} \tag{2.35}$$

The trajectory of a transmitting beam impinging under the angle θ at coordinate s is given by:

$$x\cos\theta + y\sin\theta = s. \tag{2.36}$$

Integrating $f(x, y)$ along that path can be realized using the delta function δ and is denoted as *Radon transform*:

$$p(\theta, s) = \int_{-\infty}^{\infty}\int_{-\infty}^{\infty} f(x, y)\delta(x\cos\theta + y\sin\theta - s)dxdy. \tag{2.37}$$

Figure 2.9 A illustrates this one-dimensional projection function $p(\theta, s)$. Its Fourier transform is calculated by:

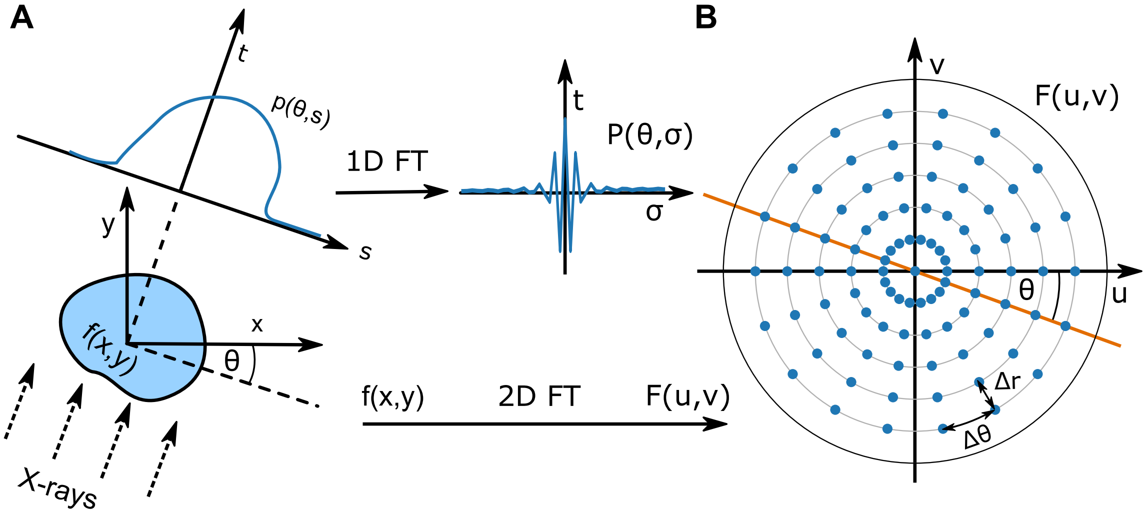

Figure 2.9: Illustration of the Fourier slice theorem. (A) The cross section of the scanned object is described by the function $f(x, y)$. The line integral of $f(x, y)$ performed under some angle θ gives the function $p(\theta, s)$ (Radon transform). A one-dimensional Fourier transform (FT) of $p(\theta, s)$ corresponds to lines in Fourier space (B) at the respective angle. A two-dimensional FT of $f(x, y)$ corresponds to the same data $F(u, v)$ in the plane of the Fourier space.

$$P(\theta, \sigma) = \int_{-\infty}^{\infty} p(\theta, s) e^{-2\pi i \sigma s} ds. \tag{2.38}$$

Integrating over $s = x \cos\theta + y \sin\theta$ yields only one non-zero value due to the delta function resulting in:

$$P(\theta, \sigma) = \int_{-\infty}^{\infty} \int_{-\infty}^{\infty} f(x, y) e^{-2\pi i \sigma (\cos\theta + y \sin\theta)} dx dy. \tag{2.39}$$

Calculating the two-dimensional Fourier transform of the function $f(x, y)$ gives:

$$F(u, v) = \int_{-\infty}^{\infty} \int_{-\infty}^{\infty} f(x, y) e^{-2\pi i (ux + vy)} dx dy. \tag{2.40}$$

For $u = \sigma \cos\theta$ and $v = \sigma \sin\theta$ which represents the blue line at angle θ in the Fourier space (see Figure 2.9 B), the one-dimensional Fourier transform $P(\theta, \sigma)$ as given by Equation 2.39 is equal to $F(u, v)$:

$$P(\theta,\sigma) = F(\sigma\cos\theta, \sigma\sin\theta). \tag{2.41}$$

This relation is known as the *Fourier slice theorem* and enables "filling up" the Fourier domain of $f(x,y)$ by taking many projections from various angles θ. Afterward, $f(x,y)$ can be obtained by performing an inverse Fourier transform. As the measurements are acquired with pixel detectors, the values in the Fourier space are also discrete values visualized by the blue dots in Figure 2.9 B. Their density decreases radially outwards (toward higher frequencies), meaning that the sampling for smaller features in $f(x,y)$ decreases. Hence, the number of angles has to be chosen such that the angular sampling ($\Delta\theta$) is similar to the radial (Δr) component, which is related to the sampling of the detector (e.g. the pixel size).

2.4.3 Filtered Back Projection

As seen in Figure 2.9 B, the sampling density has a strong radial dependence and hence does not allow a direct calculation of the inverse Fourier transform. To avoid interpolation to a rectangular grid the problem should be rewritten in polar coordinates with $u = \sigma\cos\theta$, $v = \sigma\sin\theta$ and the Jacobian determinant $dudv = \sigma d\sigma d\theta$:

$$f(x,y) = \int\limits_{-\infty}^{\infty}\int\limits_{-\infty}^{\infty} F(u,v)e^{2\pi i(ux+vy)}dudv = \int\limits_{0}^{2\pi}\int\limits_{0}^{\infty} F(\sigma,\theta)e^{2\pi i\sigma(x\cos\theta+y\sin\theta)}\sigma d\sigma d\theta. \tag{2.42}$$

Splitting the integral over θ in two parts $[0,\pi]$ and $[\pi,2\pi]$ yields:

$$\begin{aligned} f(x,y) = &\int\limits_{0}^{\pi}\int\limits_{0}^{\infty} F(\sigma,\theta)e^{-2\pi i\sigma(x\cos\theta+y\sin\theta)}\sigma d\sigma d\theta \\ &+\int\limits_{0}^{\pi}\int\limits_{0}^{\infty} F(\sigma,\theta+\pi)e^{-2\pi i\sigma(x\cos(\theta+\pi)+y\sin(\theta+\pi))}\sigma d\sigma d\theta. \end{aligned} \tag{2.43}$$

The expression can be simplified by using the symmetry of the two-dimensional Fourier transform $F(\sigma,\theta) = F(-\sigma,\theta+\pi)$ to:

$$f(x,y) = \int\limits_{0}^{\pi}\int\limits_{-\infty}^{\infty} F(\sigma,\theta)e^{-2\pi i\sigma(x\cos\theta+y\sin\theta)}|\sigma|d\sigma d\theta. \tag{2.44}$$

Using the Fourier slice theorem (eq. 2.41), the following expression is obtained:

$$f(x,y) = \int_{0}^{\pi} \int_{-\infty}^{\infty} P(\theta,\sigma) e^{-2\pi i \sigma s} |\sigma| d\sigma d\theta. \tag{2.45}$$

A closer look at this expression shows that the inner integral represents a one-dimensional inverse Fourier transform of the projection weighted by a function $|\sigma|$ which accounts for the higher sampling density towards the center. It is often referred to as *Ram-Lak* filter. To obtain $f(x,y)$, the filtered projectional data is back-projected into a two-dimensional array under the angles θ it was acquired. This standard algorithm is therefore called the *filtered back projection*.

Note that this brief treatment only applies to the simple case of a parallel X-ray beam and the acquisition of one-dimensional projection data. In practice, most CT devices have 2D detectors and cone-shaped beams originating from the X-ray source. Hence, they require a three-dimensional back projection which is done in the Feldkamp algorithm [Feldkamp, 1984]. Common reconstruction software also applies many advanced algorithms accounting for various experimental factors like the out-of-center placement of the sample, pixel-related deficiencies, flux variance of the X-ray tube, or even sample drifts during the scan. Among the more advanced and computationally heavy algorithms are algebraic and statistical iterative reconstruction approaches. They calculate virtual projections from an initial volume obtained by the filtered back projections. These projections are then compared with the measured data and the volume is updated accordingly. This process is repeated multiple times until some predefined criteria are reached. Such methods allow the reconstruction of decent images from a low number of projections making them more dose-efficient for medical applications. Additionally, physical effects like beam starvation can be handled easier and allow suppressing artifacts. For a more detailed treatment of CT reconstruction and related aspects, the interested reader should be referred to [Buzug, 2008].

3 State-of-the-Art Grating Fabrication and Characterization Methods

After elaborating on theoretical aspects of signal formation and design in Talbot-Lau interferometers, a closer look is taken at the fabrication and characterization of the required gratings. This chapter will give an overview of currently existing conventional and rather exotic approaches. The processes will be briefly described, and their advantages and drawbacks will be addressed. After that, grating characterization methods will be explored. A convenient method for fast non-destructive large-area quality control that was developed in the framework of this thesis will be elaborated.

3.1 Grating Fabrication Methods

Since the first successful fabrication endeavors [Matsumoto, 2007; David, 2007] which were developed customary to demonstrate X-ray grating interferometry, several new methods have been proposed. The procedure usually starts with creating high aspect ratio structures either in silicon via anisotropic etching or in thick layers of photoresist via deep X-ray lithography (DXRL). After that, the deep trenches are filled with absorbing or phase-shifting material employing methods such as electroplating, physical or chemical vapor deposition, hot-embossing, casting, or particle deposition. For all approaches, the high aspect ratio which is usually required for absorption gratings is the main limiting factor and poses challenges both in the fabrication of the template as well as in the filling process. The currently available methods use complex and expensive processes, which have limits in area and depend on special technologies such as DXRL, which is currently only available at synchrotron facilities. In this chapter common and new fabrication methods will be reviewed and their potential for reliable and cost-effective pathways toward grating production for medical systems will be evaluated.

3.1.1 Absorbing Materials

X-ray Applications

As previously discussed an optimal absorbing material for X-rays must have an overall high electron density, which is the case for metals with high density and atomic number Z. At the same time the material should be easy to work with (e.g. not remarkably toxic or radioactive) and chemically stable once deposited in the grating structure. Table 3.1 lists heavy metals which can be considered most relevant for the discussed application. Au with $Z = 79$ is currently the most established absorber material due to its widespread use in microfabrication processes and excellent absorbing properties. However, its high material cost and long electroplating process complicate the production of high volumes. Some of the elements like rhenium, osmium, iridium, and platinum are even denser than gold and would be well suited as absorbing material. However, respective deposition methods for high aspect ratio structures are not well established and their material cost advantage compared to Au is marginal. Affordable alternatives are tantalum (Ta), tungsten (W), lead (Pb), and bismuth (Bi). Both the latter have low melting points and are therefore interesting for casting or hot embossing approaches. Tungsten (W) has the highest density among the lower-priced alternatives and can be considered the most promising candidate for a particle-based deposition of the absorber into the grating structure. A further possibility is also Chemical Vapor Deposition (CVD) with W which is currently being developed and optimized for creating low-resistivity interconnects in integrated circuits.

Figure 3.1 A gives a plot of the attenuation coefficient μ for Au, W, and Pb showing the most remarkable K-absorption edges of the three materials in the range of 65-90 keV. In Figure 3.1 B the attenuation of a 120 kV spectrum of 200 µm of the respective materials is shown. Obviously, a K-absorption edge at a lower energy is favorable as is the case with W compared to Au and Pb since it absorbs a higher fraction of the spectrum. However, it only plays a noticeable role when the used spectrum has energies in the respective range. For e.g. dark-field imaging of the human thorax acceleration voltages of 60-70 kV have been used. In this case, the lower K-edge of W (69.5 keV) compared to Au (80.7 keV) is not particularly useful. But even if higher energies would be applied, the lower K-edge of W plays a minor role in dark-field thorax imaging, as most of the scattering contrast that is finally detected is formed below 50 keV as spectral measurements show [Andrejewski, 2017]. It is certainly possible to exploit higher energies for dark-field contrast formation, however, the sensitivity of the system has to be increased for that. That requires even smaller grating periods and higher absorption thicknesses in the gratings to cope with the higher energies and results in even higher aspect ratio requirements. For phase-contrast

Metal	Z	Density [g/cm^3]	K_α-absorption edge [kV]	Transmission at 50 keV[1]
Tantalum	73	16.7	67.4	14.9 %
Tungsten	74	19.3	69.5	10.1 %
Rhenium	75	21.0	71.7	7.4 %
Osmium	76	22.6	73.9	5.5 %
Iridium	77	22.6	76.1	5.0 %
Platinum	78	21.5	78.4	5.1 %
Gold	79	19.3	80.7	6.1 %
Lead	82	11.3	88.0	16.1 %
Bismuth	83	9.8	90.5	19.5 %

[1] calculated with a thickness of 200 µm of the respective material

Table 3.1: Characteristics of suitable metals for X-ray absorption gratings.

imaging, however, the differences in spectral visibility due to the absorption edges can be of interest, especially when they are accessed by spectral detectors and used as additional information [Mechlem, 2020]. Overall, tungsten can be considered the most affordable and similar alternative to Au in terms of absorption performance.

Neutron Applications

As previously discussed in the second chapter explaining the neutron interaction with matter the attenuation of neutrons does not follow distinct trends like in the case of X-rays. Rather, it depends on the properties of the atomic nucleus and is therefore even isotope-specific. The strongest attenuation of all elements has gadolinium (Gd) with an absorption cross section of 49700 barn at 1.8 Å in its natural isotopic composition [Sears, 1992]. All other strongly absorbing alternatives like boron (B), cadmium (Cd), or samarium (Sm) have significantly smaller mass attenuation coefficients and do not compete with Gd. Therefore, all works related to neutron absorption grating fabrication have used Gd or one of its chemical compounds such as Gd_2O_3 or Gd_2O_2S – a possible scintillating material. Compared to X-rays the required Gd thickness to absorb neutrons

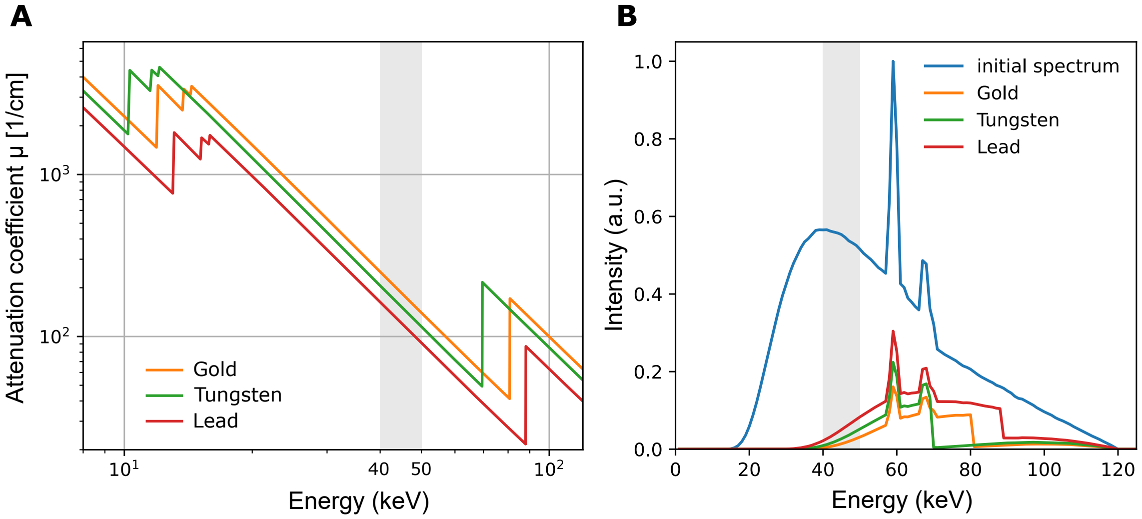

Figure 3.1: (A) Energy-dependent attenuation coefficient μ for gold (Au), tungsten (W), and lead (Pb). (B) Illustration of 120 keV tungsten spectrum attenuated by 200 µm Au, W, and Pb. The highlighted energy range between 40-50 keV is of particular interest for grating-based X-ray dark-field imaging of the lung.

used in typical neutron grating interferometer applications (of 1.5-6.0 Å wavelength) is much smaller and therefore moderate aspect ratios for gratings are sufficient. A further possibility to reduce the required thickness is to use enriched Gd with a high fraction of isotope ^{157}Gd which has a natural abundance of 15.6%. However, since isotopically-enriched materials are expensive and complex to obtain it is more practical to use a grating template with deeper trenches and increase the Gd thickness.

3.1.2 LIGA-based Method

The LIGA process (German acronym for “Lithograpie, Galvanik, Abformung”) was developed in the early 1980s at the Karlsruhe Institute for Technology (KIT) to produce microstructures with extremely high aspect ratios [Becker, 1986]. The method has proved extremely useful in the fabrication of absorption gratings in several works [Matsumoto, 2007; Noda, 2008; Mohr, 2012]. A schematic of the process is given in Figure 3.4. At first, a deep lithography step is performed with X-ray or ultraviolet radiation. For that, a thick resist (up to several hundred µm) is applied on a conductive (e.g. metal-coated) wafer consisting of silicon, polyimide, or graphite. After some resist-dependent thermal pretreatment, the structure is exposed to radiation through an absorption mask. The later typically consists of several tens of µm of gold on thin and transparent substrates.

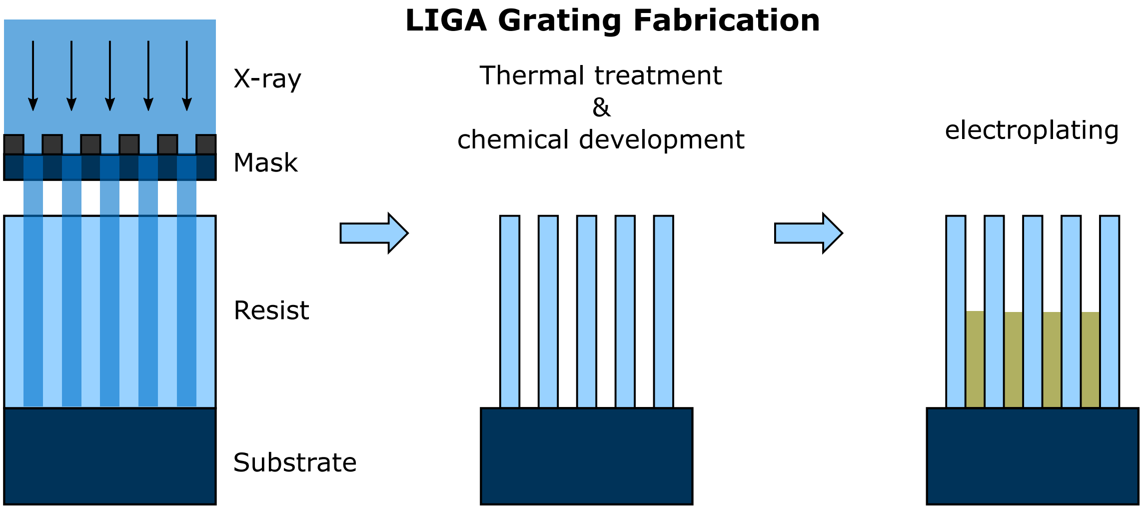

Figure 3.2: Schematic of the LIGA process consisting of an X-ray exposure of a thick resist layer, its development, and electroplating of the resulting high aspect ratio trenches.

Such special masks are usually fabricated with processes such as deep UV lithography, direct-laser writing (DLW), or electron beam lithography (EBL) when a high resolution is required. For high aspect ratios, intermediate masks are required to create "working masks" with about 30 µm thick, absorbing gold patterns. Hence, the LIGA process involves more complexity than conventional lithography techniques used in microfabrication. After the radiation exposure and subsequent thermal treatment, the exposed matrix is chemically cross-linked (in case of a negative resist like SU8). In the last development step, the unexposed resist is dissolved chemically and the grating template with electrically conductive bottoms in the trenches is formed. After that, the trenches are filled with absorbing or phase-shifting material via electroplating. This process typically takes several days for high absorption gratings and has to be carefully monitored to prevent an inhomogeneous filling or an 'overplating' which deteriorates the grating quality. After plating the residual resist can be removed by plasma etching to avoid strain and unwanted deformation when e.g. bending the grating. However, complete removal of the resist is usually not achieved which leads to residual tension and a slightly 'bent' grating substrate. For X-ray absorption and phase gratings, the last step ("Abformung") is not performed, as the electroplated substrate itself is used for imaging purposes and not as a stamp for imprinting or casting.

The LIGA process has several steps that are prone to error making the fabrication process difficult to scale in terms of cost and time. Firstly, the fabrication of a customary mask requires some intermediate steps and special know-how unlike conventional UV-masks, which are commercially available and can be delivered at short notice. Secondly, the deep X-ray lithography step, which is developed for thick resist layers must be performed with a high-intensity radiation source with suitable energy, bandwidth, and coherence. The mean energy of the radiation has to be around 10 keV to provide a sufficient dose deposition in a resist thickness of about 200-300 µm. Energies significantly below that lead to an overexposure on the top and not enough dose at the bottom of the resist. High energy photons cause a resolution loss since they generate free electrons with long ranges, which lead to diffuse radiation dose deposition. Furthermore, some source coherence requirements have to be met for a sharply delineated volume of dose deposition defined by the shadow mask. Hence, the source size, its spectrum, the exposure distance, and time as well as the properties of the shadow mask and the resist have to be tuned to each other. DXRL is typically performed at dedicated synchrotron beam lines and is therefore tied to time frames of synchrotron operation.

In previous works, the potential to translate DXRL to laboratory setups with conventional X-ray sources was evaluated [Gustschin, 2016; Pinzek, 2018]. For that, some suitable anode materials with different acceleration voltages were reviewed by simulating their spectra and calculating the dose deposition in different layers of the resist [Gustschin, 2016]. It was concluded that DXRL is possible with X-ray sauces with e.g. copper or tungsten anodes at up to 40 kV acceleration voltages in reasonable time frames. In the subsequent work [Pinzek, 2018], dose deposition maps were calculated considering the dose gradient due to attenuation in the resist layers as well as the energy and source size-related ‘dose deposition blur’. For high aspect ratios the effect of the mask shadowing with the cone beam has been estimated [Pinzek, 2018]. The fabrication of gratings by DXRL with a conventional X-ray tube has also been experimentally demonstrated for the first time [Pinzek, 2021a]. However, scaling to large areas, high aspect ratios and periods below 10 µm remain a challenge with laboratory source-based DXRL.

A third complication in LIGA processing is the expensive and time-consuming process of electroplating. Typical errors can be an inhomogeneous height of the gold filling and even result in ‘overplating’, where the grating area is partially covered with gold. In case of a deficient development process where some of the resist remains on the bottom of the trenches, the electroplating does not start resulting in ‘missing’ grating lines, defects, or partially uncovered grating area. With increasing grating sizes, the probability of degraded grating quality grows and requires much more effort in process control. Hence, most of the imaging systems with a large field of view (FOV) demonstrated so far have tiled gratings that are precisely aligned to each other and bent to the cone beam geometry [Schröter, 2017]. Finally, the material cost of the absorbing gold structures should not be

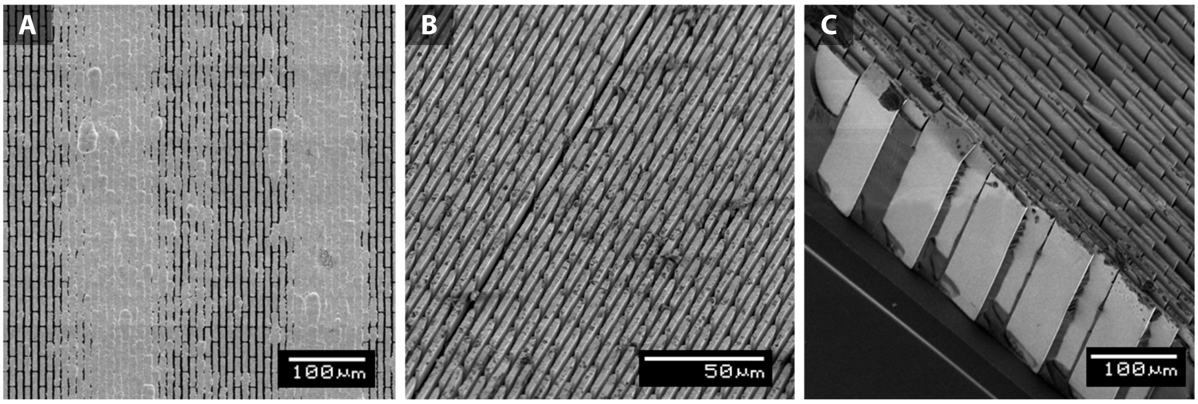

Figure 3.3: SEM images of typical grating defects fabricated by the LIGA method. (A) Overplating with Au on the grating surface. (B) Crack in the grating structure causing discontinuity of the periodic line array. (C) The inhomogeneous height of the absorbing Au lamellae is probably caused by non-simultaneous start of electroplating.

underestimated. For gratings that could cover a FOV required for the human thorax, the mere material cost would make up a high fraction of the acquisition cost.

3.1.3 Silicon-based Processes

Several different fabrication routes rely on a grating template achieved by anisotropic etching into silicon wafers. Creating high aspect ratio structures in silicon is a common process in manufacturing microelectromechanical systems (MEMS) and is, therefore, wider available, faster, and cheaper than DXRL. Several anisotropic etching techniques have been used for the fabrication of X-ray absorbing gratings. At first, the substrate has to be patterned with a masking layer which defines the area to be protected from etching (see. Figure 3.4). For that the wafer is typically coated with a photoresist, thermally treated, and exposed to UV light through a photomask. Afterward, the wafer is chemically developed, i.e. the unexposed resist is chemically dissolved (in case of a negative resist) and the area to be etched is open. If a high aspect ratio is required the etch selectivity between silicon and the organic resist might become insufficient, which limits the maximal etch depth. In that case, some "hard mask" consisting of thin layers of e.g. chromium (Cr), silicon nitride (Si_3N_4), or silicon oxide (SiO_2) can be used to increase the selectivity. The three most important anisotropic etching techniques used for grating fabrication are discussed in the following: *Deep Reactive Ion Etching* (DRIE), anisotropic wet etching with potassium hydroxide (KOH), and *Metal-Assisted Chemical Etching* (MACE). There are also less common methods such as photo-assisted chemical etching [Lei, 2014] or cryogenic reactive ion etching [Wu, 2010] that should be mentioned here without a detailed discussion.

Deep Reactive Ion Etching (DRIE)

The most common process to create high aspect ratio structures is often called Deep Reactive Ion Etching (DRIE), pioneered by Laemer and Schilp and patented by Robert Bosch GmbH in 1994, therefore also often called the “Bosch process” [Wu, 2010]. It consists of alternating etching and passivation steps to achieve an overall anisotropic process and is therefore also called time-multiplexed alternating process. To remove unmasked silicon an etching gas such as sulfur hexafluoride (SF_6) is introduced in a plasma reactor where electrically-charged ions are generated and accelerated toward the substrate. The created fluorine radicals dissociate the silicon creating SiF_4 as a volatile byproduct that is removed with the exhaust gases. In the following step, a passivation gas such octofluorocyclobutane (C_4F_8) is introduced, which creates a thin passivation layer protecting the sidewalls in the subsequent etch step. As the ion bombardment is directional the removal of the passivation layer on the bottom of the trenches is rapid and allows an anisotropic etch process. This alternation results in a characteristic scalloped shape of the sidewalls and can become problematic for subsequent metallization steps. Decreasing the duration of the individual processes and tuning other parameters reduces this effect [Wu, 2010]. State-of-the-art DRIE systems can alternate the processes in fractions of seconds with high-speed gas switching reactors and reach etch rates of several tens of µm per minute.

The limitations of DRIE are aspect ratio-dependent etch rates and consequently a more difficult profile control. With higher etch depths the exchange of reactants and byproducts at the trench bottom is impeded and the etch rate drops. To create high aspect ratio structures as needed for most gratings a dynamical adaptation of the process parameters with increasing etch depth becomes necessary [Wu, 2010]. Furthermore, loading effects, i.e. differences in etch rate and profile due to the density differences of exposed silicon area to etching, are problematic. Although gratings usually have a very homogeneous loading due to their constant periodicity and duty cycle, the etch results at the edges can deviate strongly from the desired structure. Etch uniformity over the wafer also plays an important role as the process has to produce an identical structure on the whole active area of the grating. Despite those difficulties, DRIE seems to be the most promising method to create high aspect ratio grating templates in silicon. Due to its widespread use in MEMS manufacturing the method is continuously developed and is now available on up to 300 mm silicon wafers. The aspect ratios that can be reached with DRIE highly depend on the requirements of the etch profile and the uniformity over a certain area

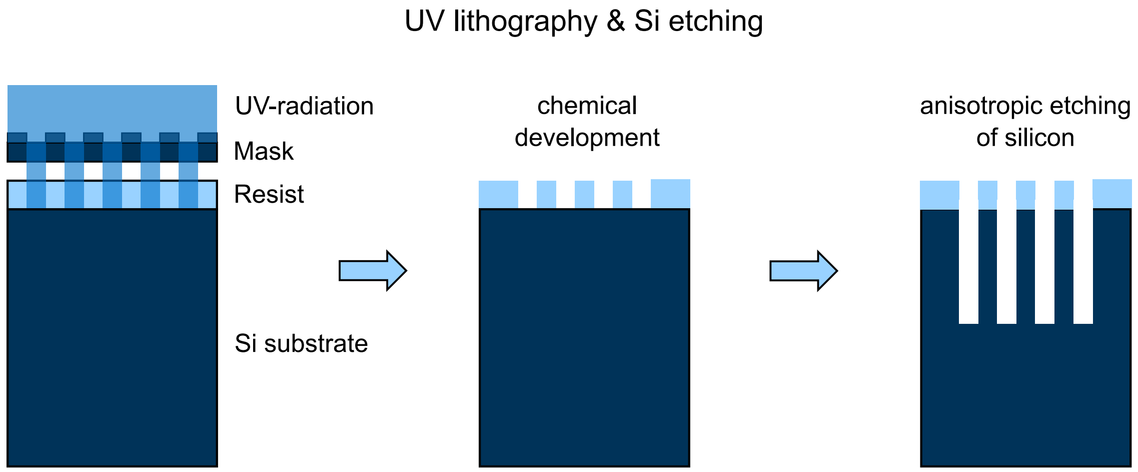

Figure 3.4: Silicon-based fabrication of the grating template by UV-lithography, resist development and high aspect ratio anisotropic etching.

on the wafer. Several works have demonstrated aspect ratios beyond 1:30 [Josell, 2020; Jefimovs, 2021].

Anisotropic KOH Wet Etch

There are several alternative techniques for high aspect ratio silicon etch to DRIE which have been employed to fabricate gratings for X-ray imaging. One of them is an intrinsically anisotropic wet etch process used in the first early reports [David, 2007] of grating fabrication. It uses the strong etch rate selectivity of e.g. potassium hydroxide (KOH) for certain crystal orientations in silicon. Dependent on the process parameters the etch rate in (100) crystal direction can be several hundred times higher than in (111) direction [Wu, 2010]. To use this principle for the fabrication of binary grating profiles, (110) silicon wafers are employed and the grating structure is patterned in an orientation so that the direction with the highest etch rate is perpendicular to the substrate and the direction of the lowest etch rate is perpendicular to the grating walls. Usually, the substrate is covered with a thin layer of Si_3N_4, patterned by UV lithography and the pattern is transferred in the hard mask by an additional RIE step. Then the substrate is immersed in a KOH solution and etched for several hours. The etch rate and anisotropy depend mainly on the temperature and the concentration of the KOH solution [Seidel, 1990]. Several additives have been also reported to have an influence and allow fine-tuning of the process [Rao, 2017]. While very high etch anisotropies have been reported in some studies, the fabrication of grating templates for X-ray applications faced several problems that prevented the technique to be widely applied. Firstly, high-quality silicon wafers with (110) orientation are required. They usually need a custom fabrication for larger wafer sizes and are therefore more expensive and difficult to obtain. Secondly, the process requires a precise mask alignment to the crystal orientations ($< 0.1^\circ$), and in most cases aligning relative to the wafer flat is not of sufficient precision. Deviations from a precise alignment lead to lower anisotropy and result in a strong duty cycle deviation. Further typical problems in KOH etching are inhomogeneities in etch depth and other structural defects probably attributed to insufficient crystal quality or the formation of H_2 bubbles complicating the exchange of reactants. Some of those aspects will be discussed in this work featuring 3D tomographic data of respective silicon grating templates.

Metal-assisted Chemical Etching (MACE)

One other anisotropic etching technique applied for grating fabrication is metal-assisted chemical etching (MACE) [Romano, 2020a]. Since the discovery of the method in 2000, its potential has been explored for various applications such as nanowires, optoelectronic devices, solar cells, sensors, and X-ray optics [Romano, 2020a]. The etch anisotropy results from a local dissolution of the substrate under a catalytic metal layer in an etching solution containing hydrofluoric acid (HF) and hydrogen peroxide (H_2O_2). The solution-metal-silicon system is assumed to act like a microscopic electrochemical cell where H_2O_2 provides free positive carriers being transferred into the silicon matrix, which is then oxidized by HF forming silicon fluoride (${SiF_6}^{2-}$). The grating fabrication process is shown in Figure 3.5. In the first step, the pattern is generated in a photoresist on a (100) silicon substrate using e.g. UV lithography. Then a thin layer (few tens of nm) of the catalyst metal (e.g. Au, Pt) is deposited on top and a lift-off step removes the organic resist leaving only the metallic pattern that will facilitate the etching. An additional annealing step introduces porosity into the catalytic metal layer which is necessary for the exchange of the reaction products when etching micrometer-sized patterns. The metallic pattern sinks into the silicon substrate as the reaction proceeds. As long as the etchant is present and the byproducts can diffuse out of the pattern the process is anisotropic and can create very high aspect ratios. The temperature was found to have a significant influence on the directionality of the etch, as the dissociation of Si in different crystal directions shows a temperature dependence [Romano, 2020a]. For a vertical etch along the (100) direction lower temperatures and etch rates are required. Furthermore, an interconnected catalyst pattern showed an improvement in the directionality and homogeneity of the etch [Romano, 2020a]. Similarly to KOH etching the formation of H_2 bubbles was observed to complicate the etch process. Alcohol additives were found to suppress the bubble formation and have an influence on the etch rate and roughness of the etched surfaces,

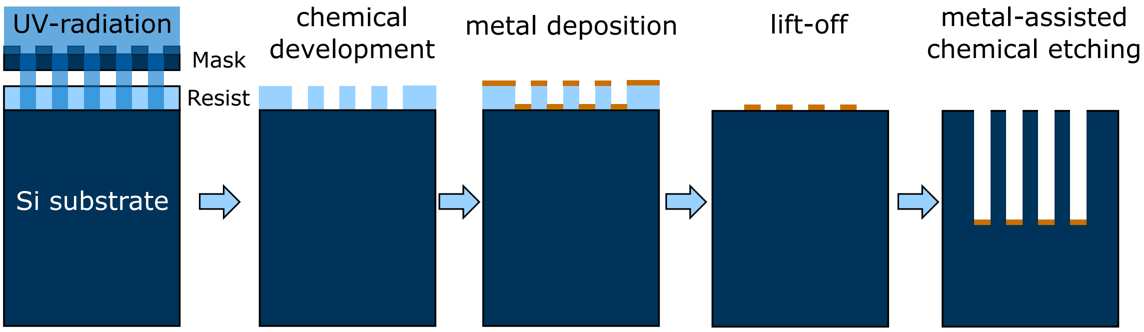

Figure 3.5: Schematic of grating fabrication by metal-assisted chemical etching (MACE) consisting of UV-lithography, chemical resist development, deposition of a thin metal layer, lift-off and anisotropic etching facilitated by the metallic deposits which also serve as a plating base in subsequent electroplating.

probably due to adsorption phenomena [Romano, 2017a]. A fundamental limitation of aspect ratio seems to be the bending and stiction of the silicon bars due to capillary forces in wet processes. To avoid that MACE was also conducted in gas phase showing promising results for X-ray optics applications [Romano, 2020b]. An advantage of MACE in grating fabrication compared to other anisotropic etching techniques is the metallic layer on the bottom of the grating trenches, which can be used as a seed layer for electroplating. As will be discussed in the following section the deposition of such a layer poses a serious problem with other silicon-based techniques at very high aspect ratios. It remains to be seen how reliable and cost-effective the process can be scaled to larger areas and high aspect ratios. Up to now, a decent uniformity could be achieved on 100 mm Si wafers with aspect ratios of 1:30 [Romano, 2016].

3.1.4 Metallization Processes

Electroplating Processes

Filling the deep grating trenches with highly absorbing metals without damaging and deforming the grating template poses a further difficulty. Common processes in semiconductor technology include electroplating with e.g. copper or gold. However, those structures are created layer-by-layer and typically have aspect ratios below 1:10. One exception might be *Through-Silicon Vias* (TSV) which provide an electric connection through the substrate for multilayered integrated circuits. Voidless filling of high aspect ratio structures via electroplating has been achieved in several ways illustrated in Figure 3.6. The most obvious approach is to create a conductive bottom layer in the trenches, which is connected to an electrode and facilitates a bottom-up filling. In this case, the grating surface and the sidewalls have to be isolated preventing a conformal growth. For that, some aluminum is evaporated under 45° from both sides to create sacrificial "cups" on the top of the grating bars (see 3.6 A). After that Au is evaporated perpendicularly to the grating substrate covering both the trench bottoms and the cups on the surface. A subsequent aluminum etch with phosphoric acid will remove the cups leaving the bottom Au layer as a plating base.

An other approach sometimes referred to as double-frequency grating is shown in Figure 3.6 B. A grating template with double periods and a duty cycle of 0.25 is created and evaporated with Au plating base from different angles to cover both the horizontal and vertical surfaces of the structure. Then an Au plating is conducted conformally until a half-period thickness is achieved. The structures plated on the sidewalls serve as the actual absorbing bars. The same principle has been employed with Atomic Layer Deposition (ALD) with iridium [Vila-Comamala, 2018]. The metallic layers on the top and bottom of the trenches are unfavorable and degrade the transmission efficiency. Furthermore, the process has to be controlled precisely as even small deviations (e.g. fractions of a µm) would alter the duty cycle and compromise the periodicity of the grating. Likewise, small deviations from the ideal trench profile degrade the grating quality. Even minuscule slope discrepancies (e.g. 0.2°) on the sidewalls would reduce the transmittance at high aspect ratios.

One further method for a controlled plating process is to use a conductive silicon substrate and passivate the sidewalls and the surface by thermal oxidation or evaporating an insulating material [Kagias, 2019]. This is schematically illustrated in Figure 3.6 C. After the creation of the grating structure a thin isolating layer of SiO_2 is formed by thermal oxidation and additional SiO_2 is applied on the structure via Plasma-Enhanced Chemical Vapor Deposition (PECVD) which mainly covers the top of the grating structure without depositing much on the bottom of the trenches. After that, the SiO_2 can be removed from the bottoms by an anisotropic inductive coupled plasma RIE step. Finally, the back of the wafer is coated with a thin Au layer and a thermal treatment induces a diffusion of the Au into the silicon substrate. This makes it conductive and allows a voidless filling of the trenches from the bottom via electroplating. With this approach, Au gratings with an aspect ratio beyond 1:20 have been demonstrated [Kagias, 2019]. Similarly, using conductive substrates, gratings with a slight bottom tapering (trapezoidal grating profile) were filled with Au by conformal electroplating [Jefimovs, 2021].

Last but not least there are efforts to modify the chemistry and kinetics of the electroplating process to achieve a voidless bottom-up filling of conformally covered plating base.

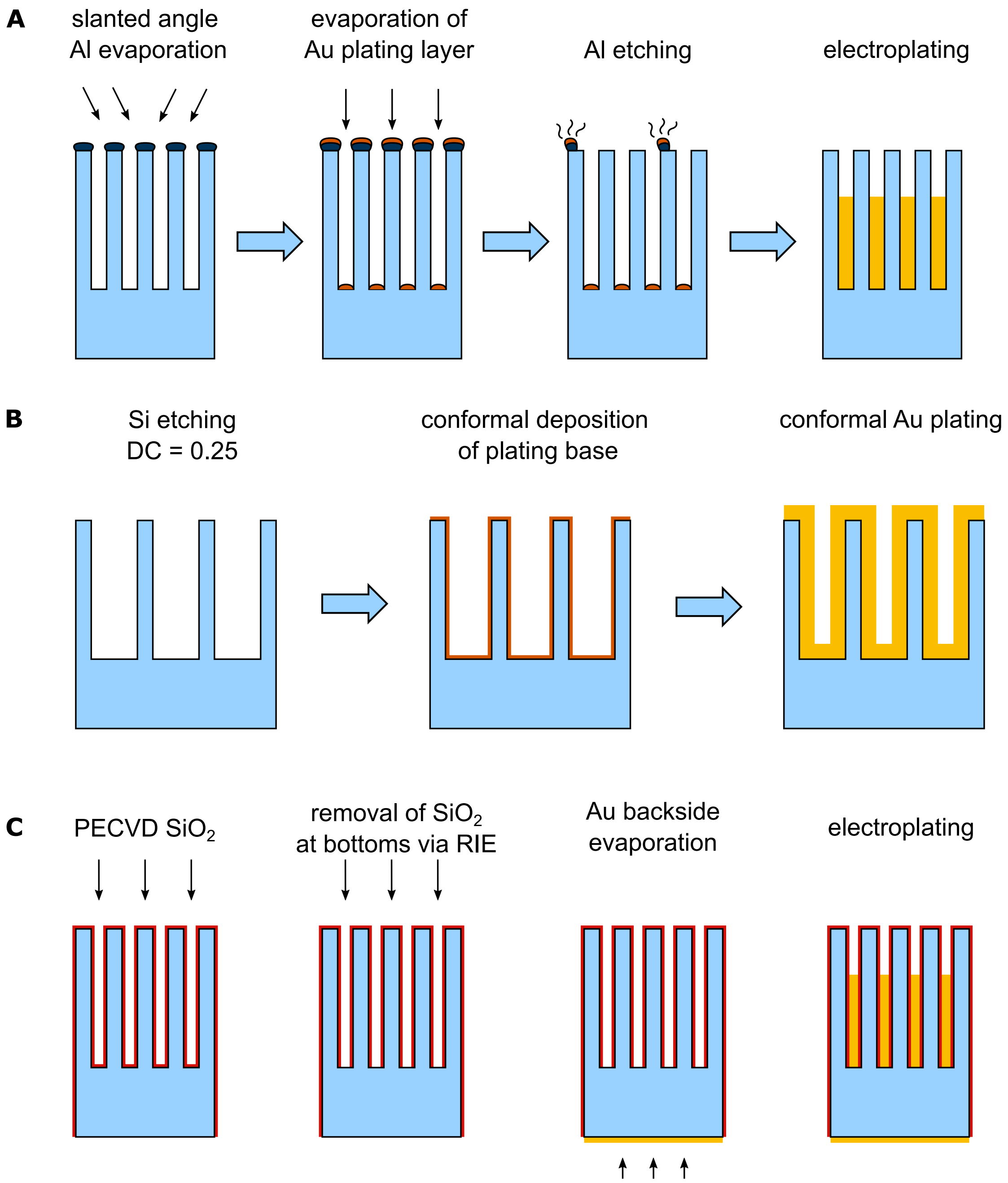

Figure 3.6: (A) Schematic of processes to deposit plating contacts at the bottoms of the grating trenches selectively to enable bottom-up plating. (B) Fabrication of "double-frequency" gratings by applying a plating base and conformal Au plating. (C) Passivation of the substrate by applying an isolating layer and removal thereof on the trench bottoms vie plasma etching. Backside Au evaporation and thermal treatment make the substrate conductive and enable bottom-up plating.

Using pulsed bias has been shown to improve the homogeneity of conformal plating [Song, 2019] as it reduces the ionic depletion in the deep trenches which usually results in a lower plating rate and consequently voids on the bottom of the trenches. Furthermore, it has been shown that a special plating chemistry with Bi additives, a fine-tuned bias, and special flow conditions create a local plating regime where the deposition rate is increased in concave cavities [Ambrozik, 2019; Josell, 2020]. This allows faster plating at the bottom of the trenches without significantly narrowing the trenches from the sidewalls.

Up to now, mostly Au was used as filling material in electroplating for X-ray absorption gratings. Alternative plating chemistries with other heavy metals have not yet been addressed in the context of X-ray absorption grating fabrication in literature. While the plating methods seem to be the most reliable in terms of voidless and homogeneous filling, their main disadvantages remain the cost of the absorbing material (Au) and the duration of the plating process. Hence, alternative absorbing metals and deposition techniques have been proposed as discussed in the following.

Micro-casting

One obvious way is to bring the metal into high aspect ratio structures in a molten form. For that only metals or alloys with a melting point significantly lower than the one of silicon are possible. Among high-density metals lead and bismuth as well as their alloys are shortlisted due to their low melting points. Such a casting procedure was already demonstrated by Lehman and Rönnebeck [Lehmann, 2002] for the fabrication of a 2D anti-scatter grid from a high aspect ratio silicon template. They filled an array of holes with 8 µm diameter, 40 µm period, and 600 µm depth (aspect ratio of 1:75) with lead in a customarily developed casting apparatus which allows evacuation of the chamber and immersion of the silicon template wafer into the liquid lead. The resulting structures are very close to the requirements for absorption gratings as lead heights of 600 µm are more than sufficient for absorbing hard X-rays used in medical imaging. However, translating that to 1D grating lines with a duty cycle close to 0.5 introduces stability issues like tensions due to thermal expansion. A similar casting approach for the fabrication of 1D gratings was reported by Lei et al. [Lei, 2014] where they implemented a micro-casting setup with liquid Bi illustrated in Figure 3.7 A. The furnace is implemented in a vacuum chamber with a pneumatic device enabling to insert and remove the grating mount into the molten bismuth. The vacuum is necessary to make the absorbing material penetrate the trenches by capillary forces and surface tension. After immersion into the liquid bismuth, the wafer is pulled out allowing the excess material on the grating surface to drop down and the substrate to cool down. One subsequent work treated the improvement of the

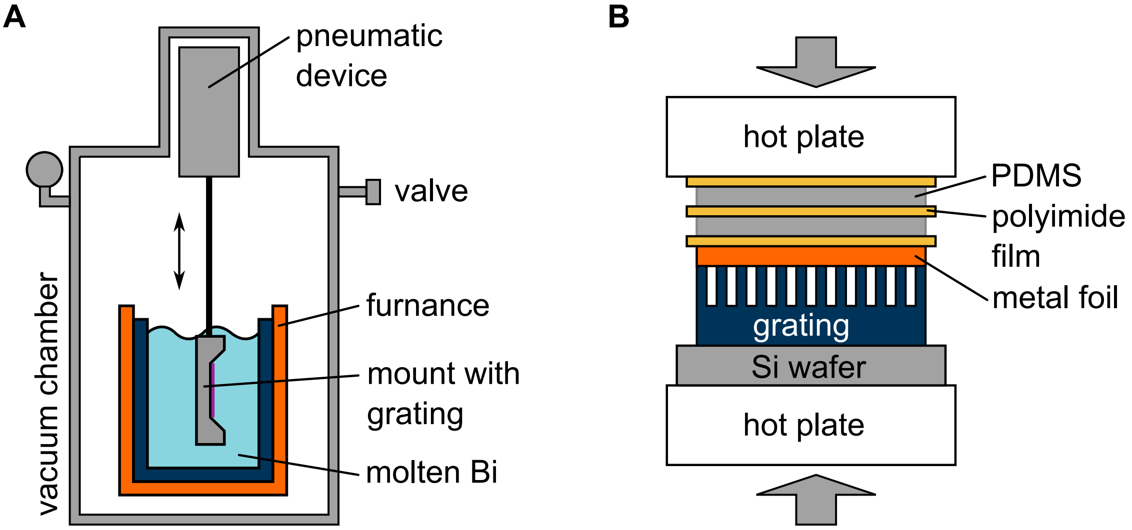

Figure 3.7: (A) Micro-casting setup consisting of a vacuum chamber with a furnace to melt the metal and an insertion device with the grating mount. (B) Hot embossing setup consisting of two hot plate stamps, the grating template, the metal foil, and several films to stabilize the process.

filling by suitable surface modification [Lei, 2016]. With that method depths of about 150 µm were reported, however, it remains unclear how dense and homogeneous the filling was at small periods and what visibilities were finally reached in the imaging system. To be comparable to gratings based on Au for hard X-ray applications a Bi filling above 300 µm is required.

Imprinting and Hot Embossing

Besides immersion of substrates into liquid absorbing material some imprint techniques have been suggested. Yashiro et al. used metallic glass containing palladium (Pd) to imprint into a silicon template under a high temperature [Yashiro, 2014]. The silicon mold was removed by etching leaving only the flat metallic glass substrate with the imprinted grating pattern. A strong disadvantage of this approach is that the “substrate” which is holding the grating lines also consists of the absorbing metallic glass reducing the transmission contrast remarkably. In a subsequent work, Yashiro et al. used Gd-based metallic glass for imprinting leaving it inside the silicon template [Yashiro, 2016]. With this approach, they achieved grating areas of $10 \times 10\,\mathrm{mm}^2$ and a visibility of $\approx$50% with a two grating interferometer at a 15 keV synchrotron source. Similarly, Saghamanesh et al. [Saghamanesh, 2017] used metallic glass containing high fractions of Pt to create absorbing masks with periods of 72 µm and 106 µm containing 43 µm absorbing material. The fabrication of such imprinted gratings with metallic glass appears to be simple, however, until now only small grating areas were reported and aspect ratios did not exceed 1:10.

A similar hot embossing approach was also proposed and demonstrated by Romano et al. [Romano, 2017c; Romano, 2017b] with metallic alloys. Thin foils (several tens of µm) of low melting point alloys are placed onto the silicon grating template, which is conformally coated with a metal to reduce the surface tension. The setup illustrated in Figure 3.7 B is evacuated, heated above the melting point of the alloy, and embossed with a pressure in the range of several MPa [Romano, 2017c]. This process has been reported using the alloys Au-Sn (80 wt.%Au), Pb-In (95 wt.%Pb), and Pb-Sn-Ag (92,5wt.%Pb) which have melting points in the range of 300 °C. Critical parameters in this process are careful temperature and pressure control and the use of precisely selected foil thicknesses, which have to be just enough to fill the grating trenches. While aspect ratios up to 1:40 have been reported with periods of 1-20µm [Romano, 2017b] it remains unclear how homogeneous the filling is on large areas and what deformations appear in the grating structure. Visibilities of about 15% have been reported with 20 keV design energy systems on 7×7 mm^2 detector area with the Au-Sn alloy as an absorber [Romano, 2017c]. The reduced material cost for the Au-Sn embossing process compared to pure Au plating seems not to be the decisive point. Rather, what is interesting is whether the Pb alloys can reach comparable performance with good grating quality and high process yield. In this regard, further studies with quantitative characterization methods of grating quality are needed to evaluate if hot embossing can develop into a robust and competitive process for higher-volume fabrication.

Physical and Chemical Vapor Deposition

Other possibilities for metallization use a deposition of the absorbing material from the gas phase. In *Physical Vapor Deposition* (PVD) the material is evaporated physically in a vacuum chamber and is then allowed to condensate on the surfaces of the substrates. To bring the material into the gas phase different techniques such as thermal heating above its boiling point e.g. using high electrical currents are available. Other methods use electron or laser beams, electric arcs, or ion bombardment (sputtering). The evaporated material can either move ballistically or be guided by electrical fields toward the substrate to be deposited on. To reach the target the reaction chamber has to be evacuated to prevent scattering with the gas molecules and unwanted chemical reactions. PVD allows to create excellent thin film coatings, however, a selective deposition into high aspect ratio structures as needed for grating fabrication is difficult. Due to their directional incidence, the particles do not cover the trench walls but tend to form cups on top of the grating lines. This leads to a closing of the trench openings and prevents an optimal filling as illustrated in Figure 3.8 A.

Despite this process limitation, the evaporation method has been used for the fabrication of neutron absorption gratings [Grünzweig, 2008b; Samoto, 2019]. At first, grating templates have been etched with a relatively large trench opening as shown in Figure 3.8 B. Then the direction of the evaporation process has been adjusted in a way that most of the absorbing gadolinium was deposited under a certain angle onto the sidewall (see Figure 3.8 B). Obviously, the resulting absorption profile is not binary as desired for the applications and the method is geometrically limited in aspect ratio. To deposit deeper trench walls the evaporation angle has to approach 90° relative to the substrate which would lead to strong material deposition in the entire trench eliminating the transparent fraction in the grating profile. Despite these limitations, the method was sufficient for neutron absorption gratings as they require smaller absorption thicknesses of Gd (e.g.10 µm) compared to hard X-ray applications (>200 µm).

Chemical Vapor Deposition (CVD) also delivers the materials to be deposited from the gas phase, however, the coating originates from a chemical reaction on the substrate surface. The reaction chamber is usually filled with so-called precursor gases and the substrate is heated to a certain temperature to facilitate the chemical reaction. In contrast to PVD the process is more conformal and allows depositing material in more complex geometries such as high aspect ratio structures. However, the deposition rates still depend on kinetic factors and tend to drop with local reaction product depletion. That results in smaller deposition rates in the deep trenches, closing the trench openings and leaving voids inside the trenches. Tungsten (W) which is well suitable as absorbing material for X-rays is a common low-resistivity material used to create interconnects between adjacent metal layers in integrated circuits. Hence, several patents issue voidless filling of high aspect ratio structures by tungsten CVD [Chandrashekar, 2012; Wang, 2015; Chandrashekar, 2015]. One possibility is to fill the trenches partially followed by a selective removal of the coating close to the trench opening by e.g. mass-transport limited etching processes. More iterations can yield a decent filling of deep structures as illustrated in Figure 3.8 C. Although structures similar to that required for X-ray absorption gratings have been demonstrated filling through silicon vias by tungsten CVD [Vitale, 2015], it has not yet been reported for the fabrication of X-ray absorption gratings.

One special approach among many CVD methods is Atomic Layer Deposition (ALD). Here, the reactant gases are inserted into the process chamber sequentially as a series of non-overlapping pulses. In each cycle, the precursor molecules react with the surface separately. Furthermore, the process is self-limiting, i.e. the reaction ends once all reactive

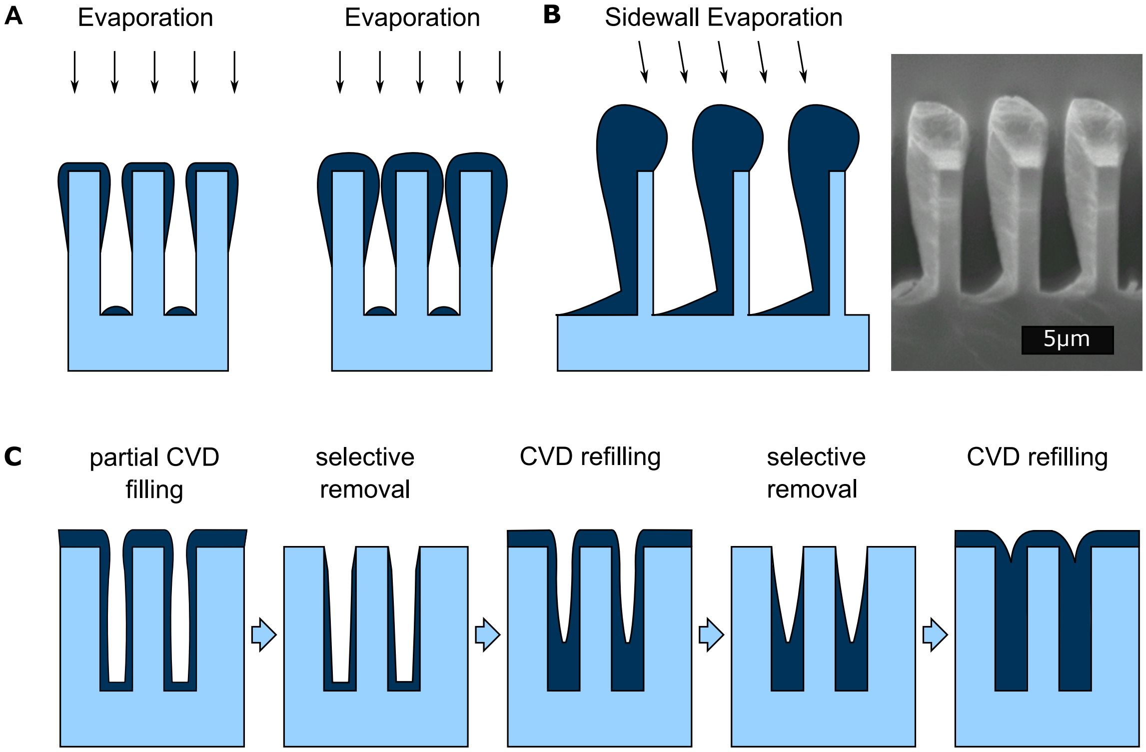

Figure 3.8: (A) Physical Vapour Deposition (PVD) of absorbing materials fills trenches inhomogeneously and closes the trench openings leaving voids in the grating structure. (B) Slanted sidewall evaporation of absorbing material creates a non-binary absorption profile. An SEM image shows a 4 µm period grating profile evaporated with gadolinium as neutron-absorbing material. (C) Voidless filling by a serial Chemical Vapor Deposition (CVD) and selective removal of deposited material in multiple steps.

sites of the surface are depleted. This technique allows covering complex surface structures uniformly with precise thickness control by adapting the number of cycles. ALD is often used to create a conductive layer as a plating base on the silicon grating template. Since the material is deposited in very thin, atomic layers the deposition for X-ray absorption gratings requires extremely long process times hardly making the method suitable for mass production. In one work absorption gratings with a period of 1 µm and an absorbing thickness of 30 µm (iridium) were fabricated by ALD [Vila-Comamala, 2018]. The deposition of 580 nm of absorbing iridium on the sidewalls of the silicon template required more than 11.000 cycles and a total deposition time of ≈ 15 days.

Particle-based Deposition

A further option to fill absorber material into the grating structure besides micro-casting and hot embossing is a deposition of micro-sized particles. The obvious disadvantage is only partial filling since lots of empty space is left between the particles. However, the advantage is that any material that can be obtained in a chemically stable particle shape can be used. For example, tungsten with a filling density of about 50-60% can reach comparable absorption to voidless bismuth or lead fillings due to its high density. One such process was described by Jung et al. [Jung, 2009] where they applied a Gd_2O_2S-powdered mixture in high aspect ratio grids to create structured scintillators for resolution increase in X-ray imaging. In some other works, Gd-containing microparticles were used as attenuating material for neutron absorption gratings. Kim et al. fabricated a source grating for a neutron interferometer with a period of 744 µm and a trench depth of 500 µm [Kim, 2013] and reduced the period to 354 µm in a subsequent work [Kim, 2014]. Seki et al. [Seki, 2017] briefly reported a source grating with 180 µm period filled with a Gd_2O_3 powder paste on an area of $30\times30\,\text{mm}^2$. In this work, a significant improvement of this filling method will be presented reaching periods down to 13.1 µm at 80 µm trench depths providing almost ideal absorption in the sub-2 Å neutron wavelength range [Gustschin, 2018]. The particle-based absorber deposition has only recently been reported for the fabrication of X-ray absorption gratings [Lei, 2019b; Lei, 2019a; Lei, 2021; Hojo, 2019]. Lei et al. used a suspension containing tungsten nanoparticles which they applied onto the surface of a grating substrate [Lei, 2019b]. The period of the filled grating was 42 µm, the duty cycle 0.25, the height 150 µm, and the aspect ratio (trench opening/height) $\approx$ 1:5. The method has been demonstrated on an 8 inch wafer reaching maximum visibilities of 10% at 28 keV mean energy [Lei, 2019a]. The filling ratio has been estimated at 33% based on weighting the grating before and after deposition. Hojo et al. deposited Au microparticles (1.5 µm) from a suspension into a small grating piece ($8\times8\,\text{mm}^2$) using centrifugation [Hojo, 2019]. They implemented a grating holder in a centrifugation tube oriented tangentially to the rotation direction so that the microparticles were pushed into the deep trenches by centrifugal forces. The grating template had a period of 30 µm and a depth of 67 µm. At 40000 rpm the sample was subjected to an acceleration of 162 000 g without breaking the silicon template. A filling density of 66% was estimated close to the theoretical value for random packing for spheres in a jammed state [Song, 2008]. In this work, a centrifugal deposition was developed independently showing the first promising results in two Master thesis projects [Gustschin, 2016; Pinzek, 2018] in 2016 and 2018. Finally, the fabrication of a tungsten particle-based X-ray absorption grating with a period of 45 µm and unprecedented effective tungsten filling thickness, area, and aspect ratio (1:20) was demonstrated with comparable imaging performance to LIGA-based Au gratings [Pinzek, 2022].

It has been found that particle-based filling of grating templates can be scaled in area and reduced in material cost compared to other methods. It circumvents the complications of currently applied approaches either requiring deep X-ray lithography or a complex deposition of plating contacts for silicon-etched gratings. Furthermore, it avoids the long and error-probe electroplating process and the high material cost of Au. To be applicable for e.g. thorax imaging at energies of about 70 kVp the period has to be further decreased to about 10-20 µm for inverse Talbot-Lau setups like reported by Willer et al. [Willer, 2021].

Other Approaches

Some rather exotic methods that are neither based on LIGA nor on filling silicon-based templates with absorbing materials have been suggested. For various reasons, they have not become relevant for medical applications yet and are therefore only briefly mentioned. First of all, there are several ideas to avoid using a source grating with laboratory sources by creating a structured source itself. Momose et al. created a multiline X-ray rotating anode with periodic grooves (300 µm) which appeared as an array with 30 µm period and a duty cycle of 0.33 under low take-off angles where the interferometer was set up [Momose, 2009]. Shimura et al. developed a multiline embedded X-ray target with a period of 15 µm for a transmission tube with Cu and Mo and demonstrated multimodal imaging at 40 kVp [Shimura, 2013]. Du et al. created a ladder-shaped tungsten anode that creates periodic line foci (42 µm) and operated it at 60 kVp and 2 mA tube current [Du, 2011]. Furthermore, they avoided an absorbing G_2 by filling the scintillator CsI into a grating structure and coupling it to a photosensitive detector. This principle circumvents the requirement of an almost complete absorption along the grating lines and instead detects only the radiation impinging on the periodic line array. Several other studies also evaluated gratings using this approach for X-rays [Rutishauser, 2011] and neutrons [Kim, 2018]. Major problems connected to this approach are a void-free filling of CsI with sufficient height (600 µm) and good light-guiding properties to reach comparable efficiencies to current flat panel detectors. Furthermore, the scintillator gratings are sensitive so scattered radiation coming from all different angles while absorption gratings have a strong “anti-scatter grid effect”. Summarizing, both these alternative approaches with a structured anode and scintillator gratings are hardly realizable with current medical systems for e.g. thorax imaging or CT. High-power rotating anode generators are required and even minuscule vibrations or drifts of such a structured rotating anode will cause a temporal displacement or smearing of the interference pattern.

One other method that has been proposed by Wan et al. in 2008 is based on stacking and slicing thin sheets of materials [Wan, 2008]. First thin transmitting and absorbing foils are alternately stacked on each other until a solid block is formed, which is thermally treated and sandwiched with high pressure between solid copper plates. After that, the block is sliced into thin pieces, which are glued on a substrate like a carbon plate and polished. They used 10 µm thick aluminum foils as the transparent spacer material and 20 µm thick tantalum (Ta) foils as the absorbing material aiming for a grating with 30 µm period and a duty cycle of 0.33. They realized a small grating piece with 600 µm absorbing thickness resulting in an aspect ratio of 1:60 that could be used as a source grating demonstrating a FOV of about 13×13 mm^2 with 35% visibility at 30 kVp. Recently, this idea was taken up by Wu et al. who used 40 µm thick silver (Ag) foils as absorbers and 40 µm aluminum (Al) foils as transparent spacers for the same principle [Wu, 2021]. They reached 2.2 cm total height of the composite grating stack with a period of 80 µm and could demonstrate a single absorption grating system with a high-resolution detector. The principle of this stacking and slicing technique appears simple and the benefits of using even weaker absorbing materials and compensating that with a higher slice thickness seem enticing. However, it is unforeseeable how precise the period and its spatial fidelity can be controlled on larger grating areas. This is particularly important, as period infidelities within a pixel would decrease the visibility, especially when large source spots are used. Furthermore, the absorber inclination plays a crucial role at high aspect ratios. Even minuscule inclinations of the lamellae – which can be caused by the slicing process – create strong shadowing effects and deteriorate the imaging performance. Up to now, no study has yet systematically quantified those effects in gratings created by this stacking-slicing approach to evaluate its potential for hard X-ray imaging. It remains to be seen how far the period can be decreased and the grating area increased while maintaining acceptable grating quality.

3.2 Grating Characterization Methods

As discussed in the previous section several different grating fabrication techniques with distinct advantages and drawbacks have been developed. They involve complex, expensive, and error-prone procedures, that make the development process difficult. Consequently, precise tools that characterize the grating quality, help to find and eliminate errors, and provide data to optimize process parameters are needed. In this section, such characterization methods are introduced and their capabilities are evaluated. Additionally to currently applied methods a new technique based on Angular X-ray Transmission measurements (AXT) that was developed as a part of the present work is introduced.

3.2.1 Light and Electron Microscopy-based Techniques

The most available and intuitive tool to visualize the grating surface is conventional light microscopy. It allows to monitor the structure between process steps and is particularly helpful for finding larger defects after lithography. In most cases, it is precise enough to measure the period and the duty cycle of the grating when the surface is not covered by the electroplated Au. However, light microscopy is limited to the surface and is not able to reveal in-depth deficiencies of the grating structures such as voids in the absorber filling, uneven depths of the trenches or inclined absorbing lamellae due to cracks in the resist structure. Confocal light microscopes are able to measure the 3-dimensional morphology of the surface and e.g. detect relative height differences of the lamellae on the grating surface.

To gain in-depth information the grating samples are often cleaved to visualize the grating profile. Here, Scanning Electron Microscopy (SEM) is very useful providing excellent resolution and contrast between the metallic filling and the template. In most cases, SEM devices also provide more flexible mounts to rotate and tilt the sample and to adapt the depth of field which allows getting a better 3-dimensional perception of the sample. Additional insights can be acquired by built-in X-ray fluorescent analysis devices that measure the fluorescent radiation created by the absorbed electrons and allow visualizing elemental distributions in the structure.

Microscopy-based techniques using light or electrons have two major disadvantages related to the characterization of gratings. Firstly, they only probe a small fraction of the grating surface. An area-wide scan can be implemented with significantly more effort, however, it would take too long and result in data-heavy processing involving automated image analysis tools. Secondly, the inner grating structure can be only visualized along cleaved edges of the sample making it a destructive technique. Again, analyzing such a grating profile on the cleaved edge provides only a small fraction of the in-depth information. A targeted defect search in the inner structure is hardly possible.

3.2.2 X-ray Microscopy (XRM)

X-rays penetrate the sample and can therefore provide valuable information from the inner grating structure. Current laboratory-based full-field X-ray microscopes (XRM) have a sufficient resolution to visualize individual grating lines and common defects like duty cycle variations, distorted grating lines, and voids in the absorber filling. Figure 3.9 (A) shows a high-resolution micrograph of a silicon grating template piece showing variations in the transmission signal. It reveals differences in the trench depth which are hardly detectable with surface-sensitive techniques described before.

Locally reduced transmission can also reveal voids in the filling and diffuse edges of the absorbing lamellae indicating inclinations or duty cycle variations. Even empty silicon templates before absorber filling can be investigated with low energy X-rays without destroying the structure. Despite being sensitive to the inner structure and being able to detect defects the full 3D information is not accessible through a single projection. Furthermore, XRM has similar limitations to light and electron microscopy and is not well suitable for large-area characterization.

3.2.3 X-ray Tomosynthesis and µCT

X-ray tomosynthesis and micro-computed tomography (µCT) use projectional images taken from different angles to access 3D data of the sample. For a full reconstruction, the specimen should ideally fit into the field of view (FOV) and be scanned over at least 180°. Figure 3.9 B shows a cross-sectional layer obtained from a µCT scan of a small silicon grating template piece shown in a projection in Figure 3.9 A. Such scans allow an excellent analysis of small pieces for e.g. defect characterization or process optimization. For gratings filled with absorber material, however, further difficulties arise. Firstly, the grating bars are absorbing strongly and cause beam starvation artifacts. Secondly, a grating µCT scan performed with a relatively large grating substrate does not allow a sufficient rotation being close to the source. Additional, strongly absorbing structures move into the FOV, which causes further artifacts in reconstruction. Hence, limited angle scans (e.g. ± 20°) also referred to as X-ray tomosynthesis can be useful. Such a limited-angle reconstruction is shown in Figure 3.9 C compared to a full-angle reconstruction in

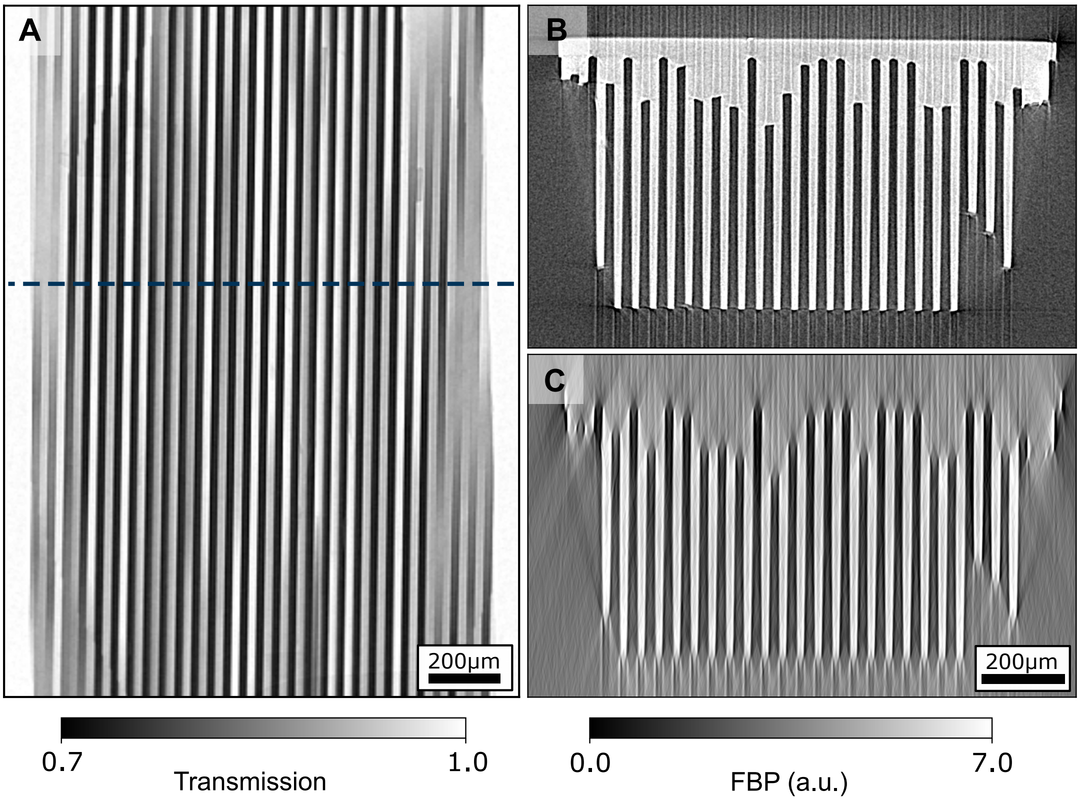

Figure 3.9: (A) X-ray radiograph of a silicon grating piece without absorbing material. The transmission signal shows local deviations indicating differences in the trench depth. (B) Cross section of the grating piece along the blue dashed line in (A) acquired by µCT (360°, 1801 projections). (C) Reconstructed tomosynthesis of the same cross section from 200 projections in the range of ± 20° enabling to resolve differences in the trench depth. Such limited-angle scans can be used to scan ROIs of larger substrates without the need for an entire sample rotation.

B. As this example shows such scans can provide helpful information on layers in the grating structure and can detect e.g. height variations in the grating trenches. Such a characterization can usually be applied on large area gratings without the need to destroy them. Still, the FOV of this method is very small rendering the technique only suitable for detailed defect inspection.

3.2.4 Interferometric Characterization

One possible full-area absorption grating characterization can be performed by visibility tests in a grating interferometer. In this approach, the grating is usually tested in the system it is designed for. Most defects of the grating usually lead to a visibility decrease.

One exception is a local increase of the duty cycle, which can arise from e.g. fabrication-related issues, poor grating alignment, or shadowing effects. The main difficulty is that the visibility depends on many parameters such as the used spectrum and source size, filter, interferometer geometry, precision of alignment and bending, quality variation of the other gratings that are used, and the spectral response of the detector. In most cases, it requires a complete three-grating setup with all required metrology, a good knowledge of hardware, and tremendous alignment effort. Furthermore, poor visibility results do not provide direct feedback on what grating parameter of which grating is responsible for the visibility decrease. In most cases, this method is used to compare gratings with each other by exchanging one grating while keeping all other hardware components unchanged. Hence, an interferometric characterization is laborious and offers a low degree of quantitative quality assessment. Therefore, such measurements should rather be understood as a characterization of the entire system.

3.2.5 Angular X-ray Transmission (AXT) Analysis

As discussed in the preceding sections high-resolution methods provide detailed information on the grating structure, however, are inefficient in large-area characterization. On the other hand, interferometric methods are suitable for large-area characterization, but are difficult to perform and provide inconclusive results, as they characterize the entire interferometric system. To close this gap, a new, non-destructive, and efficient method was developed to characterize large-area absorption gratings without the need to resolve individual grating lines [Schüttler, 2016; Gustschin, 2019]. It allows using X-ray tubes with larger focal spots and conventional flat-panel detectors for an extended FOV. The main idea is to employ a distinct angular transmission intensity function that arises at different angles and creates characteristic minima and maxima that are indicative of certain grating parameters.

Grating Transmittance

Figure 3.10 A shows the measurement geometry of an AXT scan. A grating that is projected to the detector by the cone beam of the X-ray tube is rotated in a certain angular range. Such measurements can be easily performed in X-ray computed tomography systems with rotating samples as often employed for non-destructive testing. Every pixel records a characteristic angular transmission curve as shown in Figure 3.10 B. Distinct features such as the central peak and the both first-order minima have their origin in different effective thickness profiles that are transmitted by the impinging X-rays under certain selected angles. The angular transmittance T_α is defined as the intensity I_α transmitting the grating in a certain angle normalized by the incoming intensity I_0. For its calculation, the transmitted thickness profiles for the X-rays impinging under an angle α onto the absorbing grating bars as shown in Figure 3.10 C-E have to be determined. The projected profile depends on the angle α , the period p, the duty cycle DC (fraction of absorbing area), and the lamellae height h and should be denoted as $H(\alpha, x, p, DC, h)$. The energy-dependent transmittance by this projected height profile is given by integration of one period p and the application of the Lambert-Beer law:

$$T_\alpha(E, \alpha, p, DC, h) = \frac{I_\alpha(E, \alpha, p, DC, h)}{I_0} = \int_0^p \exp(-\mu(E)H(\alpha, x, p, DC, h))\, dx \qquad (3.1)$$

for the energy E with the linear attenuation coefficient $\mu(E)$ of the absorbing material. When using a polychromatic source with an energy-normalized spectrum $S(E)$ and an energy-integrating detector with quantum efficiency $D(E)$, the transmittance is given by:

$$T_{\alpha,poly}(E, \alpha, p, DC, h) = \int_0^{E_{max}} T_\alpha(E, \alpha, p, DC, h) E S(E) D(E)\, dE. \qquad (3.2)$$

The attenuation by the grating substrate can be taken into account as a filtration of the spectrum $S(E)$. Here, secondary effects such as scattering by the absorbing material are neglected as they have much lower interaction cross sections compared to absorption. Given that the angular transmission T_α can be measured for every grating position we will discuss which grating parameters can be extracted thereof. The transmission under perpendicular incidence (Fig. 3.10 C) depends on the grating duty cycle, the height of the absorbing structure as well as the thickness and material of the substrate. Such a transmittance image is therefore sensitive to various irregularities in the grating structure and can reveal defects. The acquisition of such a transmittance image with a cone beam (as most of the X-ray imaging systems provide) is somewhat complicated. As seen in Figure 3.10 A a transmission signal under perpendicular incidence in pixel P_{ij} has to be collected under a grating rotation angle of $\alpha_{||}$, which is the same angle under which pixel P_{ij} appears relative to the central beam. One further difficulty is that during grating rotation a certain grating position is projected on different detector pixels as seen in the lower part of Figure 3.10 A. Hence, a simple pixel-wise retrieval of grating parameters would result in a geometrical distortion of the 2D transmittance image. For that a projective transformation on every angular radiograph was implemented that considers the measurement geometry. After this transformation, the angular data appears in a shape as if it would be collected with a parallel X-ray beam. Extracting the transmission signal in every pixel P_{ij} under perpendicular incidence allows calculating a cone beam-corrected transmittance image without field curvature [Gustschin, 2019].

Grating Duty Cycle

The transmission image already provides a lot of information about the grating quality. Potential duty cycle and height variations, inclinations of the lamellae, or overplated absorber material on the grating surface will be revealed. However, since all those grating parameters are intertwined in the transmission signal it will only highlight the abnormalities without providing a clear picture of what particular defect is present. In particular, it is difficult to retrieve absolute values for the duty cycle from the measured AXT curve as in most cases the source spectrum $S(E)$ and detector efficiency $D(E)$ are not known to sufficient precision. Hence, fitting a theoretically calculated T_α by Equation 3.2 with many unknown parameters to measured data is complicated, unstable, and computationally expensive. For every iteration, the algorithm would require performing a polychromatic attenuation calculation during pixel-wise cost function minimization. Alternatively, the duty cycle can be determined by performing the AXT scan at a low tube voltage at which the residual transmission through the grating bars can be neglected. At e.g. 40 kV tube voltage the spectrum created by a tungsten target is absorbed by more than 99% after passing through 150µm Au. However, the absorbing influence of the substrate which becomes significant with soft spectra has to be also considered by e.g. taking flat-fields with a filtration of an equivalent substrate. As a result, the transmittance values will be close to $1 - DC$ visualizing the spatial duty cycle distribution [Gustschin, 2019].

Grating Height

As previously noticed the AXT signal originates from the transmittance of the effective absorber profile H as shown in Figure 3.10 C-E for three cases. A minimum of the signal appears when H becomes constant at angles of

$$\alpha_n = \arctan(np/h), \tag{3.3}$$

where h is the original grating height, p the period, and n the order of the minimum. This is illustrated for the first-order minimum in Figures 3.10 E and G where the y-axis is scaled tighter to visualize the minima and maxima respectively. It is of particular importance that the position of the minimum is not affected by the duty cycle, X-ray spectrum, grating substrate, or detector type [Gustschin, 2019]. This allows retrieving

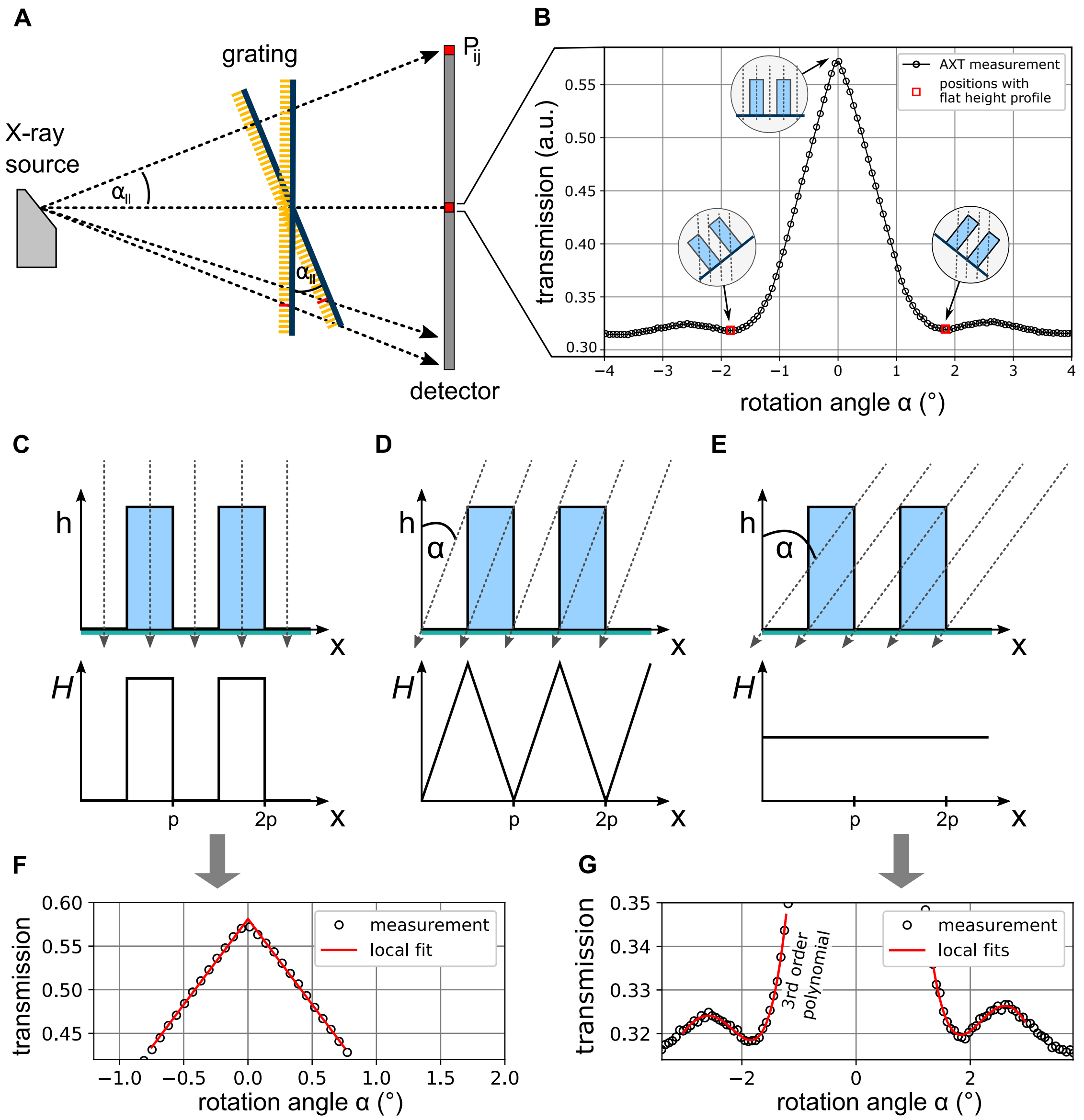

Figure 3.10: (A) Geometry of the Angular X-ray Transmission (AXT) measurement. (B) Exemplary angular transmission curve showing the characteristic central peak associated with maximal transmission at perpendicular X-ray incidence (C) and minima at the angle $\alpha = \arctan(p/h)$ associated with effective flat transmission profile as shown in (E). In (C-E) the effective profiles (H) transmitted by the X-rays under different incidence angles is shown. Figure adapted from [Gustschin, 2019].

the period-to-height ratio in every pixel of the cone beam-corrected AXT data. Since the period of the grating is usually known with high precision the height of the grating can be calculated and visualized for every pixel. The minima can be determined by iteratively fitting Equation 3.2 to the measured AXT signal when the properties of the system such as X-ray spectrum or detector efficiency are known. However, it is much easier to extract the minima by locally fitting 3rd- or 4th-order polynomials to the data as shown in Figure 3.10 G. Using this simplified model the fitting is performed with fewer parameters and without heavy numerical polychromatic attention calculations and yields good results [Gustschin, 2019]. The spatially resolved height map is directly calculated pixel-by-pixel using Equation 3.3.

Local Absorber Inclination

Characterizing high aspect ratio gratings the inclination of the absorbing lamellae from their perpendicular orientation is of interest, as in several fabrication techniques the grating template undergoes thermal and mechanical forces that can deform the microstructure. Besides that, when bending of the gratings is performed, it is of particular interest to spatially quantify how well the grating structure follows the geometrical curvature imposed by the grating holders. For this task, quantitative information can also be retrieved from the AXT data. As illustrated in Figure 3.10 A the maximal transmission signal in a pixel P_{ij} is obtained at the angle $\alpha_{||}$ where the beamlet pointing to P_{ij} is parallel to the grating lamellae. This angle is determined from the AXT curve by fitting a triangular function into the peak as shown in Figure 3.10 F. Subsequently, the cone beam-related angle α_c of the beamlet impinging on the pixel P_{ij} can be calculated directly from the measurement geometry, which is usually provided with high precision in X-ray CT devices. The local deviation to the ideal inclination of the absorber lines can then be calculated by $\Delta\alpha = \alpha_c - \alpha_{||}$ for every pixel. As shown by several examples in the original work [Gustschin, 2019] this signal can visualize and quantity minuscule deviations in the absorber lines and is also able to detect artifacts that are hardly visible in a surface inspection by microscopy.

Limitations

Despite being a practical and efficient method AXT analysis has some limitations originating from the measurement principles. To create the characteristic minima according to Equation 3.2 the grating has to have a high aspect ratio (>1:10) and the absorbing material has to be sufficiently strong compared to e.g. the substrate or the resist in case of LIGA gratings. The grating has to be approximately uniform on the area of the effective pixel size since the model relies on certain geometrical assumptions about the lamellar structure. In case of irregularities of the latter like differently inclines absorber lines or height variations on the sub-pixel range the characteristic information will not be resolved, but averaged. Still, it will be detected as an abnormality in the transmission signal. The AXT method will also have difficulties with double-frequency gratings produced by e.g. conformal electroplating, where the absorbing material is deposited at the sidewalls. In those cases, it is extremely difficult to achieve a precise periodicity as it requires a high control of the grating profile as well as the thickness plated over the entire trench. The additional absorbing material at the top and on the bottoms of the trenches would also compromise a clear signal formation originating from geometric assumptions of a binary profile. Apart from these limitations AXT was found to be a versatile method as it provides the transmission, duty cycle, height, and absorber inclination in perfectly aligned spatial maps without destroying the grating. Typical measurement times are in the range of 10-60 minutes and algorithmic retrieval is performed in negligible time frames. The method can serve both as quality control and parameter feedback and is extremely useful for process optimization. One further grating property that cannot be accessed with AXT measurements is period fidelity. Irregularities in the period can be local, i.e. the deviation of the period for individual grating lines. In most cases, they are also connected to local lamellae inclinations as they do not stem from the lithographic patterning but arise during and after electroplating. In such cases, they can be detected as abnormalities in the transmission and inclination signal. Small deviations in the period ranging over the entire grating surface, however, cannot be detected by AXT. In most cases, such deficiencies are not problematic for imaging as they only determine the phase of the recorded intensity modulation which is processed in every pixel with the respective flat field.

3.3 Summary and Outlook

Since the first reports of grating fabrication for interferometric X-ray imaging [Matsumoto, 2007; David, 2007; Noda, 2008] about 15 years ago the technology has progressed significantly, however, has not yet achieved a breakthrough in terms of production cost and quality to secure wide commercialization of grating-based imaging in medical or industrial applications. While sufficient period and aspect ratio of the absorbing material can be reached well, the most difficult part remains to achieve a constant duty cycle and lamellae inclination over a large grating area. Extended FOVs have been reached by stitching and tiling of several gratings [Schröter, 2017], sample scanning [Kottler, 2007] or the combination of both [Gromann, 2017] exploiting a relative movement of sample and interferometer. A 2D tiling of gratings such as in [Schröter, 2017] requires to prealign the gratings before e.g. gluing them on a flexible substrate, which can be bent to adapt for the cone beam. Such a procedure has been demonstrated for a $20 \times 20\,\mathrm{cm}^2$ absorption grating by 4×4 stitching of LIGA-fabricated pieces. Particular difficulties were tile-related shadowing effects and locally reduced visibility due to cracks in the grating structure [Schröter, 2017]. An adaptation of a comparable process for thorax imaging applications with grating sizes of e.g. $40 \times 40\,\mathrm{cm}^2$ is probably connected to a long, elaborate, and costly development. Using the LIGA method and Au as an absorber, even the pure material cost of the analyzer grating will account for a large part of the acquisition cost of such an imaging system. To avoid the difficulties with 2D tiling so-called line scanning systems that have a much smaller FOV have been implemented [Gromann, 2017; Willer, 2021]. Similar systems are used in many X-ray imaging applications such as airport security or product quality screening with conveyor belt systems. The VoF is "extended" by moving the sample through the linear beam and reconstructing the final image from a time series of recorded radiographs. Since it is particularly impractical to move the patient the discussed implementations perform a movement of the interferometer instead. To avoid grating-related shadowing the gratings have to be orientated perpendicularly to the cone beam in every scanning position. This requires a circular trajectory with the interferometer mounted on a swing, which can be rotated. Even though this setup gets by with a smaller grating area, other challenges such as vibrations of the interferometer, image reconstruction, and longer scan times introducing movement artifacts have to be handled.

The two most important liming factors remain grating area and production cost. It is only possible to significantly decouple area and cost if an alternative, cheaper absorption material to Au can be used. One part of the present work focuses on such an alternative process – a particle-based deposition of W into silicon-based templates. Furthermore, implementing a system with a large FOV requires much more than fabricating gratings of the respective sizes. Since all three gratings have to be bent to avoid shadowing their mechanical properties have to be understood and measured with high precision. The AXT method developed as a part of this work is an important contribution to approaching this difficult task.

It remains difficult to assess which grating fabrication method will turn out the most cost- and time efficient for high-volume production. Since DRIE systems are continuously optimized to reach even higher aspect ratios and silicon processing becomes more available on wafers up to 300 mm, significant progress can be expected here. As high aspect ratio filling with W via CVD is actively developed it might become the most optimal process for metallization. Otherwise, particle-based deposition is a simple alternative, albeit one that does not achieve such high filling densities.

At the same time, the LIGA process might gain popularity after having been demonstrated with conventional X-ray tubes [Pinzek, 2021a]. To date, it is applied to produce absorption gratings with the highest aspect ratio (>1:100) which are needed as source gratings for inverse geometry Talbot-Lau systems. However, scaling to larger areas seems to be more difficult with the complex DXRL and electroplating steps than with silicon-based methods.

4

Fabrication of Absorption Gratings by Particle Deposition

This chapter contains the development of a microparticle deposition process into high aspect ratio grating templates made by anisotropic etching techniques in silicon. The efforts in the framework of this thesis date back to 2016, when the first particle-based absorption grating pieces were fabricated with particles from a lead-bismuth alloy and tungsten in my master thesis [Gustschin, 2016]. Small grating pieces with 36-40 µm period and 430 µm depth were filled with W particles and showed a decent performance, albeit the duty cycle and other structural parameters deviated strongly from the design values. In a following master thesis project by Simon Pinzek [Pinzek, 2018], the filling density has been optimized by using a bimodal particle distribution and stronger centrifugation. In addition, the grating area was extended to about $40 \times 130\,\mathrm{mm}^2$. While the filling process appears well controllable, the quality of the silicon templates fabricated by KOH etching is still insufficient. In this chapter, such grating templates will be characterized by addressing common structural deficiencies and possible process-related aspects that are responsible for them. After that, the developed particle deposition method will be elaborated and the characterization of grating pieces by various techniques will be presented. The grating fabricated by the newly developed method will be compared to a state-of-the-art LIGA grating in a compact Talbot-Lau system designed for medical CT scanners.

In the second part of this chapter, the particle deposition process will be also applied to the fabrication of neutron absorption gratings using Gd-particles as absorber material. This is of particular interest since alternative methods for neutron gratings have achieved poor results for small grating periods. For good absorbing performance in the energy range of interest, effective Gd thicknesses of about 15 µm are desirable. For that, grating templates with a lower aspect ratio fabricated by DRIE were used and a centrifugation process was not necessary. After elaborating on the fabrication of source and analyzer gratings for a new Talbot-Lau interferometer at the ANTARES beamline at Heinz Maier-Leibnitz Zentrum (MLZ) FRM II, a characterization with microscopic methods and neutron transmission measurements will be given. A visibility evaluation will show excellent performance even in the sub-2 Å neutron wavelength range.

4.1 Tungsten Particle-based X-ray Absorption Gratings

4.1.1 Evaluation of Silicon Templates fabricated by KOH Etching

Fabrication of the Silicon Templates

As previously discussed in Section 3.1.3 wet silicon etching with KOH is a scalable method to generate HAR grating structures. It comes with some challenges in fabrication and requires precise process control to obtain good results. For the present work, the fabrication process consisting of lithography and etching was developed and optimized by *5microns GmbH* (Illmenau, Germany) as a joint research project. The period of the gratings was 45 µm and the target etching depth 500 µm which is far beyond comparable works in grating fabrication typically etching only a couple tens of µm. Accordingly, a longer etching time, a more robust lithography mask, and a careful adaptation of the latter were needed to account for under-etching and obtain the desired duty cycle. The process was conducted on 150 mm Si-wafers with a grating area of $40 \times 130\,\mathrm{mm}^2$. The silicon substrates with a (110) orientation were covered with 20 nm of SiO_2 and 80 nm of Si_3N_4 which served as a hard mask in the final wet etch process. The mask alignment for UV lithography was conducted based on the wafer flat according to the manufacturer. A precision of 0.1° to the respective silicon lattice is required for optimal etching and deviation of this orientation tends to decrease etch anisotropy [Hölke, 1999]. The mask alignment can be considered a possible process deficiency as it was necessary to rely on the wafer flat which was not precisely specified by the wafer manufacturer. After UV-lithography the pattern was transferred into the hard mask by RIE. The subsequent etching was performed at 80 °C in a 40% KOH solution. In a previous study, an etch rate of ≈ 1.7 µm/min under these conditions was observed to a depth of ≈200 µm. Under-etching in (111) Si direction was estimated to ≈ 12 nm/min. Hence, the openings in the hard masks were adjusted accordingly assuming a constant etch rate over time and a target etch depth of 500 µm. However, during the fabrication of the large gratings, the etch rate decreased after a few hours as was observed with the first batch of wafers. Thus, only a depth of 300-400 µm was achieved after 5 hours of etching and showed large local depth deviations. This is attributed to several circumstances which will be discussed later. To reach a higher depth closer to the targeted 500 µm the etch process was prolonged from the planned 5 h to about 7.7 h in the second wafer batch and has therefore introduced a higher under-etch resulting in a duty cycle deviation.

Characterization of Silicon Templates

For a large-area characterization before filling the silicon templates an AXT measurement was performed for several selected samples. As previously discussed in 3.2.5 it is sensitive to several grating properties such as duty cycle, grating height, and possible grating defects like missing lines or trenches. Even before filling the template with absorber material the transmission signal is useful for an initial quality characterization. Figure 4.1 A shows the transmission image of a selected example acquired at a relatively soft X-ray spectrum with an acceleration voltage of 40 keV. The scan was performed on a GE vtomex S µCT device collecting 100 projections in an ± 10° angular range with an effective pixel size of 140 µm. The black stripes above and below are representing the unetched silicon substrate with a thickness of 725 µm. In-between is the active area with different gray levels revealing grating irregularities. Brighter areas are indicating higher etch depths, larger duty cycles, missing grating lines, and possible combinations thereof. Four kinds of characteristic defects can be observed in Figure 4.1 A:

- Small, dark, elongated defects (e.g. ROI 1)
- Small, light, elongated defects (e.g. ROI 2)
- Larger areas with reduced transmission signal (e.g. ROI 3)
- Larger areas with increased transmission signal (e.g. ROI 4)

To acquire more information about those defects and probe the sample in depth X-ray tomosynthesis scans were performed at several selected ROIs. For that, the ZEISS Xradia 510 Versa X-ray microscope was used. For a typical scan, an angular range of ± 30° (600 projections) was collected at 40 keV tube voltage and a system configuration with an effective pixel size of 2.1 µm. In Figure 4.1 B the grating structure is shown in the plane marked by the dashed, blue arrow in C revealing a spot of about 4 periods where the mask pattern seems not to have been translated into the resist or the hard mask. Consequently, the area has not been etched as the in-trench view reveals in D and results in a characteristic slope similar to that at the edges of the active area. Such a small lithography defect (200 µm) effectively causes a 2 mm long area with a missing trench structure which is harmful to the application. In Figure 4.1 E the top view on the grating structure (ROI 2) shows several missing lines which are also very well recognizable in the grating profile in F. The in-trench view (G) shows that about 2 mm of the grating line is missing, however, it does not have a similar slope as in D. Furthermore, fractions of a grating line remain standing, as depicted by the red arrows. This type of defect

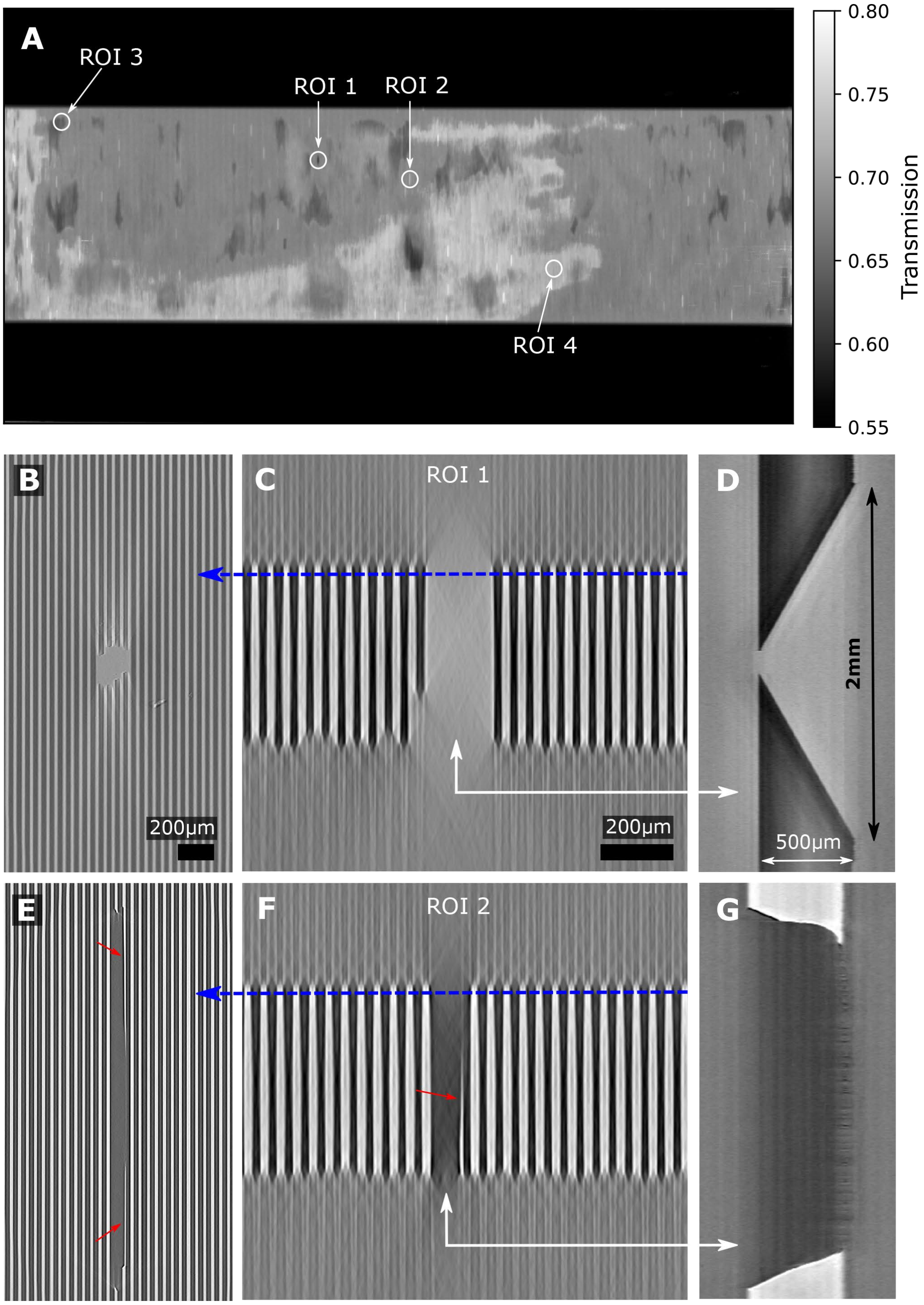

Figure 4.1: (A) X-ray transmission image of an empty silicon grating template showing structural deficiencies on the central active area. Characteristic line defects depicted in ROI 1 (dark) and ROI 2 (light) are further examined by high-resolution X-ray tomosynthesis. (B) Top view, (C) profile view and in-trench view (D) of ROI 1. Top view (E), profile view (F), and in-trench view (G) of a missing line defect in ROI 2.

can be only explained by a local loss of etch anisotropy at a certain depth in the silicon wafer caused by crystal defects, impurities, or some other kinetic conditions during etch. Hölke et al. suggested that some oxygen precipitations could increase the etch rate at the (111) planes which tend to form shallow funnels in the sidewalls and remove them entirely in a long etch process resulting in missing grating lines [Hölke, 1999]. In both cases (ROI 1 and 2) the defects become much larger than their origin as the etching time progresses due to the intrinsic properties of the etch process. This is usually not the case with e.g. DRIE and requires a particularly high substrate quality. The study of the other large-area depth deviations like ROI 3 and 4 shows that there is a general problem with etch rate control. Hölke et al. observed that with increased etch depth an apex forms at the bottom of the trench (see Figure 4.2 A) resulting in (311) planes replacing the (110) planes [Hölke, 1999]. Since the etch rate of (311) plates are smaller than the (110) planes a non-linearity is introduced which depends on the geometry of the trench. Furthermore, there seem to be other factors that prevent an apex formation and are connected to depth variations. In Figure 4.2 B a cross section of the trench bottom is shown. One part is etched to maximal depth and is surrounded by slopes typically found at the edges of the grating structure. This indicates that the etch process might have been stopped locally during the process. One possible explanation is the formation of hydrogen bubbles which are a product of the chemical reaction. They might grow in size and get stuck in the narrow trenches preventing a continuous exchange of etchant. The grating profile of an exemplary piece is visualized in Figure 4.2 C by an SEM image and a cross section of another piece is also shown from a µCT reconstruction in D. Trenches with maximal depth have an apex at the bottom highlighted by the arrows whereas other grating trenches have not formed an apex and vary in depth. Hölke et al. speculate that this decrease might also be related to crystal defects caused by oxide precipitations [Hölke, 1999]. In particular, the method of crystal growth (Czochralski or Float-Zone) that is used to produce the wafers seems to play an important role. It remains difficult to identify the main reason for the etch depth variations. Possible starting points would be e.g. trying to prevent the formation of bubbles by chemically modifying the etch solution or physically modifying the etch setup (e.g. applying vacuum). The removal of crystal defects caused by oxide precipitations might be possible with thermal treatment of the wafers at 1300 °C [Hölke, 1999]. However, it seems that the KOH wet etch process for high aspect ratio structures has serious difficulties when scaling to larger areas. Both, the acquisition of large substrates with sufficient crystal quality as well as an implementation of a stable and predictable etch process are significant drawbacks. Furthermore, the duty cycle control being one of the most important grating parameters will require additional process development as it is strongly linked to the required hard

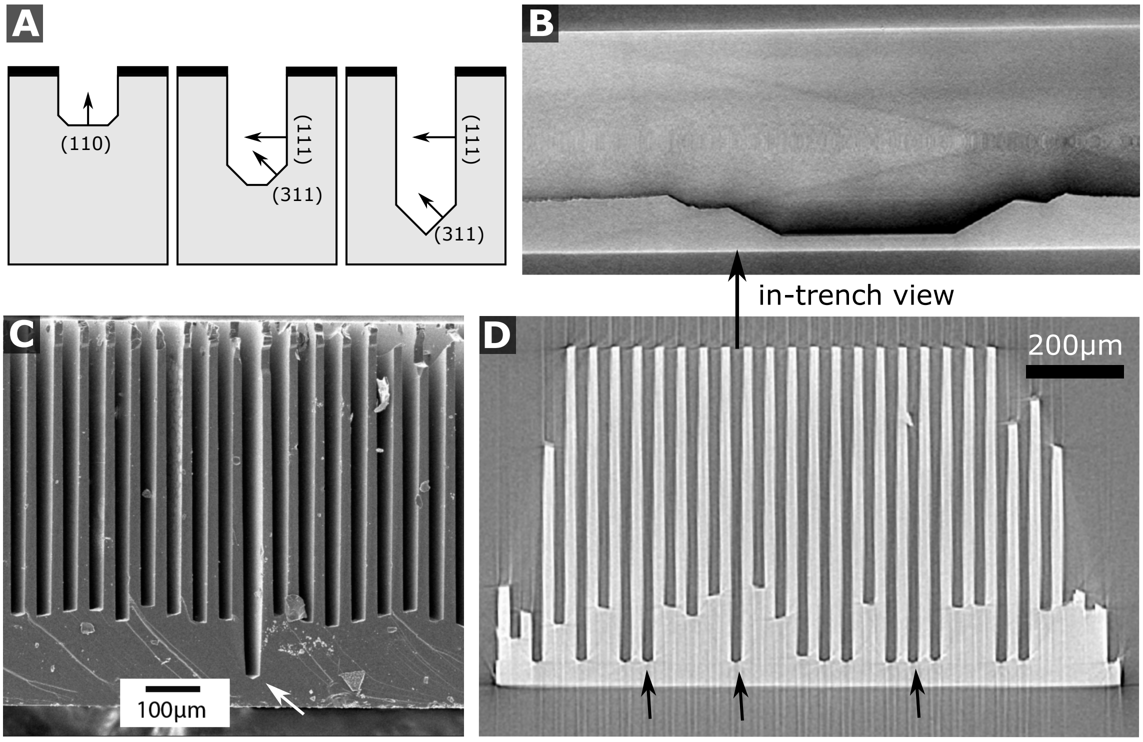

Figure 4.2: (A) Change of the etching planes in silicon determined by trench geometry. At the beginning, the (110) plane is etched at a high rate, and an apex is formed with (311) planes in the later process. CT data visualizing the trench bottom in B shows that the trench depth is not homogeneous. Deep trenches such as depicted by arrows in an SEM profile image (C) and µCT data (D) show that the deep trenches have formed an apex at the bottom.

mask opening and etching dynamics. In this respect, DRIE, despite having its own difficulties with etch profile control, might be considered a better alternative. Both, the acquisition of wafers (especially wafer size) and the fine-tuning of the etch process are less laborious and time-consuming. This alternative approach was successfully conducted in a related project and published recently [Pinzek, 2022].

4.1.2 Development of the Tungsten Particle Deposition Method

Particle Suspension

For the discussed applications the goal is to deposit tungsten particles into narrow channels with the highest possible density to achieve a strong attenuation of the X-rays. Similar processes are studied for many material science applications such as micro-injection mold-ing, screen printing, or microfluidics. The basis of such a process is the development of a suspension consisting of particles, a polymer binder, and a fluid to provide a suitable viscosity for the penetration of the particles into high aspect ratio structures. The fluid usually evaporates in the final thermal treatment or drying process and the binder facilitates better filling and fixation of the particles. Maximization of the volume fraction filled by the particles has been studied for many applications ranging from simple logistics to sophisticated techniques such as selective laser sintering which allows producing arbitrary 3D shapes from a high variety of metals. It is well established that a random arrangement of equal spheres (loose random packing) fills a volume to about 55% [Song, 2008]. Using external forces like pressure, agitation or inter-particle interaction initiated by e.g. chemical additives can increase the packing to about 64% (random close packing)[Song, 2008]. The filling fraction can be optimized by using suitable particle size distributions allowing smaller particles to fill the spaces between larger particles. Using a bimodal particle size destitution the filling can be improved when the coarse particles have a volume fraction of about 0.65-0.8 and their radii are about one order of magnitude larger than the ones of the fine particles [Ye, 2018]. Although the principle seems obvious, it does not mean that significantly better filling ratios compared to e.g. random close packing are achieved. Unfavorable effects like walling, loosening, and wedging decrease the theoretically anticipated filling fractions [Ye, 2018]. To make matters worse, the particles are deposited in narrow trenches where many voids are created at the periphery of the trench walls. In addition, their mobility is impeded and they tend to get stuck in narrow gaps instead of arranging themselves in favorable positions. Furthermore, commercially available particles deviate strongly from equally sized spheres as assumed in simple models. Finally, inter-particle interactions driven by physical and chemical forces can have a strong influence on deposition dynamics.

In the first part of the development, different commercially available tungsten powders and different binder systems were tested in the framework of a master thesis project [Pinzek, 2018]. Several combinations have been dispersed in ethanol, mixed, and introduced into thin micro-pipet tips. With an inner diameter of about 400 µm, they were found suitable for studying the deposition behavior and thin enough to be scanned by µCT. To increase the effective density some samples were also centrifuged to have an additional force driving the particle suspension into the narrow cavity at the tip. Ethanol was chosen as dispersing agent due to its low viscosity and corrosivity and fast evaporation under ambient conditions. After drying the samples were scanned with µCT and the density and porosity were evaluated from respective 3D volume reconstructions. Adding some PVP as a binder showed to improve the filling, fixate the particles, and made the process of removing the residual particle layer from the grating top more convenient. It was found that a bimodal particle mixture of a coarse W powder ($\approx 7.7 \pm 3.4\,\mu\mathrm{m}$ particle size) and a fine W powder ($\approx 0.66 \pm 0.35\,\mu\mathrm{m}$ particle size) acquired from Sigma-Aldrich (St. Luis, USA) resulted in the densest filling. The bimodal particle mixture had a weight ratio of 2:1 (coarse:fine powder). As a binder, Polyvinylpyrrolidone (PVP, $10\,000\,\mathrm{g\,mol^{-1}}$, Sigma Aldrich, St. Luis, USA) was dissolved in ethanol at a concentration of $1\,\mathrm{mg\,mL^{-1}}$. The tungsten particle mixture was suspended in the PVP solution in a W:PVP weight ratio of 450:1 and the suspension was magnetically stirred at 300 rpm until application onto the grating structures.

Centrifugal Deposition

In the second phase of the development, the deposition process was translated to actual grating samples. Some small grating pieces ($10 \times 10\,\mathrm{mm}^2$) were diced from a silicon grating template with $36\,\mu\mathrm{m}$ period and a depth of about $160\,\mu\mathrm{m}$. Respective particle suspensions were prepared with coarse W powder, fine W powder, and a bimodal mixture of both in a weight ratio of 2:1 (course:fine) to test how the results from previous experiments would translate to filling narrow grating trenches. The gratings were placed into custom-designed and 3D-printed centrifugation inlets similar to that in Figure 4.3 A which can be filled with the suspension and sealed. To compare the filling of the grating templates several samples were prepared with different particle suspensions. After placing each grating sample into the insert the surface was wetted with ethanol and the suspension was dripped onto the surface with a pipette. After filling the entire reservoir the vessel was sealed with the lid using screws. For centrifugation, we used a OneConcept WS-3500 spin dryer with a metallic drum of 240 mm diameter and attached the inlets magnetically (see Figure 4.3 B). A similar object in weight was attached to the opposite side of the drum to prevent imbalance during rotation. The centrifugation was conducted at 2800 rpm which generated a centrifugal acceleration of 1050 g close to the drum diameter for 5 minutes. To achieve a more homogeneous deposition each container was flipped and centrifuged for a second time. After that, each vessel was opened and the surface was inspected under a microscope. The liquid usually cleared up and could be partly removed with pipets from the inner cavity. The samples were allowed to dry in a fume hood overnight under ambient conditions. After that, they were carefully extracted from the vessels, and the solid covering from protruding particles on the grating surface was removed by hand with a doctor blade or a scalpel under the microscope. This cleaning process is the most time-consuming and requires some practice and fine motor skills.

In the third phase of the development, the method was scaled up to larger areas. Here, the challenge was to design and produce a centrifugation inlet for large grating areas pro-

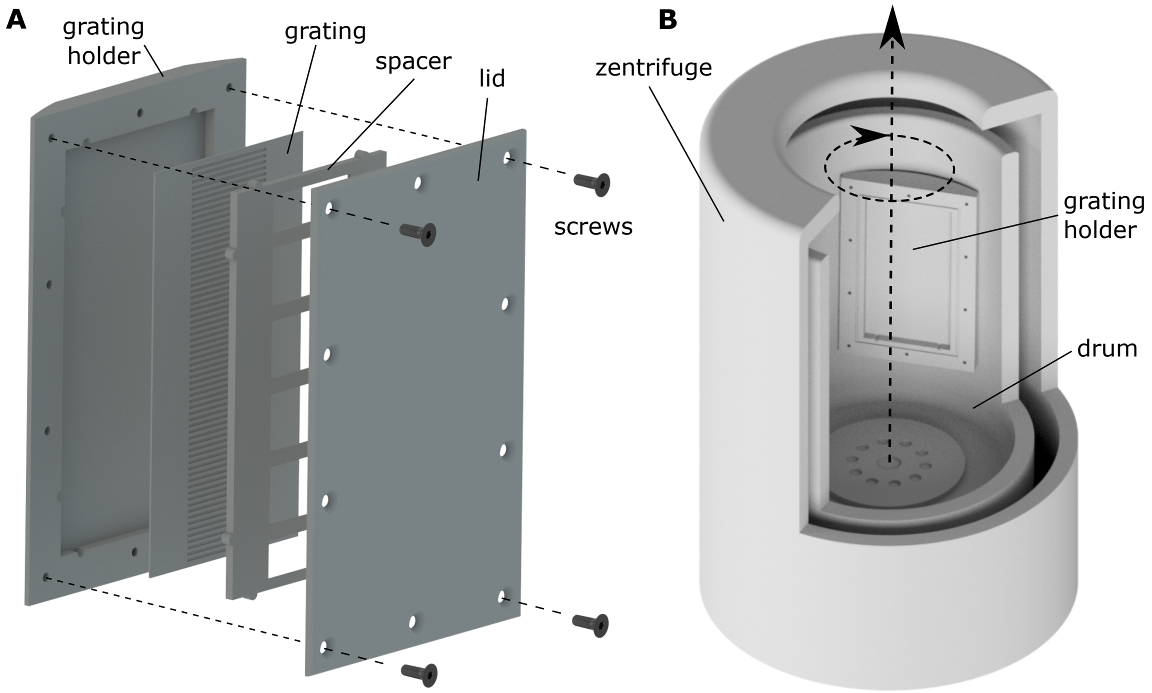

Figure 4.3: (A) grating insert consisting of a grating holder with an inner cavity for the particle reservoir, grating, spacer, and lid which can be fixed with screws. (B) Illustration of the centrifuge with the grating holder fixed on the rotating metal drums with magnets which are embedded in the insert.

viding more volume for the particle suspension reservoir while keeping its weight within reasonable boundaries compatible with the centrifuge. Several prototypes have been designed and 3D printed from VeroBlack photopolymer resin using a Stratasys Objet Eden 260V 3D printer. Before performing the first experiments with the gratings the vessels were tested with dummy substrates and could withstand several runs. The model of the latest design iteration for the large grating insert is shown in Figure 4.3 A. The active area on the substrate is $40 \times 130\,\mathrm{mm}^2$ in the central part. To restrict the suspension to the area above the grating a spacer is placed on top of the grating substrate. The vessel is sealed by a lid with a rubber layer on the inner side using screws. After closure, the vessel is weighed to prepare a comparable counterbalance for the centrifuge drum. The large-area substrates have been centrifuged under the same conditions as the small pieces described previously. However, due to the sedimentation of particles, the deposition was not conducted homogeneously resulting in poor filling towards the center of the substrate observed in microscopy. Therefore, a second centrifugation step after a refill of the suspension has been performed with the large gratings. After this, the inlet was opened and allowed to dry after residual ethanol has been removed with a pipette. After removing the residual particle layer from the surface the substrate was weighed. The mass difference of the substrate before and after the filling gives a useful measure to estimate the filling density when the duty cycle and height of the substrate are known.

During the development of the process, several substrates broke. In one case the entire grating inlet did not withstand the centrifugal forces and broke during the process. As a consequence, the thickness of the material was increased and some support structures on the back of the inlet were added. In one other case, the grating broke inside the vessel during the second centrifugation step. In two other instances, the gratings broke in the process of removal of the substrate from the inlet. This happened because after drying the grating tends to get stuck in the holder with the hardening of the polymer binder and removing it creates point loads on the substrate. To avoid this the next design iteration for larger gratings introduces an inlay (see [Pinzek, 2022]) which makes a safe removal of the gratings possible.

One crucial aspect that might be responsible for the breaking of the substrates is the poor residual substrate thickness in the active area. As shown in Figure 4.2 C and D some trenches have been etched almost through the entire substrate in case of the second batch of wafers with the prolonged etching time. When the grating is bent in the beam path, all potential inhomogeneities, especially those with thin substrates, are weak points under mechanical stress. This is another complication that arises with high etch depth variance with KOH etching and is not tolerable for the application. Three substrates from the first batch (lower etch depth) could be filled successfully without breaking. A table of all processed large-area gratings is given in the supplement in A.1.

4.1.3 Characterization of W-filled Absorption Gratings

Microscopy

Figure 4.4 shows SEM images of some grating pieces with 36 µm period and 160 µm trench depth fabricated in the initial phase of development. The filling with a coarse powder (Figure 4.4 A) shows a broad particle size and form distribution ranging from large particles hardly being able to protrude into the trenches to agglomerates of smaller particles. Empty cavities close to the trench walls are even visible from the surface. Figure 4.4 B shows the sample filled with the fine particle power only. The filling appears more homogeneous and better, especially in the periphery of the trench walls. The surface of the silicon grating lines is mostly clear, however, a few residual particles are present after the mechanical removal. In Figure 4.4 C the sample with the bimodal filling is shown with a magnified view in D. The filling seems to be improved by smaller particles which are also visible in the profile view in E. It remains unclear, however, if the visible voids in the profile view originated from the cleaving of the sample or if they have been present before. A closer look at the lower part of the grating cross section D shows that both, large and fine particles do penetrate down to the bottom of the trenches.

While giving a good impression of the micromorphology of the particle filling the SEM images cannot provide reasonable and quantitative information about the absorption power. Hence, a detailed investigation using X-ray microscopy sensitive to the filling in the entire trench is indispensable. One method to compare the absorption performance is to acquire multiple representative radiographs of each grating piece and compare histograms of the pixel's transmission values. An optimal filling should show a bimodal intensity distribution with the lower peak representing the absorbing domain of the grating. The mean value of this peak should be as small as possible and its width is a measure of the homogeneity of the absorbing matrix. Such a detailed investigation was performed in the framework of a master thesis [Pinzek, 2018] and is also addressed in a recent publication [Pinzek, 2022]. It was found that the bimodal particle mixture provided both a lower overall transmission signal and smaller width of the histogram peak compared to the samples with the coarse and the fine powder only. Hence, a bimodal filling was used for the filling of the larger grating pieces. The latter were examined with a ZEISS Xradia 510 Versa X-ray microscope at 70 keV acceleration voltage to evaluate the transmission contrast and local grating quality around defects recognizable on the grating surface with light microscopy.

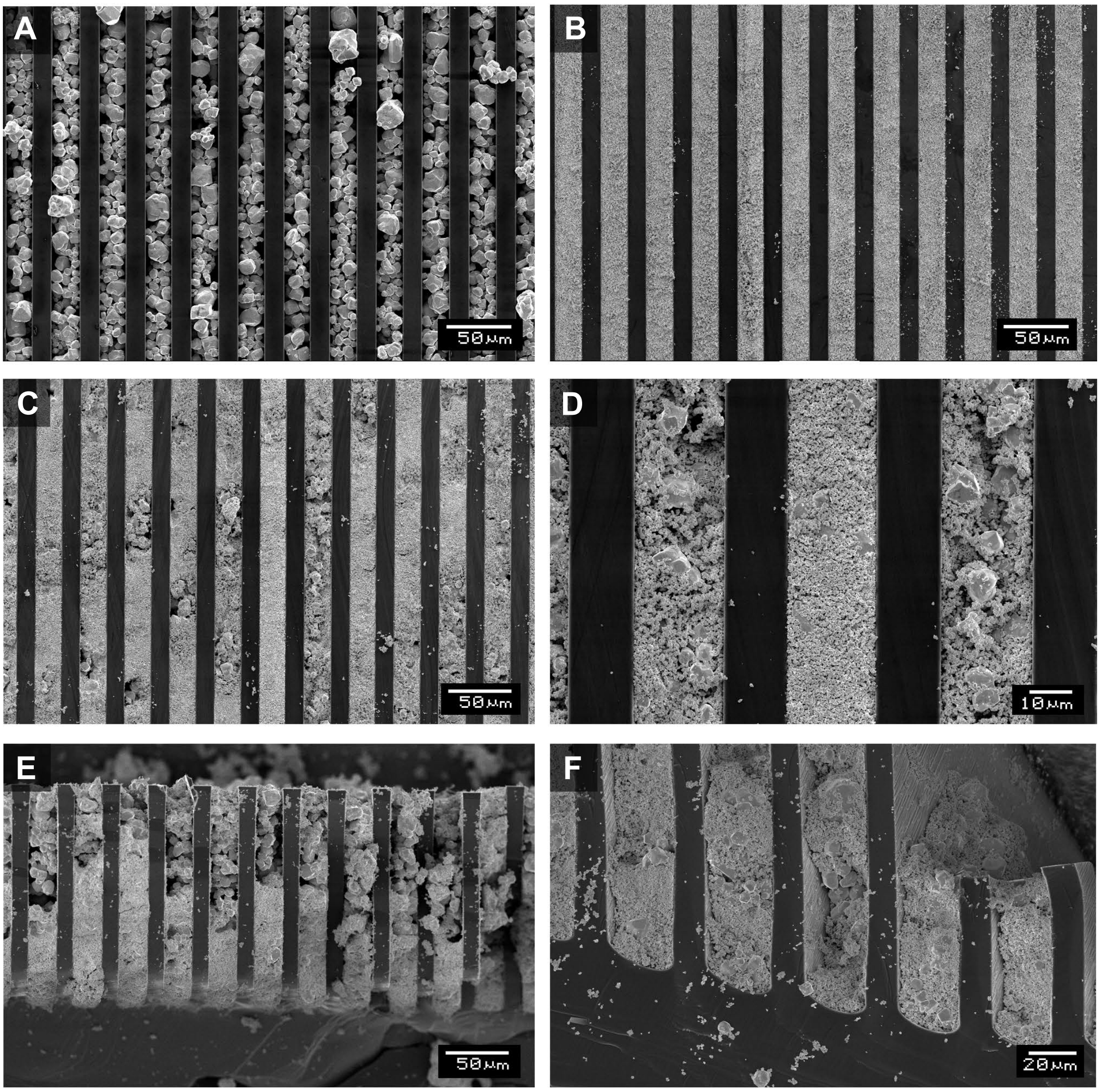

Figure 4.4: SEM images of the surface and profile of different small grating pieces with 36 µm period and 160 µm depth. (A) Grating surface with the coarse particle filling and (B) the fine particle filling. (C) Grating surface with the bimodal particle filling and a higher magnification of the latter in (D). The profile view (E) and a side view on the bottoms of the trenches (F) show that the absorbing material fills the entire trench.

Figure 4.5 A shows an X-ray transmission image of the large-area grating with 45 µm period after filling with the bimodal W particle mixture. The image shows two common defects that were also previously discussed in the analysis of the empty grating piece. The dark defects are missing grating lines originating from etching deficiencies which left cavities that were also filled with the absorbing material. The lighter defect shows an etching deficiency which also was visualized via µCT in Figure 4.1 D. This demonstrates that such kinds of defects can be recognized and characterized on large-area gratings without the need for a tomography scan. Micrographs of the W particle grating (Figure 4.5 B) and a LIGA-fabricated Au grating with 280 µm Au height (C) show comparable performance, except that the LIGA grating has transparent bridges necessary to stabilize the resist structure. Figure 4.5 D shows the normalized transmission profiles averaged over 5 pixels along the lines in B and C of both gratings. The contrast of the W grating is a few percent smaller due to the reduced filling density compared to the bulk gold filling in the LIGA grating. As previously discussed microscopy-based characterization is limited to a small FOV and is therefore of limited use for characterizing the entire grating area.

Angular X-ray Transmission

Figure 4.6 A-C shows the reconstructed results from an AXT scan (Sub. KOH CZ 3) performed on a GE vetomeX S µCT scanner at 80 keV acceleration voltage and 120 µA tube current. The grating was scanned in an ±30° angular range with 0.1° steps at an effective pixel size of 136 µm. The transmission image (Figure 4.6 A) reveals several irregularities that can be attributed to different deficiencies in the grating structure:

- Variation in the grating duty cycle
- Variation in the depth/height of the etched trenches
- Missing or tilted grating lines.

A closer look at the reconstructed height map of the filled absorber material (Figure 4.6 B) enables to differentiate between those kinds of irregularities. For example, it is visible that the streaked structures in the upper left corner of the map are not caused by variations in height of the absorbing filling. Assuming a relatively constant filling density they must be attributed to duty cycle variations. The clear and parallel strips are an indication of crystal-related defects that locally compromise the etching selectivity resulting in wider trenches. The spots with reduced height are partially connected to brighter transmission signals in the bottom right. The large defect on the central left consists of entirely

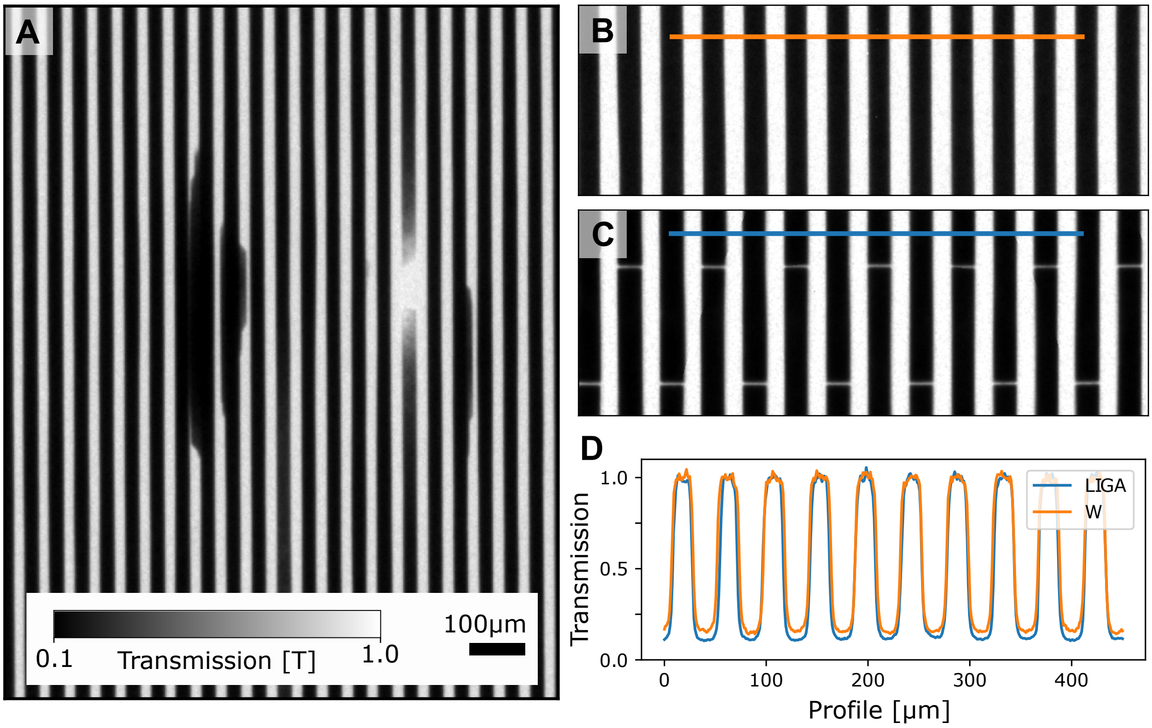

Figure 4.5: (A) X-ray transmission micrograph of the W particle grating showing common defects. Missing or thinned silicon lines due to etching deficiencies result in locally decreased transmission. Brighter areas indicate unetched or poorly filled cavities. (B) X-ray radiograph of the W particle grating and (C) a state-of-the-art LIGA grating used for comparison. The grey scale in (A) also applies to (B) and (C). (D) Normalized transmission profiles of both gratings along the lines in (B) and (C) show a slightly better absorption of the LIGA grating.

damaged structures as the height signal could not be reasonably retrieved. The lamellae inclination shown in Figure 4.6 C lies in the range of $\pm 0.1^\circ$ which is comparable to gratings fabricated with alternative methods. Only on the left side, there are some abrupt changes in the inclination angle most probably related to the duty cycle defects. Apparently, the thinned silicon lines are susceptible to the strong forces during centrifugal deposition and might tend to bend. Apart from that, the structure can be considered in good shape except for the large defect on the central left. In total, an average grating height of 320 µm is achieved. With a duty cycle of 0.6, the aspect ratio (trench opening / height) is $\approx$ 1:12. The mass difference Δm of the grating before and after filling was 10.14 g. With that, it is possible to estimate the filling fraction of the trenches via:

$$f = \frac{\Delta m}{A \cdot h \cdot DC \cdot \rho_W}, \tag{4.1}$$

where A is the grating area, h is the trench height, DC the duty cycle, and ρ_W the density of tungsten. Using this formula and estimating a duty cycle of 0.6 (width of the trench/period) the filling fraction would be ≈ 0.53. However, this value is rather an overestimation since the grating has defects with significantly wider trenches and spots with missing grating lines. Other gratings that have been successfully filled show comparable values with the main issue being the irregular duty cycle.

Visibility Analysis in a Talbot-Lau Interferometer

A final characterization of the fabricated grating is performed in a Talbot-Lau interferometer designed for dark-field computed tomography at the human scale as recently reported by [Viermetz, 2022]. The inverse geometry allows to integrate the interferometer into a gantry of a clinical CT scanner with relatively small areas of the G_0 and G_1 gratings. To cover a large FOV required for state-of-the-art clinical CT the gratings have to be bent to small radii and the analyzer grating G_2 has to be tiled and respective mechanical elements allowing to align every single tile individually have to be implemented. To induce an intensity modulation with hard X-rays at relatively short propagation distances a triangular grating profile of G_1 is necessary. A further challenge is the fabrication of a high aspect ratio G_0 that is still flexible to be bent to a radius of about 100 mm. The fabricated W particle grating used as G_2 in the setup was introduced into a bending frame with a radius of 1 m as the geometry requires. The bending of the grating is the final requirement to demonstrate the feasibility of the described fabrication method. All the hardware and system parameters used for the measurement with the Talbot-Lau interferometer are listed in Table 4.1. Additionally, a visibility comparison with the Au LIGA grating in the

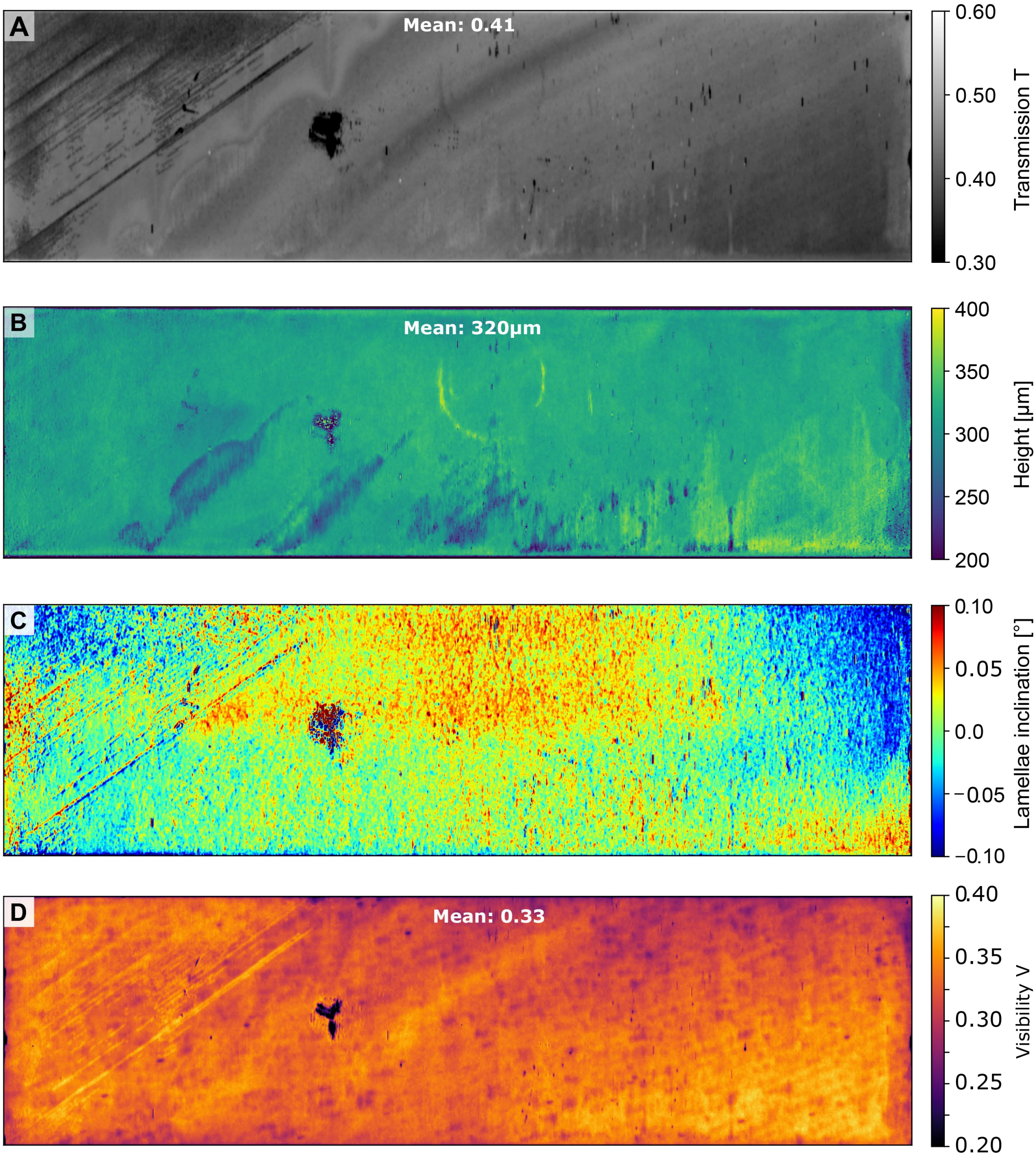

Figure 4.6: (A) Transmission, (B) grating height, and (C) lamellae inclination map acquired by AXT analysis. The complementary signals allow to identify and differentiate defects related to various grating parameters. (D) Visibility map measured in a compact Talbot-Lau interferometer at 60 keV.

same system is also provided. Figure 4.6 D shows the visibility map of the fabricated W grating acquired at 60 kV tube voltage. With a mean visibility of 0.329 ± 0.021 the grating shows a decent performance for imaging and comes close to the value achieved with the LIGA Au grating (0.354 ± 0.017). Several features are recognizable in the visibility map that can be correlated with features seen in the AXT data. Previously discussed defects are also evident with spatial visibility drops. The linear structures on the left that are related to a duty cycle increase also show a slight increase of the visibility. Furthermore, there are patterns recognizable that are not visible in the AXT data. These are related to defects in the G_0 and G_1 gratings since they can be also observed with the Au LIGA grating. Figure 4.7 shows some images of three nuts (walnut, peanut, hazelnut) acquired with the evaluated system at 60 kV tube voltage. Due to the limited FOV in the vertical direction, the image was stitched from 2 exposures. The sample position, stepping scheme, and other acquisition parameters are also listed in Table 4.1. While most of the grating defects do not degrade the image quality since they are corrected for by the flat field some artifacts from the duty cycle irregularities are visible in the transmission image of the hazelnut (Figure 4.7 A, highlighted by arrows). The large defect and the duty cycle irregularities are also visible in the dark-field image (Figure 4.7 B, marked by an arrows) leading to an artificial increase of the dark-field signal that can be falsely attributed to some feature in the sample. The phase image (Figure 4.7 C) also suffers from the large defect on the grating, which is indicated by the arrow pointing to the artificial spots in the image. Hence, such grating defects have to be avoided especially for dose-relevant and diagnostic applications.

4.1.4 Summary and Outlook

The fabrication of silicon templates via KOH etching was the first challenge of the present project. While at first glance it promises some advantages like the possibility to etch many substrates in parallel some serious difficulties arise when trying to achieve a high aspect ratio. At first, a precise compensation for underetching is necessary. This becomes particularly difficult because the etching process is no longer linear after reaching a certain depth. The origin of this behavior has not yet been fully identified. The most probable explanation is the impeded exchange of chemicals, as the etching rate is known to depend strongly on the concentration of KOH in the etchant. A further reason is a change in the etching planes of the silicon crystal. Furthermore, local defects can be probably introduced due to impurities in the crystal and hydrogen bubbles trapped in the narrow grating trenches. Common defects have been identified and characterized with different methods. X-ray transmission has proved to be the most versatile method to study the

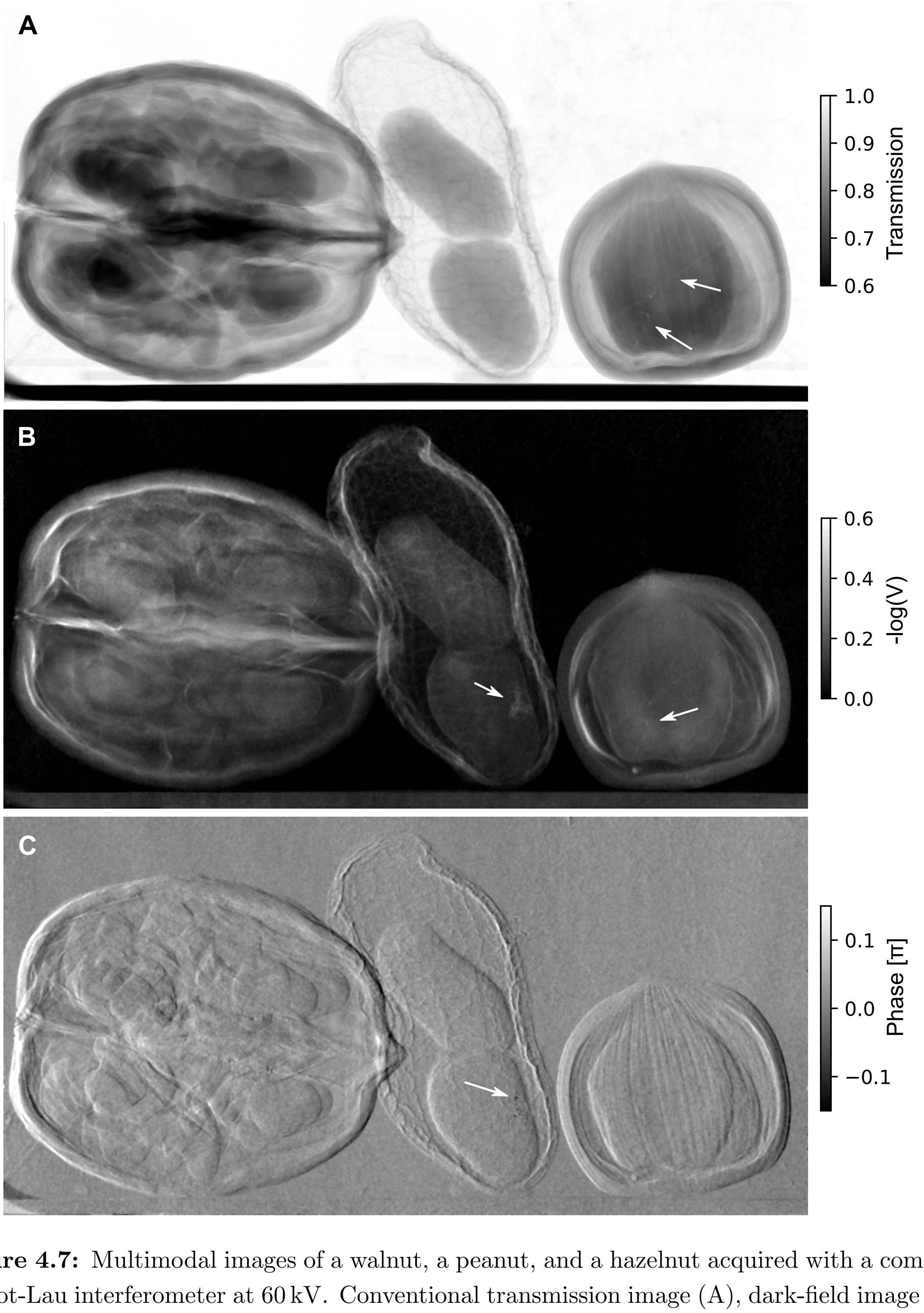

Figure 4.7: Multimodal images of a walnut, a peanut, and a hazelnut acquired with a compact Talbot-Lau interferometer at 60 kV. Conventional transmission image (A), dark-field image (B), and differential phase-contrast image (C). The white arrows denote image artifacts caused by defects such as irregular duty cycles and a larger spot with damaged grating structure.

Parameter	W particle grating	Au LIGA grating
X-ray source	XWT-160-CT, X-rayWorX	
X-ray filter	1 mm Al	
Source-G_0 distance / radius	$\approx$ 100 mm	
G_0 (period / DC / height)	4.8 µm / 0.5-0.6 / 280 µm Au	
G_1-source distance / radius	$\approx$ 200 mm	
G_1 (period / height)	4.34 µm / 18.5 µm Au triangular	
G_2-source distance / radius	$\approx$ 1000 mm	
G_2 (period / DC)	45.0 µm / 0.6 $\pm$0.05	45.0 µm / 0.54
G_2 Filling	320 µm W particles	280 µm Au bulk
Phase stepping	G_2, 45.0 µm range, 11 steps	
Source-sample distance	$\approx$ 580 mm	
Detector	XRD 4343CT (Varex) - 2 s exposure time	
Visibility 60kV	(32.9 ± 2.1) %	(35.4 ± 1.7) %

Table 4.1: Experimental parameters of the Talbot-Lau interferometer used for visibility comparison and imaging. The ± sign indicates the standard deviation.

grating templates being suitable for both, large-area characterization and high-resolution analysis of individual defects.

A deposition process of the W particles into the silicon grating templates has been developed. It was shown that a centrifugal deposition is possible with large grating areas and high aspect ratios not reached before. Different compositions of particles have been tested and respective samples have been evaluated with different techniques. It was found that a bimodal particle mixture was best suitable to achieve a denser filling. Some technical challenges had to be overcome to conduct the centrifugation process with large-area gratings. A suitable vessel containing the substrate and the particle dispersion was designed and fabricated. Several grating substrates have been filled successfully and showed an overall good performance approaching values acquired with LIGA-fabricated gratings.

However, defects remain on a considerable fraction of the grating area. As the detailed analysis shows they originate in the KOH etching process and are in most cases not the result of the filling process itself. Hence, alternatives to the KOH etching such as DRIE were investigated in recent related work [Pinzek, 2022]. Most of the KOH etch-related defects could be avoided. Additionally, a larger area and a higher etch depth (450 µm) were reached. Considering these results DRIE appears clearly advantageous in process control compared to KOH etching. In addition, it does not require (110) wafers which are much harder to procure for larger wafer sizes. Furthermore, the error-prone adjustment of the mask to the crystal planes of the substrate is no longer necessary.

The process of W deposition has made significant progress in the course of this work reaching significantly higher aspect ratios and larger areas than reported with particle-based deposition so far. With current capabilities, it is already possible to implement phase-sensitive techniques based on e.g. coded apertures or masks for hard X-rays. However, the period of 45 µm remains still high for more sensitive Talbot-Lau systems and should be further decreased to the sub-20 µm level to allow more flexibility in system design. For that, the aspect ratio of the templates has to be increased significantly above 1:20 while maintaining a profile with a constant duty cycle. Furthermore, the W filling should be optimized for higher densities. For that, the particle suspension will need further development focusing on surface-related inter-particle interactions that become stronger with decreasing particle size.

Especially with a large field of view (FOV) as needed for thorax radiography systems or CT scanners, the cost and effort of grating production increases. Both silicon-based processing such as DRIE and a rather cost-effective absorber material with a simple deposition method open up the potential for savings. Considering these advantages it remains to be seen to what extent this method can replace the conventional approaches to grating fabrication. For strongly inverse Talbot-Lau systems requiring source gratings with aspect ratios beyond 1:100 the LIGA method will remain indispensable. Especially since flexible substrates like graphite with bending radii down to 100 mm are needed, silicon-based gratings will reach their limits. But for G_2 gratings the requirements regarding period and aspect ratio are more relaxed in inverse geometries. For that, the here presented low-cost fabrication method based on silicon processing and subsequent centrifugal deposition of W particles might become a good alternative.

4.2 Gadolinium Particle-based Absorption Gratings

As discussed in Chapter 2.2.3 neutron imaging with gratings requires different absorption materials due to fundamentally different interaction cross section compared with X-rays. For imaging with cold and thermal neutrons a thickness of 10-15 µm gadolinium (Gd) is already enough to achieve decent contrast. Therefore, the requirements for the aspect ratio are by far not as high as for X-ray absorption gratings. On the other hand, there is no widespread micro-plating process for Gd as there is e.g. for Au and therefore the LIGA method is not applicable. Instead, the material is evaporated obliquely on a silicon-etched grating structure with a wide opening [Grünzweig, 2008b; Samoto, 2019] accepting a non-binary absorption profile and some difficulties in tuning the grating duty cycle. Another possibility is to use laser ablation to selectively remove Gd from coated substrates. This method is also limited in aspect ratio and is only suitable for gratings of several tens of µm period, e.g. G_0 for strongly asymmetric systems. Particle-based absorption gratings have also been fabricated with rather coarse periods before [Kim, 2013; Kim, 2014]. In the framework of this thesis, it has been shown that both, small periods and sufficient absorption thickness with a quasi-binary absorption profile for neutron grating interferometer (nGI) systems with high sensitivity can be reached.

4.2.1 Development of the Gadolinium Particle Deposition Method

For the first attempts silicon grating templates with periods of 36-45 µm were cut in $1\times1\,\mathrm{cm}^2$ pieces. Commercially available Gd powder (99.9%, Steely Rare Earth Limited, Shenzhen, China) was dispersed in ethanol under continuous magnetic stirring and applied on the surface of the grating pieces. After that, the pieces were inspected under a microscope and the particle-covered surface was cleared by hand with a doctor blade as in the case of the W particle gratings. After drying, the gratings pieces were inspected by confocal and scanning electron microscopy (SEM), X-ray microscopy (XRM), and micro-computed tomography (µCT). The results were used to optimize the particle filling as in the case of the X-ray absorption gratings with tungsten. A binder material was also found to be helpful for fixating the particles in the trenches and an easier removal of the protruding particles on the grating surface. For that, Poly(vinyl alcohol) PVA (Mowiol®4-88, Sigma Aldrich) was dissolved in deionized water under magnetic stirring and added to the particle suspension in different PVA:Gd weight ratios.

After promising results with 45 µm and 36 µm period grating pieces, the period had to be further reduced. A new interferometer design addressed in [Neuwirth, 2020] required G_2

periods of 13.3 µm and therefore Gd particles in the size range of 1-6 µm were required. Since no commercial Gd powders in that size range with reasonable particle size distribution were available, a milling process was needed to obtain finer Gd particles. For that, a planetary ball mill (Pulverisette 6, Fritsch GmbH, Germany) with an 80 mL steel vessel and 1 cm diameter tungsten carbide balls were used. The milling medium was ethanol. Different milling protocols have been tested to reduce the original powder particle size (<44 µm, mesh 325) to the sub-5 µm size range. The size and shape distribution of the milling result could be hardly narrowed. As apparent from SEM and µCT, many large, flat, and edgy particles that have poor mobility in the narrow trenches were still present in the suspension. However, this turned out not to be a serious problem during deposition. The biggest particles (> 7 µm) remained on the grating surface and could be removed later. While some medium-sized particles wedged themselves in the trenches, the smaller particles had enough mobility in the liquid to reach down to the bottom of the trenches.

4.2.2 Fabrication of Gd Particle-based Absorption Gratings

After reaching satisfactory results with pieces of 13.3 µm period a final protocol for the suspension preparation was established. 5 g of Gd powder and 10 mL of absolute ethanol were ball-milled for 30 minutes at 250rpm. PVA powder was dissolved (2wt%) in deionized water and a volume resulting in a Gd:PVA weight ratio of 50:1 was added to the Gd-particle suspension in the milling vessel. The mixture was milled again for 1 minute at 250 rpm to homogenize and transferred into a glass vessel. It was magnetically stirred until application onto the grating. A few µm of the suspension were extracted and analyzed by X-ray fluorescence (Epsilon 1, PANalytical, Netherlands) to exclude strong contamination with e.g. wear of the milling balls or vessel. No significant additional elemental abundance was found. However, it can be assumed that the surface of the particles has been oxidized during the process since all steps were performed under ambient air conditions.

In total 4 source and 2 analyzer gratings were filled up for the new nGI. The silicon templates for the 4 source grating with a period of 150 µm and duty cycles of 0.5, 0.4, 0.3, and 0.2 were provided by Fraunhofer IPMS (Dresden, Germany). They were all fabricated on a 200 mm silicon wafer employing DRIE and had sizes of $64\times64\,\mathrm{mm}^2$. The templates for the analyzer gratings with 13.3 µm period were manufactured on a 5” silicon wafer by Micromotive GmbH (Mainz, Germany). For both types of grating customized vessels were designed and 3D printed. They are used to hold the grating in place while covering its surface with the Gd particle suspension. The surface of the grating was wetted with absolute ethanol to improve the penetration of the suspension and avoid air bubbles in the deep trenches. After that, the particle suspension was stepwise applied on the wetted grating surface until the active area was covered. The casting was repeated a few times as the ethanol evaporated. In between, the suspension was redistributed on the grating surface with a doctor blade by hand (parallel to the grating lines) like in screen printing. This step is necessary to achieve a homogeneous coverage of the grating area. For each source grating $\approx 5\,\mathrm{mL}$ of the prepared suspension was cast onto the substrate.

As the analyzer grating had a more than one order of magnitude smaller period the deposition process was extended with an ultrasonication step. For that, the grating holder was carefully placed into an ultrasonic bath after the first particle application. That increases the mobility, prevents clumping of the particles, and improves their penetration into the trenches. After applying the suspension several times, the gratings were dried for 2 hours in a fume hood under ambient conditions. During that time the mixture covering the grating area became hard due to the binder. In the last step, it was removed by hand with a sharp doctor blade under a stereo microscope. The movement of the blade had to be performed parallel to the grating lines, otherwise, the fine silicon structures would break. Figure 4.8 A shows a microscopy image of the cleared and covered area of one of the G_0 gratings. After clearing the surface, the edges were cleaned with an ethanol-soaked tissue, and the surface of the gratings was carefully blown with nitrogen in a fume hood to remove residual small particles on the grating surface. Note that afterward, the grating should not get in contact with liquids as it would swell the polymer and damage the filling.

4.2.3 Characterization of Gd Particle-based Absorption Gratings

Optical and Confocal Microscopy

For a fast and qualitative surface characterization of the grating structures common optical techniques are most convenient. They enable evaluating the period, duty cycle, structure intactness, and particle filling on the grating surface. Confocal Microscopy uses elaborate optical elements to detect light only from one focal plane of the sample. Hence, it enables scanning the surface layer-by-layer and reconstructing a 3D representation of the surface by a process known as optical sectioning. With that, the filling level of the particles relative to the grating surface was measured using the NanoFocus Microsurf® (NanoFocus AG, Oberhausen, Germany) profilometer. These techniques are limited to the surface and a small FOV or require long scanning times, advanced equipment, and processing of large amounts of data. Figures 4.9 A and B show two representative micrographs of filled G_0 gratings with two different duty cycles as well as a height profile (C) showing the filling

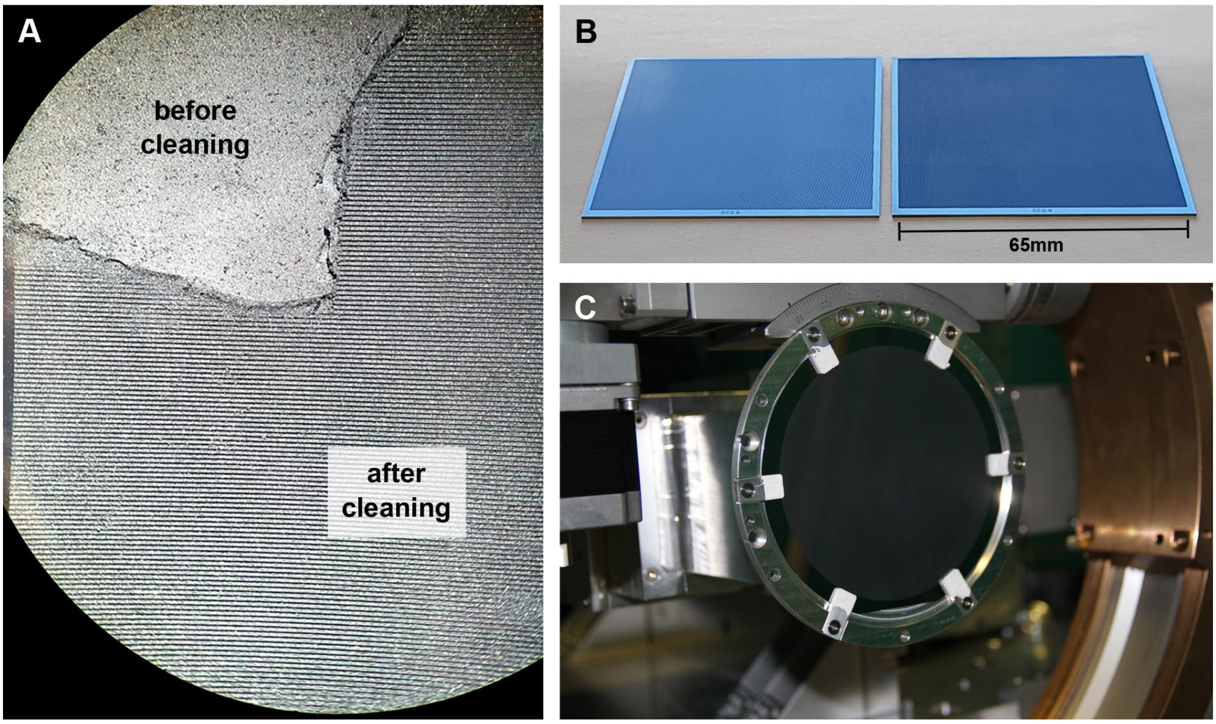

Figure 4.8: (A) Microscopy image of a filled source grating showing the difference between the particle-covered and the cleared surface. (B) Photograph of two source gratings after particle deposition and surface clearance. (C) Photograph of the analyzer grating mounted in the frame of the nGI instrument. Figure adapted from [Gustschin, 2018].

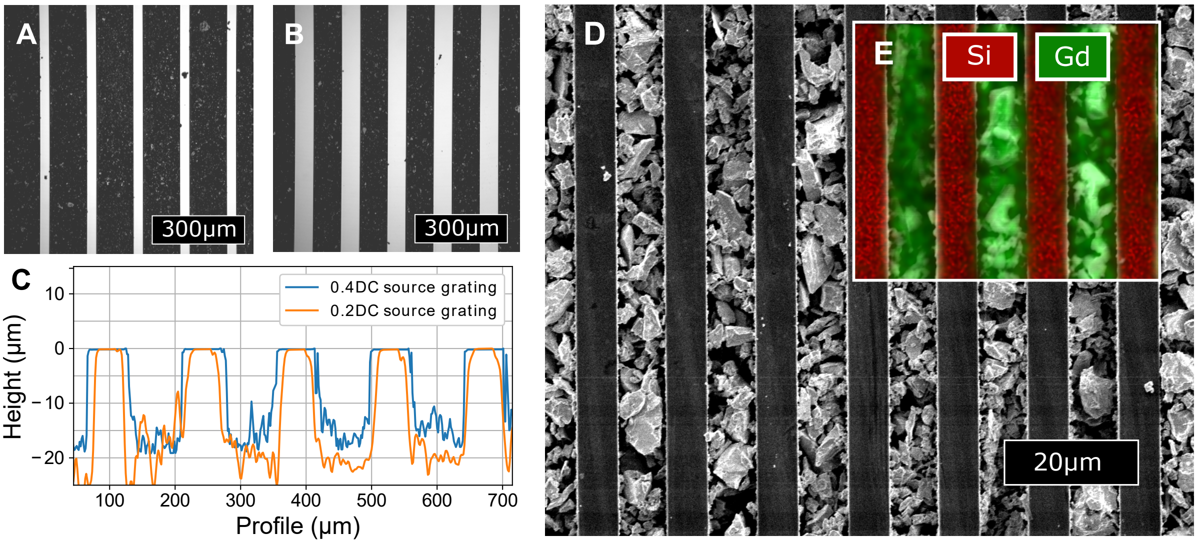

Figure 4.9: Microscopy images of the source grating surface with 0.2 (A) and 0.4 duty cycle (B). (C) Profiles of the grating surface acquired by confocal microscopy showing the filling level of the gratings after mechanical particle removal. (D) SEM image of the grating surface of the analyzer grating with 13.3 µm period and (E) EDX mapping showing the distribution of silicon and gadolinium. Figure adapted from [Gustschin, 2018].

level of the particles. For the gratings with 150 µm period about 15-20 µm of the filling seems to be removed during doctor blading. Compared to a total depth of 180 µm this does not compromise the absorbing performance significantly.

Scanning Electron Microscopy (SEM)

To visualize the shape and micromorphology of the filled particles, a higher resolution than optical microscopy is needed. Some small grating pieces were prepared and scanned with a JEOL JSM-6060LV (JEOL, Freising, Germany) microscope, which also enabled energy-dispersive X-ray fluorescence (EDX) analysis providing spatially resolved elemental maps of the sample surface. Figure 4.9 D shows an SEM micrograph of the grating sample with 13.3 µm period and an EDX map in E. The particles have rough and irregular shapes in a wide size range from 1-7 µm. The filling appears decent on the surface, however, this is not expectable for the whole depth of the grating. The irregular shapes reduce their mobility in the narrow trenches and prevent them from rearranging themselves in a higher packing density. The silicon grating lines are intact and mostly particle free showing that removal of the residual layer by doctor blading is well feasible for smaller periods.

Micro-Computed Tomography (µCT)

As mentioned in the previous sections, optical and electron microscopy techniques are limited to the sample surface. A more comprehensive analysis yielding the inner 3D structure of small grating pieces can be performed by X-ray µCT. For that, the compounds of the sample have to create sufficient absorption contrast with X-rays and the structures of interest (e.g. single particles, grating lines) should be resolved. The FOV is typically limited to several hundreds of µm and the sample should be prepared to fit into it under all angles in the ideal case. That requires breaking the grating samples into small pieces. Otherwise, the X-ray transmission will drop at low angles to the grating substrate, and beam starvation artifacts will deteriorate the scan. For the development and evaluation of the deposition process via µCT grating pieces with 45 µm period were most suitable. A ZEISS Xradia 510 Versa µCT system was employed.

Figure 4.10 shows a 3D rendering of a µCT grating scan with selected slices to illustrate the extensive capabilities of tomographic imaging for the deposition process development. The particle sizes and shapes as well as a rough measure of the particle filling density is directly accessible at all depth levels. A comparison between the top and the bottom layer shows a higher abundance of voids in the particle filling with increasing depth. Voids are also well recognizable in the profile view as well as in the in-trench view. Such µCT data is invaluable for the detailed analysis of the particle micromorphology in process development. It would allow a thorough study of the particle shapes and sizes or binder concentration and their influence on the filling density. However, it is limited to extremely small sample sizes, is destructive, and requires lots of experimental effort and data analysis. Therefore, another fast and simple method to probe the grating quality is presented in the next paragraph.

Wavelength-dependent Neutron Transmission

To probe an entire grating substrate and yield spatially resolved filling properties conventional neutron radiography is a very suitable method. Assuming a constant grating duty cycle the grating transmission signal consists of two parts. The first part is directly transmitting radiation with negligible attenuation by the grating substrate. In the ideal case, it is the transparent fraction of the grating area and is equal to the duty cycle. The second part is the radiation transmitting the opaque grating area due to non-ideal particle filling. Using this simplified model, a wavelength-dependent transmission curve T_λ can be calculated, which depends on the duty cycle DC and average effective thickness t of the particle filling inside the grating trenches:

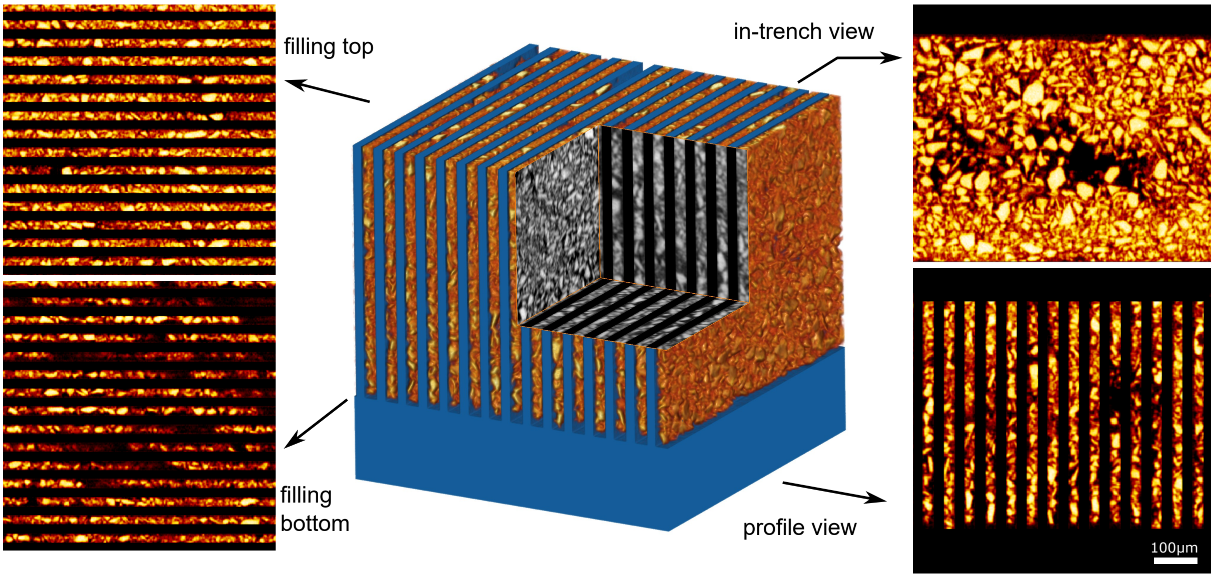

Figure 4.10: 3D data acquired by µCT of a grating piece (45 µm period) filled with Gd particles enables an in-depth insight into the filling of the silicon template. Different slices allow comparing the filling at the top and the bottom. An in-trench view reveals voids of the filling and a profile view allows to investigate the orientation and shape of the particles in the periphery of the trench wall.

$$T(\lambda) = DC + (1 - DC) \cdot e^{-\Sigma_{att}(\lambda)t}, \tag{4.2}$$

where $\Sigma_{att}(\lambda)$ is the wavelength-depended attenuation cross section. To yield a realistic estimate of t, the average Gd thickness transmitted in the filled matrix of the grating, neutron radiographs of the grating area were acquired in the suitable wavelength range. The transmission values were averaged over the active grating area and fitted to the model. The measurements of all 6 gratings listed in Table 4.2 were performed at the FRM II/ ANTARES beam line. The radiation was filtered with a neutron velocity selector providing a wavelength resolution $\Delta\lambda/\lambda$ of 20% (10%) in the range of 1.6-3 Å(3-6 Å). The detector consisted of a 100 µm thick LiF/ZnS scintillator optically coupled to an Andor iKon-L CCD camera. To ensure that the gratings were aligned perpendicular to the beam a short rocking scan was performed. After that several transmission images and flat fields were taken with an exposure time of 10 s at every wavelength in the range of 1.6-6 Å. The acquired images were corrected for gamma spots, dark current, and flat fields, and averaged $T(\lambda)$ values were extracted from the entire grating area. Figure 4.12 shows two radiographs of both analyzer gratings with 13.3 µm period acquired at 2 Å. Some inhomogeneities are recognizable, however, more than 99% of the grating area

Grating Number	Period (µm)	Duty cycle (design/actual)	Depth (µm)	Active Area (mm)	Transmission at 2 Å (%)
1 (G_2)	13.3	0.45 / 0.43	80 ± 5	110 diameter	46.8 ± 1.4
2 (G_2)	13.3	0.45 / 0.44	80 ± 5	110 diameter	47.9 ± 1.5
3 (G_0)	150	0.5 / 0.48	185 ± 13	65 × 65	48.0 ± 0.5
4 (G_0)	150	0.4 / 0.38	185 ± 10	65 × 65	38.1 ± 0.4
5 (G_0)	150	0.3 / 0.28	182 ± 17	65 × 65	28.5 ± 0.3
6 (G_0)	150	0.2 / 0.18	180 ± 13	65 × 65	18.5 ± 0.3

Table 4.2: Overview of the six fabricated neutron absorption gratings with design parameters and absorption performance.

does not deviate more than 5% from the mean transmittance. Figures 4.11 A and B show simulated and measured $T(\lambda)$ values with their standard deviations as error bars for the source and the analyzer gratings. Additionally, a comparison to previously used gratings is shown respectively to quantify the improvement. The source gratings with the different duty cycles show close to ideal performance while the previously used G_0 (18 µm Gd) features a light increase of transmission towards shorter wavelengths. The most significant improvement compared to the previous system is reached with the analyzer gratings. Figure 4.11 B shows simulated $T(\lambda)$ curves (dotted) of binary grating profiles with different Gd heights as well as the measured values. Both newly fabricated gratings show characteristic transmission behavior of binary absorption profiles with 16−17 µm Gd with slightly different duty cycles. This corresponds to filling densities of ≈20%.

4.2.4 Visibility Evaluation in a Neutron Grating Interferometer

A final demonstration of the grating performance is the visibility of the interference pattern created by the nGI, as it is directly related to the SNR in the DPC and DFI images. The gratings were conceptualized for a new nGI design with slightly reduced asymmetry compared to the previous system [Reimann, 2016] to relax the fabrication requirements of the G_2 period from 4 µm to 13.3 µm. The new setup can be operated in 3rd fractional Talbot distance at 4 Å or close to the 1st fractional Talbot distance in the sub-2 Å range with the same source and analyzer gratings. Only the phase grating needs to be exchanged. Table 4.3 gives further technical details on the interferometer geometry. The principles of

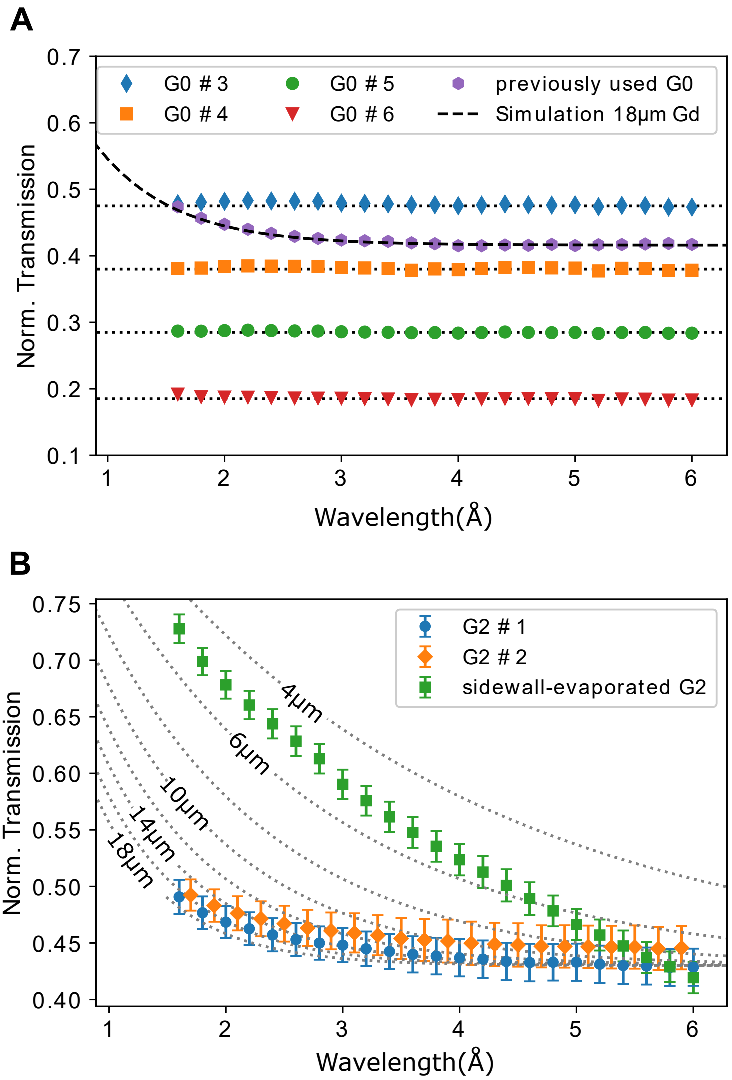

Figure 4.11: (A) Wavelength-dependent neutron transmission of the different source gratings averaged over the active area. The dotted lines indicated the theoretically expected transmission of ideally absorbing gratings based on the respective duty cycles observed from microscopy. The dashed line indicates the theoretically calculated transmission values for the previously used source grating with a Gd height of 18 µm. (B) Wavelength-dependent neutron transmission of both analyzer gratings and the previously used side-wall evaporated G_2 grating. The dotted lines indicate theoretically calculated transmission curves with respective Gd absorbing heights created by binary absorption profiles. The error bars show the standard deviation of the values on the active area. Figure adapted from [Gustschin, 2018].

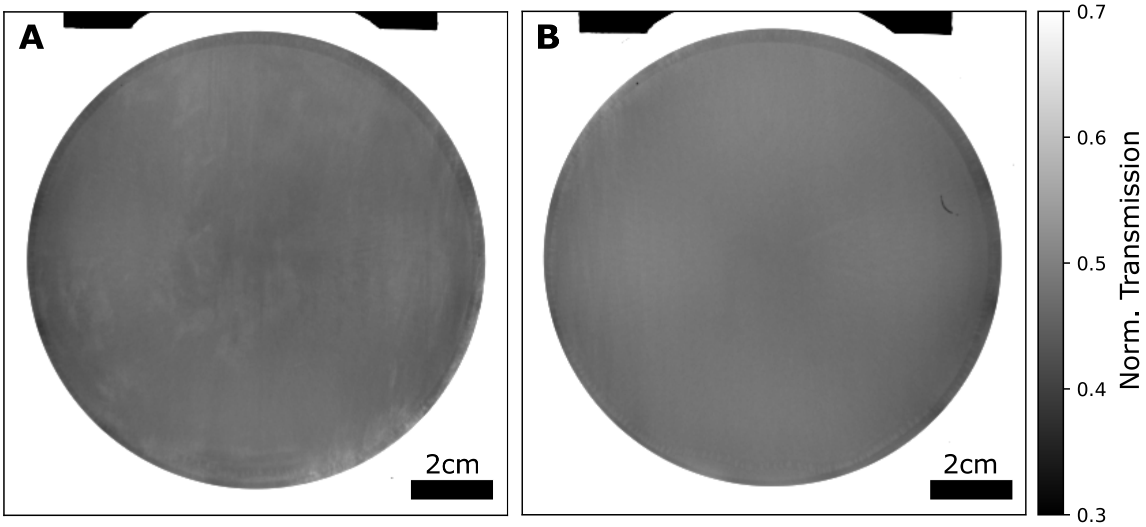

Figure 4.12: Radiographs of analyzer gratings #1 (A) and #2 (B) with 13.3 µm period at 2 Å show an overall good deposition homogeneity on the active area with a diameter of 110 mm. Figure adapted from [Gustschin, 2018].

system design as well as its optical simulation and experimental evaluation are elaborated in detail in [Neuwirth, 2020].

After the nGI was set up and adjusted to high interference fringe contrast the wavelength-dependent visibility was measured. The collimator ratio (sample distance/pinhole diameter) was 250. At every wavelength, a phase stepping scan with 10 steps over one period of G_1 was performed. At every phase step 3 frames with an exposure time of 10 s were acquired. The images were corrected with the standard procedure described in the previous section and processed with an expectation maximization (EM) algorithm, which accounts for small experimental deficiencies in the stepping positions.

The scans were performed with two silicon phase gratings (41 µm and 123 µm height) optimized for different neutron wavelengths as previously discussed. Figure 4.13 A shows a plot of the simulated and measured, wavelength-dependent visibility for both configurations of the new nGI design. Compared to the previous nGI a visibility increase by a factor of 3.5 is achieved at 4 Å and an additional configuration enables multimodal imaging of stronger absorbing samples in the thermal neutron range. A more detailed nGI evaluation of different source gratings fabricated in the framework of this project as well as the simulation and further system properties are given in [Neuwirth, 2020].

Parameter:	**Value**
Design wavelength:	$\approx 4\,\text{Å}$ / $\approx 1.6\,\text{Å}$
G_0-G_1 distance L:	6.89m
G_1-G_2 distance d:	60.9m
G_0 period:	150 µm
G_0 duty cycle:	0.28
G_0 height:	180 µm Gd particle filling
G_1 period:	24.4 µm
G_1 duty cycle:	π-shift: 0.49 / 3π-shift: 0.55
G_1 height:	π-shift: 41 µm / 3π-shift: 123 µm
G_2 period:	13.3 µm
G_2 duty cycle:	0.45
G_2 height:	85 µm Gd particle filling
Peak visibility at 4 Å:	0.69
Peak visibility at 1.6 Å:	0.54

Table 4.3: Geometry and design parameters of the nGI for the visibility evaluation. Note that the 3π-shift G_1 can operate as π-shift G_1 at $\approx 1.6\,\text{Å}$.

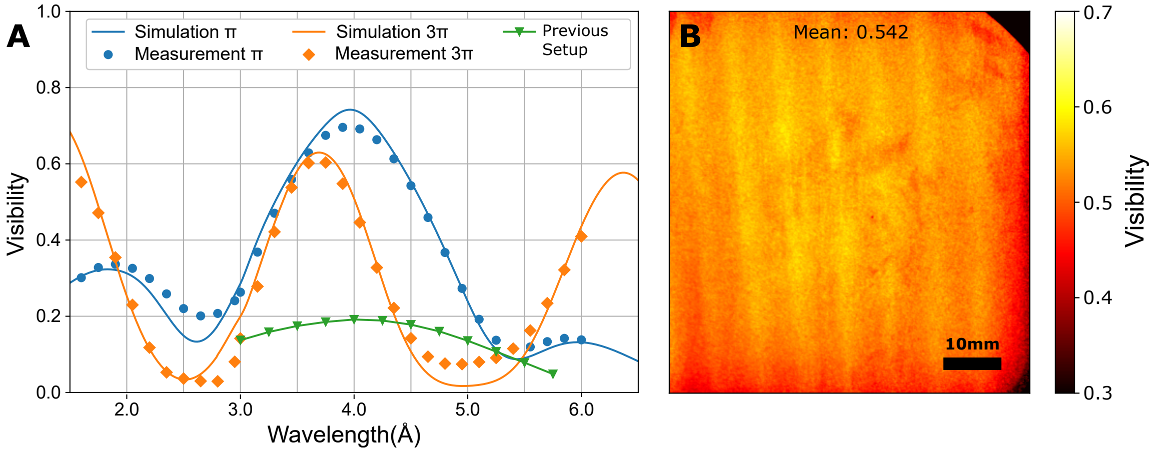

Figure 4.13: (A) Simulation and measurement of wavelength-dependent visibility with two different phase gratings (π-shift and 3π-shift) compared to the previous setup. (B) Visibility map of the 3π setup at 1.6 Å. The FOV is limited by the used detector.

4.2.5 Summary and Outlook

A fast and simple method for the fabrication of Gd particle-based absorption gratings for nGI has been developed successfully. It allows pushing the limit of current neutron-based Talbot-Lau systems in image quality, penetrative power, measurement time, and field of view. The fabricated gratings have (A) a quasi-binary absorption profile, (B) a high Gd filling level making them suitable for imaging with thermal neutrons, (C) a relatively small period, and (D) good homogeneity on a large area. The combination of all these properties has not been achieved yet with other methods like side-wall evaporation of Gd [Samoto, 2019; Grünzweig, 2008b] or metallic glass imprint [Yashiro, 2016].

The Gd particle deposition technique demonstrated in the present work reaches a filling density of ≈20% at a period of 13.3 µm and a grating trench depth of 85 µm. Presumably, this can be further increased by different particle shapes and sizes. For even smaller periods a costly but effective way would be to replace the Gd with natural isotopic abundance with isotopically enriched ^{157}Gd. Due to its higher neutron absorption cross section, it would require effective heights of less than 5 µm for excellent performance. The grating size can be increased with the presented method as well since UV lithography and DRIE technology is commercially available for up to 300 mm wafers.

The nGI at ANTARES was upgraded to a much more versatile instrument with the new gratings. It achieves peak visibilities of 0.74 at 4 Å which is an increase by a factor of 3.5 compared to the previous system [Neuwirth, 2020]. Additionally, the thermal neutron configuration is available at high visibility and neutron flux. The range of correlation lengths that can be probed increased with this both configurations by a factor of 30 and covers about two orders of magnitude [Neuwirth, 2020]. Together with a large FOV ($71\times76\,\mathrm{mm}^2$), high neutron flux of FRMII, and many sample environments, it remains the most efficient and powerful nGI instrument for multi-modal neutron imaging. An application of its imaging capabilities is given in Chapter 5 together with a comparison with the respective X-ray technique.

5

Comparison of Thermal Neutron and Hard X-ray Dark-Field CT

In this chapter, grating-based multimodal imaging is applied with thermal neutrons and hard X-rays to investigate a strongly absorbing sample. As previously discussed in Chapter 2, neutrons and X-rays have different interaction mechanisms with matter and can be therefore used to acquire complementary information. Using the principles of computed tomography, a spatial correlation between nuclear and electron density-related properties of the scanned object can be retrieved. Respective instruments scanning with X-rays and neutrons simultaneously have already been implemented at several facilities such as the Institut Laue-Langevin (ILL) in Grenoble, France [Tengattini, 2020], the Paul Scherrer Institute (PSI) in Villingen, Switzerland [Kaestner, 2017] and the National Institute of Standards and Technology (NIST), Gaithersburg, USA [Lamanna, 2017]. This method was found useful in various research domains such as cultural heritage objects [Mannes, 2015], building materials [Roubin, 2019], geosciences [Zambrano, 2019], fuel cells [Peng, 2020] or batteries [Ziesche, 2020].

With the development of phase-sensitive imaging techniques for neutrons and X-rays, more types of sample interaction have become accessible. X-ray [Momose, 2003; Pfeiffer, 2006b; Pfeiffer, 2008] and neutron grating interferometry [Pfeiffer, 2006a; Strobl, 2008] became convenient tools to access refractive and dispersive properties of samples with manageable experimental effort. Neutron dark-field imaging found some unique applications like probing magnetic properties [Grünzweig, 2008a; Manke, 2010], vortex lattice domain structures in superconductors [Reimann, 2015] and various micro-porous materials. X-ray dark-field imaging was found to be particularly useful for imaging of micro-structured biological tissue like the lung [Willer, 2021]. Furthermore, many other applications in material science and non-destructive testing have been explored.

In this chapter, multi-modal thermal neutron and hard X-ray CT have been applied to a quartz geode containing strongly absorbing and scattering structures. This sample is used to compare and discuss application cases focusing on the dark-field modality and exploiting the complementarity of X-ray and neutron radiation. The results have been published in [Gustschin, 2020].

5.1 Methods

As elaborated in Chapter 2.3.4 the dark-field image is generated by detecting a visibility loss compared to the reference modulation due to small-angle scattering. This method reaches its limit with strongly absorbing objects since the phase and scattering signals become difficult to retrieve with strong beam starvation. Further, such interferometers have energy-dependent visibility since they use phase optics that are adapted for a certain specific wavelength. This leads to artifacts in the DPC and the DFI signal [Chabior, 2011; Yashiro, 2015] when polychromatic radiation sources are used. It is well known that especially the DFI signal is affected by a disproportional amplitude reduction caused by absorbing objects [Yashiro, 2015]. Several correction approaches were suggested in the literature [Chabior, 2011; Yashiro, 2015; Pelzer, 2016], however, they reach unsatisfactory results at short exposure times with limited statistics. It remains a challenge to detect scattering structures especially when they are surrounded by highly absorbing material. One possible way is to use more penetrating radiation like neutrons. In the following two grating interferometer setups using neutrons and X-rays will be presented. After that, image processing and a quantitative evaluation of the acquired data will be discussed.

5.1.1 Neutron Grating Interferometer Setup

As already elaborated in the previous chapter the neutron grating interferometer at ANTARES/FRM II has an asymmetric Talbot-Lau design as shown in Figure 5.1 A. The sample is placed closer to the detector 55.8 cm downstream from G_1 to avoid geometrical blur by the source size which is determined by the pinhole. The interferometer design used for the measurements is identical to the configuration previously discussed in Section 4.2.4. The inter-grating distances as well as the periods are given in Table 4.3. The tomography scan was acquired with neutrons of 1.6 Å wavelength provided by a neutron velocity selector with $\Delta\lambda/\lambda$=20%. The pinhole diameter was 35.6 mm.

The detection system was an Andor Neo CMOS camera equipped with an optical system focusing on a 100 µm LiF/ZnS scintillation screen. The effective pixel size in the reconstruction was 66 µm after 2×2 binning of the original image. At every phase step, 3 frames with 5 s exposure time each were recorded. In total 8 phase steps were recorded for every tomography projection and 360 angles were collected over 180° sample rotation. To avoid potential problems with grating drifts a flat field scan was performed every 20 projections after moving out the sample. The flat-field visibility was ≈ 0.56.

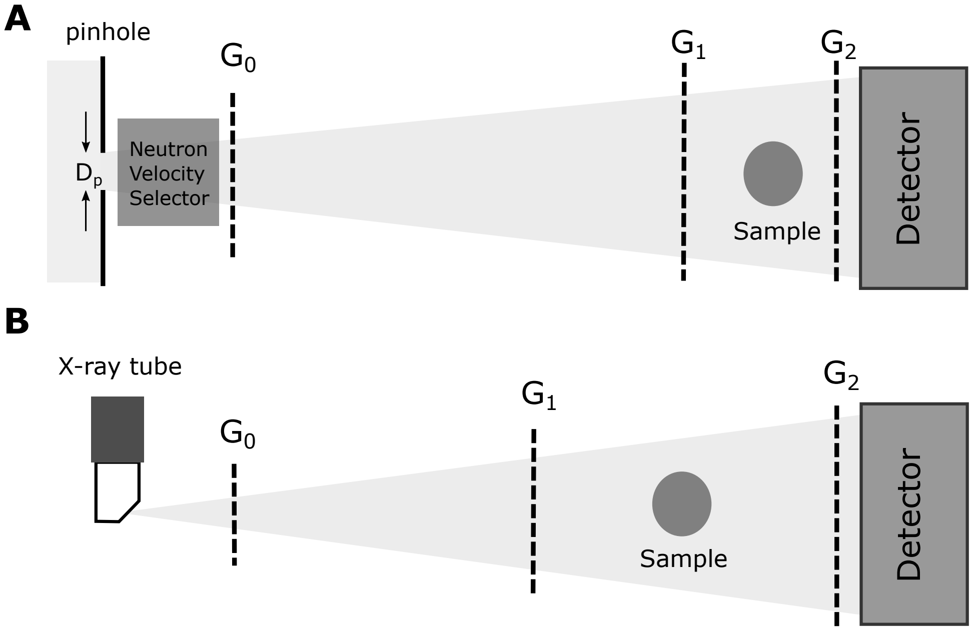

Figure 5.1: Schematic illustration (not to scale) of the neutron grating interferometer geometry (A) compared to the symmetric X-ray grating interferometer (B) used for this work. Figure adapted from [Gustschin, 2020].

5.1.2 X-ray Interferometer Setup

The multimodal X-ray CT scans were performed in a laboratory-based Talbot-Lau interferometer designed for dark-field imaging with hard X-rays. The X-ray microfocus tube (XWT-160-CT, X-rayWorX, Garbsen, Germany) was operated at 70 kV tube voltage with an additional 4 mm aluminum filtering. The setup employs a symmetric grating configuration as illustrated in Figure 5.1 B. The period of all three gratings was 10 µm. The absorption gratings (G_0 and G_2) were LIGA-fabricated with a gold height of >170 µm while the phase grating (G_1) was a silicon-etched grating with a binary profile with 60 µm height designed to introduce a π-shift at around 47 kV. Current Talbot-Lau systems are limited to this energy range due to limitations in grating fabrication. For higher energies, the absorption gratings become more transparent and the visibility decreases rapidly. Despite a significant gain in absorption beyond the K-edge (80.7 kV for Au) the phase and dark-field signals become weaker at those energies requiring even smaller grating periods for reasonable sensitivity. The $G_0 - G_1$ and $G_1 - G_2$ distances were both 90 cm and the sample was placed about 64 cm from G_1. This placement of the sample is not particularly favorable for the sensitivity and does not allow a strong geometric magnification, but had to be chosen due to the limitation of the field of view by the G_2 grating ($70{\times}55\,\mathrm{mm}^2$).

The detector was a Varex XRD 4343CT with a pixel size of 150 µm which resulted in an effective voxel size of 118 µm in the reconstructed volume. Every phase scan consisted of 11 phase steps with 2 s exposure each and 361 projections were acquired for tomography. The mean visibility was ≈ 0.24 over the entire field of view (FOV).

In addition to the multimodal data acquired with the X-ray grating interferometer, the sample was scanned with a µCT system (GE phoenix vtomex S) with a high resolution at 130 kV and 0.6 mm copper filtration. The effective pixel size of the µCT scan was 70 µm and the exposure time per frame was 6 s. In total 1601 projections were collected over a full sample rotation (360°).

5.1.3 Data Processing

For the scan with the neutron grating interferometer, some specific pre-processing was required before the tomographic reconstruction. First, dark current frames were subtracted from all acquired images and defective pixels were interpolated by a median filter with a kernel size of 3. To remove bright spots created by gamma-ray interaction typical for scintillator-based detectors an adapted algorithm was applied that merges the information obtained from a total of 3 frames at every projection and grating position. First, a median-filtered image array with a kernel size of 9×9 pixels was calculated and subtracted from the original image. This allowed calculating a binary mask with a manually selected threshold which highlights those artificial spots. Then, the 3 original images were averaged with respective mask weighting which allowed the exclusion of the affected pixels. Compared to a conventional median average of the 3 frames this procedure yields better filtering in pixels that are affected by the artifact in 2 or 3 frames and can therefore handle a higher density of gamma spots and preserve nearly all features and edges. Since the PSF of the detectors and the geometrical blur due to the pinhole were limiting the resolution significantly more than the pixel size, all frames were binned by a factor of 2 in both directions. The processing of the interferometric data was performed by an expectation-maximization algorithm estimating and optimizing the grating positions iteratively [Wang, 2004]. This is necessary as the stepping position tends to be not exactly equidistant due to experimental deficiencies connected to linear translation stages. Finally, the attenuation, differential phase-contrast, and dark-field images were retrieved with the processed flat fields. Figure 5.2 shows a photograph as well as the three image modalities in one projection.

The X-ray frames were processed with the conventional scheme after the dark current correction. To correct for X-ray flux fluctuation the frames were normalized using a

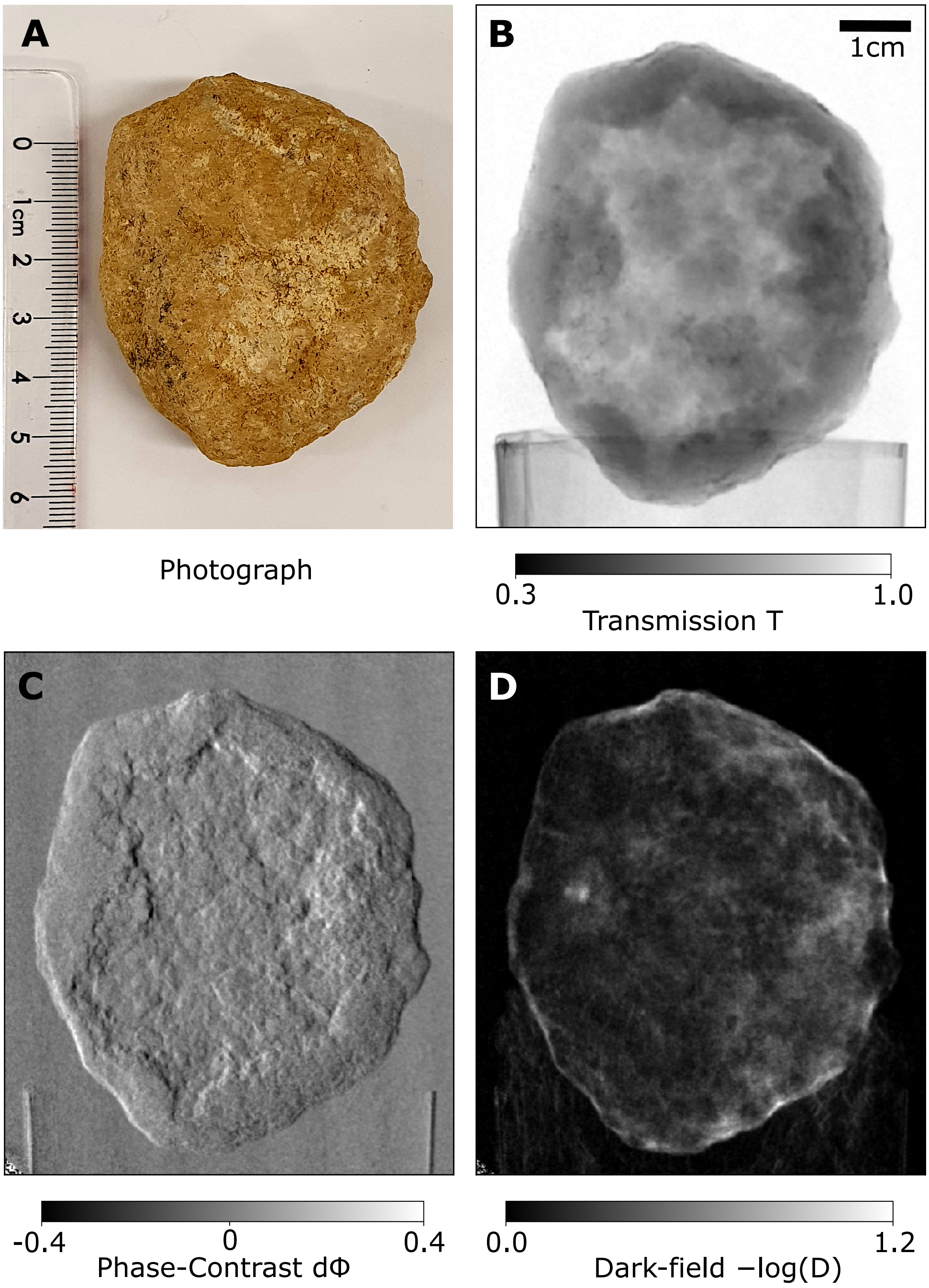

Figure 5.2: A photograph of the quartz geode (A) and a neutron projection in the three channels attenuation (B), differential phase-contrast (C), and dark-field image (D) acquired at 1.6 Å wavelength. Figure adapted from [Gustschin, 2020].

sample-free background area. Figure 5.4 shows a comparison of the attention and the dark-field image for both X-rays and neutrons. The histogram in Figure 5.4 E and the scatter plot in F show the distribution of attenuation and dark-field related visibility loss $D = V/V_0$ extracted from 500 random pixels from respective projections. Note that the entire sample is not shown due to the limited FOV of the X-ray interferometer. For the tomographic reconstruction, a filtered back-projection (FBP) of the logarithmized attenuation and dark-field signals were performed using a Ram-Lak filter. An additional center shift correction and rind artifact removal was performed using X-Aid FDK Reconstruction Suits 2020.10.2 (Mitos GmbH, Garching, Germany). As the last step, the reconstructed 3D volumes were digitally registered to each other using the software Avizo Fire 8.1.0.

Figure 5.4 A shows a 3D rendering of the quartz geode with an incision to illustrate the inter cavity covered with silica crystals and depict the different planes in the reconstructed volume. Selected horizontal (B-E) and vertical (F-I) slices of the tomographic reconstruction depicting distinct features are shown for the four image domains respectively. Additionally, Figures 5.5 (A-D) show some slices from the xy-plane featuring some interesting structures suitable for signal comparison in the four discussed modalities. For a quantitative estimation of the contrast-to-noise ratio (CNR) suitable ROIs were chosen inside (ROI_A) and outside the sample (ROI_B) depicted in Figure 5.5 for X-ray dark-field (C) and neutron dark-field (D) respectively. The scattering feature marked by blue and orange lines serves as signal S_S used for the CNR calculation according to:

$$CNR = \frac{S_S - S_B}{\sigma_B}, \tag{5.1}$$

Where S_B is the background signal and σ_B is the standard deviation in ROI_B. The respective values are given in Table 5.1.

5.2 Results and Discussion

Figures 5.3 A-B clearly show a higher transmission signal in the neutron setup. The histogram of the pixel grey values in C reveals even, that the neutron transmission values are about a factor of 2 higher than the respective X-ray transmission values. This is in line with expectations, as the sample is mostly consisting of silicon oxide crystals which are easily penetrated by neutrons compared to X-rays. Hence spectral effects like beam hardening and respective artifacts in the X-ray dark-field reconstruction are to be expected in the X-ray data.

As recognizable from Figures 5.3 C and D similar structures are present in the dark-field

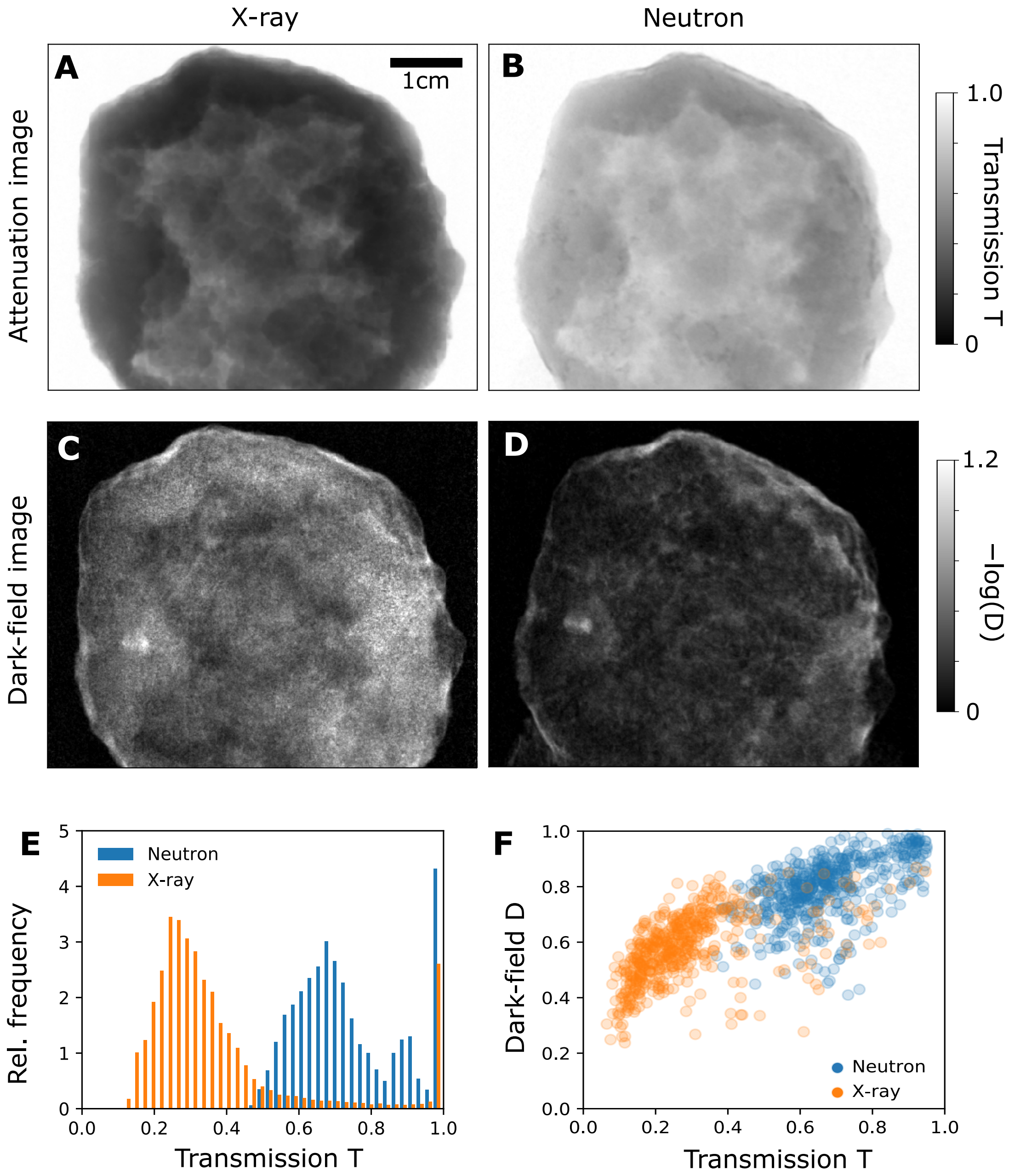

Figure 5.3: Comparison of one angular projection of the sample in all 4 image channels. X-ray attenuation image (A) at 70 kVp, neutron attenuation image (B) at 1.6Å, and histogram of the grey values of both images (E). X-ray dark-field image (C), neutron dark-field image (D), and a scatter plot (F) showing the ratio of attenuation and the dark-field related visibility loss of 500 random pixels from all projections. Figure adapted from [Gustschin, 2020].

Signal	**Background $\mathbf{ROI_B}$**	**Absorber $\mathbf{ROI_A}$**	**Signal S_S**	**CNR**
X-ray DFI	-0.0016 ± 0.0471	0.2338 ± 0.1016	0.96	7.1
Neutron DFI	-0.0005 ± 0.0176	0.0072 ± 0.0228	0.39	16.8

Table 5.1: Comparison of X-ray and neutron DFI signals and CNRs of a scattering feature shown in Figures 5.5 C and D.

image of both domains. However, the noise in the X-ray dark-field image is much stronger due to the absorptive properties of the sample. It is worth noting that an outline of the absorbing structure is also visible in the X-ray DFI (C) caused by the discussed beam hardening effect. As the scatter plot in 5.3 F shows the visibility loss correlated with respective transmission values is much smaller in the neutron DFI case. With a higher penetration power neutrons also offers a wider dynamic range for the DFI signal with samples that are strongly absorbing X-rays.

Further differences between X-ray and neutron DFI appear in the tomographic reconstruction. The most obvious difference is the higher absolute gray values in the X-ray attenuation reconstruction (Figure 5.4 D, G) compared to the respective neutron domain (B, F). Note also that the neutron attenuation slices are leveled much narrower than the X-ray CT slices as indicated by the color bars in Figures 5.4 F and G. Some strongly absorbing features appear in the neutron data (arrows in B and F) which are not recognizable in the X-ray attenuation domain. In the slices of Figure 5.5 A and B the opposite appears for some grains (see arrows in B) that are visible with X-rays but do not appear in the neutron attenuation CT. Some of the highly attenuating material located on the surface of the quartz geode (see arrow in Figure 5.4 B) was pealed off and subjected to X-ray fluorescence analysis. Additional to silicon (Si) as the most abundant material some significant amounts of calcium (Ca) and chlorine (Cl) were detected. Further, traces of sulfur (S), phosphorus (P), potassium (K), and iron (Fe) were confirmed by fluorescent K_α-radiation. The bright attenuating structures visible in the neutron domain are probably minerals of Ca and Cl as they absorb neutrons much stronger than Si. In the case of X-ray attenuation, the expected contrast is much smaller. The bright absorbing grains in the X-ray domain might be some minerals containing Fe, as some traces of it were found in X-ray fluorescence. As this example shows additional elements or compounds can be detected by combining both X-ray and neutron attenuation CT.

A comparison of the dark-field CT data shows further advantages that arise from the high

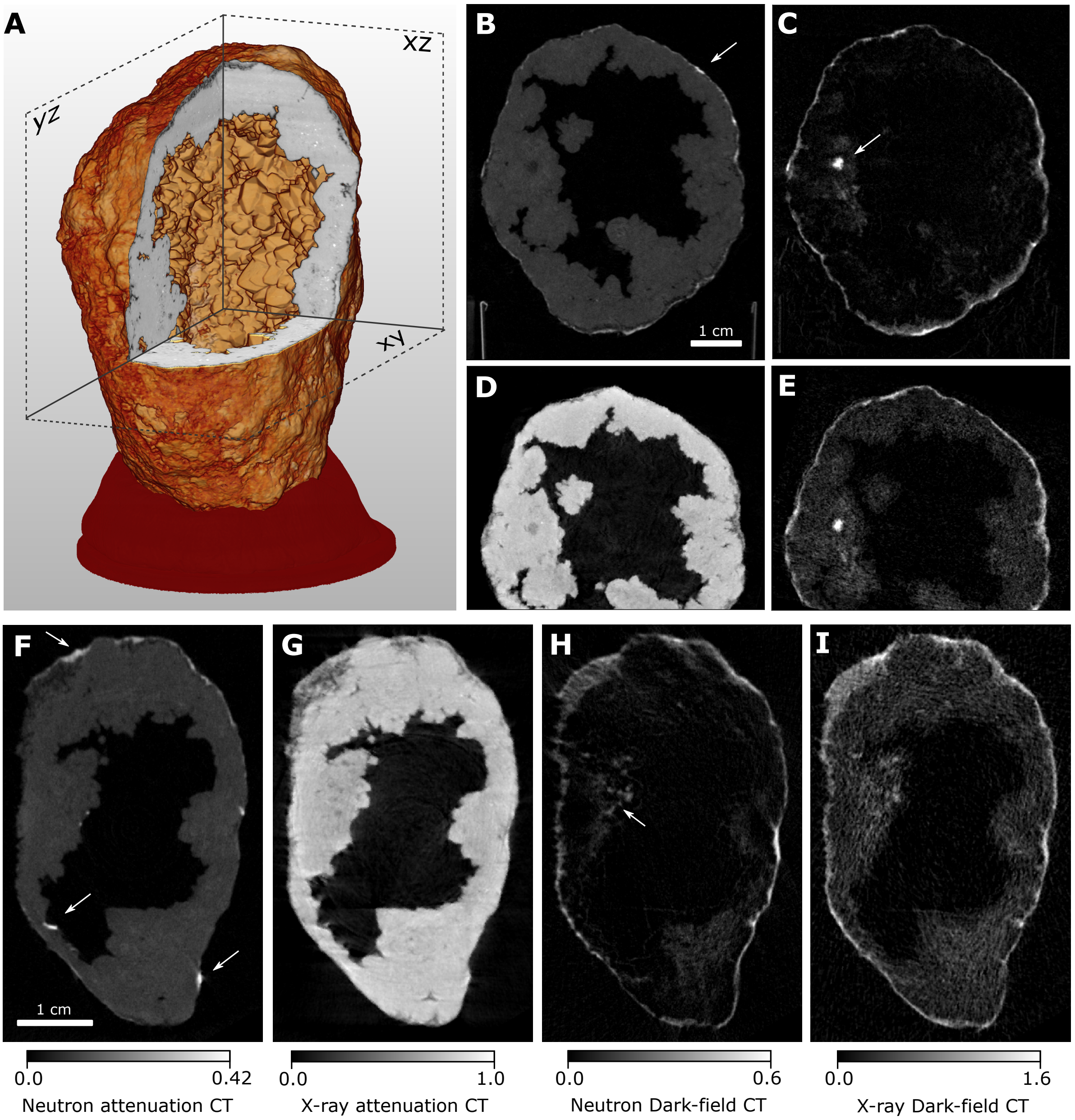

Figure 5.4: (A) Rendering of the X-ray µCT reconstruction with an incision to illustrate the hollow inner structure of the quartz geode. Slices from the filtered back-projection (FBP) (B-E) in the yz-plane showing the neutron attenuation (B), neutron dark-field (C), X-ray attenuation (D) and X-ray dark-field (E) channels. Slices (F–I) in the xy-plane depicting the neutron attenuation (F), X-ray attenuation (G), neutron dark-field (H), and X-ray dark-field (I) channels. The color bars in (F–I) apply to the respective slices in (B–E) as well, and the upper boundaries correspond to maximal values of the FBP found in the respective slices. Figure adapted from [Gustschin, 2020].

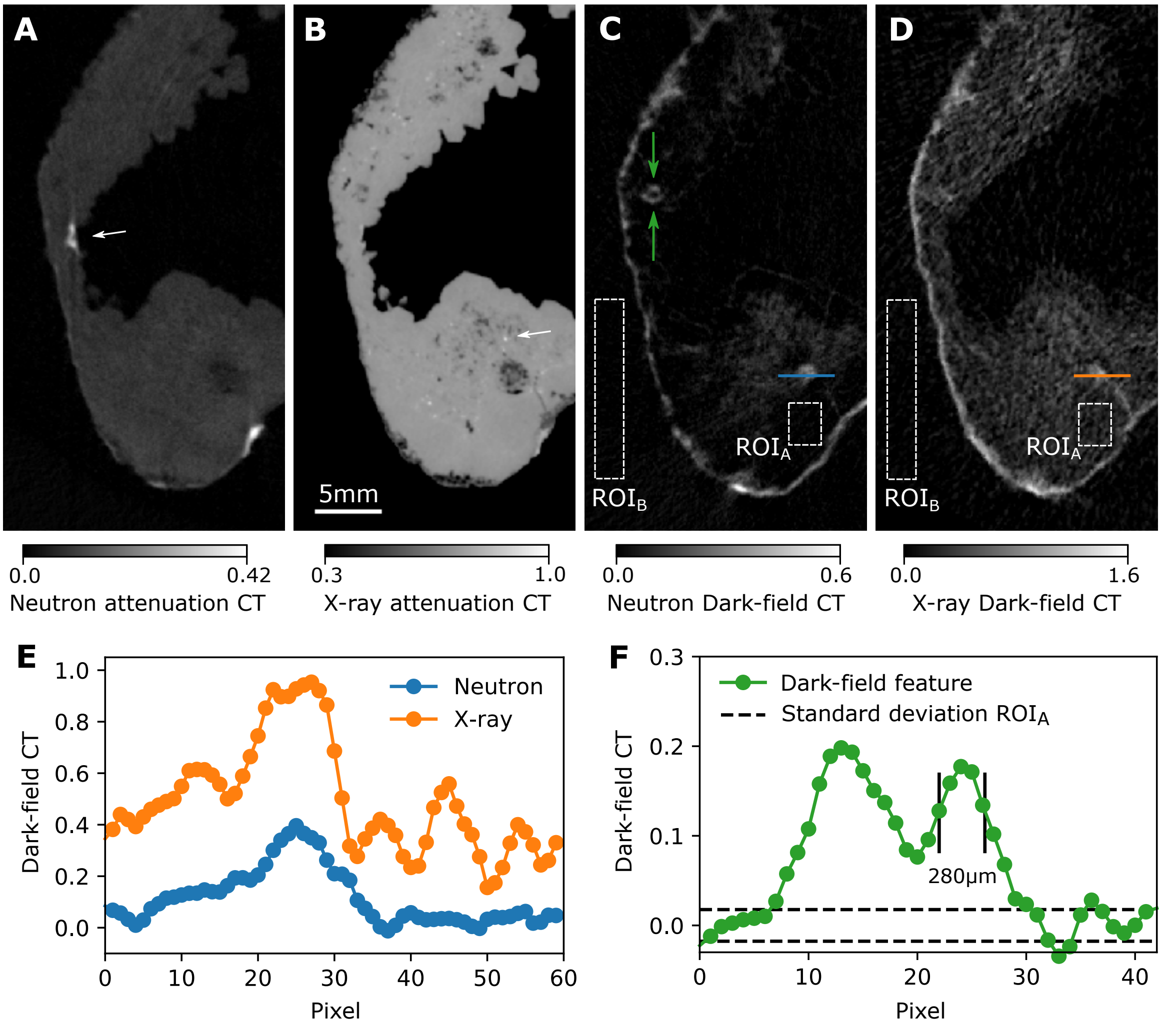

Figure 5.5: Slices in the xy-plane from the neutron attenuation volume (A), X-ray micro-CT (B), neutron DFI (C), and X-ray DFI (D). A line plot (see lines in (C,D)) through a scattering feature that is used for CNR calculation is shown in (E). Another line plot (F) of the structure marked by green arrows in (C) plotted compared to the noise level (upper and lower boundaries of the standard deviation of ROI_A). Figure adapted from [Gustschin, 2020].

penetration power of neutrons. While the absorbing fraction of the sample is overlaid with some low-frequency noise in the X-ray DFI (Figures 5.4 E,I) the respective neutron slices (C,H) hardly show this effect. Therefore, some small scattering structures (arrow in H) can be resolved while in the respective X-ray image, they cannot be distinguished from the noise. In Figure 5.5 B the slice in the xy-plane reveals porous structures depicted by the arrow which create a signal in the neutron DFI (C) around the big scattering feature. At the same position, the artificial X-ray DFI signal is too strong to distinguish any structures. A distinct scattering feature marked by two green arrows in C is not visible in the X-ray DFI domain at all. This could be an indication of some chemical compound involving elements with strong nuclear small-angle scattering cross section but no electron density modulation characteristic for X-ray DFI signal. Structures that were visible in X-ray DFI but not in the neutron DFI could not be clearly identified since the grainy noise could be easily mistaken for real scattering features in the X-ray DFI slices.

To evaluate the reduction of the CNR due to the absorption-induced artificial DFI signal some quantitative analysis is performed. ROIs inside of absorbing material (ROI_A) and outside the sample (ROI_B) show a strong increase of the DFI with X-rays while only a slight change is visible in the case of neutrons as the values in Table 5.1 suggest. Even the strongly absorbing feature (arrow in Figure 5.5 A) does not create any artificial signal in the respective neutron DFI slice C. A line plot of the most apparent scattering structure (see blue and orange lines in C and D) is given in E and was used as a signal for CNR estimation. Despite the X-ray signal being more than two times stronger compared to neutron DFI, it fades in the surrounding noise and its CNR is more than 2 times lower than in neutron DFI. Figure 5.5 F shows a line plot of the small scattering feature (280 µm) depicted by the green arrows in C. It is well resolved with a CNR of 7.5 in the DFI modality. The nGI CT scan is limited in resolution by the number of projections that could be recorded during 13 h of measurement time. In the case of the X-ray scan, the resolution was limited by the PSF of the flat panel detector. A stronger geometrical magnification would be possible, however, would require stitching due to the limited FOV of the grating interferometer.

5.3 Conclusion and Outlook

With the newly fabricated particle-based absorption gratings multimodal neutron imaging by Talbot-Lau interferometry has been successfully extended to the thermal neutron regime. At wavelengths in the sub-2 Å range, larger and stronger absorbing samples can be scanned reasonably. The nGI setup at ANTARES offers high visibility, neutron flux, and a relatively large FOV compared to other similar instruments. Neutron DFI imaging was also successfully combined with CT reaching a resolution of about 300 µm. The present study is the first to acquire an attenuation and dark-field CT with thermal neutrons and hard X-rays on the same sample. As the application example shows, the dark-field signal is difficult to access when the scattering structures are small and embedded in strongly absorbing materials. As seen in the X-ray CT the artificial background signal related to beam hardening introduces a low-frequency noise that interferes with real scattering structures of interest. For many materials, the higher penetration power of neutrons and their quasi-monochromatic filtration by neutron velocity selectors offers invaluable benefits with nGI.

6

2D Talbot-Array Illuminators for Multimodal X-ray Imaging

So far the focus of this work was the fabrication of absorption gratings for multimodal imaging enabled by Talbot-Lau interferometers. Beyond that, several other techniques for phase-contrast and dark-field imaging were developed in recent years. Most of them use coherent radiation and rely on detectors that can directly resolve the refractive or dispersive interactions of X-rays with the sample. Propagation-based methods do not require any X-ray optics and use advanced algorithms that retrieve the phase image based on certain assumptions about the sample [Davis, 1995; Paganin, 2002]. Despite their high popularity and experimental simplicity, they have limitations in terms of acquiring quantitative data. Aperture-based [Olivo, 2007; Morgan, 2011], speckle-based [Bérujon, 2012; Morgan, 2012; Zanette, 2014], some grating-based [Morimoto, 2015; Zanette, 2010] and other methods [Kagias, 2019; Dos Santos Rolo, 2018; Reich, 2018; Zakharova, 2018] use some kind of diffractive or absorptive beam modulator optics that create defined intensity patterns after propagation in space. A sample in the beam path alters this intensity modulation by attenuation, refraction, and scattering. Using certain processing algorithms enables retrieval of these interactions and yields multimodal images similar to Talbot-Lau interferometry.

This chapter covers the work published in [Gustschin, 2021]. First, the most important design aspect for creating such modulators will be discussed. The advantages and drawbacks of excising modulators in terms of efficiency and complexity in fabrication will be reviewed. Considering those aspects, an optimized 2D phase optic referred to as Talbot array illuminator (TAI) will be simulated and fabricated. Some of the TAIs will be evaluated for their diffractive properties at a synchrotron source and compared with a random modulator typically used in speckle-based imaging. A special linear phase stepping scheme will be proposed to achieve bi-modal sensitivity and increase the resolution. Finally, the modulator will be applied for projectional imaging and tomography with an unstained murine artery. The resolution and sensitivity of the method will be determined and put in context with other recent work.

6.1 Requirements and Design Aspects

Imaging with intensity modulator optics can be done in single shot mode or with a stepped or scanned modulator which increases the resolution and sensitivity [Zdora, 2018]. In both cases, the modulation should have high contrast and be clearly resolvable by the detector. Otherwise, it becomes difficult to retrieve the displacement of the diffraction pattern by the sample relative to the reference pattern. Furthermore, the density of the high-contrast features created by the modulator should be as high as possible [Zhou, 2016]. In the case of stepping the aim is to make every single pixel of the detector undergo an intensity modulation in both directions.

In speckle-based imaging (SBI) a random pattern (e.g. sandpaper) creates a grainy speckle pattern after propagation in space. The random arrangement of the grains has two main disadvantages. Firstly, it is not adapted to generate an optimal contrast through diffraction or refraction effects like in the case of refractive lens arrays, phase gratings, or other diffractive elements. Hence, the visibility and the density of highly modulated features are relatively low. Secondly, due to the random nature of this spatial modulation, it is not possible to choose an efficient sampling or stepping scheme to modulate every pixel optimally.

To avoid these disadvantages it should be possible to choose a design and fabrication method where the shape of the resulting pattern can be controlled arbitrarily. For example, one could create an absorption mask (sometimes called Hartman mask) with a regular arrangement of holes that are transparent to X-rays. Given that the thickness of the absorbing layer is sufficient and the period of the holes is in the micrometer range this can create a high contrast modulation pattern suitable for that task. In fact, the LIGA method discussed in the previous chapters is one possibility to create such absorptive elements. Several methods using such absorptive optics have been demonstrated [Zakharova, 2019; Rix, 2019; Morgan, 2011]. However, they are limited in flux efficiency since a considerable fraction of radiation is absorbed. Therefore, a remarkable effort has been put into the development of other periodic diffractive optical elements (DOF) for various imaging applications. Reich et al. created an array of stacked compound refractive lenses with a period of 65 µm [Reich, 2018]. A 3D direct-laser written Shack-Hartmann array with 20 × 20 micro-lenslets and a period of 50 µm has been demonstrated in [Dos Santos Rolo, 2018]. Circular phase arrays for omnidirectional dark-field imaging with a unit cell period of 80 µm were fabricated in [Kagias, 2019]. Mamyrbayev et al. developed a two-dimensional compound refractive lens (CRL) array with a period of 55 µm for sub-pixel resolution scanning transmission microscopy [Mamyrbayev, 2020].

As these recent examples show, the periods of those focusing arrays are still in the range of several tens of micrometers. Current X-ray detectors optimized for high-resolution applications are CCD or CMOS cameras equipped with magnifying optics that focus on thin scintillator screens and reach a resolution of 1-2 µm. Hence it would be beneficial to reduce the periods of such modulators increasing the density of high-contrast features. At the same time, the period should not be chosen too close to the resolution limit of the detector, since the created pattern will be blurred losing visibility. In summary, the task of creating the most efficient modulator consists of finding an optimal trade-off between the smallest possible period and the highest pattern contrast achievable with the PSF of the used detector. In our case, the periods of interest are in the range of 5-10 µm.

Other — rather technical – aspects of the design and fabrication of the optic are the phase-shifting material, its resistance to high doses of radiation, and the complexity of the fabrication methods involved. As the optic should attenuate as little as possible at the same time, thin wafers of silicon as substrate are the first choice. Besides that, silicon is very resistant to radiation, unlike other organic materials that have been used for e.g. CRL [Dos Santos Rolo, 2018]. It is also easily processable with common semiconductor fabrication equipment and various anisotropic etching methods are available to create arbitrary binary profiles. It remains to find a suitable 2D pattern that can create a high contrast at a reasonable propagation distance.

6.2 Simulation and Fabrication of 2D Phase Arrays

The formation of diffractive intensity patterns from periodic structures has already been mentioned in Section 2.3.2 discussing the Talbot effect. The appearance of the modulation is explained by Fresnel propagation and can even be predicted from basic analytical calculations at certain fractions of the Talbot distance $d_T = 2p^2/\lambda$, where p is the period of the array and λ is the wavelength of the radiation [Arrizón, 1994; Suleski, 1997; Szwaykowski, 1993]. Such modulators are called Talbot Array Illuminators since they create periodic illuminated lines or spots based on the Talbot Effect. [Suleski, 1997] derives and lists several grating profiles which create binary intensity modulations and concludes that the theoretically highest achievable binary modulation with a binary (two height levels) 1D phase array has a compression ratio of 1:3, which means that the entire radiation is focused onto lines of $1/3p$ width. Note that a high compression ratio results in high visibility and is therefore favorable for the task discussed here. The contrast of the modulation will be further reduced by the detector blur which is usually mathematically described by a convolution of the pattern with the PSF of the detector. To compare different designs of such phase arrays a numerical implementation of the Fresnel-Kirchhoff diffraction formula was employed:

$$\Phi(x, y, z) = \exp(ikz)F^{-1}\left[F(\Phi_0)\exp\left(-i\frac{k_x^2 + k_y^2}{2k}z\right)\right]. \tag{6.1}$$

Here $\vec{k}$ is the wave vector, $k = |\vec{k}|$ its modulus, F denotes the Fourier transform (F^{-1} is the inverse) and $\Phi_0 = \Phi(x, y, z = 0)$ is the coherent wavefront created by the grating at $z = 0$. The phase Φ at a given propagation distance is not directly accessible, but the resulting intensity $I = \left|\Phi(x, y, z)\right|^2$ is measurable by the detector and is denoted as *Fresnel image* following the terminology from [Winthrop, 1965]. Cross-sections of I plotted along the propagation direction are denoted as Talbot carpets. The calculations were performed with a virtual pixel size of 100 nm and arrays of 20 × 20 periods. The phase modulators were assumed as pure phase objects as the attenuation difference of several µm silicon due to its spatial height modulation can be neglected at the energies used in this work. To obtain realistic Fresnel images that can be compared with the measured data the simulated intensity arrays have been convolved with a Gaussian kernel of $\sigma = 0.7\,\mu\text{m}$ which models the PSF-related detector blur.

Most works that use 2D phase gratings (e.g. [Morgan, 2013; Sato, 2011; Itoh, 2011; Morimoto, 2015]) employ symmetric duty cycles ($DC = 0.5$), that also create Fresnel images with symmetric intensity patterns. However, it is known from visible light literature [Suleski, 1997] that a stronger compression of intensity can be achieved with binary phase arrays when a suitable phase shift is chosen. This is illustrated in Figures 6.1 A and B where calculated Talbot carpets of 1D linear phase gratings are compared. The grating with a symmetric duty cycle (A) and $\varphi = \pi/2$ shows a binary modulation at $d_T/4$ with a compression ratio of 1:2. Yet, the grating with $DC = 1/3$ and $\varphi = 2\pi/3$ produces a stronger focusing with a compression ratio of 1:3 at an even shorter propagation distance ($d_T = 1/6d_T$). Other similar asymmetric combinations of duty cycle and phase shift can create the same effect at other propagation distances [Suleski, 1997]. This focusing principle can be directly transferred to the second dimension and reach compression ratios of 1:9 as 2D propagation simulations show. Figures 6.1 C and D show the 2D analoga of the previously discussed linear grating patterns. The 2D modulators show higher intensity values (A-D have the same color map) since they provide an overall stronger focusing. Particularly, the 2D TAI with $DC = 1/3$ (Figure 6.1 D) shows a significantly higher intensity than its symmetric counterpart (C). In that case, even stronger modulation (depicted by arrows) before and after the binary modulation at $d_T/6$ are observable.

To estimate the visibility gain from replacing the conventional arrays with the asymmetric ones a plot of the visibility with propagation distance is shown in Figure 6.1 E. The visibility has been calculated by:

$$V = \frac{I_{\max} - I_{\min}}{I_{\max} + I_{\min}}, \tag{6.2}$$

where I_{max} and I_{min} were the maximum and minimum intensity pixel values in a window size similar to the period. Before applying formula 6.2, the Fresnel images have been convolved with a Gaussian 2D kernel to account for a typical PSF of common high-resolution detectors. The plot proposes similar visibilities for 1D and 2D gratings, however, there is a remarkable difference between the modulators with symmetric and asymmetric duty cycles. The asymmetric 2D TAI reaches about 40% higher visibility than its symmetric counterpart at respective peak performance.

It is worth mentioning that even stronger compression ratios can be achieved with two-level phase arrays having duty cycles smaller than 1/3. The created intensity pattern will not be exactly binary as in the case of the discussed examples, but the most intensity will be still focused on narrow points, which serves the purpose [Arrizón, 1994]. Besides that, there are also more complex modulators with e.g. more than two height levels, sub-periodic features [Szwaykowski, 1993], or other non-binary (e.g. triangular, trapezoidal, or sinusoidal) DOEs that can also create stronger focusing than conventional binary phase gratings. However, their fabrication on the sub-10 µm period scale is significantly more complicated since they require various etch depths unlike the TAIs proposed in this work. Furthermore, there is limited benefit in focusing on much smaller spots than the PSF of the detector, since the foci will be smeared by the latter limiting the visibility.

Based on these conclusions, periods of 5.0 µm, 6.8 µm, 10.0 µm, and 13.6 µm were chosen. For 10 keV, 15 keV, and 20 keV and a phase shift of $\approx 2/3\pi$ the etching depth was 8.5 µm, 12.8 µm, and 17.1 µm respectively. The TAIs were fabricated by 5microns GmbH (Illmenau, Germany) via UV lithography and deep reactive ion etching on a 250 µm thin silicon wafer according to the specifications above. Multiple arrays of $10 \times 10\,\mathrm{mm}^2$ could be placed on the same wafer (see Figure 6.2 A) and the three different etch depths for respective energies were realized on different wafers. Table A.2 in Appendix gives an overview of the different TAIs including the design energy and heights as well as their deviations based on measurements derived from SEM images. Figure 6.2 A shows a wafer with the different arrays and B shows a microscopy image of the 10 µm array. Several SEM cross sections of the arrays which were etched on the same wafer are illustrated in Figures 6.2 C, D, and E.

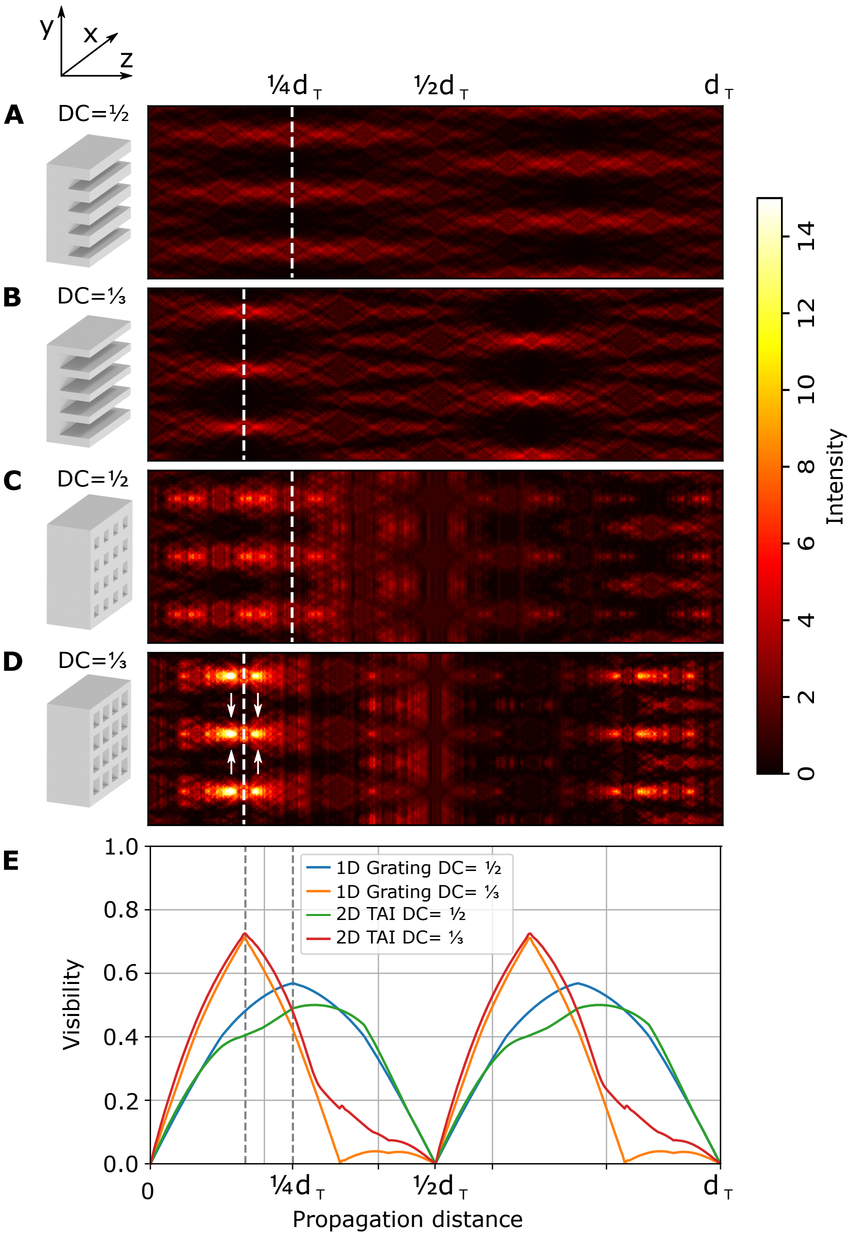

Figure 6.1: Talbot carpets simulated for (A) 1D linear grating with a symmetric duty cycle (DC) and phase shift $\varphi = \pi/2$, (B) 1D linear grating with $DC = 1/3$ and $\varphi = 2\pi/3$, (C) 2D TAI with $DC = 1/2$ and $\varphi = \pi/2$, (D) 2D TAI with $DC = 1/3$ and $\varphi = 2\pi/3$. Note that the color bar for the intensity applies to all four carpets and the intensity is normalized to 1 in the grating plane. (E) Visibility with increasing propagation distance for the gratings (A-D). The dashed lines denote the first binary intensity modulations. Note that in case of the 2D TAIs (C) and (D) the intensity modulation at $3d_T/4$ and $2d_T/3$ is not visible as it is shifted by half period out of the plotted plane in the x-direction. Figure adapted from [Gustschin, 2021].

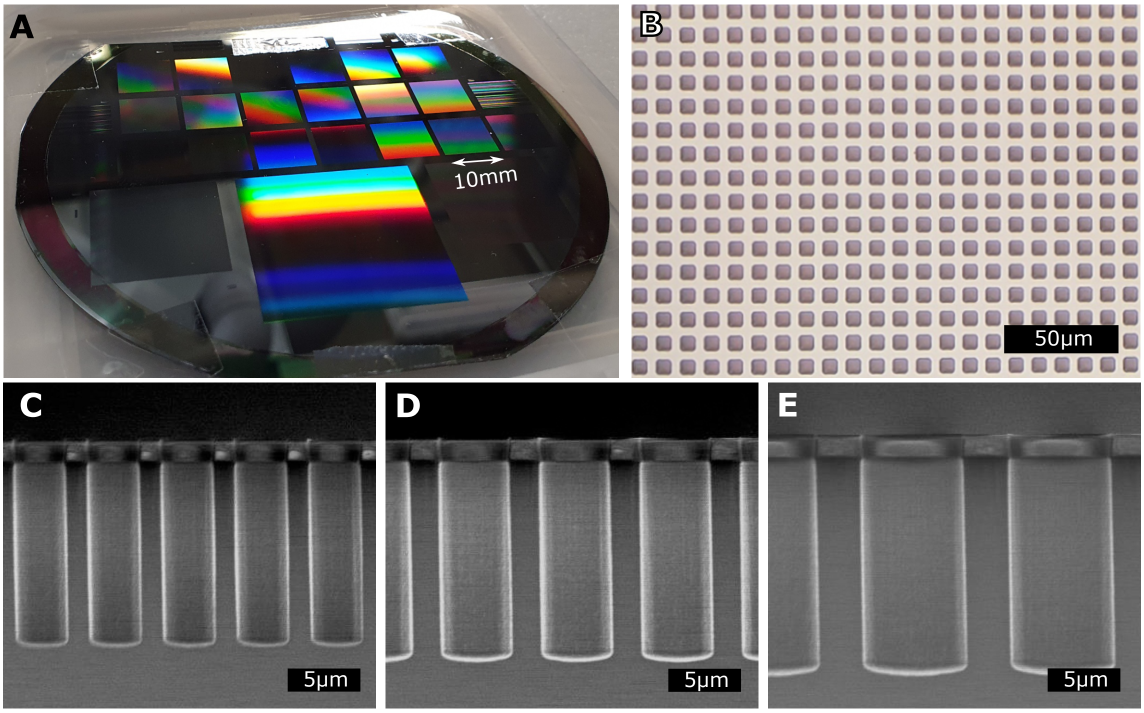

Figure 6.2: (A) Multiple Talbot Array Illuminators (TAIs) with different periods etched on a 100 mm silicon wafer. (B) Light microscopy image of the 10 μm array. (C-E) SEM profile micrographs of the 5 μm array (C), 6.8 μm array (D), and 10 μm array (E) etched simultaneously on the same wafer. Images (C-E) were kindly provided by 5microns GmbH (Illmenau, Germany). Figure adapted from [Gustschin, 2021].

6.3 Evaluation of TAIs at a Synchrotron Source

6.3.1 Measurement of Talbot-Carpets

To evaluate the performance of the fabricated modulators and confirm the simulations some Talbot carpet scans were performed at the P05 imaging beamline at PETRA III at DESY. The source with the dimensions of $36{\times}6\,\mu\mathrm{m}^2$ is generated in an undulator 86 m before the setup. A double crystal monochromator provided a narrow energy bandwidth of $\Delta E/E = 10^{-4}$ of the resulting beam. The imaging detector consists of a 50 µm thick lutetium-aluminum garnet (LuAG) scintillator optically coupled (10× magnification) to a CMOSIS CMV20000 chip yielding an effective pixel size of 0.64 µm. Images were taken every 5 mm from 40 mm to 540 mm downstream from the TAI. The exposure time per frame was 200 ms. Additionally, a sandpaper piece (P1000 graining) generating a speckle pattern was measured under the same protocol for comparison. The visibilities calculated for every distance were calculated according to equation 6.2 and typical FWHMs of the foci in x- and y-direction generated by the TAIs are listed in Table 6.1. As seen in the data the difference in the horizontal and vertical source size does not affect the visibility and resolution at the discussed propagation distances. The predicted effect of sub-periodic focusing with a higher compression ratio is clearly observed for all TAIs. In Figures 6.3 A and B, some simulated and measured Fresnel images at different propagation distances acquired with the 6.8 µm TAI at 15 keV are shown. The agreement with simulation is well recognizable despite the lower contrast of the measured pattern due to the detector PSF.

6.3.2 Visibility-Distance Evaluation

Figure 6.4 A shows the visibility increase with propagation distance for different TAI periods measured at 15 keV beam energy. As expected from the simulations, the phase arrays induce strongly modulated patterns near the fractional Talbot distances. The 5 µm TAI generates the first visibility peak in the vicinity of 100 mm and the second around 400 mm, which correspond to $d_T/6$ and $2/3d_T$. For high-sensitivity measurements, the 5 µm TAI can be used at a propagation distance of e.g. 420 mm with over 30% visibility. Due to its smaller period, the 5 µm TAI enables a finer sampling compared to e.g. the 6.8 µm TAI, which has comparable visibility at that propagation distance. It is worth mentioning that the highest visibility does not necessarily have to be at the exact fractional Talbot distances since even stronger focusing is occurring before and after them as seen in the respective Talbot-Carpet simulations. The 10 µm TAI achieves the highest visibility

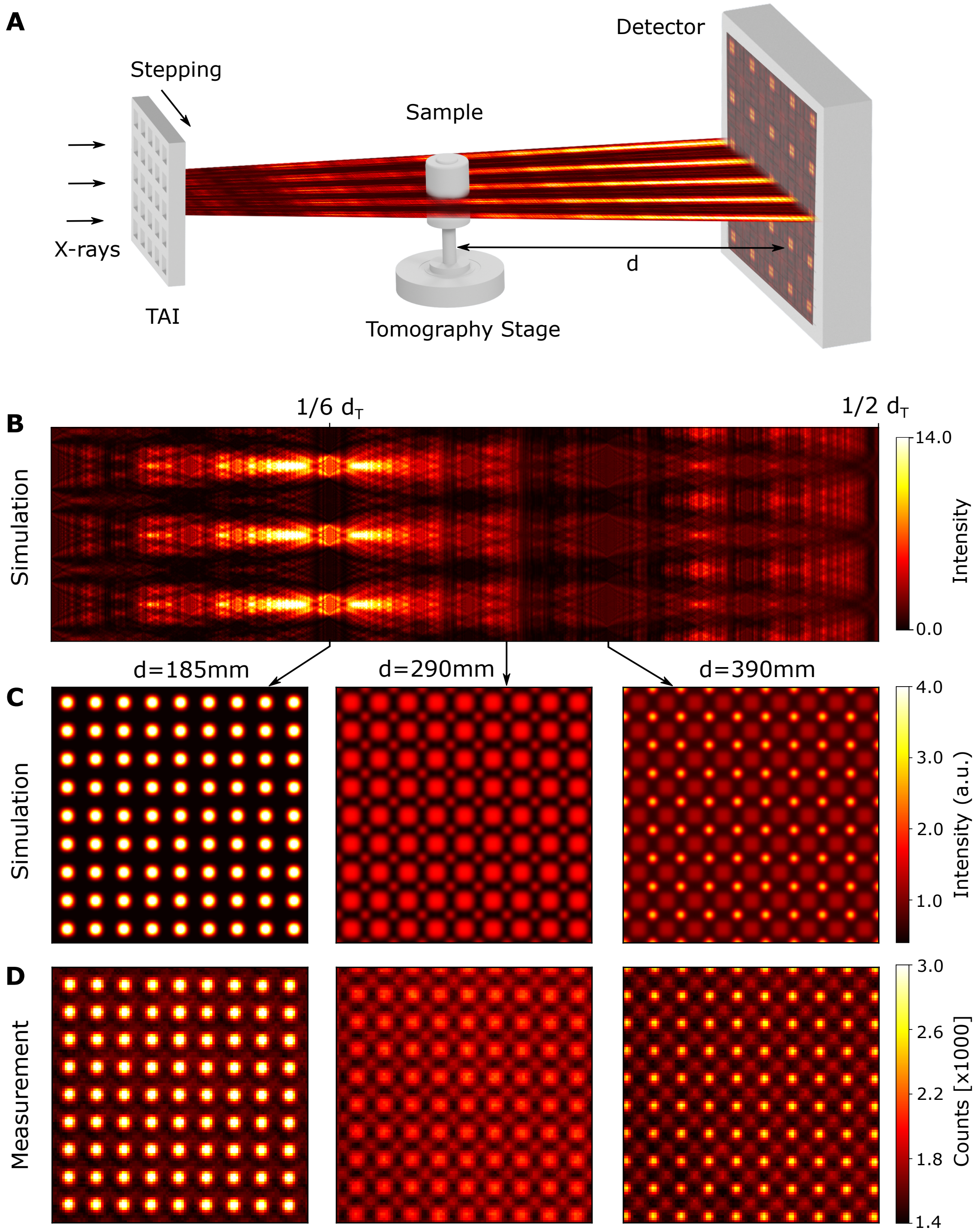

Figure 6.3: (A) General setup of the imaging system illustrating the formation of the intensity modulation. (B) Simulation of the Talbot carpet for the 6.8 µm TAI at 15 keV and (B) some Fresnel images at selected propagation distances after a convolution considering the detector PSF. (C) Acquired Fresnel images at the same propagation distances as in (B) agree well with the simulated data. Figure adapted from [Gustschin, 2021].

of 0.54 at 380 mm which is close to the $d_T/6$ modulation. In comparison to the TAIs, the speckle visibility of the P1000 diffuser increases slowly with propagation distance and stays still below the 10 µm TAI, although the average speckle size is significantly larger than the foci created by the 10 µm TAI. Thus, the influence of the PSF on the speckle pattern should be much smaller. Nevertheless, the TAI produces a pattern with more contrast and a higher modulation density.

One could argue that the speckle visibility might become higher at longer propagation distances beyond 540 mm. But with longer propagation several other effects increase which reduces the contrast. The limited beam coherence starts to degrade the contrast at about 1000 mm propagation distance. Furthermore, the modulation density of the speckle pattern changes. This degrades the efficiency of the modulator for sampling in a phase stepping scheme as further discussed in Appendix A.4. This limitation is even more severe when laboratory sources with larger focal spots and divergent beams are used. With longer propagation distances, the insanity drops by the inverse-square law, and the source-related geometrical blur of the generated pattern decreases. Thus, the TAIs show strong advantages for creating high contrast modulations at short propagation distances with precisely controllable periods.

6.3.3 1D Phase Stepping Scheme for Bi-directional Sensitivity

As previously discussed the spatial resolution of such a scan can be increased by the acquisition of multiple frames with a stepped modulator [Zdora, 2018]. Ideally, every pixel should be modulated with high contrast in both directions. The foci created by the modulator can be understood as sampling points that are distributed over the detector matrix. One could perform a 2D stepping with e.g. 4×4 steps in one unit cell of the grating structure yielding a total of $N = 16$ steps. The sampling is in that case 1/4 of the TAI period. For random phase modulators that are used in e.g. SBI, a bi-directional sensitivity can be also achieved with linear 1D stepping, as the random speckle pattern contains intensity gradients in all directions [Zdora, 2018]. That reduces complexity, as only one linear stage is sufficient for stepping. In this work, a stepping scheme for the TAI is introduced which also copes with one linear stepping direction and allows different numbers of steps N with regular sampling. Its principle is illustrated in Figure 6.5 A and B. The points on a rectangular grid that have the same color represent the foci generated by the modulator. Different colors represent different stepping positions of the same modulator. The stepping direction and range illustrated by the dashed vector are chosen such that it is a linear combination of several unit cell vectors of the periodic grid. When

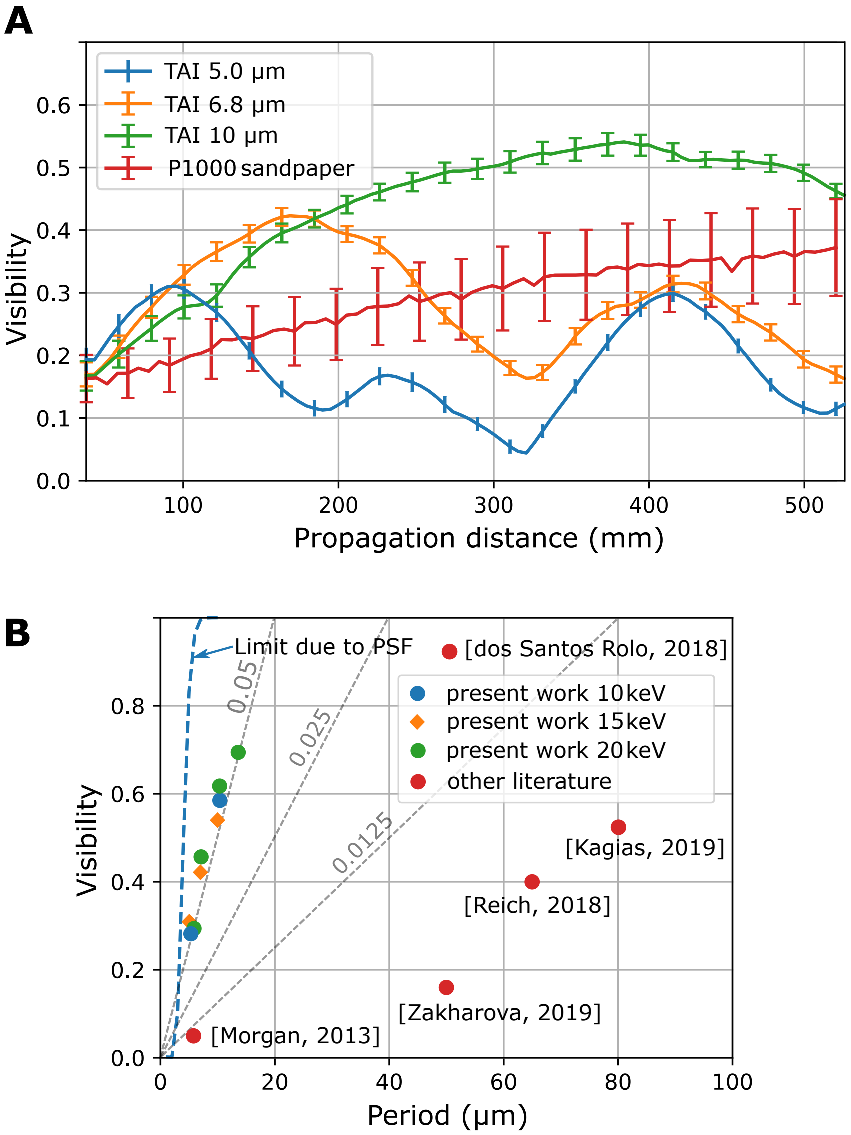

Figure 6.4: (A) Distance-dependent visibility and its standard deviation (error bars) for the different TAIs and the P1000 diffuser extracted from the Talbot carpet scans at 15 keV. (B) Comparison of the evaluated TAIs in terms of visibility and period with recent literature and the achievable limit due to the detector PSF. The dashed grey lines depict visibility-to-period ratios. Figure adapted from [Gustschin, 2021].

Modulator	Energy[keV]	Analysis window [px]	FWHM Foci [µm]	Max. Visibility
TAI 5-10	10	8	1.9	0.27
TAI 10-10	10	16	4.2	0.58
TAI 5-15	15	8	2.0	0.31
TAI 6-15	15	12	2.5	0.42
TAI 10-15	15	16	3.5	0.54
P 1000	15	18	6.9*	0.36
TAI 5-20	20	8	2.4	0.29
TAI 6-20	20	12	2.8	0.45
TAI 10-20	20	16	3.9	0.61
TAI 13-20	20	22	5.3	0.68

Table 6.1: Experimental parameters for the evaluated phase modulators. *For the P1000 diffuser the average speckle size is given instead of the FWHM focus size.

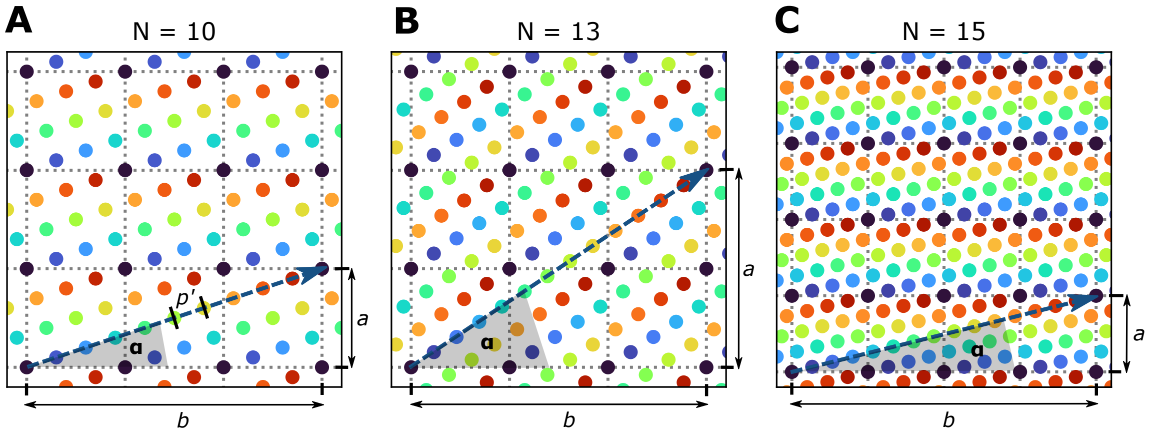

Figure 6.5: Illustration of different 1D stepping schemes to achieve bi-directional phase sensitivity. Dots of the same color represent the periodic foci generated by the TAIs in a square lattice. Different colors illustrate the subsequent stepping positions and the dashed arrows depict the stepping direction and range. The modulator grid and the stepping direction are tilted at an angle α to each other. Exemplary stepping schemes ($a = 1$, $b = 3$) with $N = 10$ steps (A) and ($a = 2$, $b = 3$) with $N = 13$ steps (B). Such a linear stepping scheme with periodic modulators also allows other schemes such as e.g. an irregular hexagonal sampling shown in (C) with $a = 1$, $b = 4$, and $N = 15$ steps. Figure adapted from [Gustschin, 2021].

the stepping range is divided into an integer number of steps N and a step distance p' the Pythagorean theorem in the rectangular triangle yields:

$$a^2 + b^2 = (Np')^2. \tag{6.3}$$

If a homogeneous square sampling is desired the step distance p' is also the sampling period and has to conform to $Np'^2 = 1$ assuming that the period of the modulator is 1. By considering that and equation 6.3 the number of steps is given by $N = a^2 + b^2$. Note here that it is only valid if a and b are coprime, otherwise, the stepping will result in redundant sampling points. The resulting grid that samples the space is oriented in an angle $\alpha = \arctan(a/b)$ to one direction of the modulator. Hence, for the experiment, the TAI has to be mounted at an angle α between the stepping direction and the modulator lattice. This can be implemented experimentally with a rotation frame that is manually adjustable by a micrometer screw.

For better image quality, the sampling should be adjustable, as it determines the resolution and sensitivity. Equation 6.3 gives possibilities for available N by choosing coprime a and b. The case with $a = 1$ and $b = 3$ with $N = 10$ is illustrated in Figure 6.5 A. The next densest sampling can be chosen with $a = 2$ and $b = 3$ with $N = 13$ steps as illustrated in B. This allows additional combinations for N compared to e.g. possible 2D samplings which result in a square number of steps such as 4, 9, 16, 25 etc...

It is worth noticing that many other sampling schemes can be achieved with 1D stepping. It is known that hexagonal sampling is more efficient compared to square sampling. Such a quasi-hexagonal sampling scheme can be also achieved by exploiting the square periodicity of the TAI. Figure 6.5 C shows a stepping with $a = 1$, $b = 4$, and $N = 15$ which results in an irregular hexagonal sampling having a higher efficiency than a square sampling. Note, however, that in this example the hexagonal grid is not regular but slightly compressed in one direction. While this scheme requires only one motorized linear stepping direction the modulator angle has to be carefully adjusted for every stepping scheme. In this work, several 1D stepping scans with different numbers of frames from 13 to 25 have been performed. The achieved visibilities and sensitivities are given in Table A.3 in Appendix A.5.

6.3.4 Comparison with other Phase Modulators

Comparing the efficiency of different phase modulators is a complex task and involves various factors. Firstly, they can be compared in terms of flux efficiency. This does not only involve how transparent to X-rays the modulators are but also at what distance the desired pattern is created. A shorter distance makes the setup more flux efficient regarding the intensity drop due to the inverse square low. But a more important factor is the created intensity pattern itself and its ability to sample the pixel matrix. As previously discussed the visibility has been used as a performance metric [Zdora, 2018]. However, there is no clear definition of the area on which the visibility is calculated. A speckle pattern can have some randomly distributed points with high contrast, however, it is not possible to modulate the entire pixel matrix with those "high visibility areas" with a reasonable number of phase steps since they are randomly distributed. Using a periodic modulator with high visibility but with a rather big period, one does require too many steps to reach reasonable sampling. Considering e.g. a refractive phase array [Dos Santos Rolo, 2018] with 50 µm period and a desired sampling of 2 µm it takes $25 \times 25 = 225$ phase steps. The same sampling can be realized e.g. with the 10 µm TAI in $5 \times 5 = 25$ steps. Thus, not only the visibility but the density of those modulations and the sampling scheme that can be realized with them play a decisive role. Hence, it is suggested to use the visibility-to-period ratio as a performance metric to compare such modulators. Figure 6.4 B shows a comparison of other recent literature on regular 2D modulator arrays with the performance reached in this work. Compared to [Reich, 2018] the 6.8 µm TAI achieves similar visibility at about 10× smaller period. Thus it enables e.g. single-shot imaging at about 1 order of magnitude higher resolution or a sampling with much fewer steps to reach a certain desired resolution. Compared to, e.g. [Morgan, 2013] the configuration with the 5 µm TAI gives 6× higher visibility. The refractive lens array [Dos Santos Rolo, 2018] creating 20×20 foci with 50 µm period reaches very high visibility, however, it is limited in the field of view (FOV) and required many steps for a finer sampling. Compared to that the 6.8 µm TAI creates about 1000×360 foci (limited by detector FOV) and allows a factor 50 denser sampling. In terms of the visibility-to-period ratio (see dashed lines in Figure 6.4 B) it performs more than a factor 2 better. Furthermore, Figure 6.4 B also shows the theoretical limit in terms of the visibility-to-period ratio imposed by the detector PSF. It was calculated by convolving a periodic 2D square array of intensity points (resembling an ideally point-focusing modulator) with a Gaussian of $\sigma = 1.5\,\mu\text{m}$ estimating the blur of the used detector. The data shows that the TAIs are already very close to the theoretical limit imposed by current high-resolution detectors.

A comparison with random phase modulators such as the P1000 used for SBI is also not straightforward. Here, one has to consider the stepping scheme including the number of phase steps and the contrast it can generate in every pixel. For that different steppings have to be composed or measured and the visibility has to be calculated pixel-by-pixel. Such a detailed analysis has been performed for the P1000 data and compared to the 10 µm TAI with various 1D linear phase stepping schemes that have been proposed. The results show that similar visibilities can be achieved with a factor of 3 fewer steps with the TAI compare to the P1000 diffuser. Beyond that, a statistical analysis based on the underlying UMPA algorithm described in [Zhou, 2016] is used to estimate the resulting phase sensitivities. This analysis is based on calculating the intensity gradients which are used as a performance metric. As elaborated in more detail in Appendix A.4 the TAI outperforms the P1000 diffuser by a factor of 6 in dose efficiency. It is attributed to the strong intensity gradients and their periodic nature which allows efficient sampling.

6.4 Imaging Application

6.4.1 Multimodal Projectional Imaging

After evaluating the optimal propagation distance and sampling schemes for the fabricated TAIs the imaging performance should be addressed. For that, a sample consisting of silica particles with partially porous inner structures glued to a plastic micropipette tip was created. It was measured at 15 keV beam energy with the 6.8 µm TAI placed 170 µm from the detector close to its peak visibility performance. The sample-to-detector distance was $d = 70\,\mathrm{mm}$ and the TAI was manually rotated to different angles enabling configurations with a different number of steps. The stepping distance was varied to achieve a homogeneous sampling. Optimal ranges were found when the sum of all phase steps is an array with a low standard deviation of the pixel intensities. This way good configurations for 13, 15, 17, and 25 phase steps were found. This somewhat elaborate procedure was chosen since there was no positioning hardware available that could allow adjusting the angle relative to the stepping direction precisely. To acquire the flat fields the procedure was repeated without the sample in the beam. To account for possible experimental deficiencies like drifts of the beam, sample, and optic mounts or the imprecise reproducibility of the linear stepping stage a digital matching algorithm for the flat fields was developed. Every sample frame was matched with an optimal flat field using an image similarity algorithm on a sample-free area. Additionally, the best flat field was digitally shifted with sub-pixel interpolation in both directions to achieve optimal registration with the sample frame. The processing was performed by Unified Modulated Pattern Analysis (UMPA). Table A.3 in Appendix A.5 gives an overview of the configurations with respective N, the window size w for analysis, and what visibilities and sensitivities were achieved. The differential phase-contrast images were used for a Fourier transform-based phase integration described in detail in [Kottler, 2007].

Figure 6.6 shows the multimodal X-ray radiographs acquired in a scan with $N = 17$ steps. The transmission image (A) shows some distorted features close to sharp edges or grainy regions by edge enhancement effects. The dark-field image (B) also shows a characteristic enhancement of edges, but also a clear signal from porous structures inside the spheres. The differential phase-contrast images in x-direction (C) and y-direction (D) show rough edges of the silicon sphere, which is probably due to a somewhat low window size in processing ($w = 5$ pixel). An increase in the window size would avoid these artificial edges, however, would also impair the resolution. Interestingly, those artifacts are not recognizable anymore in the integrated phase image (Figure 6.6 E). In this scan, the

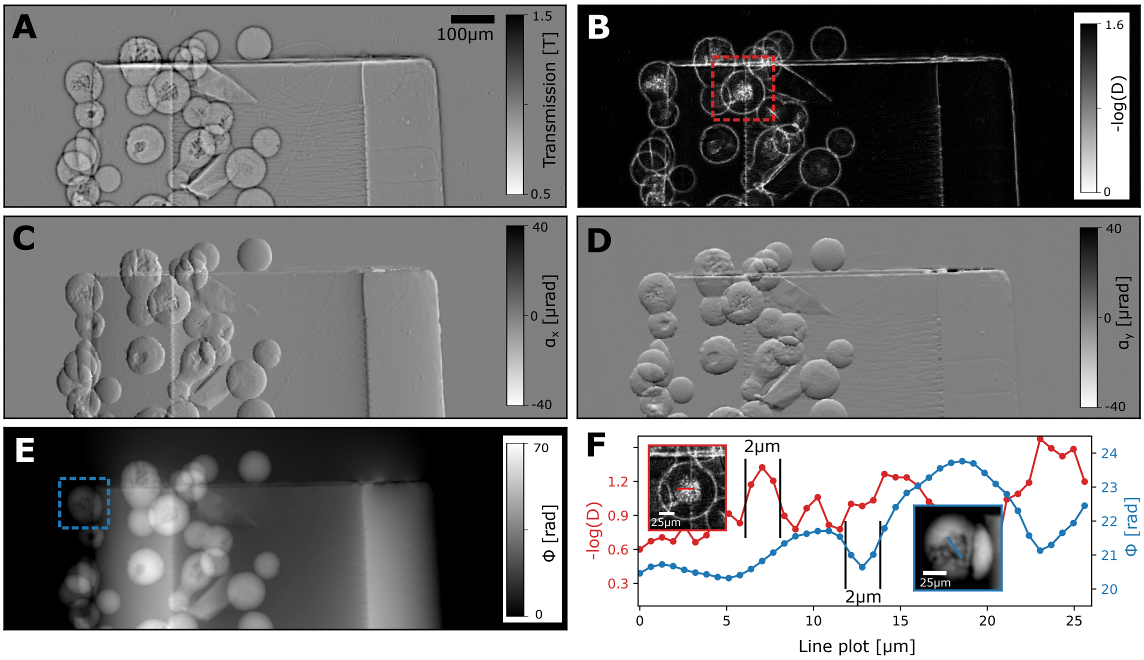

Figure 6.6: (A) Transmission image, (B) dark-field image, differential phase-contrast image in (C) x-direction and (D) y-direction as processed by UMPA and (E) the integrated phase image. (F) Line plots of the dark-field and phase signal from some selected features shown in the red and blue ROIs, respectively. Figure adapted from [Gustschin, 2021].

sensitivity in both directions was similar ($\sigma_x = 175$ nrad, $\sigma_y = 186$ nrad) which is an indication of a good sampling in both directions.

A higher resolution was reached with $N = 25$ steps and a window size of $w = 3$. Line plots extracted from these high-resolution scans in distinct ROIs of the dark-field and integrated phase channels depicted in Figure 6.6 F show that features of about 2 µm full width at half-maximum (FWHM) can be resolved. This is close to the theoretical resolution limit of UMPA imposed by the window size as well as the PSF of the detector.

6.4.2 Phase CT of a Murine Artery

To demonstrate the possibilities of phase CT with its soft tissue contrast possibilities a non-stained murine artery embedded in paraffin wax featuring fine lamellar structures in the tunica media was chosen. The sample preparation and description are elaborated in detail in Appendix A.6. Since the sample was larger than the previous specimen with the silica particles the detector configuration had to be adapted for a larger FOV. The Ximea CB500MG camera (4.6 µm pixel size) was coupled to a 5× optical magnification lens system yielding an effective pixel size of 0.91 µm. The scintillator screen was a 100 µm cadmium tungstate ($CdWO_4$) scintillator crystal. It has a lower resolution compared to the previously used LuAG, however, its photon efficiency is higher. The measurement was performed at 20 keV beam energy with the respective 6.8 µm period TAI. In this configuration, the FOV was $7{\times}2.5\,\mathrm{mm}^2$. The sample was placed on the tomography stage at a propagation distance of $d = 150\,\mathrm{mm}$ to the detector. For every projection, 15 phase steps were recorded with an exposure time of 200 ms, and in total 4001 projections were acquired over 180° rotation. During the scan, the sample was laterally shifted in-between projections to avoid ring artifacts in the later reconstruction. Flat fields were acquired multiple times during the scan to be able to correct setup-related drifts. The experimental overhead like mechanical stepping and sample shifts prolonged the scan time to about 5 h in total. The pre-processing consisted of a dark current correction, defect pixel interpolation, and flux normalization with independently measured ring current of the synchrotron source. Every frame was also matched with the most suitable flat field using the algorithm previously described for the silica particles. Phase retrieval was performed by UMPA with a window size of 3 pixels. This step was computationally heavy and was distributed on up to 20 servers of the DESY Maxwell cluster. Typical processing times of the over 60000 frames were a few hours – a further motivation to reduce the number of required phase steps. The phase integration was conducted as previously described for the silica particles. The tomographic reconstruction was performed via filtered back-projection (Ram-Lak filter) of the integrated phase images using the software X-Aid FDK Reconstruction Suite 2020.10.2 (Mitos GmbH, Garching, Germany).

A 3D rendering of the artery is shown in Figure 6.7 A, where a fissure in the vascular wall is depicted by the white arrow. The aorta was extracted from an animal with a pathological condition (atherosclerosis). Such fissures of the elastin fibers as shown in a slice in Figure 6.7 B are commonly seen in frail, old animals, but also in humans. A magnified view in C illustrates the degree of resolution and contrast achieved. A line plot of the refractive index decrement δ along the blue line in B is given in D. Two distinct elastin fibers 6 µm apart can still be well resolved. Features with 2.6 µm FWHM can be clearly distinguished from the noise. The background noise level in the paraffin matrix is 0.015×10^{-7} and the signal generated by the elastin fibers is about 0.765×10^{-7}. Consequently, a CNR of > 50 is achieved between these different soft matter components.

For a quantitative resolution determination, two different methods were used. First, an automatic edge detection algorithm was implemented to find steep edges between the paraffin matrix (embedding material) and the lamellar structures of the vessel wall. First, pixels in the vicinity of the wall were detected by taking the spatial derivative of the image

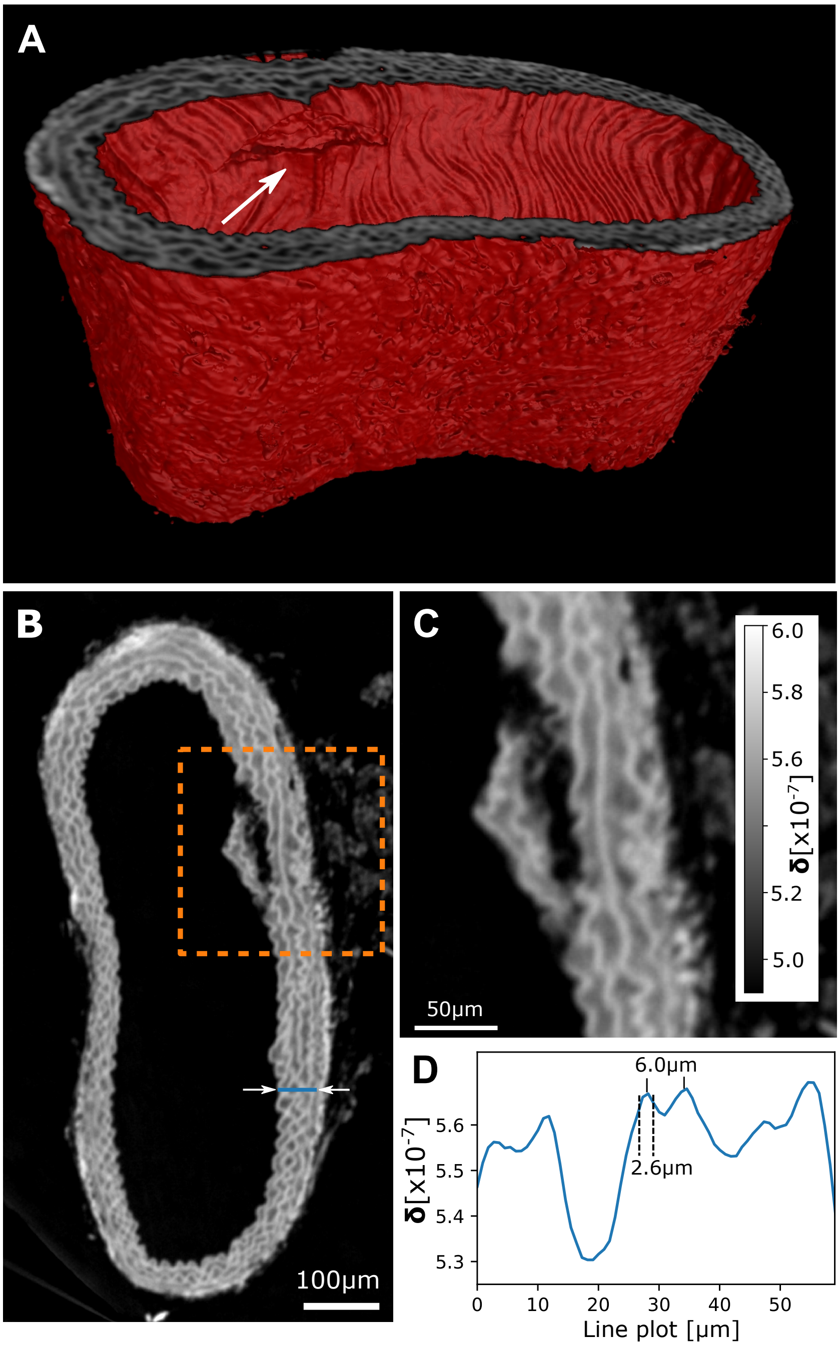

Figure 6.7: (A) 3D Rendering of a mouse aorta CT phase scan depicting a fissure in the vascular wall (white arrow) and (B) a respective slice showing its cross section consisting of lamellar structures. (C) Magnified image of the ROI in (B) shows the fissure in more detail. (D) Line plot (see blue line in (B)) showing that two lamellae distanced 6 µm apart can be well resolved. Figure adapted from [Gustschin, 2021].

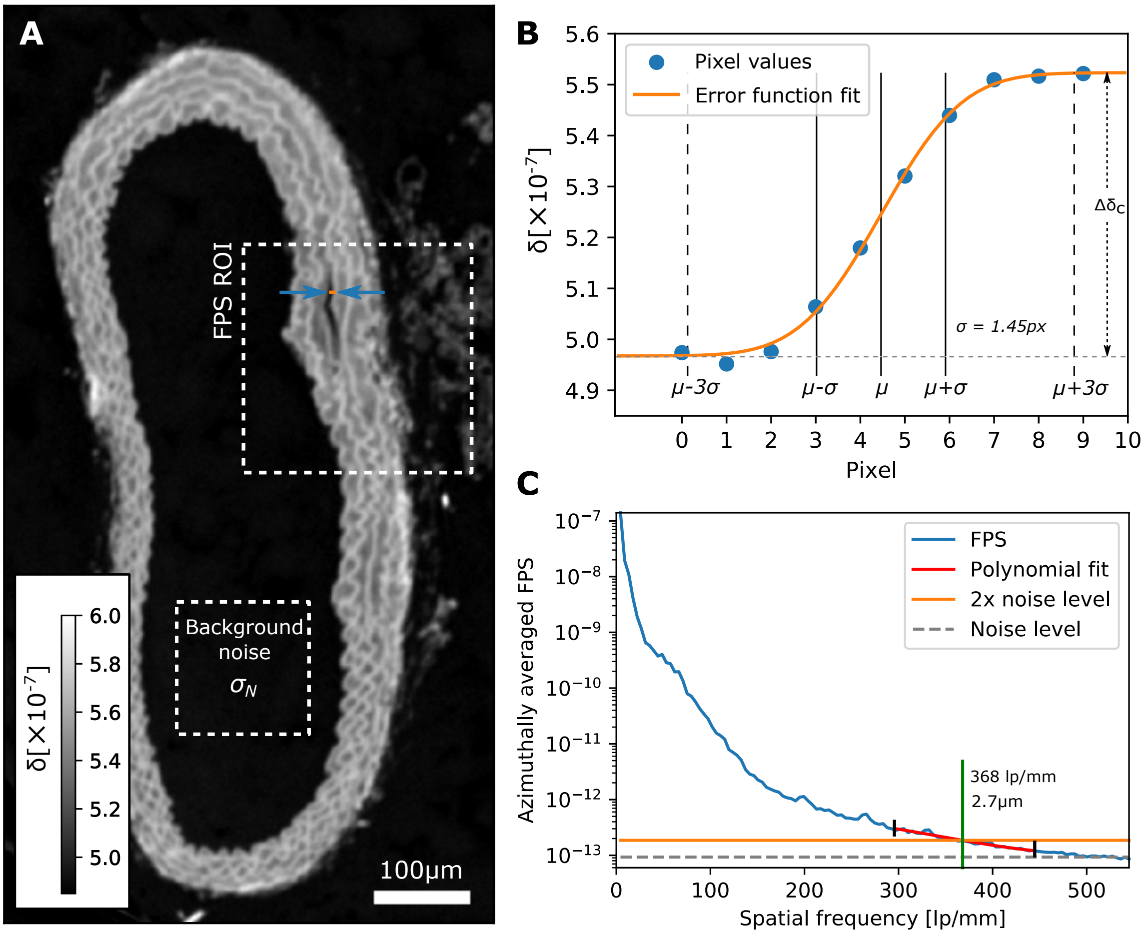

Figure 6.8: (A) CT slice of the murine artery used for the determination of the spatial resolution and the CNR analysis. The ROI used for the FPS analysis and the background noise determination are depicted by white dashed lines. Further, the blue arrows indicate an exemplary edge between the paraffin wax and the fiber. Its pixel values are plotted in (B) together with a Gauss error function fit. (C) Plot of the azimuthally averaged FPS from the respective ROI in (A) showing the noise background level as well as the intersection of the FPS with the doubled noise level. Figure adapted from [Gustschin, 2021].

(Figure 6.8 A) in the x-direction and applying a threshold filter. Then several pixel values of the edge along the x-direction were automatically extracted and fitted by a Gaussian error function as shown in Figure 6.8 B. To select only clear edges several criteria had to be met: (1) The contrast of the edge δ_c had to be at least 20× higher than the noise level in the background of the paraffin wax. (2) The edge had to include a number of pixels covering the range of 3σ around the mean μ. (3) The residuum (measurement-fit) of every pixel value had to be less than 5% of the contrast δ_c to only select clear edges with a homogenous signal on the lower and upper site.

This edge fining algorithm was executed over 20 equidistant slices of the CT volume of interest and from every slice, the 10 steepest edges were selected. From that 200 edge fits an average σ of 1.43 ±0.088 was determined which corresponds to an average FWHM of 3.06 µm ± 0.19 µm.

An alternative method proposed in [Modregger, 2007] is based on the Fourier power spectrum (FPS). For that, an ROI (see Figure 6.8 A) featuring some fine structures and the paraffin background was chosen. The FPS (see Figured 6.8 C) was calculated as described in [Modregger, 2007] and azimuthally averaged. The noise level was determined by taking the average of the 10 last frequency bins. To determine the intersection of the FPS with the ”double noise level threshold” it was fitted with a 2nd order polynomial in the range indicated by the red line (see Figure 6.8 C). The green line depicts the intersection at 368 lp/mm which corresponds to a feature size of 2.7 µm.

Both methods suggest a spatial resolution of about 3µm approaching the limit imposed by the UMPA window size and the detector PSF. A recent comparable work employing state-of-the-art SBI achieved about 8 µm resolution at $N = 20$ phase steps. This work can be considered a significant improvement as it reached a 2× higher resolution with only $N = 15$ phase steps.

6.5 Conclusion and Outlook

In this chapter optimized 2D phase arrays with small periods were designed, fabricated, and evaluated for 10-20 keV X-ray beam energy. The TAIs employ the Talbot effect to create periodic diffraction patterns with higher compression ratios than conventional phase gratings used before for X-ray imaging. They have several advantages over apertures or absorbing gratings, refractive micro-lens arrays, or random phase modulators like e.g. sandpaper. Finer periods used in this work allow more efficient phase sampling compared to other current diffractive optical elements while still maintaining reasonable visibility due to the higher compression ratio. Their periodicity also enables more efficient sampling schemes compared to e.g. random modulators. [Kashyap, 2016] compares speckle-based imaging (SBI) with grating-based imaging (GBI), pointing out crucial disadvantages of the latter technique. In this work, it was demonstrated that the drawbacks can be avoided by using a hybrid technique between GBI and SBI. The demonstrated method does not use absorptive elements and copes with a single optic which reduces setup complexity. Bi-directional phase sensitivity can be reached with 1D linear phase stepping when some effort is invested for an angular alignment of the TAI. When 2D stepping is available the alignment becomes obsolete and the setup complexity is virtually identical to that of SBI. Furthermore, many different sampling schemes are available to optimize phase sensitivity and resolution. In the present case structures of 2.0 µm were well resolvable in the integrated phase and dark-field images in single projections. In computed tomography, a resolution of 3.0 µm has been reached with unprecedented CNRs with as little as $N = 15$ phase steps.

The dynamic range for the differential phase signal is limited by the modulator period as phase-induced displacements of the foci can create phase wrapping similar to GBI. With random modulators, this problem seems to be less severe as larger displacements than the average speckle size can be matched as long as the imaged object itself does not consist of grainy structures that cause additional speckle-like distortion. Similarly strong and sharp spatial modulations of δ (edges, air bubbles,...) are problematic, as they deteriorate the diffraction pattern, which cannot be reasonably matched with the reference anymore. Hence, it is important to adapt the sensitivity by e.g. choosing an optimal sample-detector distance, beam energy, or modulator period. Pixels that have not been matched well can be also identified by the fitting residuum in UMPA processing. They can be e.g. interpolated by their neighbors or completely excluded from the CT reconstruction using iterative reconstruction algorithms [Hahn, 2015]. Another, computationally more expensive method would be to develop ptychographic phase retrieval algorithms, which can be combined with structured illumination [Stockmar, 2013].

Several potential improvements can be made to reduce measurement time, radiation dose, and setup instabilities. A 2D stepping stage will increase flexibility for different sampling schemes and allow acquiring densely sampled flat fields which are useful for correction of drifts and instabilities. Furthermore, it will simplify alignment, since a rotational adjustment required in 1D stepping will not be necessary. The implementation of a fly-scan [Wang, 2019] with a continuous sample rotation and frame rate will also reduce experimental overhead. For that, an entire sample rotation will be performed at every phase step thus reducing the number of the required movements of the TAI. Using this scheme the total exposure time can be significantly reduced, however, the sample cannot be shifted in every projection for ring artifact removal. Respective corrections have to be implemented with software. Some of the improvements have already been implemented in a subsequent work. Further, the method yielding the absolute δ values has been compared to propagation-based phase tomography in [Riedel, 2023].

Going towards non-destructive, quantitative virtual histology the absolute δ values should be further verified and the results compared to propagation-based phase tomography in future work.

The potential to extend TAI-based imaging to laboratory-based X-ray sources should be further explored. As previously discussed the TAIs can be designed to generate high-visibility modulation at relatively short propagation distances, which is beneficial for low-coherence sources. The period can be chosen to be compatible with lower detector resolution. For higher X-ray energies the phase shift of the modulator can be also tuned precisely. This is a significant advantage compared to other techniques. SBI uses strongly absorbing diffusers (e.g. steel wool [Wang, 2016]) or multiple layers of sandpaper (up to 20 layers at 65 keV [Berujon, 2017]) to generate reasonable visibility. The high fraction of absorption and the random nature of the speckles makes it extremely inefficient. The TAIs demonstrated in this work can be fabricated on thin, transparent silicon wafers for energies above 100 keV at periods of about 10 µm. For that aspect ratios of 1:20 are sufficient which is routinely performed by current anisotropic etch technologies such as DRIE.

The discussed TAIs can be also used for other applications where focused X-ray spots are necessary. This can be wavefront sensing or X-ray optic characterization which is often performed with Shack-Hartman sensors. It can be also used for precise scintillator adjustment, focusing, and characterization as it can probe the resolution across the entire FOV in just one single exposure. Another field of applications might be the recently demonstrated full-field structured illumination super-resolution X-ray microscopy [Mamyrbayev, 2020; Günther, 2019] where arrays of sharp, periodic foci are required. The sub-periodic focusing with stronger compression ratios tuned by the grating duty cycle can be also employed in Talbot-Lau interferometers to increase their visibility. Respective systems with absorptive source gratings may be used to develop diagnostic systems to gain bi-directional sensitivity with shorter setups compared to conventional binary symmetric phase gratings.

7 Conclusion and Outlook

This chapter provides an overview of the results of this work and offers a perspective on future developments.

After an overview and evaluation of current grating fabrication methods in Chapter 3, one of the first main objectives was to develop an efficient procedure for grating quality characterization combining different complementary methods. Commonly applied methods like light or electron scanning microscopy are only probing the grating surface and are difficult to implement for automated quantitative data acquisition. X-ray microscopy, tomosynthesis, and µCT were successfully applied to gain in-depth information and study both silicon grating templates and filled substrates with absorber material. Despite a small field of view, µCT was particularly helpful to identify different kinds of grating defects that appeared from KOH etching. The three-dimensional data is extremely helpful as it shows the etched structures without the need to cleave the sample for profile analysis by microscopy techniques. Further, it has been found that X-ray tomosynthesis can be used to analyze the lamellar structure and height of large grating substrates by collecting limited-angle projection data. The angular X-ray transmission (AXT) signal can also be used to obtain different grating properties without resolving the individual grating lines. This newly developed method allows a fast and non-destructive characterization of large grating areas. Compared to other methods, it offers a high degree of quantitative data and is of great benefit for both process development and quality control.

Chapter 4 addresses the fabrication of absorption gratings by anisotropic silicon etching and deposition of absorbing material in the form of particles. This approach aims to avoid the complex X-ray lithography process as well as the error-prone and expensive Au electroplating. First, silicon grating templates fabricated by anisotropic KOH etching were evaluated. Several challenges have been faced when etching to several hundreds of µm with this technique. While the etching process seems to be linear with time for low aspect ratios the etching rate slows down at depths beyond 200 µm and becomes inhomogeneous over the grating area. Even neighboring trenches can have differences of several tens of µm in depth. Different plausible explanations have been discussed and several types of emerging defects have been identified. It was concluded that the method is of limited suitability for high-volume production due to several delicate process requirements such as the required silicon wafers with (110) crystal orientation, the precise mask alignment to the crystal lattice, and the susceptible etching process. Compared to that, DRIE offers more advantages in terms of process control and is more common in commercial microfabrication.

After their characterization, the fabricated silicon grating templates were used for the deposition of tungsten particles as absorber material. First, a tungsten particle dispersion with ethanol and a binding polymer was developed. It contained a bimodal particle distribution as it was previously established that such a mixture results in a higher filling density. Centrifugation was used to provide an additional driving force to the particles for penetrating the deep trenches. For that, various vessels were designed and fabricated to process grating pieces of different sizes. Starting with small grating samples, the deposition process was optimized by characterizing the filled templates with various techniques. After that, the grating area was increased up to $40 \times 130\,\mathrm{cm}^2$ – a size that can replace 2 grating tiles fabricated by the conventional LIGA method on a $100\,\mathrm{mm}^2$ wafer. With increasing area, some challenges arose with the 3D printed centrifugation vessel as it had to withstand strong g-forces without transmitting mechanical stress to the rigid and susceptible substrate. Several gratings with 300 - 350 µm depth could be processed successfully, while other substrates with inhomogeneous etch depths beyond 400 µm broke during the deposition process. The insights gained in the process were used to further improve the centrifugation inlet design and the handling process. In the follow-up project, the area and the grating thickness could be even further increased [Pinzek, 2022].

The fabricated samples were thoroughly characterized by optical and X-ray microscopy as well as angular X-ray transmission (AXT) and interferometer-based visibility measurements. The grating defects after the deposition were identified and discussed. Among them, duty-cycle deviations and missing grating lines were the most critical. It should be noted, that they originated in the silicon etching process and were not the result of the centrifugal tungsten deposition. The AXT measurements confirmed the structural integrity of the grating structure. In particular, there were no significant deficiencies in the lamella inclination, as the thin grating bars were the most susceptible structures to the strong g-forces. The final qualification was performed in a Talbot-Lau imaging system designed for medical dark-field CT. For that, the fabricated gratings were inserted into a bending frame with a radius of 1m without breaking. At 60 kV, a visibility of ≈ 0.33 was achieved, which was close to the reference LIGA grating (0.35). Multimodal imaging of an exemplary sample with scattering and refractive structures could also be demonstrated.

Compared to recent literature where particle-based absorber deposition for X-ray gratings was approached, the efforts conducted in this work show significant progress. Compared to [Lei, 2019a], the aspect ratio of filled structures could be more than doubled while also achieving a higher filling density. Compared to [Hojo, 2019], the centrifugation could be conducted with a much larger grating area, albeit using a much lower rotation speed. The fabrication capabilities achieved so far meet the requirements of several phase-sensitive techniques based on coded apertures or masks, as they typically use larger periods. For more sensitive and compact Talbot-Lau systems, the period should be further decreased to the sub-20 µm range in future developments. At the same time, the effective deposited absorber thickness should remain above 150 µm for decent performance with hard X-rays. This requires further optimization toward a higher filling density and a higher aspect ratio of silicon templates. Current state-of-the-art DRIE devices can reach significantly higher aspect ratios than the silicon templates used in this work. However, for absorption gratings, strict requirements are imposed on the perpendicularity of the trench walls to keep the duty cycle constant. Furthermore, the fraction of etched area is typically higher for gratings compared to other common DRIE applications. Hence, achieving a homogenous result on 200 mm or even 300 mm wafers requires an elaborate development of the etch parameters. With smaller periods, the particle sizes have to be further reduced. Presumably, the filling density in the vicinity of the sidewall will be lower due to limited particle mobility, which will become more and more critical with the decrease of the trench opening. One possible way to increase the absorbing matrix of the grating structure would be a double-sided patterning. For that, alignment technology with sufficient precision is available with common equipment, albeit the particle deposition process might pose challenges with the occurring mechanical forces. Alternatively, aligning and bonding more substrates on top of each other might be a possible solution.

For systems with a large field of view like thorax radiography or CT scanners, the cost and effort of grating production must be decreased for commercial application. Using silicon-based processing and tungsten as absorber material seems to be a viable alternative for gratings with a larger period in strongly inverse Talbot-Lau systems. At the same time, those systems require source gratings with extremely flexible substrates such as graphite and an aspect ratio close to 1:100. Here, the LIGA method with a bulk absorber filling via electroplating will certainly remain indispensable.

In the second part of Chapter 4, the particle deposition of absorber material into silicon gratings was applied for neutron-based grating interferometry. As the requirement of aspect ratio was much lower for neutrons due to the excellent absorption behavior of gadolinium, centrifugation was not necessitated and significantly lower periods could be approached (13.3 µm). Since there was no powder commercially available in the sub-10 µm size range, a wet milling process was established to reduce the particle size. It resulted in a wide distribution of particle size and shape less suitable for dense packing. The deposition was performed by simply casting the particle dispersion on the grating substrate and ultrasonic excitation of the vessel, which provided some additional movement of the particles. The achieved estimated filling density was in the range of 20% for the smallest grating period (13.3 µm) and 85 µm trench depth. The fabricated gratings were characterized by wavelength-dependent neutron transmission measurements and showed excellent absorption performance up to the thermal neutron range. Both source and analyzer gratings fabricated with the developed method were used for a new grating interferometer design at ANTARES. With that, the visibility could be increased to peak values of 0.74 at 4 Å and the operational range could also be extended to the thermal neutron regime. Together with the high flux at FRMII and the large field of view the nGI at ANTARES is a powerful instrument for multi-modal neutron imaging.

Compared to other systems reported in the literature, the period of the analyzer grating is still relatively large. Gratings with the smallest period (4 µm) with Gd absorber have been fabricated by sidewall evaporation of Gd [Grünzweig, 2008b; Reimann, 2016], however, do not show an absorption behavior typical for binary absorption profiles as the transmission measurements suggested. To compensate for the larger period and still reach a comparable sensitivity, the system was designed in the third fractional Talbot distance enabling longer propagation distances compared to previous geometries. However, placing the sample further away from the detector increases the geometrical blur with larger pinholes and deteriorates the resolution. Taking these factors into account, it might be of interest to further reduce the period of the analyzer grating to the sub-10 µm range in future upgrades. For that, the Gd particle size distribution should be narrowed and optimized towards more compact, spherical shapes to achieve higher filling density. Using centrifugation as with tungsten particle gratings would be an additional measure to improve the packing. Finally, also isotopically enriched ^{157}Gd would significantly facilitate the absorption properties, albeit being a quite expensive approach. With those possibilities, a halving of the period with limited effort appears realistic.

In Chapter 5, the new neutron grating interferometer was employed for a multimodal thermal neutron tomography scan at 1.6 Å. A quartz geode sample containing scattering structures and some strongly absorbing features embedded in a matrix of silica crystals was chosen. The same sample was also scanned in an X-ray grating interferometer at 70 kV tube voltage. The aim was to compare the results in different modalities and explore the possibilities of the highly transmitting thermal neutron radiation for the scattering signal. The latter is difficult to access when the scattering structures are embedded in strongly absorbing material. Additional difficulties arise when polychromatic spectra are used, as they generate a disproportional reduction of the modulation amplitude leading to an artificial signal. The results of the scans showed some clear complementarity in the absorption domain revealing features that were not distinguishable from just one modality.

The dark-field signal acquired with both X-rays and neutrons showed mostly similar structures. However, there were several features recognizable in the neutron domain which were not visible in the X-ray dark-field CT. Since the attenuation with X-rays was significantly stronger than with neutrons, the noise in the X-ray dark-field CT reconstruction was expectedly higher. Hence, small scattering features were not distinguishable in the characteristic low-frequency noise of the dark-field signal. In the neutron domain, however, scattering features down to 280 µm in size were well recognizable with more than two times higher CNR compared to the respective X-ray dark-field reconstruction. As this example application shows, thermal neutrons can be used to detect scattering structures embedded in strongly absorbing materials that are hardly accessible with X-rays. Additionally, a decent filtration of the neutrons spectrum by velocity selectors offers benefits with nGI imaging as it avoids artificial dark-field signal due to beam hardening. With the newly developed nGI system operating in the thermal neutron range, various samples containing heavy metals, magnetic materials, or other unique micro-morphologies can be investigated. In the near future, the ANTARES beamline will be equipped with an X-ray imaging module which will enable the simultaneous acquisition of X-ray radiographs during neutron inspection. This will further extend the potential for multi-modal imaging at the instrument.

In Chapter 6, the simulation, fabrication, and evaluation of 2D phase arrays for multimodal single-grid imaging were presented. First, some requirements and design aspects were discussed and placed into context with similar currently available techniques using apertures or absorption gratings, refractive micro-lens arrays, or random phase modulators. It was argued that a trade-off between period and visibility needs to be found. The design of the modulator has to be carefully adapted to the detector resolution and the coherence of the radiation. At the same time, the modulator should not employ absorptive elements to maintain a high flux efficiency if an application with laboratory sources is envisioned. Talbot array illuminators (TAIs) are diffractive arrays that employ the Talbot effect and can focus radiation to small spots similar to compound refractive lens arrays. Although TAIs do not achieve comparably sharp foci, their simple geometry makes them much easier to produce in the sub-10 µm period range.

To evaluate TAIs for multimodal X-ray imaging, some simulations have been performed to compare different designs in terms of their focusing capacities. A two-dimensional binary modulator with an asymmetric duty cycle and a compression ratio of 1:9 was found to be a good option. Modulators of this design for different periods and beam energies were fabricated via DRIE and evaluated at a synchrotron source. The achieved visibility-to-period ratios were found to be significantly better than comparable work. The relatively small periods enabled an efficient sampling scheme with a low number of phase steps and achieve unprecedented resolution for this method. A linear one-dimensional modulator stepping scheme to achieve bi-directional phase sensitivity and vary the sampling density by tuning the modulator grid angle was also suggested as an option. A tomography scan of a non-stained embedded murine artery featuring a pathological condition (atherosclerosis) was scanned to evaluate the system's capabilities. With 15 phase steps per projection, a resolution of 3 µm and a CNR of > 50 between the embedding material and the elastin fibers in the vessel walls were reached.

Several improvements of the method are in progress to further exploit the potential of TAI imaging. The reduction of the period below 5 µm will require thinner scintillators and higher optical magnification to maintain reasonable visibility. In this context exploring more complex modulators with several phase-shifting levels per period to achieve a higher compression ratio might be a rewarding approach. Using hexagonal sampling schemes or even hexagonal modulators will also increase efficiency. The experimental overhead can be further reduced by performing an entire sample rotation at every phase step instead of stepping the modulator at every projection. Further, a continuous sample rotation at low rotational velocity and periodic frame acquisition (fly-scan) will reduce the measurement time. Progress on some of the improvements is reported in a recent work [Riedel, 2023]. The current phase retrieval and CT reconstruction algorithms should be further adapted to deal with typical image artifacts and optimized in terms of computation time. Finally, a ptychographic phase retrieval algorithm as an alternative to UMPA combined with a structured illumination approach using the TAIs might reduce the phase wrapping-related artifacts and increase the resolution.

A Supplemental Material

A.1 Table of Fabricated Tungsten Gratings

No. / Substrate ID	Period [µm]	DC	filling density	comment
1 / KOH CZ 1	45	0.6	0.51	intact, height and DC variations
2 / KOH CZ 2	45	0.6	0.48	intact, height and DC variations
3 / KOH CZ 3	45	0.6	0.53	intact, height and DC variations
4 / KOH FZ 6	45	0.6	-	partially broke during removal from inlet
5 / KOH FZ 10	45	0.6	-	broke during centrifugation with inlet
6 / KOH FZ 11	45	0.6	-	partially broke during removal from inlet

Table A.1: Overview of the processed particle-based W absorption gratings. The active area of every grating is $40 \times 130\,\mathrm{mm}^2$.

A.2 Table of Fabricated TAI Modulators

Modulator	Period[µm]	Energy[keV]	Height [µm] (design/actual)	Duty Cycle (design/actual)
TAI 5-10	5.0	10	8.5 / 8.1	0.33 / 0.31
TAI 10-10	10.0	10	8.5 / 9.1	0.33 / 0.31
TAI 5-15	5.0	15	12.8 / 12.5	0.33 / 0.30
TAI 6-15	6.8	15	12.8 / 13.5	0.33 / 0.29
TAI 10-15	10.0	15	12.8 / 14.9	0.33 / 0.31
TAI 5-20	5.0	20	17.1 / 15.5	0.33 / 0.27
TAI 6-20	6.8	20	17.1 / 17.1	0.33 / 0.29
TAI 10-20	10.0	20	17.1 / 18.7	0.33 / 0.30
TAI 13-20	13.6	20	17.1 / 19.9	0.33 / 0.31

Table A.2: Fabrication-related parameters of the evaluated TAIs.

A.3 Characterization of the P1000 Diffuser

To compare the TAIs with random phase modulators such as e.g. sandpaper typically used in SBI the speckle pattern was measured with the same protocol as the Talbot carpets. To decide what window size is suitable to calculate the visibility and compare it to the TAIs the average speckle size had to be calculated. Figure A.1 A shows a 1000×1000 ROI from the center of the speckle pattern at 15 keV and 380 mm propagation distance. It was selected where the visibility of the 10 µm TAI is maximal to have a reasonable comparison. Figure A.1 B shows the azimuthally averaged and normalized plot of the 2D autocorrelation function of the speckle pattern. In an inlet of Figure A.1 B the 2D autocorrelation is also given, showing that beam coherence in both directions is sufficiently high and does not impair the contrast of the speckle pattern at this propagation distance. With a half-width at about 5.4 pixels, the averaged speckle size (FWHM) can be estimated to be about 6.9 µm. The minimum at about 18 pixels (11.5 µm) can be understood as the average distance at which the pattern is least correlated with itself, i.e. the maximal intensity modulation can be expected within this window size on average. Hence, a window size of 18 pixels was chosen for the visibility evaluation. The visibility was calculated by Equation A.1 and is given in Figure A.1 D. Note that there are also other conventions to define the visibility of speckle patterns, which are not comparable to each other [Zdora, 2018]. It is e.g. possible to calculate the visibility from the standard deviation of the intensity values in a certain window:

$$V_{std} = \frac{\sigma_w}{\overline{I_w}}, \tag{A.1}$$

where I_w is the mean of the intensity and σ_w is the standard deviation in the window. Figure A.1 C shows the visibility calculated by this convention in a window size of 50×50 pixels with a mean value of 0.236. It is also possible to perform a random phase stepping with a certain number of steps N and then calculate the visibility by Equation 6.2 in every pixel of the stepped array. Such a visibility map is given in Figure A.1 E for $N = 40$ steps. Note that the color bar of C is different from D and E.

A.4 Comparison of TAI and P1000 Diffuser

To compare the P1000 modulation with the periodic modulators used in this work the 10 µm TAI was chosen since it has the closest speckle size of all measured at 15 keV. Hence the detector PSF is not supposed to impair the visibility disproportionally. Figure A.2 A shows a comparison of the modulation acquired with the TAI and the P1000 speckle pattern. The respective line plot shows that some features are generating higher intensities with the P1000, however, their density is much lower compared to the TAI.

To compare the visibility under realistic conditions which can be reached with N steps with both modulators the following calculations have been made: First, various sets of steppings of the P1000 speckle pattern have been created with different N from 5 to 100. The individual frames have been generated by digitally shifting the speckle pattern on a spiral trajectory to avoid similar or equal steps which would be redundant. Then a visibility map was calculated from every stepping using the Formula 2.26 for every pixel. For different N the average visibility and its standard deviation were extracted.

For the TAI different sets of steppings have been generated by using the 1D phase stepping scheme previously discussed. Hence, there are only certain configurations of N that are available, since they have to satisfy the condition given by Equation 6.3. The visibilities for P1000 and the 10 µm TAI reached by N steps are plotted in Figure A.2 B and the

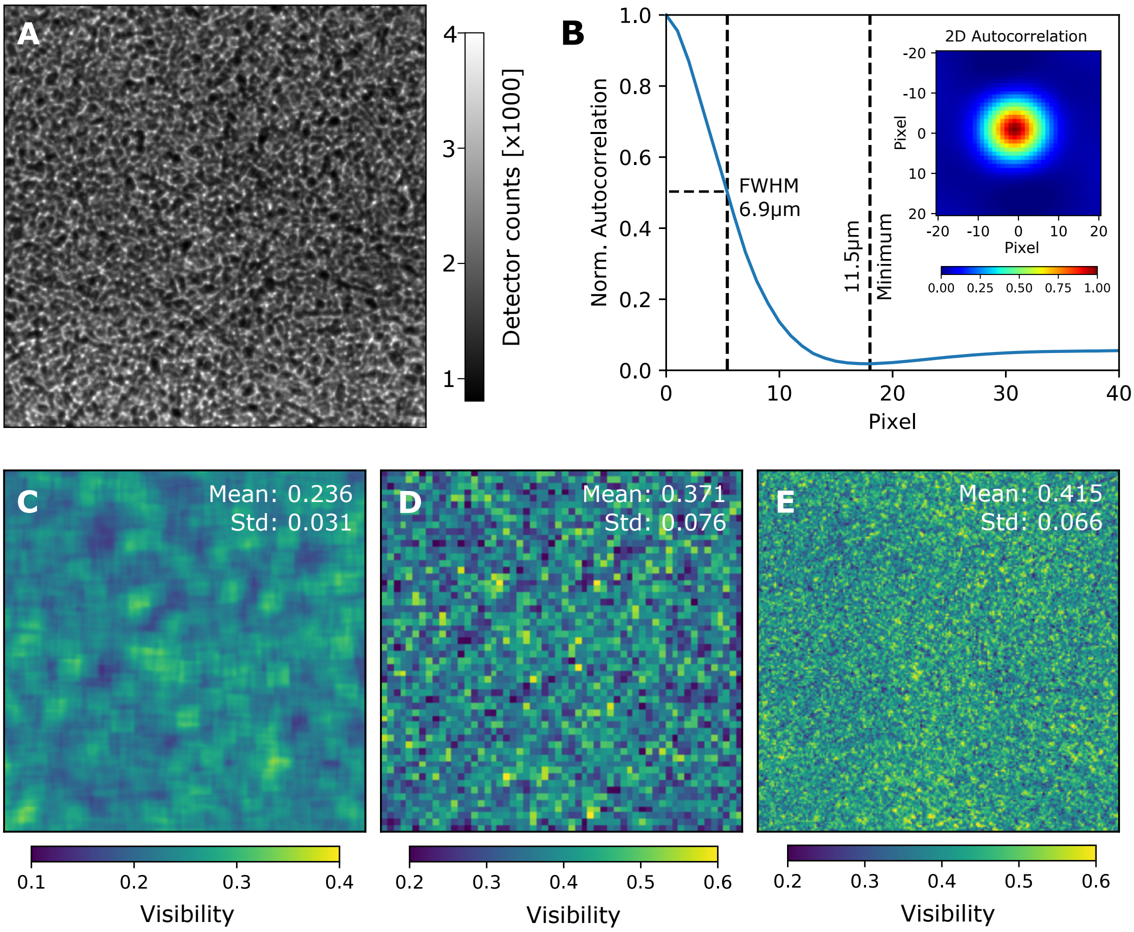

Figure A.1: (A) Speckle intensity pattern (1000 × 1000 pixel central ROI) created by the P1000 modulator at 380 mm propagation distance. (B) Azimuthally-averaged plot of the 2D autocorrelation of (A) suggesting an average speckle size of 6.9 µm. (C) Visibility map calculated by convention from Equation A.1 with a window size of 50 × 50 pixels and (D) calculated by Equation 2.26. (E) Visibility map calculated pixel-by-pixel from a spiral stepping with $N = 40$ steps. Figure adapted from [Gustschin, 2021].

error bars represent the respective standard deviations. The plot shows the TAI can reach higher visibility with $N = 13$ steps than the P1000 with $N = 40$ steps. Further, it also provides a more homogenous visibility map as shown by the respective inlets for both cases. Consequently, the TAI can be operated more than 3× efficiently when visibility is used as a performance metric.

A more substantial statistical analysis of image quality with UMPA processing was performed in [Zhou, 2016]. It was concluded that the variance of the differential phase image (which is a measure of the quality in terms of noise) is:

$$\sigma_x^2 = \frac{2\sigma_{\mathrm{ph}}^2}{\sum \left|\frac{\partial I}{\partial x}\right|^2} = \frac{2\sigma_{\mathrm{ph}}^2}{N\left\langle \left|\frac{\partial I}{\partial x}\right|^2 \right\rangle}, \tag{A.2}$$

where σ_{ph}^2 is the variance of the photon noise, N is the number of pixels in a window (in case of single-shot speckle tracking like in [Zhou, 2016]) or the number of phase steps. The mean of the intensity values in a window or a pixel's phase stepping data set is denoted by $\langle ... \rangle$. As this expression shows a good intensity modulation should have strong intensity gradients characterized by high contrast and a high density of bright spots. Therefore, the visibility-to-period ratio can be considered another useful metric for such phase modulators. If the speckle pattern does not have a certain period one can also directly evaluate the intensity gradients of the image. Figures A.2 C and D show the absolute partial derivatives in both directions of the P1000 diffuser speckle pattern and the respective TAI pattern. It is noteworthy that the TAI modulation has both greater absolute gradient values as well as a much higher density of such structures. For a more quantitative comparison a metric $m = \left\langle \left|\frac{\partial I}{\partial x}\right|^2 \right\rangle^{-1}$ should be defined which scales linearly with σ_x^2 as Equation A.2 suggests. Histograms of these m values have been calculated for some exemplary cases and shown in Figure A.2 C.

The TAIs with a period of 6.8 µm and 10 µm show both lower m values and a much narrower distribution of the latter compared to the P1000. The mean of TAI 10-15 (0.246×10^{-4}) is about 6× smaller than that of P1000 (1.49×10^{-4}). Since σ_{ph}^2 is proportional to the intensity the TAI allows to reach comparable σ_x^2 with a dose and flux reduction by a factor of 6. It is also noteworthy that performing much more phase steps with the P1000 diffuser (e.g. 40) does not reach comparable σ_x^2 despite similar visibilities as shown in Figure A.2 B. In fact, despite performing much more steps the TAI with only 13 steps is still 5× more dose efficient than the P1000 diffuser with $N = 40$ steps ($\mathrm{m} = 1.24 \times 10^{-4}$). Considering these results it seems that a gradient-based analysis together with a defined stepping scheme is more useful as a performance metric than the visibility map.

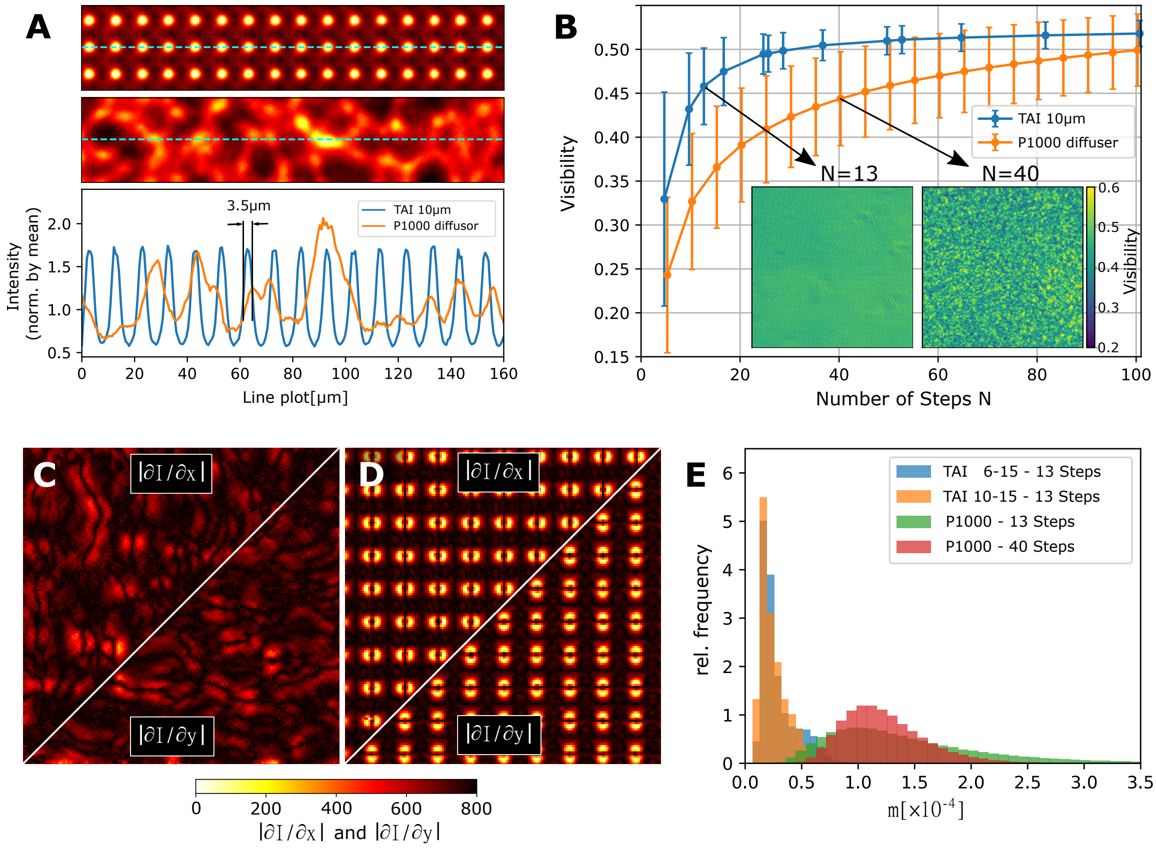

Figure A.2: (A) Intensity modulations created by the 10 µm TAI and the P1000 diffuser with respective line plots illustrating the speckle sizes and densities. The images are normalized to the respective mean of the overall intensity values for a better comparison. (B) Comparison of visibilities and their standard deviations (error bars) with different numbers of steps N. Additionally, inlets showing the visibility maps to the TIA at $N = 13$ and the P1000 at $N = 40$ are shown. Modulus of partial derivatives of the P1000 speckle pattern (C) and the TAI 10-15 modulator (D) in a 150×150 pixel ROI in both directions. (E) Histograms of the proposed metric m calculated for different modulators and phase stepping scenarios. Figure adapted from [Gustschin, 2021].

A.5 Angular Sensitivity Analysis

To show that the angular sensitivity of the discussed 1D stepping scheme is well in both directions the following analysis was performed. A 150 × 150 pixels sample-free ROI was extracted from the scans with 13, 15, 17, and 25 steps and processed with a window size of 3 and 5 pixels. The angular sensitivity in both directions was calculated by:

$$\begin{pmatrix} \sigma_x \\ \sigma_y \end{pmatrix} = \frac{p_{\text{eff}}}{d} \begin{pmatrix} \text{STD}(\text{ROI}_{\text{dx}}) \\ \text{STD}(\text{ROI}_{\text{dy}}) \end{pmatrix}. \tag{A.3}$$

Here, p_{eff} is the effective pixel size. All sensitivities are tabulated in Table A.3. The averaged visibility values were calculated pixel-wise from the respective flat-field steppings based on Equation 2.26.

Here, d is the propagation distance, and p_{eff} is the effective pixel size. The calculated sensitivities and visibilities for the different scans are given in Table A.3. The visibilities are calculated pixel-wise from the respective phase stepping sets.

Scan	N	Window [px]	Visibility	Sensitivity (σ_x/σ_y)[nrad]
Silica Particles	13	5	0.33	198 / 179
Silica Particles	15	5	0.34	179 / 176
Silica Particles	17	3	0.35	331 / 349
Silica Particles	17	5	0.35	175 / 186
Silica Particles	25	3	0.36	293 / 296
Silica Particles	25	5	0.36	153 / 156
Murine artery CT	15	3	0.42	199 / 217
Murine artery CT	15	5	0.42	95 / 107

Table A.3: Different image acquisition modes with respective visibilities and sensitivities.

A.6 Sample Preparation

The vessel was extracted from a 17-moth-old C57BL6/J mouse purchased from Charles River UK and was transduced with AAV8-PCSK9 (6×10^{12} vg/mouse i.v.). After 12 weeks of a high-fat Western-type diet, (829100, Special Diet Services, UK) atherosclerosis was induced. The mouse was terminally anesthetized at 20 months of age with pentobarbital. It was perfusion fixed via the left ventricle with saline (2 mL) to remove the blood and with 10% v/v buffered formalin (5 mL). Then, the entire aortic tree (aortic arch, surrounding vessels, and heart) was dissected as a single entity and stored in a fixation solution at 4 °C. The sample is consisting of the brachiocephalic artery which is embedded in paraffin wax in a plastic vessel. The experiments were made in agreement and with the approval of the local review board and the UK Home Office under license P5395C858.

Bibliography

[Als-Nielsen, 2011] Als-Nielsen, J. & McMorrow, D. *Elements of Modern X-ray Physics: Second Edition* (2011) (Cited on pages 16–21, 23, 24).

[Ambrozik, 2019] Ambrozik, S., Moffat, T. P., Zhang, C., Miao, H. & Josell, D. Bottom-Up Gold Filling of High Aspect Ratio Trenches. *Journal of The Electrochemical Society* **166,** D443–D451 (2019) (Cited on page 64).

[Andrejewski, 2017] Andrejewski, J. *Characterization of a large field-of-view X-ray dark-field setup and energy-resolved dark-field measurements* MA thesis (Technical University Munich, 2017) (Cited on page 52).

[Andrejewski, 2021] Andrejewski, J. *et al.* Whole-body x-ray dark-field radiography of a human cadaver. *European radiology experimental* **5,** 6 (2021) (Cited on page 9).

[Arai, 2009] Arai, M. & Crawford, K. Neutron Sources and Facilities, Chapter in Neutron Imaging and Applications, p.13–30 (2009) (Cited on pages 30, 31).

[Arrizón, 1994] Arrizón, V. & Ibarra, J. G. Trading visibility and opening ratio in Talbot arrays. *Optics Communications* **112,** 271–277 (1994) (Cited on pages 131, 133).

[Bech, 2013] Bech, M. *et al.* In-vivo dark-field and phase-contrast x-ray imaging. *Scientific Reports* **3,** 3209 (2013) (Cited on page 9).

[Bech, 2010] Bech, M. *et al.* Quantitative x-ray dark-field computed tomography. *Physics in Medicine and Biology* **55,** 5529–5539 (2010) (Cited on page 43).

[Becker, 1986] Becker, E. W., Ehrfeld, W., Hagmann, P., Maner, A. & Münchmeyer, D. Fabrication of microstructures with high aspect ratios and great structural heights by synchrotron radiation lithography, galvanoforming, and plastic moulding (LIGA process). *Microelectronic Engineering* **4,** 35–56 (1986) (Cited on page 54).

[Behling, 2023] Behling, R. *Modern diagnostic X-ray sources: Technology, manufacturing, Reliability* (CRC PRESS, 2023) (Cited on page 5).

[Berujon, 2017] Berujon, S. & Ziegler, E. Near-field speckle-scanning-based x-ray tomography. *Physical Review A* **95,** 063822. eprint: `1612.09286` (2017) (Cited on page 151).

[Bérujon, 2012] Bérujon, S., Ziegler, E., Cerbino, R. & Peverini, L. Two-Dimensional X-Ray Beam Phase Sensing. *Physical Review Letters* **108,** 158102 (2012) (Cited on page 129).

[Birnbacher, 2016] Birnbacher, L. *et al.* Experimental Realisation of High-sensitivity Laboratory X-ray Grating-based Phase-contrast Computed Tomography. *Scientific Reports* **6,** 24022 (2016) (Cited on page 8).

[Buzug, 2008] Buzug, T. *Computed tomography: From photon statistics to modern cone-beam CT* (Springer Berlin Heidelberg, 2008) (Cited on page 50).

[Chabior, 2012] Chabior, M., Schuster, M., Goldammer, M., Schroer, C. & Pfeiffer, F. Influence of the grating profiles on the image quality in grating-based x-ray imaging. *Nuclear Instruments and Methods in Physics Research, Section A: Accelerators, Spectrometers, Detectors and Associated Equipment* **683,** 71–77 (2012) (Cited on page 40).

[Chabior, 2011] Chabior, M. *et al.* Beam hardening effects in grating-based x-ray phase-contrast imaging. *Medical Physics* **38,** 1189–1195 (2011) (Cited on page 118).

[Chadwick, 1932] Chadwick, J. The existence of a neutron. *Proceedings of the Royal Society of London. Series A, Containing Papers of a Mathematical and Physical Character* **136,** 692–708 (1932) (Cited on page 29).

[Chandrashekar, 2015] Chandrashekar, A. & Humayun, R. *Void free tungsten fill in different sized features* US Patent. US20150024592A1. 2015 (Cited on page 67).

[Chandrashekar, 2012] Chandrashekar, A., Humayun, R., Danek, M., Fellis, A. R. & Chang, S. *Depositing tungsten into high aspect ratio features* US Patent. US20120009785A1. 2012 (Cited on page 67).

[Clauser, 1992] Clauser, J. F. & Reinsch, M. W. New theoretical and experimental results in fresnel optics with applications to matter-wave and X-ray interferometry. *Applied Physics B* **54,** 380–395 (1992) (Cited on page 40).

[Clauser, 1997] Clauser, J. F. *Ultrahigh resolution interferometric x-ray imaging* US Patent. US5812629A. 1997 (Cited on page 40).

[Cormack, 1963] Cormack, A. M. Representation of a function by its line integrals, with some radiological applications. *Journal of Applied Physics* **34,** 2722–2727 (1963) (Cited on page 46).

[Crow, 2009] Crow, L. Neutron Detectors for Imaging, Chapter in Neutron Imaging and Applications, p.47–63 (2009) (Cited on pages 33, 34).

[David, 2007] David, C. *et al.* Fabrication of diffraction gratings for hard X-ray phase contrast imaging. *Microelectronic Engineering* **84,** 1172–1177 (2007) (Cited on pages 51, 59, 80).

[Davis, 1995] Davis, T. J., Gao, D., Gureyev, T. E., Stevenson, A. W. & Wilkins, S. W. Phase-contrast imaging of weakly absorbing materials using hard X-rays. *Nature* **373,** 595–598 (1995) (Cited on page 129).

[Donath, 2009] Donath, T. *et al.* Inverse geometry for grating-based x-ray phase-contrast imaging. *Journal of Applied Physics* **106,** 054703 (2009) (Cited on pages 37, 43, 44).

[Dos Santos Rolo, 2018] Dos Santos Rolo, T. *et al.* A Shack-Hartmann Sensor for Single-Shot Multi-Contrast Imaging with Hard X-rays. *Applied Sciences* **8,** 737 (2018) (Cited on pages 36, 129–131, 142, 143).

[Du, 2011] Du, Y., Liu, X., Lei, Y., Guo, J. & Niu, H. Non-absorption grating approach for X-ray phase contrast imaging. *Optics Express* **19,** 22669–22674 (2011) (Cited on page 70).

[Feldkamp, 1984] Feldkamp, L. A., Davis, L. C. & Kress, J. W. Practical cone-beam algorithm. *J. Opt. Soc. Am. A* **1,** 612–619 (1984) (Cited on page 50).

[Frank, 2022] Frank, M. *et al.* Dark-field chest X-ray imaging for the assessment of COVID-19-pneumonia. *Communications Medicine* **2,** 147 (2022) (Cited on page 10).

[Goodman, 1996] Goodman, J. W. *Introduction to Fourier Optics* (McGraw-Hill Series, 1996) (Cited on page 37).

[Gromann, 2017] Gromann, L. B. *et al.* In-vivo X-ray Dark-Field Chest Radiography of a Pig. *Scientific Reports* **7,** 4807 (2017) (Cited on pages 9, 80, 81).

[Grünzweig, 2008a] Grünzweig, C. *et al.* Bulk magnetic domain structures visualized by neutron dark-field imaging. *Applied Physics Letters* **93,** 112504 (2008) (Cited on page 117).

[Grünzweig, 2008b] Grünzweig, C. *et al.* Design, fabrication, and characterization of diffraction gratings for neutron phase contrast imaging. *Review of Scientific Instruments* **79,** 053703 (2008) (Cited on pages 67, 103, 114, 156).

[Günther, 2019] Günther, B. *et al.* Full-field structured-illumination super-resolution X-ray transmission microscopy. *Nature Communications* **10,** 2494 (2019) (Cited on page 151).

[Gustschin, 2018] Gustschin, A., Neuwirth, T., Backs, A., Schulz, M. & Pfeiffer, F. Fabrication of gadolinium particle-based absorption gratings for neutron grating interferometry. *Review of Scientific Instruments* **89,** 103702 (2018) (Cited on pages 69, 106, 107, 111, 112).

[Gustschin, 2016] Gustschin, A. *Alternative Absorption Grating Fabrication Methods for Talbot-Lau Interferometry* MA thesis (Technical University Munich, 2016) (Cited on pages 56, 69, 83).

[Gustschin, 2020] Gustschin, A. *et al.* Comparison of Thermal Neutron and Hard X-ray Dark-Field Tomography. *Journal of Imaging* **7,** 1 (2020) (Cited on pages 117, 119, 121, 123, 125, 126).

[Gustschin, 2021] Gustschin, A. *et al.* High-resolution and sensitivity bi-directional x-ray phase contrast imaging using 2D Talbot array illuminators. *Optica* **8,** 1588–1595 (2021) (Cited on pages 8, 129, 134, 135, 137, 139, 141, 145, 147, 148, 162, 164).

[Gustschin, 2019] Gustschin, N. *et al.* Quality and parameter control of X-ray absorption gratings by angular X-ray transmission. *Optics Express* **27,** 15943–15955 (2019) (Cited on pages 75, 77–79).

[Hahn, 2015] Hahn, D. *et al.* Statistical iterative reconstruction algorithm for X-ray phase-contrast CT. *Scientific Reports* **5,** 10452 (2015) (Cited on page 150).

[Hellbach, 2017] Hellbach, K. *et al.* X-ray dark-field radiography facilitates the diagnosis of pulmonary fibrosis in a mouse model. *Scientific Reports* **7,** 340 (2017) (Cited on page 9).

[Hellerhoff, 2019] Hellerhoff, K. *et al.* Assessment of intraductal carcinoma in situ (DCIS) using grating-based X-ray phase-contrast CT at conventional X-ray sources: An experimental ex-vivo study. *PLOS ONE* **14,** (1): e0210291 (2019) (Cited on page 8).

[Hojo, 2019] Hojo, D., Kamezawa, C., Hyodo, K. & Yashiro, W. Fabrication of X-ray absorption grating using an ultracentrifuge machine. *Japanese Journal of Applied Physics* **58,** 088003 (2019) (Cited on pages 69, 155).

[Hölke, 1999] Hölke, A. & Henderson, H. T. Ultra-deep anisotropic etching of (110) silicon. *Journal of Micromechanics and Microengineering* **9,** 51 (1999) (Cited on pages 84, 87).

[Holler, 2014] Holler, M. *et al.* X-ray ptychographic computed tomography at 16 nm isotropic 3D resolution. *Scientific Reports* **4,** 3857 (2014) (Cited on page 6).

[Hounsfield, 1973] Hounsfield, G. N. Computerized transverse axial scanning (tomography): I. Description of system. *British Journal of Radiology* **46,** 1016–1022 (1973) (Cited on page 46).

[Itoh, 2011] Itoh, H. *et al.* Two-dimensional grating-based X-ray phase-contrast imaging using Fourier transform phase retrieval. *Optics Express* **19,** 3339–3346 (2011) (Cited on page 132).

[Jefimovs, 2021] Jefimovs, K. *et al.* Fabrication of X-ray Gratings for Interferometric Imaging by Conformal Seedless Gold Electroplating. *Micromachines* **12,** 517 (2021) (Cited on pages 59, 62).

[Josell, 2020] Josell, D. *et al.* Pushing the Limits of Bottom-Up Gold Filling for X-ray Grating Interferometry. *Journal of The Electrochemical Society* **167,** 132504 (2020) (Cited on pages 59, 64).

[Jung, 2009] Jung, I. D. Flexible Gd2O2S:Tb scintillators pixelated with polyethylene microstructures for digital x-ray image sensors. *Journal of Micromechanics and Microengineering* **19,** 015014 (2009) (Cited on page 69).

[Kaestner, 2017] Kaestner, A. P. *et al.* Bimodal Imaging at ICON Using Neutrons and X-rays. *Physics Procedia* **88,** 314–321 (2017) (Cited on page 117).

[Kagias, 2019] Kagias, M. *et al.* Diffractive small angle X-ray scattering imaging for anisotropic structures. *Nature Communications* **10,** 5130 (2019) (Cited on pages 36, 62, 129, 130).

[Kak, 2001] Kak, A. C. & Slaney, M. *Principles of Computerized Tomographic Imaging* (Society for Industrial and Applied Mathematics, 2001) (Cited on page 47).

[Kashyap, 2016] Kashyap, Y., Wang, H. & Sawhney, K. Experimental comparison between speckle and grating-based imaging technique using synchrotron radiation X-rays. *Optics Express* **24,** 18664–18673 (2016) (Cited on page 150).

[Kim, 2014] Kim, J., Lee, S. W. & Cho, G. Visibility evaluation of a neutron grating interferometer operated with a polychromatic thermal neutron beam. *Nuclear Instruments and Methods in Physics Research, Section A: Accelerators, Spectrometers, Detectors and Associated Equipment* **746,** 26–32 (2014) (Cited on pages 69, 103).

[Kim, 2013] Kim, J. *et al.* Fabrication and characterization of the source grating for visibility improvement of neutron phase imaging with gratings. *Review of Scientific Instruments* **84,** 063705 (2013) (Cited on pages 69, 103).

[Kim, 2018] Kim, Y., Kim, J., Kim, D., Hussey, D. S. & Lee, S. W. Feasibility evaluation of a neutron grating interferometer with an analyzer grating based on a structured scintillator. *Review of Scientific Instruments* **89,** 033701 (2018) (Cited on page 70).

[Kio, 2018] Kio, O. J. *et al.* Non-destructive evaluation of additively manufactured polymer objects using X-ray interferometry. *Additive Manufacturing* **24,** 364–372 (2018) (Cited on page 10).

[Korenblum, 1958] Korenblum, B., Tetelbaum, S. & Tyutin, A. About one Scheme of Tomography. *Proceedings of Higher Educational Institutions - Radiophysics* **1.** Translation: `https://arxiv.org/abs/2004.03750` (1958) (Cited on page 46).

[Kottler, 2007] Kottler, C., Pfeiffer, F., Bunk, O., Grünzweig, C. & David, C. Grating interferometer based scanning setup for hard X-ray phase contrast imaging. *The Review of scientific instruments* **78,** 043710 (2007) (Cited on pages 80, 144).

[Lamanna, 2017] Lamanna, J. M., Hussey, D. S., Baltic, E. & Jacobson, D. L. Neutron and X-ray Tomography (NeXT) system for simultaneous, dual modality tomography. *Review of Scientific Instruments* **88,** 113702 (2017) (Cited on page 117).

[Lau, 1948] Lau, E. Beugungserscheinungen an Doppelrastern. *Annalen der Physik* **437,** 417–423 (1948) (Cited on page 39).

[Lehmann, 2002] Lehmann, V. & Rönnebeck, S. MEMS techniques applied to the fabrication of anti-scatter grids for X-ray imaging. *Sensors and Actuators A: Physical* **95,** 202–207 (2002) (Cited on page 64).

[Lei, 2016] Lei, Y., Liu, X., Li, J., Guo, J. & Niu, H. Improvement of filling bismuth for x-ray absorption gratings through the enhancement of wettability. *Journal of Micromechanics and Microengineering* **26,** 065011 (2016) (Cited on page 65).

[Lei, 2021] Lei, Y. *et al.* 8-inch-diameter field of view for X-ray differential phase-contrast imaging. *Nuclear Instruments and Methods in Physics Research, Section A: Accelerators, Spectrometers, Detectors and Associated Equipment* **1004,** 165375 (2021) (Cited on page 69).

[Lei, 2019a] Lei, Y. *et al.* An 8-inch absorption grating used in cascaded Talbot-Lau interferometers for X-ray phase-contrast imaging. *Applied Physics Express* **12,** 126504 (2019) (Cited on pages 69, 155).

[Lei, 2014] Lei, Y. *et al.* Fabrication of x-ray absorption gratings via micro-casting for grating-based phase contrast imaging. *Journal of Micromechanics and Microengineering* **24,** 015007 (2014) (Cited on pages 57, 64).

[Lei, 2019b] Lei, Y. *et al.* Tungsten nanoparticles-based x-ray absorption gratings for cascaded Talbot–Lau interferometers. *Journal of Micromechanics and Microengineering* **29,** 115008 (2019) (Cited on page 69).

[Ludwig, 2018] Ludwig, V. *et al.* Non-Destructive Testing of Archaeological Findings by Grating-Based X-Ray Phase-Contrast and Dark-Field Imaging. *Journal of Imaging* **4,** 58 (2018) (Cited on page 10).

[Malecki, 2012] Malecki, A., Potdevin, G. & Pfeiffer, F. Quantitative wave-optical numerical analysis of the dark-field signal in grating-based X-ray interferometry. *Europhysics Letters* **99,** 4 (2012) (Cited on page 43).

[Mamyrbayev, 2020] Mamyrbayev, T. *et al.* Development of an Array of Compound Refractive Lenses for Sub-Pixel Resolution, Large Field of View, and Time-Saving in Scanning Hard X-ray Microscopy. *Applied Sciences* **10,** 4132 (2020) (Cited on pages 130, 151).

[Manke, 2010] Manke, I. *et al.* Three-dimensional imaging of magnetic domains. *Nature Communications* **1,** 125 (2010) (Cited on page 117).

[Mannes, 2015] Mannes, D., Schmid, F., Frey, J., Schmidt-Ott, K. & Lehmann, E. Combined Neutron and X-ray Imaging for Non-invasive Investigations of Cultural Heritage Objects. *Physics Procedia* **69,** 653–660 (2015) (Cited on page 117).

[Mappes, 2012] Mappes, T. *et al.* The Invention of Immersion Ultramicroscopy in 1912—The Birth of Nanotechnology? *Angewandte Chemie International Edition* **51,** 11208–11212 (2012) (Cited on page 2).

[Matsumoto, 2007] Matsumoto, M. *et al.* Fabrication of diffraction grating for X-ray Talbot interferometer. *Microsystem Technologies* **13,** 543–546 (2007) (Cited on pages 51, 54, 80).

[Mechlem, 2020] Mechlem, K., Sellerer, T., Viermetz, M., Herzen, J. & Pfeiffer, F. A theoretical framework for comparing noise characteristics of spectral, differential phase-contrast and spectral differential phase-contrast X-ray imaging. *Physics in Medicine and Biology* **65,** 065010 (2020) (Cited on page 53).

[Modregger, 2007] Modregger, P., Lübbert, D., Schäfer, P. & Köhler, R. Spatial resolution in Bragg-magnified X-ray images as determined by Fourier analysis. *Physica Status Solidi (A) Applications and Materials Science* **204,** 2746–2752 (2007) (Cited on page 149).

[Mohr, 2012] Mohr, J. *et al.* High aspect ratio gratings for X-ray phase contrast imaging. *AIP Conference Proceedings* **1466,** 41–50 (2012) (Cited on page 54).

[Momose, 2009] Momose, A., Yashiro, W., Kuwabara, H. & Kawabata, K. Grating-based X-ray phase imaging using multiline X-ray source. *Japanese Journal of Applied Physics* **48,** 076512 (2009) (Cited on page 70).

[Momose, 2003] Momose, A. *et al.* Demonstration of X-Ray Talbot Interferometry. *Japanese Journal of Applied Physics* **42,** L866–L868 (2003) (Cited on pages 39, 117).

[Morgan, 2011] Morgan, K. S., Paganin, D. M. & Siu, K. K. W. Quantitative single-exposure x-ray phase contrast imaging using a single attenuation grid. *Optics Express* **19,** 19781 (2011) (Cited on pages 129, 130).

[Morgan, 2012] Morgan, K. S., Paganin, D. M. & Siu, K. K. W. X-ray phase imaging with a paper analyzer. *Applied Physics Letters* **100,** 124102 (2012) (Cited on page 129).

[Morgan, 2013] Morgan, K. S. *et al.* A sensitive x-ray phase contrast technique for rapid imaging using a single phase grid analyzer. *Optics Letters* **38,** 4605–4608 (2013) (Cited on pages 132, 143).

[Morimoto, 2015] Morimoto, N. *et al.* Design and demonstration of phase gratings for 2D single grating interferometer. *Optics Express* **23,** 29399–29412 (2015) (Cited on pages 129, 132).

[Neuwirth, 2020] Neuwirth, T. *et al.* A high visibility Talbot-Lau neutron grating interferometer to investigate stress-induced magnetic degradation in electrical steel. *Scientific Reports* **10,** 1764 (2020) (Cited on pages 10, 103, 112, 114, 115).

[Noda, 2008] Noda, D. *et al.* Fabrication of large area diffraction grating using LIGA process. *Microsystem Technologies* **14,** 1311–1315 (2008) (Cited on pages 54, 80).

[Olivo, 2007] Olivo, A. & Speller, R. A coded-aperture technique allowing x-ray phase contrast imaging with conventional sources. *Applied Physics Letters* **91,** 074106 (2007) (Cited on pages 36, 129).

[Paganin, 2002] Paganin, D., Mayo, S. C., Gureyev, T. E., Miller, P. R. & Wilkins, S. W. Simultaneous phase and amplitude extraction from a single defocused image of a homogeneous object. *Journal of Microscopy* **206,** 33–40 (2002) (Cited on page 129).

[Pelzer, 2016] Pelzer, G. *et al.* A beam hardening and dispersion correction for x-ray dark-field radiography. *Medical Physics* **43,** 2774–2779 (2016) (Cited on page 118).

[Peng, 2020] Peng, X. *et al.* Using operando techniques to understand and design high performance and stable alkaline membrane fuel cells. *Nature Communications* **11,** 3561 (2020) (Cited on page 117).

[Pfeiffer, 2008] Pfeiffer, F. *et al.* Hard-X-ray dark-field imaging using a grating interferometer. *Nature Materials* **7,** 134–137 (2008) (Cited on pages 9, 42, 117).

[Pfeiffer, 2006a] Pfeiffer, F. *et al.* Neutron phase imaging and tomography. *Physical Review Letters* **96,** 215505 (2006) (Cited on pages 40, 117).

[Pfeiffer, 2017] Pfeiffer, F. X-ray ptychography. *Nature Photonics* **12,** 9–17 (2017) (Cited on pages 6, 35).

[Pfeiffer, 2006b] Pfeiffer, F., Weitkamp, T., Bunk, O. & David, C. Phase retrieval and differential phase-contrast imaging with low-brilliance X-ray sources. *Nature Physics* **2,** 258–261 (2006) (Cited on pages 8, 40, 117).

[Pinzek, 2018] Pinzek, S. *Towards Low Cost and Large Area Grating Fabrication for Grating-based X-Ray Imaging* MA thesis (Technical University Munich, 2018) (Cited on pages 56, 69, 83, 89, 93).

[Pinzek, 2022] Pinzek, S., Gustschin, A., Gustschin, N., Viermetz, M. & Pfeiffer, F. Fabrication of X-ray absorption gratings by centrifugal deposition of bimodal tungsten particles in high aspect ratio silicon templates. *Scientific Reports* **12,** 5405 (2022) (Cited on pages 70, 88, 92, 93, 102, 154).

[Pinzek, 2021a] Pinzek, S. *et al.* Fabrication of x-ray absorption gratings via deep x-ray lithography using a conventional x-ray tube. *Journal of Micro/Nanopatterning, Materials, and Metrology* **20,** 043801 (2021) (Cited on pages 56, 82).

[Pinzek, 2021b] Pinzek, S. *et al.* Signal Retrieval from Non-Sinusoidal Intensity Modulations in X-ray and Neutron Interferometry Using Piecewise-Defined Polynomial Function. *Journal of Imaging 2021* **7,** 209 (2021) (Cited on page 40).

[Prade, 2017] Prade, F. *et al.* Nondestructive characterization of fiber orientation in short fiber reinforced polymer composites with X-ray vector radiography. *NDT & E International* **86,** 65–72 (2017) (Cited on page 10).

[Prade, 2016] Prade, F. *et al.* Time resolved X-ray Dark-Field Tomography Revealing Water Transport in a Fresh Cement Sample. *Scientific reports* **6,** 29108 (2016) (Cited on page 10).

[PSI, 2022] PSI. *Neutron Physics - Paul Scherrer Institute Website* `https://www.psi.ch/de/niag/neutron-physics` (2022) (Cited on page 30).

[Radon, 1917] Radon, J. Über die Bestimmung von Funktionen durch ihre Integralwerte längs gewisser Mannigfaltigkeiten. *Berichte über die Verhandlungen der Sächsische Akademie der Wissenschaften* **69,** 262–277 (1917) (Cited on page 46).

[Rao, 2017] Rao, A. V. N., Swarnalatha, V. & Pal, P. Etching characteristics of Si110 in 20 wt% KOH with addition of hydroxylamine for the fabrication of bulk micromachined MEMS. *Micro and Nano Systems Letters* **5,** 23 (2017) (Cited on page 59).

[Reich, 2018] Reich, S., dos Santos Rolo, T., Letzel, A., Baumbach, T. & Plech, A. Scalable, large area compound array refractive lens for hard X-rays. *Applied Physics Letters* **112,** 151903 (2018) (Cited on pages 36, 129, 130, 142).

[Reimann, 2015] Reimann, T. *et al.* Visualizing the morphology of vortex lattice domains in a bulk type-II superconductor. *Nature Communications* **6,** 8813 (2015) (Cited on page 117).

[Reimann, 2016] Reimann, T. *et al.* The new neutron grating interferometer at the ANTARES beamline: design, principles and applications. *Journal of Applied Crystallography* **49,** 1488–1500 (2016) (Cited on pages 110, 156).

[Revol, 2011] Revol, V. *et al.* Sub-pixel porosity revealed by x-ray scatter dark field imaging. *Journal of Applied Physics* **110,** 044912 (2011) (Cited on page 10).

[Riedel, 2023] Riedel, M. *et al.* Comparing x-ray phase-contrast imaging using a Talbot array illuminator to propagation-based imaging for non-homogeneous biomedical samples. *Scientific Reports* **13,** 6996 (2023) (Cited on pages 151, 158).

[Rix, 2019] Rix, K. R., Dreier, T., Shen, T. & Bech, M. Super-resolution x-ray phase-contrast and dark-field imaging with a single 2D grating and electromagnetic source stepping. *Physics in Medicine & Biology* **64,** 165009 (2019) (Cited on page 130).

[Romano, 2016] Romano, L., Kagias, M., Jefimovs, K. & Stampanoni, M. Self-assembly nanostructured gold for high aspect ratio silicon microstructures by metal assisted chemical etching. *RSC Advances* **6,** 16025–16029 (2016) (Cited on page 61).

[Romano, 2017a] Romano, L., Vila-Comamala, J., Jefimovs, K. & Stampanoni, M. Effect of isopropanol on gold assisted chemical etching of silicon microstructures. *Microelectronic Engineering* **177,** 59–65 (2017) (Cited on page 61).

[Romano, 2017b] Romano, L. *et al.* High aspect ratio metal microcasting by hot embossing for X-ray optics fabrication. *Microelectronic Engineering* **176,** 6–10 (2017) (Cited on page 66).

[Romano, 2020a] Romano, L. & Stampanoni, M. Microfabrication of X-ray Optics by Metal Assisted Chemical Etching: A Review. *Micromachines 2020* **11,** 589 (2020) (Cited on page 60).

[Romano, 2017c] Romano, L., Vila-Comamala, J., Schift, H., Stampanoni, M. & Jefimovs, K. Hot embossing of Au- and Pb-based alloys for x-ray grating fabrication. *Journal of Vacuum Science and Technology B* **35,** 06G302 (2017) (Cited on page 66).

[Romano, 2020b] Romano, L. *et al.* Metal assisted chemical etching of silicon in the gas phase: a nanofabrication platform for X-ray optics. *Nanoscale Horizons* **5,** 869–879 (2020) (Cited on page 61).

[Röntgen, 1895] Röntgen, W. C. Über eine neue Art von Strahlen. Vorläufige Mitteilung. *Sitzungsberichte der Würzburger Physikalisch- Medizinischen Gesellschaft zu Würzburg,* 137–147 (1895) (Cited on page 14).

[Roubin, 2019] Roubin, E., Andò, E. & Roux, S. The colours of concrete as seen by X-rays and neutrons. *Cement and Concrete Composites* **104,** 103336 (2019) (Cited on page 117).

[Rutishauser, 2011] Rutishauser, S. *et al.* Structured scintillator for hard x-ray grating interferometry. *Applied Physics Letters* **98,** 171107 (2011) (Cited on page 70).

[Saghamanesh, 2017] Saghamanesh, S. *et al.* Edge-illumination x-ray phase contrast imaging with Pt-based metallic glass masks. *Review of Scientific Instruments* **88,** 063705 (2017) (Cited on page 65).

[Samoto, 2019] Samoto, T., Takano, H. & Momose, A. Gadolinium oblique evaporation approach to make large scale neutron absorption gratings for phase imaging. *Japanese Journal of Applied Physics* **58,** SDDF12 (2019) (Cited on pages 67, 103, 114).

[Sato, 2011] Sato, G. *et al.* Two-dimensional gratings-based phase-contrast imaging using a conventional x-ray tube. *Optics Letters* **36,** 3551–3553 (2011) (Cited on page 132).

[Scherer, 2017] Scherer, K. *et al.* X-ray Dark-field Radiography - In-Vivo Diagnosis of Lung Cancer in Mice. *Scientific Reports* **7,** 402 (2017) (Cited on page 9).

[Schoonjans, 2011] Schoonjans, T. *et al.* The xraylib library for X-ray-matter interactions. Recent developments. *Spectrochimica Acta - Part B Atomic Spectroscopy* **66,** 776–784 (2011) (Cited on page 32).

[Schröter, 2017] Schröter, T. J. *et al.* Large-area full field x-ray differential phase-contrast imaging using 2D tiled gratings. *Journal of Physics D: Applied Physics* **50,** 225401 (2017) (Cited on pages 11, 56, 80, 81).

[Schüttler, 2016] Schüttler, M. *et al.* Height control for small periodic structures using x-ray radiography. *Measurement Science and Technology* **27,** 025015 (2016) (Cited on page 75).

[Sears, 1992] Sears, V. F. Neutron scattering lengths and cross sections. *Neutron News* **3,** 26–37 (1992) (Cited on pages 32, 53).

[Seidel, 1990] Seidel, H., Csepregi, L., Heuberger, A. & Baumgärtel, H. Anisotropic Etching of Crystalline Silicon in Alkaline Solutions: I . Orientation Dependence and Behavior of Passivation Layers. *Journal of The Electrochemical Society* **137,** 3612–3626 (1990) (Cited on page 59).

[Seki, 2017] Seki, Y. *et al.* Development of multi-colored neutron Talbot-Lau interferometer with absorption grating fabricated by imprinting method of metallic glass. *Journal of the Physical Society of Japan* **86,** 044001 (2017) (Cited on page 69).

[Senck, 2018] Senck, S. *et al.* Microcrack characterization in loaded CFRP laminates using quantitative two- and three-dimensional X-ray dark-field imaging. *Composites Part A: Applied Science and Manufacturing* **115,** 206–214 (2018) (Cited on page 10).

[Shimura, 2013] Shimura, T. *et al.* Hard x-ray phase contrast imaging using a tabletop Talbot-Lau interferometer with multiline embedded x-ray targets. *Optics Letters* **38,** 157–159 (2013) (Cited on page 70).

[Song, 2008] Song, C., Wang, P. & Makse, H. a. A phase diagram for jammed matter. *Nature* **453,** 629–632 (2008) (Cited on pages 69, 89).

[Song, 2019] Song, T.-E. *et al.* Evaluation of grating realized via pulse current electroplating combined with atomic layer deposition as an x-ray grating interferometer. *Journal of Vacuum Science and Technology A* **37,** 030903 (2019) (Cited on page 64).

[Squires, 2012] Squires, G. L. *Introduction to the Theory of Thermal Neutron Scattering* 3rd ed. (Cambridge University Press, 2012) (Cited on pages 29, 32).

[Stockmar, 2013] Stockmar, M. *et al.* Near-field ptychography: phase retrieval for inline holography using a structured illumination. *Scientific Reports* **3,** 1927 (2013) (Cited on page 150).

[Strobl, 2008] Strobl, M. *et al.* Neutron dark-field tomography. *Physical Review Letters* **101,** 123902 (2008) (Cited on page 117).

[Suleski, 1997] Suleski, T. J. Generation of Lohmann images from binary-phase Talbot array illuminators. *Applied Optics* **36,** 4686–4691 (1997) (Cited on pages 37, 131, 132).

[Szwaykowski, 1993] Szwaykowski, P. & Arrizon, V. Talbot array illuminator with multilevel phase gratings. *Applied Optics* **32,** 1109–1114 (1993) (Cited on pages 131, 133).

[Talbot, 1836] Talbot, H. LXXVI. Facts relating to optical science. No. IV. *Philosophical Magazine Series 3* **9,** 401–407 (1836) (Cited on page 37).

[Tao, 2021] Tao, S., He, C., Hao, X., Kuang, C. & Liu, X. Principles of Different X-ray Phase-Contrast Imaging: A Review. *Applied Sciences 2021* **11,** 2971 (2021) (Cited on page 35).

[Tengattini, 2020] Tengattini, A. *et al.* NeXT-Grenoble, the Neutron and X-ray tomograph in Grenoble. *Nuclear Instruments and Methods in Physics Research, Section A: Accelerators, Spectrometers, Detectors and Associated Equipment* **968,** 163939 (2020) (Cited on page 117).

[Tetelbaum, 1957] Tetelbaum, S. About a Method of Obtaining Volumetric Images by Means of X-ray Radiation. *Bulletin of the Kiev Polytechnic Institute* **22.** Translation: `https://arxiv.org/abs/2001.03806` (1957) (Cited on page 46).

[Viermetz, 2022] Viermetz, M. *et al.* Dark-field computed tomography reaches the human scale. *Proceedings of the National Academy of Sciences of the United States of America* **119,** e2118799119 (2022) (Cited on pages 10, 45, 97).

[Viermetz, 2018] Viermetz, M. *et al.* High resolution laboratory grating-based X-ray phase-contrast CT. *Scientific Reports* **8,** 15884 (2018) (Cited on page 8).

[Vila-Comamala, 2018] Vila-Comamala, J. *et al.* Towards sub-micrometer high aspect ratio X-ray gratings by atomic layer deposition of iridium. *Microelectronic Engineering* **192,** 19–24 (2018) (Cited on pages 62, 68).

[Vitale, 2015] Vitale, W. A. *et al.* Fine pitch 3D-TSV based high frequency components for RF MEMS applications. *IEEE Proceedings - Electronic Components and Technology Conference (ECTC)* **65,** 585–590 (2015) (Cited on page 67).

[Wan, 2008] Wan, K., Takeda, Y., Yashiro, W. & Momose, A. Fabrication of multiple slit using stacked-sliced method for hard X-ray Talbot-Lau interferometer. *Japanese Journal of Applied Physics* **47,** 7412–7414 (2008) (Cited on page 71).

[Wang, 2016] Wang, H., Kashyap, Y., Cai, B. & Sawhney, K. High energy X-ray phase and dark-field imaging using a random absorption mask. *Scientific Reports* **6,** 30581 (2016) (Cited on page 151).

[Wang, 2019] Wang, H. *et al.* High-energy, high-resolution, fly-scan X-ray phase tomography. *Scientific Reports* **9,** 8913 (2019) (Cited on page 150).

[Wang, 2015] Wang, X., Liu, J., Wang, A. & Ingle, N. *Even tungsten etch for high aspect ratio trenches* US Patent. US9190293B2. 2015 (Cited on page 67).

[Wang, 2004] Wang, Z. & Han, B. Advanced iterative algorithm for phase extraction of randomly phase-shifted interferograms. *Optics Letters* **29,** 14 (2004) (Cited on page 120).

[WHO, 2020] WHO. *The top 10 causes of death* URL: `https://www.who.int/news-room/fact-sheets/detail/the-top-10-causes-of-death`. 2020 (Cited on page 9).

[Willer, 2021] Willer, K. *et al.* X-ray dark-field chest imaging for detection and quantification of emphysema in patients with chronic obstructive pulmonary disease: a diagnostic accuracy study. *The Lancet Digital Health* **3,** e733–e744 (2021) (Cited on pages 9, 70, 81, 117).

[Willer, 2018] Willer, K. *et al.* X-ray dark-field imaging of the human lung—A feasibility study on a deceased body. *PLOS ONE* **13,** e0204565 (2018) (Cited on page 9).

[Willner, 2016] Willner, M. *et al.* Quantitative Three-Dimensional Imaging of Lipid, Protein, and Water Contents via X-Ray Phase-Contrast Tomography. *PLOS ONE* **11,** e0151889 (2016) (Cited on page 8).

[Winthrop, 1965] Winthrop, J. T. & Worthington, C. R. Theory of Fresnel Images I Plane Periodic Objects in Monochromatic Light. *Journal of the Optical Society of America* **55,** 373–381 (1965) (Cited on page 132).

[Wolff, 2023] Wolff, J. O. *et al.* MINFLUX dissects the unimpeded walking of kinesin-1. *Science* **379,** 1004–1010 (2023) (Cited on page 4).

[Wu, 2010] Wu, B., Kumar, A. & Pamarthy, S. High aspect ratio silicon etch: A review. *Journal of Applied Physics* **108,** 051101 (2010) (Cited on pages 58, 59).

[Wu, 2021] Wu, H. *et al.* Fabrication of X-ray absorption grating by thermal composite method. *Japanese Journal of Applied Physics* **60,** 076506 (2021) (Cited on page 71).

[Yaroshenko, 2014] Yaroshenko, A. *et al.* Non-binary phase gratings for x-ray imaging with a compact Talbot interferometer. *Optics Express* **22,** 547 (2014) (Cited on page 45).

[Yashiro, 2015] Yashiro, W., Vagovič, P. & Momose, A. Effect of beam hardening on a visibility-contrast image obtained by X-ray grating interferometry. *Optics Express* **23,** 23462–23471 (2015) (Cited on pages 43, 118).

[Yashiro, 2014] Yashiro, W. *et al.* A metallic glass grating for X-ray grating interferometers fabricated by imprinting. *Applied Physics Express* **7,** 032501 (2014) (Cited on page 65).

[Yashiro, 2016] Yashiro, W. *et al.* X-ray phase imaging using a Gd-based absorption grating fabricated by imprinting technique. *Japanese Journal of Applied Physics* **55,** 048003 (2016) (Cited on pages 65, 114).

[Ye, 2018] Ye, X., Li, Y., Ai, Y. & Nie, Y. Novel powder packing theory with bimodal particle size distribution-application in superalloy. *Advanced Powder Technology* **29,** 2280–2287 (2018) (Cited on page 89).

[Zakharova, 2018] Zakharova, M. *et al.* Development and Characterization of Two-Dimensional Gratings for Single-Shot X-ray Phase-Contrast Imaging. *Applied Sciences* **8,** 468 (2018) (Cited on page 129).

[Zakharova, 2019] Zakharova, M. *et al.* Inverted Hartmann mask for single-shot phase-contrast x-ray imaging of dynamic processes. *Optics Letters* **44,** 2306–2309 (2019) (Cited on page 130).

[Zambrano, 2019] Zambrano, M., Hameed, F., Anders, K., Mancini, L. & Tondi, E. Implementation of Dynamic Neutron Radiography and Integrated X-Ray and Neutron Tomography in Porous Carbonate Reservoir Rocks. *Frontiers in Earth Science* **7,** 329 (2019) (Cited on page 117).

[Zanette, 2014] Zanette, I. *et al.* Speckle-Based X-Ray Phase-Contrast and Dark-Field Imaging with a Laboratory Source. *Physical Review Letters* **112,** 253903 (2014) (Cited on page 129).

[Zanette, 2010] Zanette, I., Weitkamp, T., Donath, T., Rutishauser, S. & David, C. Two-Dimensional X-Ray Grating Interferometer. *Physical Review Letters* **105,** 248102 (2010) (Cited on page 129).

[Zdora, 2018] Zdora, M.-C. State of the Art of X-ray Speckle-Based Phase-Contrast and Dark-Field Imaging. *Journal of Imaging* **4,** 60 (2018) (Cited on pages 35, 130, 138, 142, 161).

[Zhou, 2016] Zhou, T. *et al.* Noise analysis of speckle-based x-ray phase-contrast imaging. *Optics Letters* **41,** 5490–5493 (2016) (Cited on pages 130, 143, 163).

[Ziesche, 2020] Ziesche, R. F. *et al.* 4D imaging of lithium-batteries using correlative neutron and X-ray tomography with a virtual unrolling technique. *Nature Communications* **11,** 777 (2020) (Cited on page 117).

Publications / Presentations

Publications as (shared) first author

A. Gustschin, T. Neuwirth, A. Backs, M. Schulz & F. Pfeiffer. Fabrication of gadolinium particle-based absorption gratings for neutron grating interferometry
Review of Scientific Instruments **89**, 103702 (2018).

N. Gustschin, A. Gustschin, P. Meyer, M. Viermetz, P. Riederer, J. Herzen, J. Mohr & F. Pfeiffer. Quality and parameter control of X-ray absorption gratings by angular X-ray transmission *Optics Express* **27**, (11) 15943-15955 (2019).

A. Gustschin, T. Neuwirth, A. Backs, M. Viermetz, N. Gustschin, M. Schulz & F. Pfeiffer. Comparison of Thermal Neutron and Hard X-ray Dark-Field Tomography
Journal of Imaging **7**, 1 (2020).

A. Gustschin, M. Riedel, K. Taphorn, C. Petrich, W. Gottwald, W. Noichl, M. Busse, S.E. Francis, F. Beckmann, J. U. Hammel, J.Moosmann, P. Thibault & J. Herzen. High-resolution and sensitivity bi-directional X-ray phase-contrast imaging using 2D Talbot array illuminators *Optica* **8**, (12) 1588-1595 (2021).

Conference/Poster presentations

Fabrication and Characterization of Gd particle-based Neutron Absorption Gratings
International Conference on X-ray and Neutron Phase Imaging with Gratings (XNPIG), Sendai, Japan, October 2019

Quality assessment of X-ray absorption gratings by angular X-ray transmission
International Symposium on Biomedical Applications of X-ray Phase-Contrast Imaging (IMXP), Garmisch-Partenkirchen, Germany, January 2019

Publications as coauthor

K. Willer, A. A. Fingerle, W. Noichl, F. De Marco, M. Frank, T. Urban, R. Schick, A. Gustschin, B. Gleich, J. Herzen, T. Koehler, A. Yaroshenko, T. Pralow, G. S. Zimmermann, B. Renger, A. P. Sauter, D. Pfeiffer, M. R. Makowski, E. J. Rummeny, P. A. Grenier & F. Pfeiffer. X-ray dark-field chest imaging for detection and quantification of emphysema in patients with chronic obstructive pulmonary disease: a diagnostic accuracy study *The Lancet Digital Health* **3**, (11) 733-744 (2021).

T. Neuwirth, A. Backs, A. Gustschin, S. Vogt, F. Pfeiffer, P. Böni & M. Schulz. A high visibility Talbot-Lau neutron grating interferometer to investigate stress-induced magnetic degradation in electrical steel *Scientific Reports* **10**, (1) 1-12 (2020).

J. Rus, A. Gustschin, H. Mooshofer, J. Grager, K. Bente, M. Gaal, F. Pfeiffer & C. U. Grosse. Qualitative comparison of non-destructive methods for inspection of carbon fiber-reinforced polymer laminates
Journal of Composite Materials **54**, (27) 4325-4337 (2020).

E. Braig, N. Roiser, M. A. Kimm, M. Busse, J. Andrejewski, J. Scholz, C. Petrich, A. Gustschin, A. Sauter, J. Bodden, F. Meurer, R. Korbel, F. Pfeiffer, J. Herzen & D. Pfeiffer. X-ray dark-field radiography: potential for visualization of monosodium urate deposition *Investigative radiology* **55**, (8) 494-498 (2020).

S. Allner, A. Gustschin, A. Fehringer, P. B. Noël & F. Pfeiffer. Metric-guided regularisation parameter selection for statistical iterative reconstruction in computed tomography *Scientific reports* **9**, (1) 6016 (2019).

S. Vogt, T. Neuwirth, B. Schauerte, H. A. Weiss, P. M. Falger, A. Gustschin, M. Schulz, K. Hameyer & Wolfram Volk. Extent of embossing-related residual stress on the magnetic properties evaluated using neutron grating interferometry and single sheet test
Production Engineering **13**, 211-217 (2019).

J. Andrejewski, F. De Marco, K. Willer, W. Noichl, A. Gustschin, T. Koehler, P. Meyer, F. Kriner, F. Fischer, C. Braun, A. A. Fingerle, J. Herzen, F. Pfeiffer & D. Pfeiffer. Whole-body x-ray dark-field radiography of a human cadaver
European Radiology Experimental **5**, (1) 1-9 (2021).

M. Riedel, A. Gustschin, L. Ushakov, W. Noichl, K. Taphorn, M. Busse, F. Beckmann, J. U. Hammel, J. Moosmann, P. Thibault & J. Herzen. High-resolution quantitative phase-contrast x-ray imaging for biomedical samples at PETRA III
SPIE Conference: Developments in X-Ray Tomography XIII **11840**, 123-131 (2021).

W. Noichl, F. De Marco, K. Willer, T. Urban, M. Frank, R. Schick, B. Gleich, L. Hehn, A. Gustschin, P. Meyer, T. Koehler, H. Maack, K. Engel, B. Lundt, B. Renger, A. Fingerle, D. Pfeiffer, E. Rummeny, J. Herzen & F. Pfeiffer. Correction for mechanical inaccuracies in a scanning Talbot-Lau interferometer
TechRxiv, https://doi.org/10.36227/techrxiv.21201475.v1 (2022).

S. Pinzek, T. Beckenbach, M. Viermetz, P. Meyer, A. Gustschin, J. Andrejewski, N. Gustschin, J. Herzen, J. Schulz & F. Pfeiffer. Fabrication of x-ray absorption gratings via deep x-ray lithography using a conventional x-ray tube
Journal of Micro/Nanopatterning, Materials, and Metrology, **20**, (4) 43801 (2021).

S. Pinzek, A. Gustschin, N. Gustschin, M. Viermetz & F. Pfeiffer. Fabrication of X-ray absorption gratings by centrifugal deposition of bimodal tungsten particles in high aspect ratio silicon templates
Scientific Reports, **12**, (1) 5405 (2022).

N. Gustschin, A. Gustschin, F. Epple, S. Allner, K. Achterhold, J. Herzen & F. Pfeiffer. Signal-to-thickness calibration and pixel-wise interpolation for beam-hardening artefact reduction in microCT
Europhysics Letters, **125**, (3) 38003 (2019).

S. Pinzek, A. Gustschin, T. Neuwirth, A. Backs, M. Schulz, J. Herzen & F. Pfeiffer. Signal Retrieval from Non-Sinusoidal Intensity Modulations in X-ray and Neutron Interferometry Using Piecewise-Defined Polynomial Function
Journal of Imaging, **7**, (10) 209 (2021).

J. Andrejewski, F. De Marco, K. Willer, W. Noichl, T. Urban, M. Frank, A. Gustschin, P. Meyer, T. Koehler, F. Pfeiffer & Julia Herzen. Retrieval of 3D information in X-ray dark-field imaging with a large field of view
Scientific reports, **11**, (1) 23504 (2021).

J. Andrejewski, F. De Marco, K. Willer, W. Noichl, T. Urban, M. Frank, A. Gustschin, P. Meyer, T. Koehler, F. Pfeiffer & Julia Herzen. Retrieval of 3D information in X-ray dark-field imaging with a large field of view
Scientific reports, **11**, (1) 23504 (2021).

M. Riedel, K. Taphorn, A. Gustschin, M. Busse, J. U. Hammel, J. Moosmann, F. Beckmann, F. Fischer, P. Thibault & J. Herzen. Comparing x-ray phase-contrast imaging using a Talbot array illuminator to propagation-based imaging for non-homogeneous biomedical samples
Scientific reports, **13**, (1) 6996 (2023).

Acknowledgments

I would like to express my gratitude to many people who have accompanied me along this journey. Without their support and assistance, it would hardly be possible to achieve the scientific results presented in this work. I want to express my gratitude to:

- Prof. Franz Pfeiffer for giving me the opportunity to work on this challenging topic and providing funding, infrastructure, and a prolific research environment with many unique and wonderful people. Thank you Franz for believing in some of my unconventional ideas and giving me freedom and possibilities to explore them.

- Prof. Julia Herzen for supporting and mentoring me, providing advice and guidance, and helping to come up with appropriate answers to the reviewers. Thank you Julia for introducing me to the synchrotron work at DESY and for your tireless support during the long beam times in Hamburg!

- Simon Pinzek for taking the challenge to work with me on the grating fabrication methods in his Master Thesis and decided to explore this subject in further depth in his dissertation. Thank you Simon for your invaluable contribution to the success of our project through a lot of work, creativity, patience, and perseverance.

- Niko Gustschin, who supported me in many various ways from experimental work, software development, 3D printing, and manuscript writing to free time activities and endless night talks about new ideas. Thanks, Niko for keeping me motivated and exploring many exciting ideas with me.

- Konstantin Willer, who supervised me during my Master's Thesis and introduced me to the experimental work for grating-based imaging. I also enjoyed helping with the assembly of the clinical radiography dark-field scanner, which was an exciting project with many things to learn and challenges to master. Great respect for you, Konstantin, for building the scanner from scratch and following through to the end, setting a milestone for dark-field radiography!

- Manuel Viermetz for implementing lots of hardware for our setups and designing the dark-field CT system that we could test our gratings with. Thanks also for the implementation of the simulation framework gXsim which proved extremely helpful for design and experimental work.

- Our grating fabrication specialists. I would like to acknowledge the efforts of the former group of Dr. Jürgen Mohr at the Karlsruhe Institute of Technology (KIT), particularly Pascal Meyer and Tobias Schröter who provided gratings for most of our setups. Joachim Schulz, Thomas Beckenbach, and others at Microworks GmbH are acknowledged for their close collaboration and for accepting our challenging grating specifications. I would also thank Thomas Geiling and his colleagues from 5 microns GmbH as well as Fritz Herrmann and colleagues from Fraunhofer IPMS for close collaboration in grating fabrication. Without the expertise and hard work of all these microfabrication specialists most of our research work would not be possible.

- The Neutron Imaging group at MLZ / FRM II led by Michael Schulz for all the collaborative efforts regarding the neutron gratings and nGI measurements. Thank you, Michel Schulz, Tobias Neuwirth, Alex Backs, and Simon Sebold for the exciting collaboration and for becoming my new colleagues in my next employment.

- All the people who joined the beamtimes at DESY and supported us during the experiments: Mirko Riedel, Kirsten Taphorn, Fabio De Marko, Wolfgang Noichl, Jana Andrejewski, Christian Petrich, Lev Ushakov, Elena Moralez, Wolfgang Gottwald and instrument scientists Felix Beckmann, Jörg U. Hammel, Fabian Wilde, and Julian Moosman. Sheila E. Francis and Madleen Busse are acknowledged for providing samples.

- Klaus Achterhold for keeping the microCT scanners maintained and working, which were very important tools for this thesis.

- Madleen Busse for keeping the chemistry lab well equipped and safe as well as all useful advice regarding working with chemicals.

- Martin Dierolf, Wolfgang Noichl, and Clemens Schmid for keeping the compute servers and the IT infrastructure at E17 running.

- The X-AID development team for their great software solution for CT reconstruction.

- Alen Begic for machining various customized parts for our setups.

- Nelly de Leiris for her help with processing orders, receiving packages and taking care of many other administrative tasks.
- Simon Pinzek, Niko Gustschin, and Christopher Smith for proofreading parts of the thesis and coming up with helpful suggestions for improvement.
- All my other office colleagues and lab partners at E17, who made it a productive, fun, and enjoyable time: Benedikt, Florian, Johannes, Manuela, Jakob, Maximilian, Clemens, Manuel, Thorsten, Theresa, Juanjuan, Lisa, Stephan, Eva, Simone, Fabio, Stephanie, Korbinian, Lorenz, Jonathan, Regine, Mark, and Christoph.

Finally, I would like to thank my friends and family who have supported me throughout my doctoral studies. Sometimes they encouraged and motivated me to persevere, other times they kept me from working too much and made sure I maintained a reasonable work-life balance. Thank you for standing by me through this challenging endeavor.